

This Page Is Inserted by IFW Operations
and is not a part of the Official Record

BEST AVAILABLE IMAGES

Defective images within this document are accurate representations of the original documents submitted by the applicant.

Defects in the images may include (but are not limited to):

- BLACK BORDERS
- TEXT CUT OFF AT TOP, BOTTOM OR SIDES
- FADED TEXT
- ILLEGIBLE TEXT
- SKEWED/SLANTED IMAGES
- COLORED PHOTOS
- BLACK OR VERY BLACK AND WHITE DARK PHOTOS
- GRAY SCALE DOCUMENTS

IMAGES ARE BEST AVAILABLE COPY.

**As rescanning documents *will not* correct images,
please do not report the images to the
Image Problem Mailbox.**

THIS PAGE BLANK (USPTO)

STABILITY OF A COATING FLOW

BIXLER, NATHAN EPH

DEGREE DATE: 1982

UMI Dissertation
Services

This is an authorized facsimile, made from the microfilm master copy of the original dissertation or master thesis published by UMI.

The bibliographic information for this thesis is contained in UMI's Dissertation Abstracts database, the only central source for accessing almost every doctoral dissertation accepted in North America since 1861.

UMI Dissertation Services

A Bell & Howell Company

300 North Zeeb Road
P.O. Box 1346
Ann Arbor, Michigan 48106-1346
1-800-521-0600 734-761-4700
<http://www.umi.com>

Printed in 1998 by digital xerographic process
on acid-free paper

DPGT

INFORMATION TO USERS

This reproduction was made from a copy of a document sent to us for microfilming. While the most advanced technology has been used to photograph and reproduce this document, the quality of the reproduction is heavily dependent upon the quality of the material submitted.

The following explanation of techniques is provided to help clarify markings or notations which may appear on this reproduction.

1. The sign or "target" for pages apparently lacking from the document photographed is "Missing Page(s)". If it was possible to obtain the missing page(s) or section, they are spliced into the film along with adjacent pages. This may have necessitated cutting through an image and duplicating adjacent pages to assure complete continuity.
2. When an image on the film is obliterated with a round black mark, it is an indication of either blurred copy because of movement during exposure, duplicate copy, or copyrighted materials that should not have been filmed. For blurred pages, a good image of the page can be found in the adjacent frame. If copyrighted materials were deleted, a target note will appear listing the pages in the adjacent frame.
3. When a map, drawing or chart, etc., is part of the material being photographed, a definite method of "sectioning" the material has been followed. It is customary to begin filming at the upper left hand corner of a large sheet and to continue from left to right in equal sections with small overlaps. If necessary, sectioning is continued again—beginning below the first row and continuing on until complete.
4. For illustrations that cannot be satisfactorily reproduced by xerographic means, photographic prints can be purchased at additional cost and inserted into your xerographic copy. These prints are available upon request from the Dissertations Customer Services Department.
5. Some pages in any document may have indistinct print. In all cases the best available copy has been filmed.

University
Microfilms
International

300 N. Zeeb Road
Ann Arbor, MI 48106

8308026

Bixler, Nathan Ephraim

STABILITY OF A COATING FLOW

University of Minnesota

Ph.D. 1982

University
Microfilms
international 300 N. Zeeb Road, Ann Arbor, MI 48106

Copyright 1983

by

Bixler, Nathan Ephraim

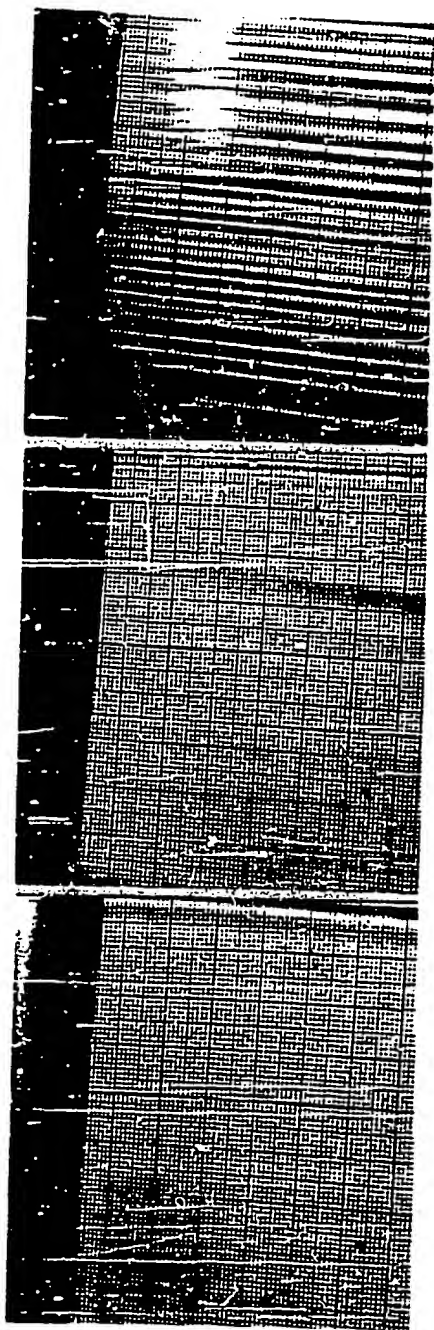
All Rights Reserved

PLEASE NOTE:

In all cases this material has been filmed in the best possible way from the available copy.
Problems encountered with this document have been identified here with a check mark ☒.

1. Glossy photographs or pages ☒
2. Colored illustrations, paper or print ☐
1. Photographs with dark background ☒
1. Illustrations are poor copy ☐
1. Pages with black marks, not original copy ☐
1. Print shows through as there is text on both sides of page ☐
1. Indistinct, broken or small print on several pages ☒
1. Print exceeds margin requirements ☐
1. Tightly bound copy with print lost in spine ☐
3. Computer printout pages with indistinct print ☐
1. Page(s) lacking when material received, and not available from school or author.
2. Page(s) seem to be missing in numbering only as text follows.
1. Two pages numbered . Text follows.
1. Curling and wrinkled pages ☐
1. Other

University
Microfilms
International



WEB SPEED = 0.5 cm/s
 $Ca = 0.09$

WEB SPEED = 2.5 cm/s
 $Ca = 0.45$

WEB SPEED = 10 cm/s
 $Ca = 1.8$

STABILITY OF A COATING FLOW

A THESIS
SUBMITTED TO THE FACULTY OF THE GRADUATE SCHOOL
OF THE UNIVERSITY OF MINNESOTA

BY

NATHAN EPHRAIM BIXLER

IN PARTIAL FULFILLMENT OF THE REQUIREMENTS
FOR THE DEGREE OF
DOCTOR OF PHILOSOPHY

JUNE 1932

Antispiece: A uniform flow (left) beneath a cylindrical spreader loses stability (center: onset of instability) to a transversely periodic ribbing disturbance (right) as web speed increases (see Figure 1.7). Web motion is from top to bottom in each of the frames.

TABLE OF CONTENTS

	<u>Page</u>
Acknowledgements	i
1. Prelude	1
1.1. Introduction	1
1.2. Governing equations and boundary conditions	5
1.3. Steady two-dimensional coating flows	8
1.4. Steady three-dimensional coating flows	12
1.5. Stability of steady two-dimensional coating flows	16
2. Steady, Three-Dimensional, Liquid Film Redistribution on a Moving Web	
2.1. Introduction	26
2.2. Oseen and lubrication equations	33
2.3. Lubrication solution	37
2.4. Oseen solution	38
2.5. Limiting cases and numerical results	56
2.6. Discussion	65
2.7. Extensions of the Oseen analysis	86
3. Lubrication Analysis of the Stability of Slot and Knife Coating	
3.1. Introduction	89
3.2. Lubrication equation and boundary conditions	90
3.3. Two-dimensional base flows	100
3.4. Stability of base flows	102
3.5. Discussion	111

	<u>Page</u>
1. Analysis of Steady Two-Dimensional Slot and Knife Coating Flows	
4.1. Introduction	113
4.2. Galerkin/finite element formulation	118
4.3. Comparison of outflow boundary conditions	133
4.4. Discussion	142
2. Finite Element Analysis of Coating Instabilities	
5.1. Introduction	147
5.2. Formulation of the stability problem	152
5.3. Methods of eigenanalysis for the stability problem	171
5.4. Discussion	180
3. Stability of Slot and Knife Coating	
6.1. Introduction	183
6.2. Stability analysis	184
6.3. Stability of slot and knife coating	186
6.4. Mechanism of instability	193
6.5. Discussion	206
4. Conclude	215
5. Appendix A: Stewart's Algorithm for the Asymmetric Eigenproblem	223
6. Bibliography	244

ACKNOWLEDGEMENTS

I wish to acknowledge my sincere appreciation to my advisor, Professor L. E. Scriven, for his wisdom, encouragement, and constant insistence on excellence during the course of this work.

I am also indebted to my colleagues in Room 60, especially to Bob Brown, Bill Silliman, Brian Higgins, and Hiroki Saito, for many valuable ideas and insights. The success of this thesis is due largely to their contributions.

Financial support was provided by the National Science Foundation, a Kodak Fellowship, and the University Computer Center.

Finally, the constant encouragement of my wife, Mary, and of my parents is recognized as the most important support of all.

CHAPTER 1 - PRELUDE

1.1. Introduction

Coating the surface of a solid or flexible sheet uniformly with a thin film of liquid is important in a variety of scientific and industrial applications. Imperfections in the coating, especially as the speed of coating is increased or the coating thickness is decreased, are mostly due to flow instabilities and various wetting and edge effects. The goal of this thesis is to understand, by means of theoretical analysis and computer simulation, some of the instabilities in thin liquid films as they are deposited, and the nonuniformities of film thickness that result. These are matters of hydrodynamic instability and bifurcation or branching of families of flow states, for which conventional theoretical approaches and more novel computer-based methods are advancing. At the center of this thesis is the extension to film-flow problems of Galerkin/finite element methods of stability analysis recently developed by Brown and Scriven (1980a) and also reported in Brown's thesis (1979) for liquid drops in hydrostatic equilibrium, which are simpler to treat than flowing liquid films.

This thesis is built upon a foundation laid by a host of contributors. As mentioned in the foregoing paragraph, one of the most important of them was Brown. Much of the success of this thesis is owed to the experience and insights gained by Orr (1976), Silliman (1979, 1980 with Scriven), and Saito (1981 with Scriven) by their efforts to develop and improve Galerkin/finite element algorithms for solving steady, two-dimensional, free surface flow problems. These earlier works are sum-

marized in a recent article by Kistler and Scriven (1982), who also describe several improvements and generalizations that have been recently devised. Finally, an asymptotic analysis worked out by Higgins (1980, 1982) showing how film flows approach a final regime is the cornerstone of Chapter 2 and plays an important role in the methods described in Chapters 4 and 5.

Understanding the mechanisms of instability of uniform flowing films is not only a scientific challenge on the frontier of capillary hydrodynamics: such understanding will point the way to avoiding or at least controlling imperfections and incipient film breakdowns wherever they are not absolutely inherent in a coating system.

Capillary Hydrodynamics and Coating Flows. By their very nature, coating flows are free surface flows. Free surfaces are menisci, i.e. liquid/gas interfaces, and their presence greatly complicates flow field analyses because their location, and thus the flow domain, is not known a priori. Menisci are in reality layers of finite thickness in which density varies rapidly from that of bulk liquid to that of bulk gas. However, the thicknesses are usually no more than tens of Angstroms and therefore are nearly infinitesimal in comparison with fluid mechanical length scales. It is convenient to approximate menisci as mathematical surfaces. The steep density gradients at a meniscus give rise to a property known as surface tension which produces an isotropic capillary stress within the meniscus not unlike that in a stretched rubber membrane.

Another feature common to coating flows is that they contain three-

phase contact lines where menisci intersect solid surfaces. Contact lines come in two varieties: (1) they are static if their position relative to the solid boundary is steady; (2) they are dynamic if they translate relative to the solid boundary. Dynamic contact lines are also called wetting lines. Every coating flow has a wetting line because liquid must come in contact with a dry web, i.e. the sheet being coated. Most coating flows also have static contact lines at the place where the liquid being coated leaves the coating die.

Figure 1.1 portrays five commonly used devices; apart from the knife coater they are suitable for premetered, precision coating. The slot coater, also called the extrusion coater, consists of a solid die through which liquid is extruded at a metered rate. The die may be parallel or inclined to the moving web that is supported on the opposite side by a back-up roll, or in some cases stretched between two rolls not far apart. The downstream separating contact line can be pinned at a geometrical or compositional discontinuity, as it is in Figure 1.1, or it can be free to move along the solid die. The knife coater is essentially the downstream portion of the slot coater. The roll coater consists of two rolls, one of which usually supports a web. The liquid entrained between the rolls splits at the meniscus so that part adheres to the web and the remainder is carried away by one of the rolls. A common variation on roll coating is reverse roll coating in which the two rolls are made to corotate instead of counterrotate. Coyle et al. (1992a,b) have investigated roll coating in both modes of operation by finite element analysis. The slide coater is made up of a die which is

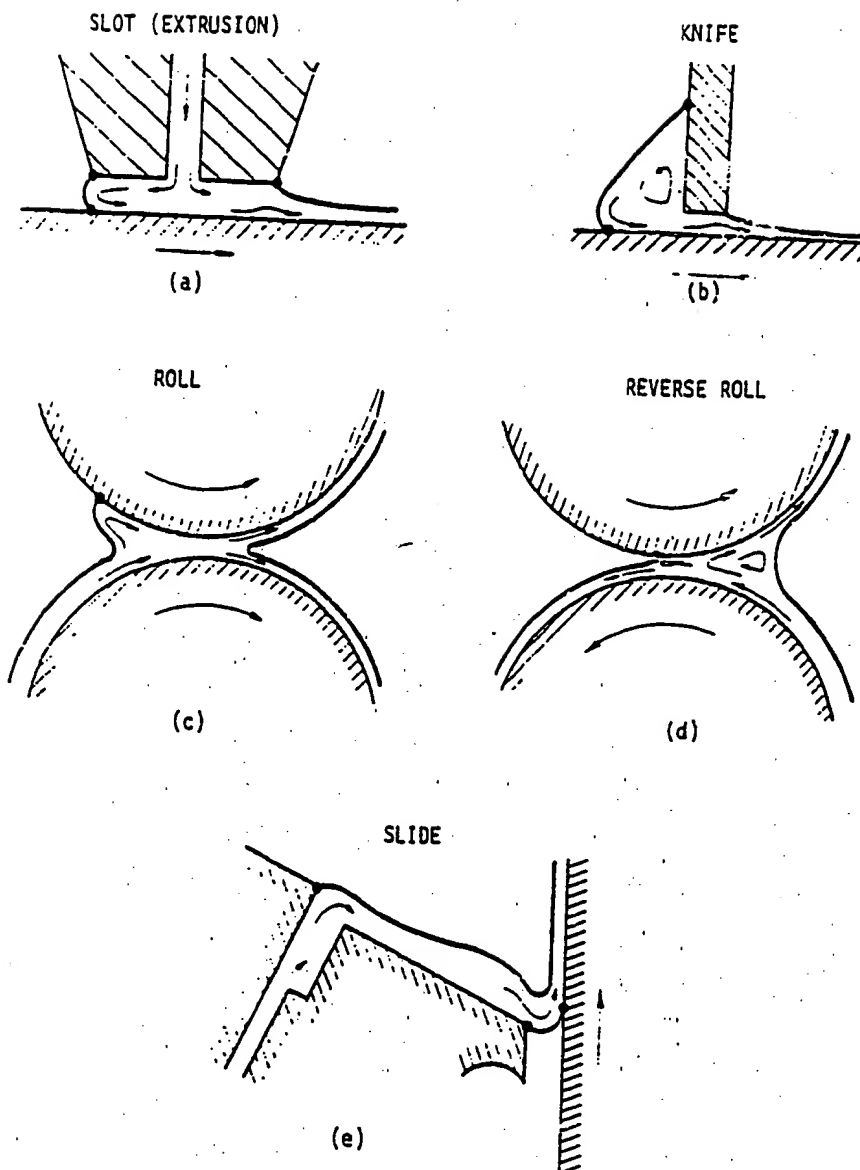


Figure 1.1. Schematic of five commonly used coaters.

inclined with respect to gravity and a web backed by a roll which is separated from the die by a small gap. Liquid flows down the die, or slide, by gravity and is transferred to the web.

Each of the coaters pictured in Figure 1.1 has finite width, but because the width is usually much greater than the other length scales of the coater it is common to make the mathematical idealization that coating flows are transversely uniform, i.e. two-dimensional. Indeed, one of the important tasks of coating engineers is to design coaters so that edge effects are minimized in order to make the whole width of the coating as uniform as possible. Ideally, coating flows are not only transversely uniform but also steady, for otherwise the coating thickness would not be uniform in the streamwise direction. However, in practice it is never possible to maintain complete transverse or streamwise uniformity. The degree to which uniformity can be achieved is controlled not only by the amplitude and frequency of disturbances such as mechanical vibrations and pressure fluctuations, but also by the sensitivity of the flow to these disturbances or even to infinitesimal disturbances due to thermal fluctuations.

1.2. Governing Equations and Boundary Conditions

Coating flows obey well-known equations which are devised from physical principles. These principles are conservation of momentum and mass, and they are expressed mathematically for incompressible flows by the Navier-Stokes equations:

$$\text{Re}[\partial \underline{u} / \partial t + \nabla \cdot (\underline{u} \underline{u})] = \nabla \cdot \underline{T} + \text{St} \underline{e}_g \quad (1.2.1)$$

$$0 = \nabla \cdot \underline{u} \quad (1.2.2)$$

Here \underline{u} is a vector representing local velocity, \underline{T} is a dyadic or tensor expressing the local state of stress, and \underline{e}_g is a unit vector pointing in the direction of gravity. Reynolds number, $\text{Re} \equiv U d / \nu$, measures the relative importance of inertia to viscous force; Stokes number, $\text{St} \equiv g d^2 / \nu U$ measures the relative importance of the force due to gravitational acceleration to viscous force. Here U is a characteristic velocity, e.g. web speed; d is a characteristic length, e.g. gap width; ν is kinematic viscosity; and g is local gravitational acceleration. This thesis deals exclusively with flows in which the liquids are Newtonian and have uniform properties. In this case \underline{T} is given by:

$$\underline{T} = \tau \underline{u} + (\nabla \underline{u})^T - p \underline{I}$$

The superscript T indicates the transpose of the dyadic or tensor, and p is the isotropic portion of the state of stress. The tensor $\underline{I} \equiv \underline{i} \underline{i} + \underline{j} \underline{j} + \underline{k} \underline{k}$, and \underline{i} , \underline{j} , and \underline{k} are unit vectors denoting the x-, y-, and z- directions in a Cartesian coordinate system.

Ordinarily liquids adhere to solid walls, or very nearly so. When this is so, the liquid velocity at a wall is identical to wall velocity \underline{U} :

$$\underline{u} = \underline{U} \quad (1.2.3)$$

This adherence condition appears to be violated, however, in some cases

where shear stress becomes very high at the wall, such as at contact lines and especially at dynamic contact lines as hypothesized by Huh and Scriven (1971) and observed experimentally by Kraynik and Schowalter (1977) and others. In a forerunner of this thesis, Silliman (1979, 1980 with Scriven) showed that allowing some slip at wetting lines relieves the nonintegrable mathematical singularities which would otherwise be present. One way to allow slip is to replace (1.2.3) by

$$\underline{u} = f(s) \underline{u}_{CL} + [1 - f(s)] \underline{u} \quad (1.2.4)$$

Here \underline{u}_{CL} is the velocity of the contact line and $f(s)$ is a function of arclength s measured from the contact line along the wall so that $f(0) = 1$, $f(\epsilon) = 0$, and $f(s) = 0$ when $s > \epsilon$ for some small distance ϵ . Equation (1.2.4) serves the same purpose as the slip boundary condition proposed by Navier (1827), but has the advantage of being easier to employ. However, (1.2.4) has the disadvantage that it can lead to aphysical results — i.e. it can predict momentum transport up a velocity discontinuity, in violation of the second law of thermodynamics — unless one is careful to select a function $f(s)$ which decreases monotonically on the interval $[0,1]$.

Three boundary conditions apply at a free surface. The first two are derived from a force balance there; the third is a statement of mass conservation. The difference in the total normal stress exerted on an interface by the liquid phase (L) and gas phase (G) must be equal to the capillary stress:

$$0 = (\underline{T}^L - \underline{T}^G) : \underline{nn} - Ca^{-1} 2H \quad (1.2.5)$$

Here \underline{n} is the outward unit normal to the interface, H is the mean curvature of the interface, and $Ca \equiv \mu U/\sigma$ is the capillary number, σ and μ being respectively the surface tension and dynamic viscosity. A useful approximation is that the gas is inviscid, which is usually valid whenever the liquid viscosity is much higher than that of the gas. If in addition the gas pressure is taken as a datum, T^G vanishes altogether. When surface tension is uniform, as it is taken to be throughout this thesis, the condition that shear stresses balance at an interface leads to the condition

$$0 = [(\underline{T}^L - \underline{T}^G) \cdot \underline{n}] \times \underline{n} \quad (1.2.6)$$

Finally, the condition that the interface be a material surface is the kinematic equation

$$\frac{\partial h}{\partial t} = \underline{u} \cdot \nabla(y-h) \quad (1.2.7)$$

Here $y = h$ represents the location of the free surface.

1.3. Steady Two-Dimensional Coating Flows

The starting point in any analysis of a coating flow is to look for steady solutions of the governing equations and boundary conditions as given in (1.2.1)-(1.2.7). In most instances transverse uniformity of the coating is sought and so flows are idealized as being two-dimensional. Even with these simplifications, constructing solutions by conventional mathematical methods is not a trivial matter unless further approximations are made.

A set of approximations, collectively termed the lubrication approximation, can be made in order to simplify the governing equations so that they can be handled by conventional mathematical methods. The approximations are: (1) Reynolds number times a characteristic slope of the die is small, i.e. web speed times gap thickness times a characteristic slope divided by kinematic viscosity is small; (2) flow is nearly rectilinear, i.e. velocity profiles are superpositions of shear-driven Couette and pressure-driven Poiseuille components, because the flow is confined to a channel which is nearly parallel; (3) liquid properties are uniform; and (4) acceleration due to gravity is unimportant (removable restriction). The lubrication approximation is used in Chapter 3 to investigate slot or knife coating flows when the die has an exponential shape.

The chief drawback of lubrication theory is that the approximation breaks down in the region near a separating contact line because the assumption of nearly rectilinear flow fails there. The usual remedy is to represent the flow field only as far downstream as the meniscus, and to impose a set of ad hoc conditions there. However, it is not certain which is worse: the remedy or the disease. The problem is that a collection of ad hoc boundary conditions have been postulated, and they each predict a different meniscus location as shown in Figure 1.2.

The alternative is to construct solutions to Equations (1.2.1)-(1.2.7) by the Galerkin/finite element method. The idea of finite element analysis of steady flow states is to represent the velocity and pressure fields and the free surface location in terms of particularly convenient sets of basis functions. These are each nonzero on only a

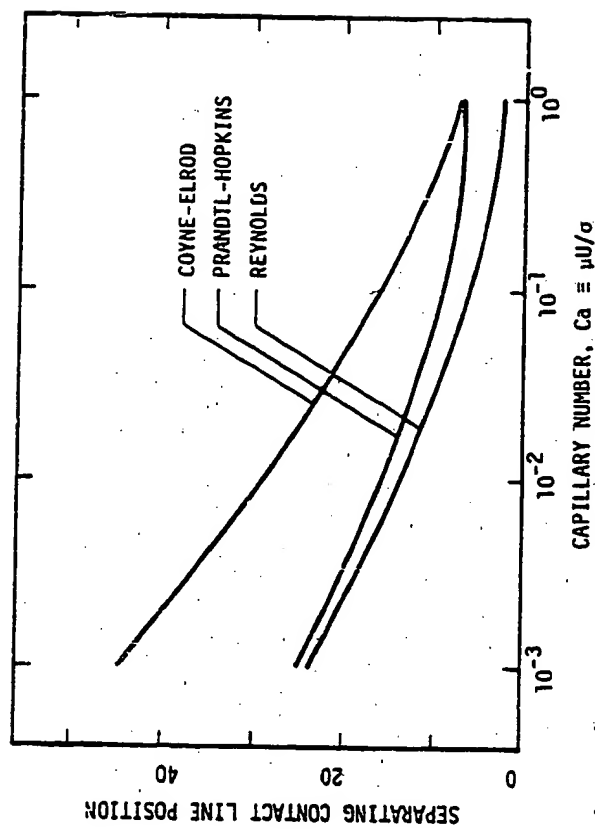


Figure 1.2. The predicted position of the separating contact line under the lubrication approximation varies widely depending on which of the postulated boundary conditions is chosen. Example is for exponential slot or knife coater.

subdomain of the flow domain, in contrast to the traditional functions of mathematical physics, which span an entire domain. Moreover, the basis function on each subdomain is a simple polynomial, so that more and more accurate estimates of the flow field and free surface shape can be calculated by dividing the domain into more and more subdomains. However, as the number increases, more computations are required to find the coefficients in all the polynomial basis functions so that (1) mass and momentum are conserved and boundary conditions are satisfied on the scale of the subdomains, and (2) the estimate of the solution has the desired degree of continuity. Not only is the idea straightforward; it is also consistent with rigorous mathematics. But its implementation is so tedious as to be impracticable without sophisticated matrix calculations for the large systems of algebraic equations to which the finite element method ultimately leads. Such calculations have become feasible only with the advent of large, fast digital computers. Analyses of coating flow problems by the finite element method are expensive. Thus, it is imperative to find efficient techniques and to look for ways of reducing the number of equations and unknowns without sacrificing accuracy.

One way to reduce the number of equations and unknowns without sacrificing accuracy is to impose conditions at inflow and outflow boundaries which represent well the physics there so that the computational domain can be shrunk. The idea is to split up the domain into three zones, as illustrated in Figure 1.3. In the upstream channel zone the flow is nearly parabolic so that perturbation analysis can be used to

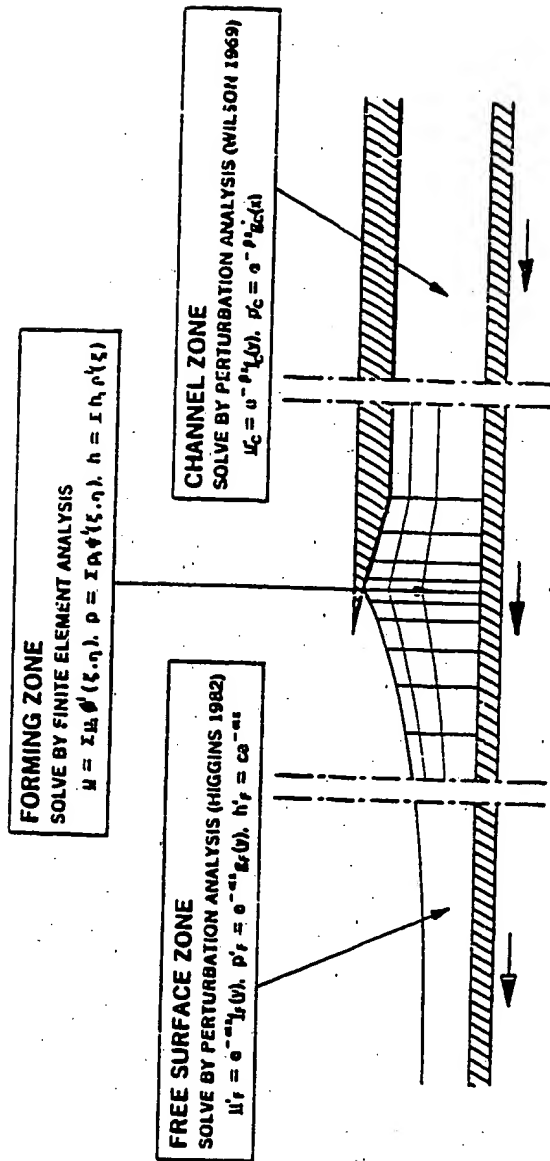


Figure 1.3. Strategy to analyze steady two-dimensional flow fields is based on dividing the domain into three zones. Perturbation analyses are used in the channel and free surface zones; Galerkin/finite element analysis is used in the forming zone.

solve the governing equations there. Likewise, flow is nearly solid body translation in the downstream free surface zone so that perturbation analysis can be used there as well. These analyses were carried out by Wilson (1969) and Higgins (1980, 1982) for the channel and free surface zones, respectively. The Galerkin/finite element method is used to represent the flow in the forming zone. Matching conditions between forming zone and channel zone, i.e. at the inflow boundary of the forming zone, and between forming zone and free surface zone, i.e. at the outflow boundary of the forming zone, take the form of Robin conditions, i.e. boundary conditions of the third kind. The details are set out in Chapter 4. The main findings there are that at the inflow boundary the Robin condition offers little advantage in comparison with more conventional Dirichlet or Neumann conditions, i.e. boundary conditions in which either the dependent variables or derivatives of the dependent variables are specified. On the other hand, the length of the forming zone measured downstream of the contact line can be reduced by as much as fourfold without sacrificing computational accuracy by using a Robin condition there instead of a Dirichlet or Neumann condition, as shown in Figure 1.4.

1.4. Steady Three-Dimensional Film Flows

Because coatings are never flawless in practice, coating engineers are forced to aim only for uniformity within some tolerance. Surface leveling can play an important role by reducing the amplitude of coating imperfections. Estimates of leveling rates could aid significantly in the design of coating dies by making clear which disturbances level so

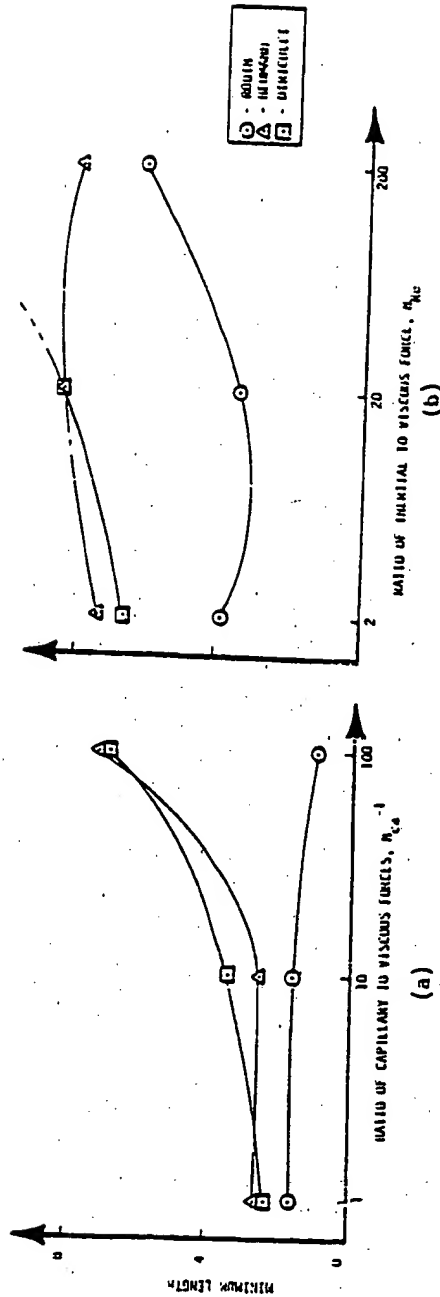


Figure: 1.4. Minimum domain length measured downstream of the contact line in slot or knife coating to obtain a specified degree of accuracy. Figure 1.4a is for negligible Reynolds number N_{Re} ; Figure 1.4b is for capillary number $N_{Ca} = 0.01$. The new Robin condition allows substantially smaller domain lengths to be used without loss of accuracy as compared with the conventional Dirichlet and Neumann conditions.

slowly that they cannot be tolerated.

In Chapter 2 Higgins' (1980, 1982) asymptotic analysis of the two-dimensional development of viscocapillary film flows is extended to include three-dimensional disturbances. Three-dimensional disturbances are representable in a doubly infinite expansion in domain-spanning basis functions, which are the eigenvectors of the eigenproblem to which the perturbation analysis reduces. However, one mode generally persists further downstream than any of the others, especially when the upstream disturbance consists of a single Fourier mode, so that only this dominant mode need be considered if one's primary interest is in the flow far downstream.

The main results are the dominant decay rates as functions of Reynolds number, capillary number, and wavenumber, i.e. the inverse of the transverse wavelength of the disturbance, as contained in Tables 2.1-2.5. An important distinction with the earlier work of Higgins (1980, 1982) is that the dominant mode can be one of damped standing waves when disturbances are three-dimensional, as illustrated in Figure 1.5a, whereas Higgins found that the dominant mode always decays exponentially when disturbances are two-dimensional. Figure 1.5b shows an example of a three-dimensional disturbance that decays exponentially.

An important use of the results of Chapter 2 is to extend the Robin condition tested in Chapter 4 to a three-dimensional analogue:

$$\underline{\underline{f}} \cdot \underline{\underline{T}} = \underline{\underline{A}} \cdot \underline{\underline{u}} \quad (1.4.1)$$

Here $\underline{\underline{T}}$ is the three-dimensional state of stress tensor, $\underline{\underline{u}}$ is the three-

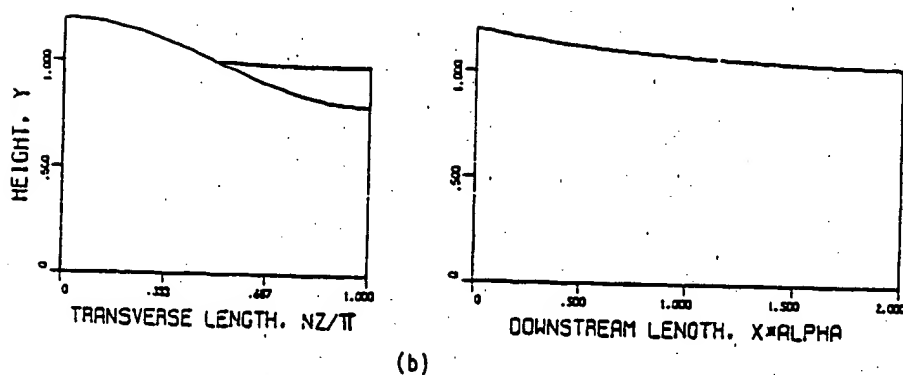
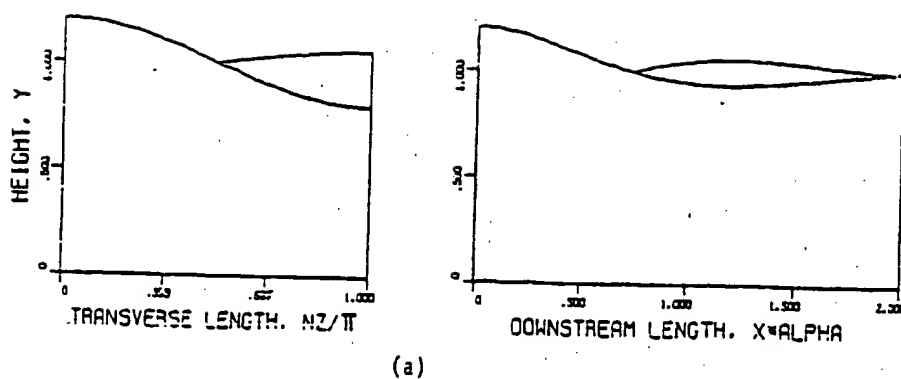


Figure 1.5 Examples of upstream disturbances that decay with downstream length (a) to form damped standing waves, and (b) exponentially. Damped standing waves only appear when the disturbance is three-dimensional. Both cases are at Reynolds number $Re = 100$, and wavenumber $N = 1$. Case (a) is at capillary number $Ca = 100$, and case (b) is at capillary number $Ca = 1$.

dimensional velocity vector, and A is a proportionality tensor that is constructed from the asymptotic solution. Equation (1.4.1) is especially useful in stability analyses of steady two-dimensional flows to three-dimensional disturbances.

1.5. Stability of Steady Two-Dimensional Coating Flows

Even when coating die imperfections or misalignment, mechanical vibrations, and pressure fluctuations are held in check, there is no guarantee that a coating will be uniform. For if the flow is fluid-mechanically unstable, even infinitesimal disturbances due to thermal fluctuations or the like can be amplified to finite size. It is therefore insufficient to show that steady two-dimensional solutions of the governing equations exist; it is also necessary to show that they are stable.

One of the most prevalent of coating flow instabilities is the ribbing instability. Ribbing is a steady pattern of waves which leads to nonuniformity of the coating in the transverse direction. Each of the coaters shown in Figure 1.1 is known to produce ribbed coatings under certain conditions. Usually, the faster the coating speed, the lower the surface tension, the higher the liquid viscosity, or the thinner the coating, the less stable is a transversely uniform flow to a ribbing disturbance.

Figure 1.6 is a photograph taken by Dennis Coyle showing ribbing in a two-roll setup similar to the one shown in Figure 1.1c except that the two rolls were half-immersed in a bath. Even though the apparatus

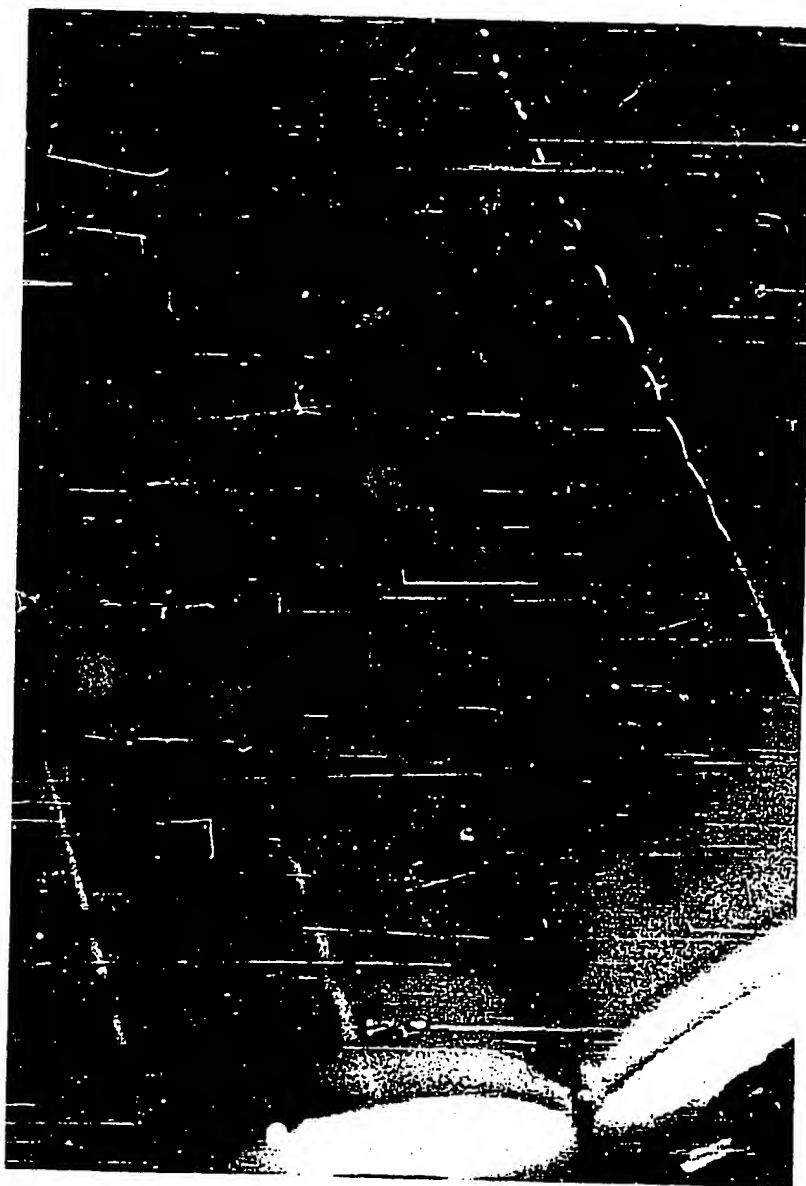


Figure 1.6. The ribbing instability in a two-roll set-up.

is nearly transversely symmetric (aside from effects of the edges), the liquid film that adheres to the rolls is far from being uniform. Instead, the film thickness is remarkably periodic in the transverse, or axial, direction.

Figure 1.7 shows some results of a visualization experiment that was performed at a research facility of Minnesota Mining and Manufacturing with the aid of Gary Zvan. The coater that was used is equivalent to the knife coater shown in Figure 1.1 except that the upper die was a cylinder of 3.5 centimeter diameter. The minimum gap between the cylinder and the web was set to 0.025 centimeters. The liquid used was glycerin, which had a measured viscosity of 1250 centipoise and surface tension of 69.5 dynes per centimeter. Coatings were made by depositing a small puddle of liquid upstream of the cylinder so that liquid was spread by the cylinder onto the traveling web. The coating was then photographed by a camera mounted directly above the web. A sheet of graph paper having millimeter rulings was held slightly below and parallel to the transparent web so that nonuniformities could be more readily observed. Web motion is from top to bottom in the three frames in Figure 1.7. The coating appeared uniform at the slowest web speed shown in Figure 1.7a. At the intermediate speed, a pattern of ribs similar to those in Figure 1.6 was observed, although they are barely noticeable in Figure 1.7b. Figure 1.7c shows a distinct pattern of ribs which have a dimensionless wavenumber of about 0.53 (made dimensionless by the minimum gap clearance), i.e. the dimensional wavenumber is $2\pi/\text{wavelength}$.

CYLINDRICAL SPREADER

RIBBING SETS IN AS WEB SPEED IS INCREASED

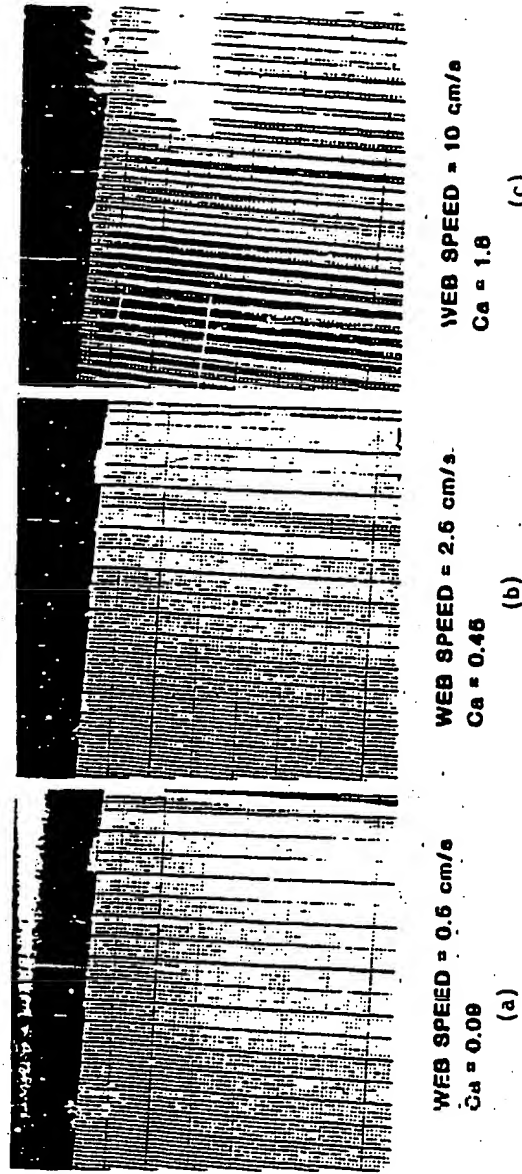


Figure 1.7. Onset of ribbing occurs as web speed (capillary number) is increased. The coating in (a) is uniform. In (b), ribbing is very slight. In (c) ribs are quite pronounced. Web motion is from top to bottom in each of the frames.

Stability of Coating Flows Under the Lubrication Approximation.

The stability of a steady two-dimensional coating flow can be estimated by using the lubrication approximation to account not only for the steady two-dimensional flow but also for possible unsteady three-dimensional disturbances to it. Pearson (1960) was the first to show how this can be done in his classical analysis of ribbing in a wedge-shaped spreader. However, the same question arises in stability analysis as in steady flow analysis: what conditions should be imposed at the separating contact line? A comparison of the stability predictions for three of the postulated boundary conditions is carried out in Chapter 3. The main result is that stability analysis under the lubrication approximation is unreliable because the results are sensitive to the choice of boundary condition, as shown in Figure 1.8.

Finite Element Stability Analysis. The idea of finite element stability analysis is to subject the finite element estimate of a steady flow to all infinitesimal disturbances of velocity, pressure, and free surface that can be represented with the very same set of basis functions used to estimate the steady base flow. Three-dimensional disturbances are represented by finite element basis functions multiplied by Fourier basis functions, i.e. sines and cosines:

$$\underline{u}' = \sum_i \underline{u}_i' \phi^i(x,y) \cdot [\underline{ii} \cos(Nz) + \underline{jj} \cos(Nz) + \underline{kk} \sin(Nz)] e^{-\lambda t} \quad (1.5.1)$$

$$p' = \sum_i p_i' \phi^i(x,y) \cos(Nz) e^{-\lambda t} \quad (1.5.2)$$

$$h' = \sum_i h_i' \phi^i(x) \cos(Nz) e^{-\lambda t} \quad (1.5.3)$$

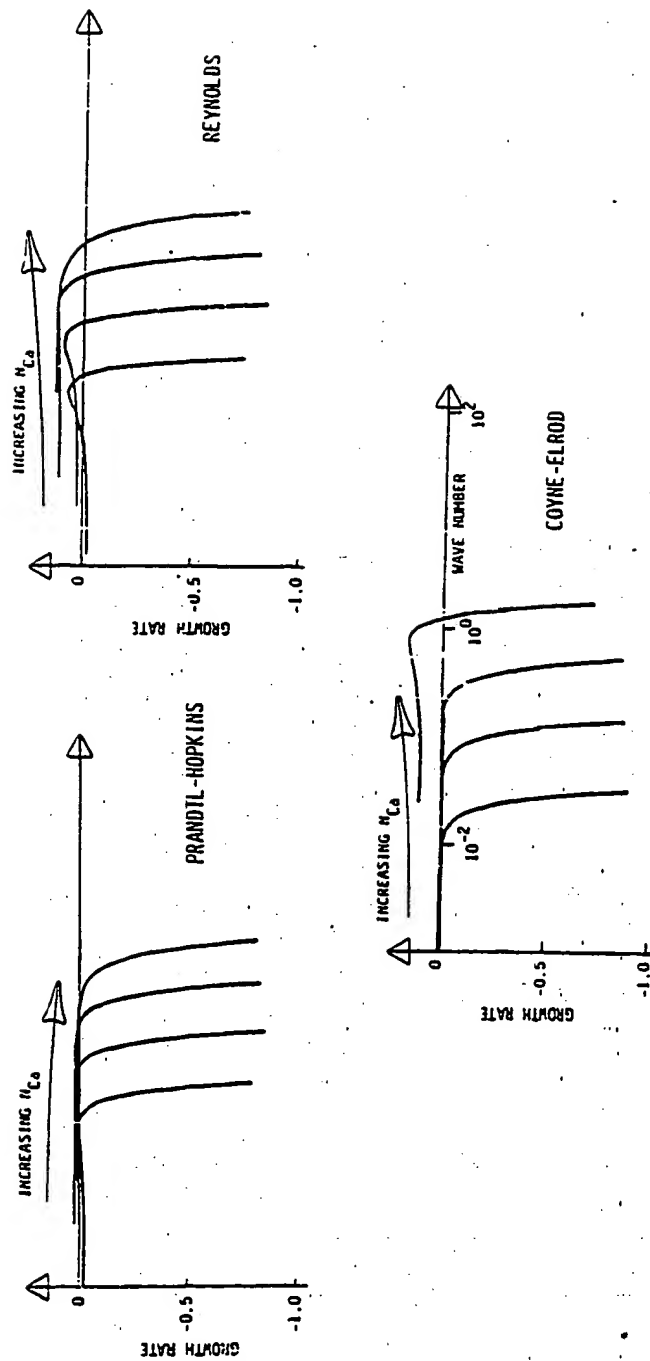


Figure 1.8. Stability results under the lubrication approximation depend strongly on which of the postulated boundary conditions is selected. The Coyne-Elrod boundary condition predicts instability, i.e. growth rate greater than zero, at only the highest capillary number whereas the others predict instability even at the smallest value.

Here the u_i^j , p_i^j and h_i^j are nodal parameters that determine the disturbance mode; $\phi^j(x,y)$, $\psi^j(x,y)$ and $c^j(x)$ are finite element basis functions; K is the transverse wavenumber of the disturbance; and the exponential decay rate λ determines whether a disturbance decays, in which case λ is positive, or grows, in which case λ is negative. The analysis leads to a large algebraic eigenproblem of the form:

$$J_{ij}x_j = \lambda M_{ij}x_j \quad (1.5.4)$$

Entries in the Jacobian matrix, represented by J_{ij} , measure the sensitivity of the residuals of the Navier-Stokes equations and boundary conditions, as given in (1.2.1)-(1.2.7), to changes in the nodal velocities and pressures, i.e. the finite element solution. The residuals measure whatever momentum and mass discrepancies remain in the solution. Entries in the mass matrix M_{ij} measure the overlap of basis functions. A solution of (1.5.4) is an eigenvector x_j , which represents a possible mode of instability, and an eigenvalue λ , which is the decay rate of that mode, i.e. the negative of its growth rate. In contrast to the hydrostatic stability analyses carried out by Brown (1979), in which the eigenproblem is symmetric, it is asymmetric for film-flow problems. This is a crucial complication because methods to solve asymmetric eigenproblems are still in their infancy.

A general method for determining the stability of a coating flow is laid out in Chapter 5. The same strategy is used to represent perturbations to a steady two-dimensional base flow as illustrated in Figure 1.3, i.e. the flow domain is divided into three zones. Perturbation

analyses worked out in Chapter 2 describe the three-dimensional flows in the upstream channel and downstream free surface zones. Matching conditions at the inflow and outflow boundaries of the forming zone result in Robin conditions similar to the one in Equation (1.4.1). Only the most dangerous disturbance modes, i.e. the eigenvectors which satisfy (1.5.4) and correspond to the fastest growth rates, are of interest.

Stewart's method is used here to track the most dangerous disturbance modes. It is described in Chapter 5 and more fully in Appendix A. Stewart's method is a comparatively new and sophisticated algorithm based on an old sure-fire method known as inverse subspace iteration, which relies on repeated solutions of a set of linear equations. Ordinarily, complex arithmetic is required because the eigenvalues and eigenvectors of an asymmetric eigenproblem are generally complex. However, the need for complex arithmetic is cleverly avoided by the use of a special basis, the quasi-Schur basis, to represent the most dangerous disturbance modes. Because real arithmetic is used exclusively, computational efficiency is improved and computer memory requirements are reduced. Furthermore, the rate of convergence is enhanced by a Schur-Rayleigh-Ritz scheme, which brings about an improvement in the basis defining the dominant disturbance modes. Continuation, i.e. using a previously calculated set of dominant disturbance modes as initial guess, is used in the implementation of Stewart's method to cut computational costs. The overall scheme is efficient: so efficient that it usually costs only a little more to make one stability calculation than to generate a steady two-dimensional flow field.

The general method of finite element stability analysis laid out in Chapter 5 is illustrated in Chapter 6 with exponential slot and knife coating. The main findings are how coating stability depends on each of the operating parameters, and also why the ribbing instability arises. The ribbing instability is shown to be promoted by increasing capillary number $Ca \equiv \mu U/\sigma$, decreasing coating thickness h , increasing the separating contact angle that the meniscus makes with the die, decreasing channel divergence angle, or decreasing Reynolds number $Re \equiv U d/\nu$. The stability predictions are in close agreement with the results of the visualization experiment pictured in Figure 1.7. The close agreement appears to validate the accuracy of the Galerkin/finite element approximation to the stability problem. A comparison in Figure 1.9 shows that the lubrication stability predictions are off the mark. Evidence that the cause of failure is due to the breakdown of the assumption of nearly rectilinear flow in the region near the meniscus is presented in Chapter 6.

The method of finite element stability analysis described in Chapter 5 is especially useful because it not only predicts the stability of a flow, it also points out the mode of instability. Knowing the mode of instability is essential to understanding the mechanism, i.e. which forces contribute to instability and where the seat of instability is. The mechanism of ribbing instability in slot and knife coating is examined in Chapter 6. The main conclusions are that normal viscous stresses acting on the meniscus near the contact line play an important role in the mechanism of ribbing, and that the ribbing instability is largely explained by examining the normal tractions on the meniscus near the contact line.

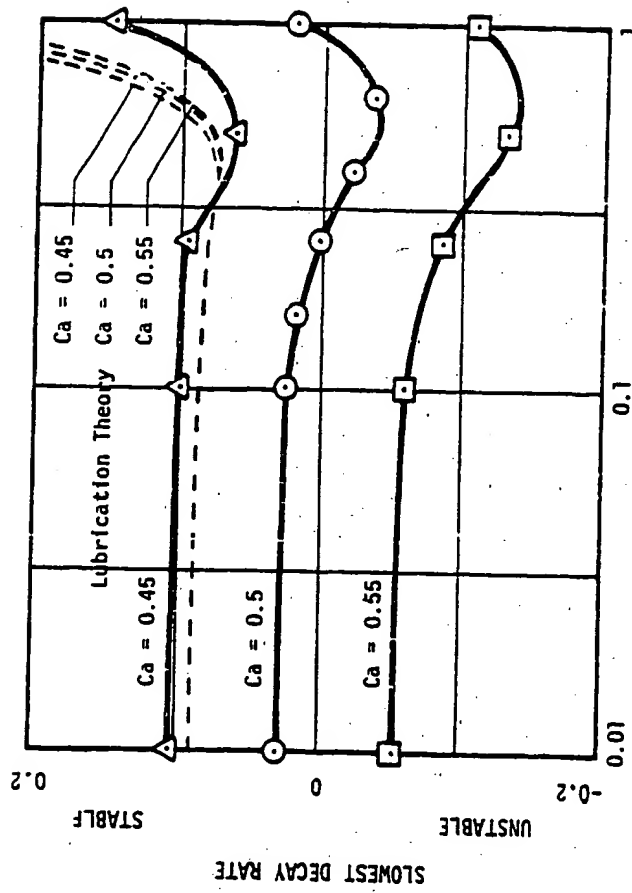
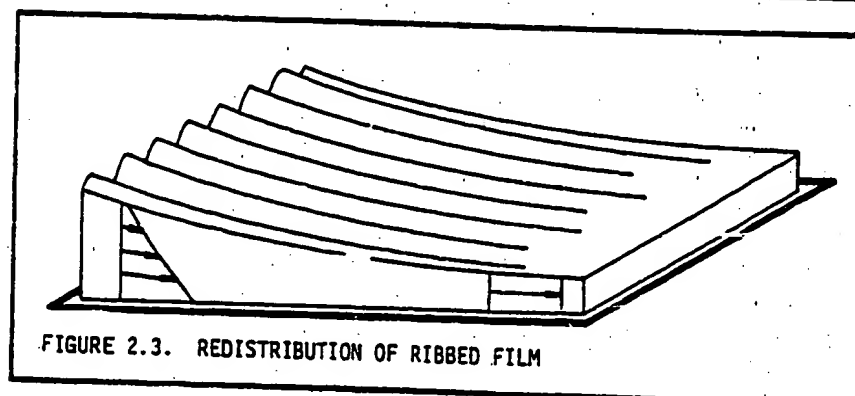
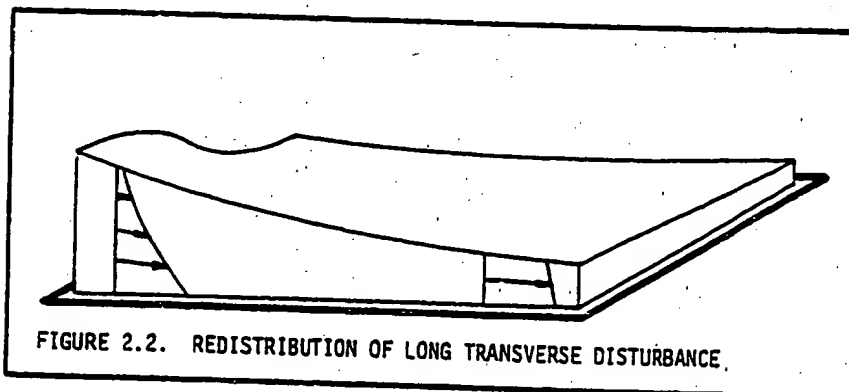
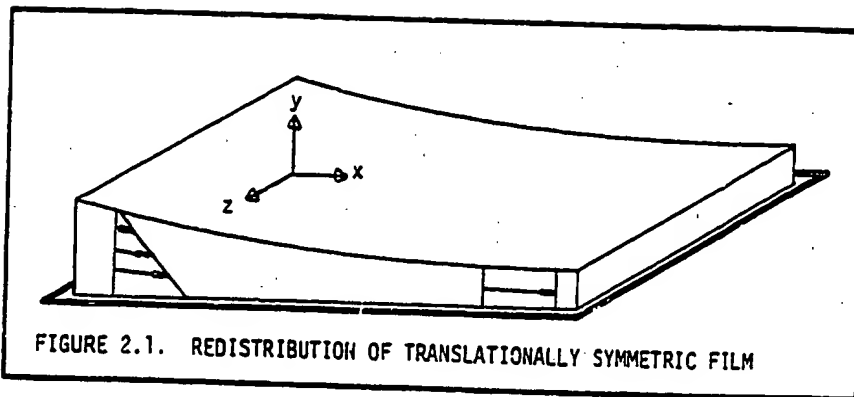


Figure 1.9. Finite element stability analysis predicts that exponential slot or knife coating flows are unstable at capillary numbers higher than 0.5 (curves falling below zero indicate an unstable base flow because disturbances can grow). Lubrication theory fails to correctly predict onset of instability.

CHAPTER 2 - STEADY, THREE-DIMENSIONAL, LIQUID FILM REDISTRIBUTION ON A MOVING WEB

2.1. Introduction

Downstream of almost every coating device is a zone in which the deposited film approaches an asymptotic regime. The asymptotic regime is usually solid body translation or nearly solid body motion because the force of gravity is small in comparison with the viscous drag exerted by the moving web, and furthermore the role of gravity vanishes altogether when the web is horizontal. In this chapter the steady approach to a downstream plug-flow regime, i.e. solid body translation, is analysed. The analysis is of the decay of small, three-dimensional departures upstream from the downstream regime when the deposited film is incompressible Newtonian liquid having uniform viscosity and surface tension. Gravity is regarded as negligible, and thus either capillary force, viscous force, or both lead to downstream decay of an upstream departure from plug flow. Viscous force resists liquid deformation and thus plays a dual role: (1) it opposes transverse, i.e. cross-web redistribution of liquid and (2) it causes decay of filmwise velocity gradients. Capillary force resists departure from planar meniscus shape, and thus it also plays a dual role: (1) it promotes transverse redistribution of liquid that tends to flatten the meniscus and (2) it counteracts streamwise meniscus curvature which results from decay of filmwise velocity gradients. Three possibilities are illustrated in Figures 2.1-2.3. Figure 2.1 shows a transversely symmetric (in the z-dimension) disturbance decaying to a plug profile. Here viscous force is driving and capillary force is resisting decay to uniform plug flow. Figure 2.2



shows the situation when a coating device is either not well aligned or nonuniformly fed: plug flow is reached only after the liquid is redistributed across a long transverse distance. Here the primary effects of viscous and capillary forces are, respectively, to resist and to drive the transverse redistribution of liquid. In Figure 2.3 the coating is ribbed by a fluid mechanical instability in the forming zone; here, the liquid need redistribute only across a relatively short transverse distance. In this situation the roles of viscous and capillary forces are truly dual because fluid redistributes in the downstream and transverse directions over approximately the same length scale. This chapter focuses on understanding the rate and manner of spatial decay of a disturbed flow to its final plug flow state. There are two primary applications: the first is coating die design and the second is coating stability.

While the object of most coating devices is to apply a uniform layer of liquid onto a moving web, in practice the liquid film is marred by irregularities due to coating die imperfection or misalignment, mechanical vibrations, pressure nonuniformity or fluctuation, and perhaps even fluid mechanical instabilities — such as the ribbing instability. What is crucial is that these imperfections be held down so that the final film thickness is maintained uniform to within some tolerance. Surface leveling may play an important role in achieving this goal by reducing the amplitude of coating imperfections. Quantitative estimates of leveling rates could aid significantly in the design of coating dies by making clear which disturbances level so slowly that they cannot be tolerated.

This analysis also applies to the construction of a Robin boundary condition at the matching plane between forming and free surface zones (see Figure 5.1). The idea is that knowledge of how a flow decays to the final plug regime can be incorporated advantageously into a boundary condition at the outflow boundary of a forming zone. The advantage of using a Robin boundary condition over Dirichlet or Neumann conditions at the outflow boundary downstream of an exponential slot coater is demonstrated in Chapter 4. Higgins' (1982) analysis is sufficient to construct a Robin condition for two-dimensional flows like the one considered in Chapter 4, but a three-dimensional asymptotic analysis is necessary whenever three-dimensional flows or the stability of two-dimensional flows to three-dimensional perturbations are sought. The asymptotic analysis of this chapter is particularly useful for investigating the ribbing instability, the subject of Chapters 5 and 6.

Several papers have dealt with the onset of three-dimensional ribbing instabilities in thin liquid films (see for example Pearson 1960, Pitts and Greiller 1961, Taylor 1963, and Savage 1976), but to the best of the author's knowledge only Fall (1978) has investigated the downstream decay of ribbing disturbances. Fall used lubrication theory to analyze the problem. His results are limited to small wavenumber and large capillary number (Fall's claim that his analysis is valid for small capillary number is shown to be incorrect in Section 2.3).

Much more headway has been made in understanding the approach to a final flow regime where upstream departure from the final regime is two-dimensional rather than three-dimensional. Higgins (1980, 1982) was the

first to treat the two-dimensional problem in its full generality. He even considered the effect of gravity, but could solve the resulting equations only when either gravity or convective inertial forces could be neglected. The mathematical analysis used here in Section 2.4 resembles closely that of Higgins. Higgins' analysis in turn was inspired by that of Wilson (1969), who examined the approach to Poiseuille flow in a channel. Both Higgins and Wilson were able to use a streamfunction representation for their two-dimensional flows; here the three-dimensional analogue of streamfunction, vector potential (see Aris 1962 and Morse and Feshbach 1953) is used to facilitate representation of three-dimensional flows.

Earlier investigations that were less general than Higgins' include those of Bretherton (1961), Cox (1962), Coyne and Elrod (1969), Groenvelt and van Dortmund (1970), and Ruschak (1974). Both Bretherton's and Cox's analyses were aimed at understanding their experimental investigations of bubbles moving through capillary tubes. Coyne and Elrod were interested in the final acceleration of liquid in the cavitated region of a journal bearing. Higgins (1980) pointed out an error in one of Coyne and Elrod's boundary conditions, however, and thereby showed their results to be incorrect. Groenvelt and van Dortmund examined the liquid film entrained on a web being withdrawn from a bath, i.e. dip coating. None of these analyses account for liquid inertia, and so represent no more than limiting cases. Ruschak investigated the same problem as Higgins, but his analysis is valid solely for very large surface tension as well as negligible inertia.

Orchard (1962) and Anshus (1973) investigated the problem of the temporal leveling of small two-dimensional and three-dimensional initial disturbances of a stagnant pool, respectively. Both analyses are limiting cases of negligible Reynolds number, i.e. the acceleration term in the momentum equations is set to zero.

Two methods are used here to analyse the asymptotic approach to plug flow. The first begins with the lubrication assumptions and leads to an approximate solution, valid when inertia is small and disturbances have long transverse wavelength, i.e. small transverse wavenumber. The second method employs no assumptions other than that disturbances be small, and leads to a result which is valid for the entire range of parameters. The second method is to construct a solution of the exact governing equations linearized about the final plug flow regime. The linearized equations are of Oseen type (see Oseen 1927).

Both the lubrication and Oseen solutions are constructed with the aid of normal mode analysis. Arbitrary disturbances can be represented as Fourier series or integrals — depending on whether the finiteness of the web in the transverse direction is taken into account or not. Because the lubrication and Oseen equations are linear, disturbances of individual wavenumber can be singled out and studied independently. A solution could then be constructed for a given upstream disturbance as a series or integral in wavenumber. However, the construction of such a series or integral solution would be difficult in practice. Fortunately, much can be learned by studying the decay of disturbances which have single Fourier components. Furthermore, linearized three-dimensional

stability analysis is performed by investigating one Fourier component at a time, and so it is desirable to do the same in constructing a Robin boundary condition (see Section 2.6 and Chapter 5).

Both the lubrication and Oseen analyses reduce to eigenproblems. Each solution is an eigenpair, i.e. an eigenvalue and corresponding eigenfunction, and represents a possible mode of disturbance and its spatial decay rate. All disturbances decay with downstream distance because no forces which could cause disturbances to grow with downstream distance are included in this analysis. The characteristic equation to which the Oseen analysis leads has an infinite number of roots. Any disturbance of specified wavenumber could be represented as a series in the corresponding eigenfunctions. In general, some of the eigenvalues, i.e. spatial decay rates, are complex. These correspond to modes which are oscillatory in downstream coordinate, i.e. damped standing waves. Real eigenvalues on the other hand correspond to modes that decay exponentially in downstream distance. By contrast with the Oseen problem, the characteristic equation of the lubrication analysis has only two allowable roots, and both are real. Physically, this is because the lubrication assumptions dictate that velocity disturbances be parabolic in the filmwise coordinate, y . Thus, the possible disturbances are severely limited.

In Section 2.2 the Oseen equations, boundary conditions, and the lubrication equation are laid out. In Sections 2.3 and 2.4 solutions of the lubrication and Oseen equations are constructed, respectively. Section 2.5 contains limiting and numerical results for the Oseen solu-

tion. The Oseen and lubrication results are discussed and compared with those of Fall and Higgins in Section 2.6. Finally, in Section 2.7, Wilson's (1969) analysis is extended to include three-dimensional disturbances.

2.2. Oseen and Lubrication Equations

The governing equations and appropriate boundary conditions for viscous free-surface flows of incompressible, isothermal, Newtonian liquids were given in Equations (1.2.1)-(1.2.3) and (1.2.5)-(1.2.7). In the free surface zone downstream of a forming zone, the linearized form of these equations applies. The linearization is about the final uniform plug flow state:

$$\underline{U} = 1, \quad P = 0, \quad H = 1, \quad (2.2.1)$$

where \underline{U} is the velocity, P is the pressure, and H is the elevation of the free surface above the moving web. The capital letters designate the base flow. The governing equations linearized about this state are

$$N_{Re} \frac{\partial \underline{u}}{\partial x} = \nabla^2 \underline{u} - \nabla p, \quad (2.2.2)$$

$$\nabla \cdot \underline{u} = 0, \quad (2.2.3)$$

where $N_{Re} \equiv UH/\nu$, U being the web speed, ν the kinematic viscosity, \underline{u} the velocity, with components (u,v,w) , and p the pressure. The lower case letters designate a disturbance to the base flow. The disturbance must obey the following set of linearized boundary conditions:

$$\underline{u} = 0 \quad \theta \quad y = 0 \quad , \quad (2.2.4)$$

$$(\underline{t} \cdot \underline{j}) \times \underline{j} = 0 \quad \theta \quad y = 1 \quad , \quad (2.2.5)$$

$$N_{ca} \underline{t} : \underline{j} \underline{j} = \nabla_{II}^2 h \quad \theta \quad y = 1 \quad , \quad (2.2.6)$$

$$\underline{j} \cdot \underline{u} = \frac{\partial h}{\partial x} \quad \theta \quad y = 1 \quad . \quad (2.2.7)$$

Equations (2.2.4)-(2.2.7) are the no-slip and no-penetration, shear stress, normal stress, and kinematic conditions, respectively, for a small disturbance from uniform plug flow. \underline{t} is the stress tensor, which under the restrictions that the liquid is incompressible and Newtonian is given by

$$\underline{t} = [\nabla \underline{u} + (\nabla \underline{u})^T] - \nabla p \quad , \quad (2.2.8)$$

$N_{ca} \equiv uU/\sigma$ is the capillary number, μ being the dynamic viscosity and σ the surface tension, and ∇_{II} is the two-dimensional gradient in the plane of the moving web, so that ∇_{II}^2 is the two-dimensional Laplacian. Disturbances must eventually decay to zero at very large distances downstream; hence the additional restriction that

$$\underline{u} \rightarrow 0 \quad , \quad p \rightarrow 0 \quad , \quad \text{and} \quad h \rightarrow 0 \quad \text{as} \quad x \rightarrow \infty \quad (2.2.9)$$

must be satisfied by any allowable disturbance. The disturbance velocity must satisfy the matching condition

$$\underline{u}(x,y,z) = \underline{u}_0(y,z) \quad \theta \quad x = 0 \quad , \quad (2.2.10)$$

where $\underline{u}_0(y,z)$ is the velocity disturbance at the upstream boundary of the free surface zone (see Figure 1.1). The solution of Equations (2.2.2)-(2.2.10) is constructed in Section 2.4.

Equations (2.2.2)-(2.2.10) can be simplified by means of the lubrication approximation (see Cameron 1976, Mitchell 1950, and Tipei 1962), which rests on the following conditions: (1) convective inertial forces are negligible and thus Reynolds number, N_{Re} , is effectively zero; (2) flow is nearly rectilinear, and hence the filmwise velocity component, v , is small compared with streamwise and transverse velocities, u and w , respectively, and filmwise gradients are larger than streamwise and transverse gradients; and (3) gravity is negligible (already imposed above). With these assumptions, Equations (2.2.2)-(2.2.10) are reduced by the standard scaling arguments of lubrication theory to:

$$\partial^2 \underline{u}_{II} / \partial y^2 = \nabla_{II} p \quad (2.2.11)$$

$$\nabla \cdot \underline{u} = 0 \quad (2.2.12)$$

$$\underline{u} = \underline{0} \quad @ \quad y = 0 \quad (2.2.13)$$

$$\partial \underline{u}_{II} / \partial y = 0 \quad @ \quad y = 1 \quad (2.2.14)$$

$$- N_{Ca} p = \nabla_{II}^2 h \quad @ \quad y = 1 \quad (2.2.15)$$

$$\underline{j} \cdot \underline{u} = 0 \quad @ \quad y = 1 \quad (2.2.16)$$

$$\underline{u}_{II} \rightarrow \underline{0}, \quad h \rightarrow 0 \quad \text{as } x \rightarrow \infty \quad (2.2.17)$$

$$\underline{u}_{II}(x,y,z) = \underline{u}_0(y,z) \quad @ \quad x = 0 \quad (2.2.18)$$

Here the subscript II again indicates that the vectors have components in only the streamwise and transverse directions, x and z , respectively. The pressure field can be found from equations (2.2.11)–(2.2.14) in the usual way (see for example, Cameron 1976) by solving Equation (2.2.11) with boundary conditions (2.2.13) and (2.2.14), integrating that result and Equation (2.2.12) over y from the web to the free surface with Equations (2.2.13) and (2.2.16) as boundary conditions, and combining the results of these integrations to eliminate velocity. The result is

$$\nabla_{II} \cdot (h^3 \nabla_{II} p/6) = (\partial h / \partial x)/2. \quad (2.2.19)$$

This differs from the well-known lubrication result by a factor of one-half on the left side because the velocity profile is semi-parabolic rather than parabolic. Finally, because pressure is not a function of the filmwise coordinate, y , Equation (2.2.15) can be used to eliminate pressure in favor of film thickness:

$$\nabla_{II} \cdot [h^3 \nabla_{II} (\nabla_{II}^2 h)] = 3N_{ca} \partial h / \partial x \quad (2.2.20)$$

The gradients of free surface elevation, h , are small by assumption, and so it is consistent to linearize about the base state, $H = 1$. Therefore, Equation (2.2.20) is approximated by

$$\nabla_{II}^4 h = 3N_{ca} \partial h / \partial x \quad (2.2.21)$$

To the author's knowledge, this equation has not appeared in the literature before. Solutions are constructed in the following section.

2.3. Lubrication Solution

Solutions of Equation (2.2.21) can be found by separation of variables and have the form

$$h = \tau(x) \cos(Nz) + \bar{\tau}(x) \sin(Nz), \quad (2.3.1)$$

where N is the wavenumber and is inversely proportional to the wavelength, which is $2\pi/N$. Inserting this in Equation (2.2.21) produces the ordinary differential equation:

$$\begin{aligned} & [\tau'''' - 2N^2\tau'' + 3N_{ca}\tau' + N^4\tau] \cos(Nz) \\ & + [\bar{\tau}'''' - 2N^2\bar{\tau}'' + 3N_{ca}\bar{\tau}' + N^4\bar{\tau}] \sin(Nz) = 0. \end{aligned} \quad (2.3.2)$$

Both bracketed terms must be equal to zero because z is arbitrary, and thus

$$\tau'''' - 2N^2\tau'' + 3N_{ca}\tau' + N^4\tau = 0; \quad \bar{\tau}'''' - 2N^2\bar{\tau}'' + 3N_{ca}\bar{\tau}' + N^4\bar{\tau} = 0. \quad (2.3.3)$$

Because both τ and $\bar{\tau}$ satisfy the same differential equation, it suffices to solve for τ alone. The auxiliary equation for (2.3.3) is

$$\alpha^4 - 2N^2\alpha^2 - 3N_{ca}\alpha + N^4 = 0, \quad (2.3.4)$$

where $\tau = ce^{-\alpha x}$ and α is the spatial decay rate. Only roots α of Equation (2.3.4) which have positive real part are of interest because otherwise the requirement that disturbances disappear far downstream, Equation (2.2.17), would be violated. Descartes' rule of signs shows that Equation (2.3.4) has either two or no positive real roots. By

rewriting it in the form

$$[(\alpha/N)^2 - 1]^2 - 3(N_{ca}/N^3)(\alpha/N) = 0, \quad (2.3.5)$$

it can be seen that (α/N) depends solely on (N_{ca}/N^3) , i.e. the ratio of exponential decay rate to wavenumber is a function exclusively of the ratio of capillary number to wavenumber cubed. Equation (2.3.5) can be solved by perturbation analysis (see Lin and Segal 1974) when the parameter (N_{ca}/N^3) is small; the result is

$$\alpha/N = 1 \pm \sqrt{3N_{ca}/4N^3}. \quad (2.3.6)$$

In the other limit, that is when (N_{ca}/N^3) is large, perturbation analysis leads to the roots

$$\alpha/N = (N^3/3N_{ca}) ; (3N_{ca}/N^3)^{1/3}. \quad (2.3.7)$$

The first result in Equation (2.3.7) matches Fall's (1978). The solutions at intermediate values of the parameter (N_{ca}/N^3) are easily found by Newton's method. The smallest positive root, (α/N) , of Equation (2.3.5) for parameter (N_{ca}/N^3) ranging from 0.01 to 10.0 is shown in Figure 2.4.

2.4. Oseen Solution

Any solenoidal vector field, i.e. one that satisfies the continuity equation (2.2.3), can be represented by a vector potential (see, e.g. Aris 1962):

$$\underline{u} = \nabla \times \underline{A}, \quad \nabla \cdot \underline{A} = 0. \quad (2.4.1)$$

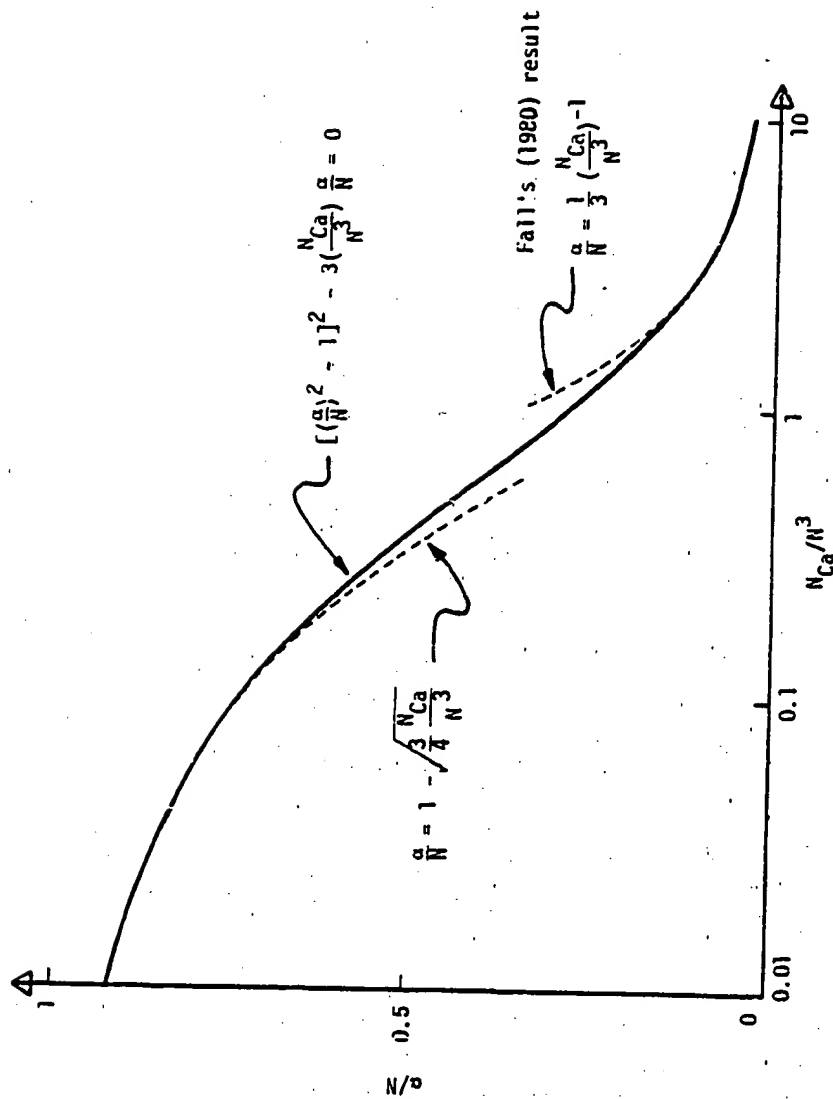


Figure 2.4. Ratio of decay rate to wavenumber, α/N , versus ratio of capillary number to wavenumber cubed, N_{Ca}/N^3 , as predicted by lubrication theory.

The divergence of the vector potential \underline{A} does not affect the velocity field, \underline{u} , and therefore can be set to zero as in Equation (2.4.1). This property, that the divergence of the vector potential can be chosen arbitrarily, is known as gauge invariance (Morse and Feshbach 1953). Taking the vector potential to be solenoidal simplifies the curl of the velocity field:

$$\nabla \times \underline{u} = \nabla \times \nabla \times \underline{A} = -\nabla^2 \underline{A} + \nabla(\nabla \cdot \underline{A}) = -\nabla^2 \underline{A} \quad (2.4.2)$$

which is needed below. The pressure field can be eliminated from Oseen's equation, Equation 2.2.2, by taking the curl to get an equation for vorticity, i.e. the curl of the velocity field. Equation (2.4.4) can then be used to replace vorticity by the vector potential to give

$$\nabla^4 \underline{A} - N_{Re} \frac{\partial}{\partial x} \nabla^2 \underline{A} = \underline{0} \quad (2.4.3)$$

This equation has a separation of variables solution of the form

$$\underline{A} = e^{-\alpha x} [\underline{a}(y) \sin(Nz) + \underline{\tilde{a}}(y) \cos(Nz)] \quad (2.4.4)$$

where N is again the wavenumber in transverse coordinate, z , and α is exponential decay rate in the streamwise coordinate, x . Replacing \underline{A} in Equation (2.4.3) by its equivalent in Equation (2.4.4) and dividing out the common $e^{-\alpha x}$ gives the fourth-order differential equation:

$$\begin{aligned} & [\underline{a}^{(4)} + [2(\alpha^2 - N^2) + \alpha N_{Re}] \underline{a}'' + [(\alpha^2 - N^2)(\alpha^2 - N^2 + \alpha N_{Re})] \underline{a}] \sin(Nz) \\ & + [\underline{\tilde{a}}^{(4)} + [2(\alpha^2 - N^2) + \alpha N_{Re}] \underline{\tilde{a}}'' + [(\alpha^2 - N^2)(\alpha^2 - N^2 + \alpha N_{Re})] \underline{\tilde{a}}] \cos(Nz) = \underline{0}, \end{aligned} \quad (2.4.5)$$

a prime denoting differentiation with respect to y . Because the origin of z is arbitrary, each bracketed expression must be zero:

$$\underline{a}'''' + [2(\alpha^2 - N^2) + \alpha N_{Re}] \underline{a}'' + [(\alpha^2 - N^2)(\alpha^2 - N^2 + \alpha N_{Re})] \underline{a} = 0, \quad (2.4.6)$$

and likewise for $\bar{\underline{a}}$. Because the differential equation for $\bar{\underline{a}}$ is identical, it has the same general solution as (2.4.6), namely

$$\underline{a} = \underline{c}_1 \cos(\beta y) + \underline{c}_2 \sin(\beta y) + \underline{c}_3 \cos(\gamma y) + \underline{c}_4 \sin(\gamma y) \equiv \underline{c}_i S_i \quad (2.4.7)$$

where $\beta^2 \equiv \alpha^2 - N^2$, $\gamma^2 \equiv \alpha^2 - N^2 + \alpha N_{Re}$, \underline{c}_i is a vector containing three arbitrary constants, and

$$[S_i] \equiv [\cos(\beta y), \sin(\beta y), \cos(\gamma y), \sin(\gamma y)] \quad (2.4.8)$$

is matrix vector that is convenient for subsequent manipulations. Summation over a repeated index is implied. Each of the vector coefficients \underline{c}_i contains three scalar coefficients, for a total of twelve. $\bar{\underline{a}}$ also contains twelve scalar coefficients, and thus by (2.4.4) the vector potential contains twenty-four. However, the requirement that \underline{A} be solenoidal in (2.4.1) imposes eight linear constraints on the twenty-four unknown scalar coefficients. Furthermore, four of the scalar coefficients do not affect velocity field. To understand why this is so, it is instructive to express the vector potential in Helmholtz' representation (see e.g. Aris 1962):

$$\underline{A} = \nabla \phi + \nabla \times \underline{\psi},$$

where ϕ is a scalar function and $\underline{\psi}$ is a solenoidal vector field. The

requirement that \underline{A} be solenoidal implies that ϕ must satisfy Laplace's equation:

$$\nabla \cdot \underline{A} = \nabla^2 \phi = 0$$

There are four solutions of this equation that have the same form as terms in \underline{A} , which are

$$\begin{aligned} \phi = & (\phi_1 \cos y + \phi_2 \sin y) e^{-\alpha x} \cos(Nz) \\ & + (\phi_3 \cos y + \phi_4 \sin y) e^{-\alpha x} \sin(Nz) . \end{aligned}$$

This result is not fortuitous because the differential operator in Equation (2.4.3) for the vector potential can be factored into two commuting operators, and thus $\underline{A} = \underline{A}_1 + \underline{A}_2$ where

$$\nabla^2 \underline{A}_1 = 0 \quad , \quad (\nabla^2 - \frac{\partial}{\partial x}) \underline{A}_2 = 0 .$$

The first of these is the vector Laplace equation. It is therefore possible to find solutions ϕ which both satisfy Laplace's equation and can be used in Helmholtz' representation of the vector potential. But their contributions to the vector potential disappear from the curl of the vector potential, i.e. the velocity field.

The final count of independent scalar coefficients in the vector potential \underline{A} that affect the velocity field is twelve: eight of the original twenty-four scalar coefficients are restricted by the requirement that \underline{A} be solenoidal (2.4.1) and four more play no role in determining the velocity field. To find the remaining twelve unknown coefficients would require that boundary conditions (2.2.4)-(2.2.7) be translated

into ones on \underline{a} and $\bar{\underline{a}}$. This is difficult because pressure cannot easily be eliminated from the normal stress equation (2.2.6). It is much more convenient to return to the primitive variables, \underline{u} , p , and h . \underline{u} can be constructed by taking the curl of the vector potential \underline{A} and has the following form:

$$\begin{aligned} \underline{u} + \bar{\underline{u}} &= \begin{bmatrix} \underline{i} \cos(Nz) \\ \underline{j} \cos(Nz) \\ \underline{k} \cos(Nz) \end{bmatrix} \begin{bmatrix} u_1 & u_2 & u_3 & u_4 \\ v_1 & v_2 & v_3 & v_4 \\ w_1 & w_2 & w_3 & w_4 \end{bmatrix} \\ &+ \begin{bmatrix} \underline{i} \cos(Nz) \\ \underline{j} \cos(Nz) \\ \underline{k} \cos(Nz) \end{bmatrix} \begin{bmatrix} \bar{u}_1 & \bar{u}_2 & \bar{u}_3 & \bar{u}_4 \\ \bar{v}_1 & \bar{v}_2 & \bar{v}_3 & \bar{v}_4 \\ \bar{w}_1 & \bar{w}_2 & \bar{w}_3 & \bar{w}_4 \end{bmatrix} \begin{bmatrix} \cos(\beta y) \\ \sin(\beta y) \\ \cos(\gamma y) \\ \sin(\gamma y) \end{bmatrix} e^{-\alpha x} \\ &= \{ \underline{D}_i u_{ij}^c + \bar{\underline{D}}_i \bar{u}_{ij}^c \} s_j e^{-\alpha x} \end{aligned} \quad (2.4.9)$$

Here $\underline{D}_1 \equiv \underline{i} \cos(Nz)$, $\underline{D}_2 \equiv \underline{j} \cos(Nz)$, $\underline{D}_3 \equiv \underline{k} \sin(Nz)$, $\bar{\underline{D}}_1 \equiv \underline{i} \sin(Nz)$, $\bar{\underline{D}}_2 \equiv \underline{j} \sin(Nz)$, and $\bar{\underline{D}}_3 \equiv \underline{k} \cos(Nz)$ are vectors and u_{ij}^c and \bar{u}_{ij}^c are the elements in the i -th row and j -th column of the velocity coefficient matrices which appear in Equation (2.4.9a). Coefficients u_{ij}^c and \bar{u}_{ij}^c are related to \underline{c}_i and $\bar{\underline{c}}_i$ by the general solution for velocity (2.4.9), the relationship between velocity and vector potential (2.4.1), and the equations that give the general solution of the vector potential — (2.4.4), (2.4.7), and the equivalent of (2.4.7) for $\bar{\underline{a}}$. This relationship is displayed in Figure 2.5, where M_{ij} and \bar{M}_{ij} are transformation matrices that connect velocity coefficients with vector potential coef-

ficients. Each transformation matrix has two null vectors as shown, and therefore only twenty of the twenty-four velocity coefficients are independent. The null vectors result from contributions to the vector potential which are gradients of a scalar function, as explained in the preceding paragraph. Only eight of the twelve scalar coefficients in the four \underline{c}_i are independent, as explained above, and likewise for \bar{c}_i . Thus, only six of the twelve scalar coefficients u_{ij}^C are independent, and likewise for \bar{u}_{ij}^C . Pressure can be found by substituting velocity as given by Equation (2.4.9) into the Oseen equation (2.2.2) and integrating. It has the following form:

$$p + \bar{p} = \{ \cos(Nz)[p_1, p_2, p_3, p_4] + \sin(Nz)[\bar{p}_1, \bar{p}_2, \bar{p}_3, \bar{p}_4] \} \begin{bmatrix} \cos(\delta y) \\ \sin(\delta y) \\ \cos(\gamma y) \\ \sin(\gamma y) \end{bmatrix} e^{-\alpha x} \\ \equiv \{ \cos(Nz)p_i + \sin(Nz)\bar{p}_i \} S_i e^{-\alpha x}, \quad (2.4.10)$$

where p_i and \bar{p}_i , the pressure coefficients that appear in (2.4.10a), are related through the Oseen equation to the velocity coefficients in (2.4.9), and thus are not independent. The free surface elevation can be shown by substituting velocity from (2.4.9) into the kinematic boundary condition (2.2.7) and integrating in the streamwise coordinate, to have the form:

$$h + \bar{h} = \{ \cos(Nz)h_1 + \sin(Nz)\bar{h}_1 \} e^{-\alpha x}, \quad (2.4.11)$$

where \bar{h}_1 and h_1 are scalar unknowns.

The simplest means to find the linear constraints on the velocity and pressure coefficients defined in Equations (2.4.9) and (2.4.10) is to return to the basic equations that they must satisfy, namely the Oseen and continuity equations, (2.2.2) and (2.2.3). Before doing this, it is convenient to choose a particular phase of the perturbation in transverse coordinate, z : a crest of the free surface is located at $z = 0$, i.e. $\partial h / \partial z = 0$ and $\partial^2 h / \partial z^2 < 0$ there. With this choice, the coefficients that have tildes in (2.4.9)-(2.4.11) drop out. (Were the choice to retain only the coefficients with tildes, the following results would be identical except that the signs of some terms containing wavenumber would change; the characteristic equation for decay rate α would be identical.) The linear constraints on u_{ij}^C and p_i from the Oseen and continuity equations are

$$\begin{aligned} (u_{1j}^C [\gamma^2 \delta_{jk} + R_{jk}^2] + \alpha p_k) S_k &= 0 \\ (u_{2j}^C [\gamma^2 \delta_{jk} + R_{jk}^2] - p_j R_{jk}) S_k &= 0 \end{aligned} \quad (2.4.12)$$

$$\begin{aligned} (u_{3j}^C [\gamma^2 \delta_{jk} + R_{jk}^2] + N p_k) S_k &= 0 \\ [-\alpha u_{1j}^C - u_{21}^C R_{1j} + N u_{3j}^C] S_j &= 0 \end{aligned} \quad (2.4.13)$$

where δ_{jk} is the Kronecker delta, i.e. $\delta_{jk} = 1$ if $j = k$ and $\delta_{jk} = 0$ otherwise, and

$$[R_{ij}] = \begin{bmatrix} 0 & -\beta & 0 & 0 \\ \beta & 0 & 0 & 0 \\ 0 & 0 & 0 & -\gamma \\ 0 & 0 & \gamma & 0 \end{bmatrix}, [R_{ij}^2] = [R_{ik}R_{kj}] = - \begin{bmatrix} \beta^2 & 0 & 0 & 0 \\ 0 & \beta^2 & 0 & 0 \\ 0 & 0 & \gamma^2 & 0 \\ 0 & 0 & 0 & \gamma^2 \end{bmatrix} \quad (2.4.14)$$

Because each S_i is an independent function of the filmwise coordinate y (see Equation (2.4.8)) and Equations (2.4.12) and (2.4.13) must hold throughout the domain, it follows that:

$$u_{1j}^C [\gamma^2 \delta_{jk} + R_{jk}^2] + \alpha p_k = 0$$

$$u_{2j}^C [\gamma^2 \delta_{jk} + R_{jk}^2] - p_j R_{jk} = 0 \quad k = 1, 2, 3, 4 \quad (2.4.15)$$

$$u_{3j}^C [\gamma^2 \delta_{jk} + R_{jk}^2] + N p_k = 0$$

$$- \alpha u_{1j}^C - u_{2j}^C R_{1j} + N u_{3j}^C = 0 \quad j = 1, 2, 3, 4 \quad (2.4.16)$$

These are sixteen equations in the sixteen scalar coefficients of velocity and pressure. However, only ten of the equations are independent, leaving six coefficients unknown as anticipated on page 2-17. Ten independent equations from the set of sixteen are:

$$\alpha N_{Re} u_1 + \alpha p_1 = 0 \quad (2.4.17)$$

$$\alpha N_{Re} u_2 + \alpha p_2 = 0 \quad (2.4.18)$$

$$\alpha N_{Re} v_1 - \beta p_2 = 0 \quad (2.4.19)$$

$$\alpha N_{Re} v_2 + \beta p_1 = 0 \quad (2.4.20)$$

$$\alpha N_{Re} w_1 + N p_1 = 0 \quad (2.4.21)$$

$$\alpha N_{Re} w_2 + N p_2 = 0 \quad (2.4.22)$$

$$p_3 = 0 \quad (2.4.23)$$

$$p_4 = 0 \quad (2.4.24)$$

$$- \alpha u_3 + \gamma v_4 + N w_3 = 0 \quad (2.4.25)$$

$$- \alpha u_4 - \gamma v_3 + N w_4 = 0 \quad (2.4.26)$$

The Oseen solution is completed by enforcing the boundary conditions at the moving web, at the free surface, and at inflow and far-downstream boundaries. The no-slip and no-penetration boundary condition (2.2.4) imposes three constraints on the velocity coefficients:

$$u_1 + u_3 = 0 \quad (2.4.27)$$

$$v_1 + v_3 = 0 \quad (2.4.28)$$

$$w_1 + w_3 = 0 \quad (2.4.29)$$

The kinematic condition (2.2.7) relates the free surface elevation perturbation to velocity:

$$\alpha h_1 + u_{21}^C S_1(\cdot) = 0 \quad (2.4.30)$$

The shear stress boundary condition (2.2.5) dictates that both components of viscous shear at the free surface must be zero:

$$- N u_{21}^C S_1(1) + u_{31}^C R_{1j} S_j(1) = 0 \quad (2.4.31)$$

$$u_{11}^C R_{1j} S_j(1) - \alpha u_{21}^C S_1(1) = 0 \quad (2.4.32)$$

The normal stress boundary condition (2.2.6) equates the viscous normal stress and pressure at the free surface with capillary stress due to meniscus curvature:

$$2u_{2i}^C R_{ij} S_j(1) - p_i S_i(1) - \frac{1}{N_{ca}} \sigma^2 h_1 = 0. \quad (2.4.33)$$

Equations (2.4.17)-(2.4.33) are seventeen homogeneous scalar equations for the seventeen unknown coefficients — twelve in the velocity field, four in the pressure field, and one in free surface elevation, as defined in Equations (2.4.9)-(2.4.11) — plus the unknown decay rate, α . Equations (2.4.17)-(2.4.33) appear in matrix form in Figure 2.6, and the determinant of that matrix must be zero in order for a solution to exist. The condition that this be so is the characteristic equation for spatial decay rate, α . The seventeen scalar coefficients in the velocity, pressure, and free energy surface elevation can be determined once α is known, but only up to an arbitrary constant.

It is convenient to eliminate most of the unknown coefficients in the set of seventeen in order to reduce the order of the determinant and thereby simplify calculation of the characteristic equation. Equations (2.4.17)-(2.4.29) each contain at most three of the unknown coefficients, and so they are easily rearranged and combined to express each of the unknown coefficients as functions of a set of four coefficients. The optimal set of coefficients found by applying the strategy of Stadtherr et al. (1974) are u_1 , u_2 , and u_4 , and the resulting expressions are

$$p_1 = - \frac{N_{ca}}{Re} u_1 \quad (2.4.34)$$

[illegible]

Figure 2.6. Matrix representation of Equations (2.4.17)–(2.4.33). The characteristic equation (2.4.52) is the condition that the determinant of this matrix be zero.

$$p_2 = -N_{Re} u_2 \quad (2.4.35)$$

$$p_3 = 0 \quad (2.4.36)$$

$$p_4 = 0 \quad (2.4.37)$$

$$u_3 = -u_1 \quad (2.4.38)$$

$$v_1 = -\beta u_2 / \alpha \quad (2.4.39)$$

$$v_2 = \beta u_1 / \alpha \quad (2.4.40)$$

$$v_3 = \beta u_2 / \alpha \quad (2.4.41)$$

$$v_4 = -\beta^2 u_1 / \alpha \gamma \quad (2.4.42)$$

$$w_1 = Nu_1 / \alpha \quad (2.4.43)$$

$$w_2 = Nu_2 / \alpha \quad (2.4.44)$$

$$w_3 = -Nu_1 / \alpha \quad (2.4.45)$$

$$w_4 = (\alpha u_4 + \beta \gamma u_2 / \alpha) / N \quad (2.4.46)$$

All but four coefficients — u_1 , u_2 , u_4 , and h_1 — can now be eliminated from Equations (2.4.30)-(2.4.33):

$$u_1 \left[\sin \beta - \frac{\beta}{\gamma} \sin \gamma \right] + u_2 [\cos \gamma - \cos \beta] + h_1 \left[\frac{\alpha^2}{\beta} \right] = 0 \quad (2.4.47)$$

$$u_1 \left[\frac{\beta^2 + \gamma^2}{\gamma^2} \sin \gamma - \frac{\beta}{\gamma} \sin \beta \right] + u_2 \left[\frac{\beta}{\gamma} (2 \cos \beta - \cos \gamma) \right] + u_4 [\cos \gamma] = 0 \quad (2.4.48)$$

$$u_1 \left[\frac{\beta^2 + \gamma^2}{\gamma^2} \sin \gamma - 2 \frac{\beta}{\gamma} \sin \beta \right] + u_2 \left[\frac{\beta}{\gamma} \left(\cos \beta + \frac{\gamma^2 - N^2}{N^2} \cos \gamma \right) \right] + u_4 \left[\frac{\alpha}{N^2} \cos \gamma \right] = 0 \quad (2.4.49)$$

$$u_1 \left[2(\cos \beta - \cos \gamma) + \frac{\alpha N_{Re}}{\beta^2} \cos \beta \right] + u_2 \left[2 \left(\sin \beta - \frac{\gamma}{\beta} \sin \gamma \right) + \frac{\alpha N_{Re}}{\beta^2} \right] + h_1 \left[\frac{-\alpha}{N_{ca}} \right] = 0 \quad (2.4.50)$$

Equations (2.4.47) and (2.4.50) can be combined to eliminate h_1 and Equations (2.4.48) and (2.4.49) to eliminate u_4 . The characteristic equation is found by setting the determinant of the two resulting equations equal to zero:

$$\begin{vmatrix} -\frac{\gamma^2 + \beta^2}{2\gamma} \sin\gamma + 2\sin\beta & -2\cos\beta + \frac{\gamma^2 + \beta^2}{\beta^2} \cos\gamma \\ \frac{\beta^2}{N_{ca}} (\sin\beta - \frac{\beta}{\gamma} \sin\gamma) & \frac{\beta^2}{N_{ca}} (\cos\gamma - \cos\beta) \\ +\alpha(\frac{\beta^2 + \gamma^2}{\beta} \cos\beta - 2\beta \cos\gamma) & +\alpha(\frac{\beta^2 + \gamma^2}{\beta} \sin\beta - 2\gamma \sin\gamma) \end{vmatrix} = 0 \quad (2.4.51)$$

In the limiting case that wavenumber equals zero, this equation is equivalent to Higgins' (1980) Equation (2.4.40). When wavenumber, N , equals zero the following simplifications result: (1) β is equal to α , the exponential decay rate and (2) γ is equal to $\sqrt{\alpha^2 + \alpha N_{Re}}$. These quantities correspond to Higgins' in the following way: (1) α used here is the negative of Higgins' α_n (compare Equation (2.4.4) with Higgins' Equation (2.2.21)); (2) therefore, β is also the same as the negative of Higgins' α_n ; and (3) γ is the same as the negative of Higgins' λ_n . When Higgins' symbols are substituted for α , β , and γ , the first column in Equation (2.4.51) is scaled by γ/β , and the two columns are interchanged, the result is Higgins' Equation (2.4.10). Equations (2.4.51) can be rearranged and simplified to get the result:

$$\begin{aligned} \frac{N_{Re}}{N_{Ca}} \beta^2 \left[\sin(\beta) \cos(\gamma) - \frac{\beta}{\gamma} \cos(\beta) \sin(\gamma) \right] + (5\beta^4 + 2\beta^2 \gamma^2 + \gamma^4) \cos(\beta) \cos(\gamma) \\ + \frac{\beta}{\gamma} (\beta^4 + 6\beta^2 \gamma^2 + \gamma^4) \sin(\beta) \sin(\gamma) - 4\beta^2 (\beta^2 + \gamma^2) = 0 \quad (2.4.52) \end{aligned}$$

This equation is transcendental in decay rate, α . The coefficients, u_1 and u_2 , can be determined up to an arbitrary constant from the elements of a column of the adjugate (see Amundson 1966, who uses the word adjoint in place of adjugate) of the matrix in Equation (2.4.51):

$$u_1 = 2\cos(\beta) - \frac{\gamma^2 + \beta^2}{\beta^2} \cos(\gamma) \quad (2.4.53)$$

$$u_2 = 2\sin(\beta) - \frac{\gamma^2 + \beta^2}{\beta\gamma} \sin(\gamma) \quad (2.4.54)$$

The coefficients, h_1 and u_4 are found by inserting the above equations for u_1 and u_2 in Equation (2.4.47) and (2.4.48), respectively:

$$h_1 = \frac{N_{Re}}{\alpha} \left[\frac{1}{\beta} \sin(\beta) \cos(\gamma) - \frac{1}{\gamma} \cos(\beta) \sin(\gamma) \right] \quad (2.4.55)$$

$$u_4 = -2 \frac{\gamma}{\beta} \sin(\beta) + \frac{\gamma^2 + \beta^2}{\beta^2} \sin(\gamma) \quad (2.4.56)$$

The remaining coefficients are easily found from Equations (2.4.34)-(2.4.46).

A unique solution can be constructed by invoking the inflow and far-downstream boundary conditions. The far-downstream boundary condition (2.2.9) restricts the allowable values of the decay rate α to the set of complex numbers with positive real parts, because those are the ones that

correspond to disturbances which decay with downstream distance. The decay rates which belong to the set of complex numbers with negative real parts correspond to modes which decay with upstream distance, and thus represent solutions which have an upstream asymptotic plug-flow regime. Examples are uniform film flows which meet stationary obstructions, such as the upstream edge of a knife coater. The number of decay rates that have positive real part and satisfy the characteristic equation (2.4.52) is infinite, as demonstrated in Section 2.5. Each decay rate corresponds to a distinct mode, i.e. a distinct flow pattern. An arbitrary perturbation of given transverse wavenumber N can contain any or all of these modes. Furthermore, an arbitrary perturbation can have infinitely many Fourier components, i.e. infinitely many values of transverse wavenumber N . Therefore, an arbitrary perturbation with arbitrary phase is described by

$$\begin{aligned} \underline{u}^A &= \sum_{i=1}^{\infty} \sum_{j=1}^{\infty} \{ b_{ij} \bar{D}_k(N_i) u_{k\ell}^C + \bar{b}_{ij} \bar{D}_k(N_i) \bar{u}_{k\ell}^C \} S_{\ell}(\alpha_j) e^{-\alpha_j x} \\ &\equiv \sum_{i=1}^{\infty} \sum_{j=1}^{\infty} \{ b_{ij} \underline{u}(N_i, \alpha_j) + \bar{b}_{ij} \bar{\underline{u}}(N_i, \alpha_j) \} \end{aligned} \quad (2.4.57)$$

where b_{ij} and \bar{b}_{ij} are arbitrary constants, N_i are the wavenumbers which fit the transverse dimension, L :

$$N_i = \frac{\pi i}{L}, \quad i = 1, 2, \dots, \quad (2.4.58)$$

and α_j are the roots of the characteristic equation (2.4.52) that have positive real part. Finding the constants in Equation (2.4.57) so that \underline{u}^A satisfies the inflow boundary condition (2.2.10) would be a difficult

task: it would require the solution of the adjoint problem (see Friedman 1956), \underline{u}^* and $\bar{\underline{u}}^*$, so that the biorthogonality conditions,

$$\begin{aligned} \langle \underline{u}(N_1, \alpha_j), \underline{u}^*(N_k, \alpha_2) \rangle &= \delta_{jk} \delta_{j2} \langle \underline{u}(N_1, \alpha_j), \underline{u}^*(N_1, \alpha_j) \rangle \\ \langle \bar{\underline{u}}(N_1, \alpha_j), \bar{\underline{u}}^*(N_k, \alpha_2) \rangle &= \delta_{jk} \delta_{j2} \langle \bar{\underline{u}}(N_1, \alpha_j), \bar{\underline{u}}^*(N_1, \alpha_j) \rangle \\ \langle \underline{u}(N_1, \alpha_j), \bar{\underline{u}}^*(N_k, \alpha_2) \rangle &= 0 \\ \langle \bar{\underline{u}}(N_1, \alpha_j), \underline{u}^*(N_k, \alpha_2) \rangle &= 0 \end{aligned} \quad (2.4.59)$$

could be used. Here, the inner product is

$$\langle \underline{a}, \underline{b} \rangle \equiv \int_0^L \int_0^1 (\bar{\underline{a}} \cdot \underline{b}) dy dz,$$

where the overbar indicates the complex conjugate. If \underline{u}^* and $\bar{\underline{u}}^*$ were known, the constants could be determined by the inner products:

$$\begin{aligned} b_{1j} &= \langle \underline{u}_0, \underline{u}^*(N_1, \alpha_j) \rangle / \langle \underline{u}(N_1, \alpha_j), \underline{u}^*(N_1, \alpha_j) \rangle \\ \bar{b}_{1j} &= \langle \bar{\underline{u}}_0, \bar{\underline{u}}^*(N_1, \alpha_j) \rangle / \langle \bar{\underline{u}}(N_1, \alpha_j), \bar{\underline{u}}^*(N_1, \alpha_j) \rangle \end{aligned} \quad (2.4.59)$$

However, the difficulties of calculating the adjoint solutions and then using them to construct the constants in (2.4.59) can be avoided when the inflow boundary of the asymptotic domain is far enough downstream so that only one mode, the most slowly decaying one, persists. This simplification is used to advantage in the three-dimensional stability analysis described in Chapter 6 as explained in Section 2.6.

2.5. Limiting Cases and Numerical Results

The characteristic equation (2.4.52) is a complicated transcendental function of the decay rate α . Two methods are employed here to solve it. The first is to construct approximate solutions valid only for limiting parameter values — the parameters being Reynolds number, N_{Re} , capillary number, N_{Ca} , and wavenumber, N . The second is to employ secant iteration on a digital computer to track the roots of (2.4.52) as parameters are varied. The numerical results are set out below in Tables 2.1-2.5.

A useful limit is when inertia is negligible compared with viscous forces, i.e. when Reynolds number is approximately zero. However, setting Reynolds number to zero in the characteristic equation (2.4.52) produces the trivial equality $0 \equiv 0$. One remedy is to expand each term in a Taylor series in Reynolds number, collect the lowest order terms — in this case these are the linear terms in Reynolds number — and set them to zero. The result is

$$2\alpha[\cos^2(\beta) - \beta^2] + [\beta \cos(\beta)\sin(\beta) - \beta^2]/N_{Ca} = 0 \quad N_{Re} = 0. \quad (2.5.1)$$

When wavenumber is zero this is identical to Higgins' (1980) result (compare by replacing both α and β in (2.5.1) by the negative of Higgins' $\tilde{\alpha}_n$). Equation (2.5.1) is not readily solved, but two limiting cases in capillary number are easily investigated by standard perturbation methods described in Lin and Segel (1974).

First, when capillary number is small so that capillary forces dominate viscous forces the slowest decay rate is

$$\alpha_1 = N - \sqrt{3N_{Ca}}/N \quad N_{Ca} \ll 1, N_{Re} = 0 \quad (2.5.2)$$

Thus the slowest decay rate is slightly less than the wavenumber. This is so only when $N_{ca}/N^3 \ll 1$; otherwise

$$\alpha_1 = N^4/3N_{ca} \quad N \ll N_{ca} \ll 1, N_{Re} = 0, \quad (2.5.3)$$

so the slowest decay rate goes to zero much more rapidly than wavenumber. The results in Equations (2.5.2) and (2.5.3) are identical to those of lubrication theory as given in Equations (2.4.6) and (2.4.7), respectively. Note, however, that (2.5.3) is invalid in the two-dimensional limit of wavenumber going to zero because the primary velocity component of the corresponding mode is transverse. The easiest way to see that this is so is to examine the pressure field as given by Equation (2.4.10); the streamwise pressure gradient is proportional to decay rate and therefore goes as the fourth power of wavenumber by (2.5.3), but the transverse pressure gradient goes as the first power of wavenumber and therefore dominates in the limit of wavenumber approaching zero. Because pressure gradients are the only forces that drive flow when Reynolds number is zero, the above assertion that the primary velocity component is transverse is validated. Higgins (1980) shows the slowest decay rate at zero Reynolds number and small capillary number in the two-dimensional limit to be

$$\alpha_2 = (3N_{ca})^{1/3} \quad N_{ca} \ll 1, N = N_{Re} = 0. \quad (2.5.4)$$

More rapidly decaying modes have decay rates which satisfy

$$2\beta_{n+2} = \sin(2\beta_{n+2}) \quad n = 1, 2, 3, \dots \quad (2.5.5)$$

Higgins (1980) gives the approximate result:

$$\beta_{2n+1} = (n + \frac{1}{4})\pi + i \frac{1}{2} \ln[(4n+1)\pi] \quad N_{ca} = N_{Re} = 0 \quad (2.5.6)$$

$$\beta_{2n+2} = (n + \frac{1}{4}\pi) - i \frac{1}{2} \ln[(4n+1)\pi] \quad N_{ca} = N_{Re} = 0, \quad (2.5.7)$$

where $i \equiv \sqrt{-1}$, and $\alpha \equiv \sqrt{\beta^2 + N^2}$.

The second limiting case at negligible Reynolds number is for very large capillary number, i.e. capillary forces small compared with viscous forces. The slowest decay rate is

$$\alpha_1 = \frac{1}{2N_{ca}} \frac{N \cosh N \sinh N - N^2}{\cosh^2 N + N^2} \quad N_{ca} \gg 1, \quad N_{Re} = 0. \quad (2.5.8)$$

As before, $\alpha_1 = 0$ when $N = 0$, and should be disregarded. Other roots satisfy the equation

$$\cos^2 \beta_n = \beta_n^2 \quad (2.5.9)$$

and are approximately (see Higgins 1980)

$$\beta_2 = 0.73909 \quad (2.5.10)$$

$$\beta_{2n+1} = n\pi + i \ln(2n\pi) \quad 1/N_{ca} = N_{Re} = 0 \quad (2.5.11)$$

$$\beta_{2n+2} = n\pi - i \ln(2n\pi) \quad 1/N_{ca} = N_{Re} = 0 \quad (2.5.12)$$

where $n = 1, 2, \dots$

Another useful limit is when inertia dominates over viscous forces, i.e. Reynolds' number is very large. Equation (2.4.52) reduces to

$$\sin(\beta)\cos(\gamma) - \frac{\beta}{\gamma} \cos(\beta)\sin(\gamma) = 0 \quad 1/N_{Re} = 0. \quad (2.5.13)$$

For large wavenumber, i.e. short wavelengths, (2.5.13) can be simplified further to get:

$$\tan(\gamma)/\gamma = 1/N \quad (2.5.14)$$

which has roots given approximately by

$$\alpha_n = \frac{1}{N_{Re}} (n^2 \pi^2 + N^2) \quad N, N_{Re} \gg 1, \quad (2.5.15)$$

where $n = 1, 2, \dots$. When wavenumber is small, the dominant term in Equation (2.4.52) is $(5\beta^2 + 2\beta^2\gamma^2 + \gamma^4)\cos(\beta)\cos(\gamma)$. Setting this to zero gives the roots

$$\alpha_{n+1} = \frac{1}{N_{Re}} \left[\frac{\pi^2}{4} (2n-1)^2 \right] \quad 1/N, N_{Re} \gg 1, \quad (2.5.16)$$

where $n = 1, 2, \dots$. The dominant decay rate, α_1 , is given by Equation (2.5.3) provided $N^4 N_{Re} / N_{Ca} \ll 1$, which is ordinarily true when wavenumber, N , is small.

The characteristic equation (2.4.52) was solved numerically by the IMSL subroutine ZANLYT, which uses secant iteration (see e.g. Hildebrand 1974) to find complex roots of equations. The five slowest decay rates were tracked through the three-dimensional parameter-space represented

N	N_{Re}	0.01	0.1	1	10	100	1000
0	$\alpha_I = 0$ $\alpha_{II} = 0.2935696$	0	0	0	0	0	0
0.01	$\alpha_I = 0.0000003$ $\alpha_{II} = 0.2937903$	0.2924906	0.0000003	0.2817059	0.1829279	0.0246370	0.0024674
0.1	$\alpha_I = 0.0032675$ $\alpha_{II} = 0.3145486$	0.0000003	0.0000003	0.0000003	0.0000003	0.0000003	0.0000003
1	$\alpha_I = 0.9000111$ $\alpha_{II} = 1.0734632$	0.2927113	0.0000003	0.2819260	0.1831008	0.0246448	0.0024675
10	$\alpha_I = 9.9568648$ $\alpha_{II} = 10.0164796$	0.0032679	0.0032717	0.0032717	0.0033104	0.0038487	0.0012797
		0.3134655	0.3026050	0.3026050	0.1981077	0.0216618	± 1 0.0025698
		0.9014355	0.9176146	0.9176146	0.9699689	0.2056313	0.0065380
		1.0718390	1.0536028	1.0536028	± 1 0.1528617	0.6089049	± 1 0.2936522
		9.9624112	9.9885216	9.9885216	6.7493428	1.1087945	0.1120722
		10.0117286	± 1 0.0459452	± 1 0.0459452	8.3129121	1.4542026	0.1474033

Table 2.1. Dependence of the two slowest decay rates, α_I and α_{II} , on Reynolds number, N_{Re} , and wavenumber, N , when capillary number is 0.01.

N_{Re} N	0.01	0.1	1	10	100	1000
0	$\alpha_I = 0$ $\alpha_{II} = 0.5283241$	0 0.5244427	0 0.4860346	0 0.2185073	0 0.0246479	0 0.0024674
0.01	$\alpha_I = 0.0000000$ $\alpha_{II} = 0.5284373$	0.0000000 0.5245558	0.0000000 0.4861465	0.0000000 0.2185669	0.0000000 0.0246524	0.0000000 0.0024678
0.1	$\alpha_I = 0.0003274$ $\alpha_{II} = 0.5394809$	0.0003274 0.5355937	0.0003275 0.4970612	0.0003279 0.2242312	0.0003318 0.0247696	0.0003862 0.0021274
1	$\alpha_I = 0.6142074$ $\alpha_{II} = 1.1627852$	0.6167753 1.1581293	0.6457144 1.1077108	0.7454070 + 1 0.3962146	0.0384961 + 1 0.2843577	0.0040885 + 1 0.0859528
10	$\alpha_I = 9.6914236$ $\alpha_{II} = 10.0241735$	9.7154030 10.0159031	9.9412024 + 1 0.1029049	6.7952682 8.4732960	1.1097297 1.4577853	0.1120818 0.1474400

Table 2.2. Dependence of the two slowest decay rates, α_I and α_{II} , on Reynolds number, N_{Re} , and wavenumber, N , when capillary number is 0.1.

N	N_{Re}	0.01	0.1	1	10	100	1000
0	$\alpha_I = 0$		0	0	0	0	0
	$\alpha_{II} = 0.6960480$	0.6883670	0.6143299	0.2249166	0.0246498	0.0024674	0.0024674
0.01	$\alpha_I = 0.0000000$	0.0000000	0.0000000	0.0000000	0.0000000	0.0000000	0.0000000
	$\alpha_{II} = 0.6961235$	0.6884425	0.6144042	0.2249544	0.0246531	0.0024678	0.0024678
0.1	$\alpha_I = 0.0000328$	0.0000327	0.0000327	0.0000327	0.0000328	0.0000332	0.0000332
	$\alpha_{II} = 0.7035540$	0.6958692	0.6217169	0.2286626	0.0250286	0.0024756	0.0024756
1	$\alpha_I = 0.1180290$	0.1182354	0.1203828	0.1600181	0.0302182	0.0032170	0.0032170
	$\alpha_{II} = 1.2273564$	1.2193105	1.1372767	0.4201566	+ 1 0.0790441	+ 1 0.0265648	+ 1 0.0265648
10	$\alpha_I = 4.4736145$	4.4872483	4.6373978	5.2703976	1.1189283	0.1121771	0.1121771
	$\alpha_{II} = 10.0259567$	10.0167353	9.7709034	+ 1 2.4577632	+ 1 2.5548473	+ 1 2.5548473	+ 1 2.5548473

Table 2.3. Dependence of the two slowest decay rates, α_I and α_{II} , on Reynolds number, N_{Re} , and wave-number, N , when capillary number is 1.

$N \backslash N_{Re}$	0.01	0.1	1	10	100	1000
0	$\alpha_I = 0$ $\alpha_{II} = 0.7332993$	0 0.7244468	0 0.6400034	0 0.2256201	0 0.0246491	0 0.0024674
0.01	$\alpha_I = 0.0000000$ $\alpha_{II} = 0.7333679$	0.0000000 0.7245154	0.0000000 0.6400710	0.0000000 0.2256555	0.0000000 0.0246532	0.0000000 0.0024678
0.1	$\alpha_I = 0.0000033$ $\alpha_{II} = 0.7401201$	0.0000033 0.7312663	0.0000033 0.6467334	0.0000033 0.2291445	0.0000033 0.0250541	0.0000033 0.0025050
1	$\alpha_I = 0.0120270$ $\alpha_{II} = 1.2407892$	0.0120292 1.2318475	0.0120513 1.1423186	0.0122819 0.5049033	0.0168214 0.0419853	0.0029781 +1 0.0078701
10	$\alpha_I = 0.4993892$ $\alpha_{II} = 10.0262407$	0.4995631 10.0168284	0.5012618 9.8172216	0.5198273 5.8479247	0.5856065 +1 0.4114138	0.1095737 +1 0.2530954

Table 2.4. Dependence of the two slowest decay rates, α_I and α_{II} , on Reynolds number, N_{Re} , and wavenumber, N , when capillary number is 10.

N	N_{Re}	0.01	0.1	1	10	100	1000
0		$\alpha_I = 0$	0	0	0	0	0
		$\alpha_{II} = 0.7375944$	0.7285968	0.6428856	0.2256912	0.0246491	0.0024674
0.01		$\alpha_I = 0.0000000$	0.0000000	0.0000000	0.0000000	0.0000000	0.0000000
		$\alpha_{II} = 0.7376622$	0.7286645	0.6429525	0.2257263	0.0246532	0.0024678
0.1		$\alpha_I = 0.0000003$	0.0000003	0.0000003	0.0000003	0.0000003	0.0000002
		$\alpha_{II} = 0.7443376$	0.7353391	0.6495424	0.2291931	0.0250567	0.0025079
1		$\alpha_I = 0.0012029$	0.0012029	0.0012032	0.0012054	0.0012284	0.0016831
		$\alpha_{II} = 1.2423048$	1.2332570	1.1428633	0.5104091	0.0574102	0.0041976
10		$\alpha_I = 0.0499111$	0.0500005	0.0500181	0.0501804	0.0520494	0.0585775
		$\alpha_{II} = 10.0262629$	10.0168378	9.8202649	5.9435653	0.8834074	+ 1 0.0414190

Table 2.5. Dependence of the two slowest decay rates, α_I and α_{II} , on Reynolds number, N_{Re} , and wavenumber, N , when capillary number is 100.

by N_{Re} , N_{Ca} , and N by using continuation, i.e. by using as initial guess a solution to (2.4.52) at a nearby point in the parameter-space. The asymptotic results in Equations (2.5.2)-(2.5.4), (2.5.6)-(2.5.8), (2.5.10)-(2.5.13), (2.4.15), and (2.4.16) provided initial guesses to begin continuation and checks to certify that the numerically determined roots were indeed the five slowest decay rates. The two slowest decay rates, α_1 and α_{11} , are given in Tables 2.1-2.5 for Reynolds number ranging from 0.01 to 1000, capillary number ranging from 0.01 to 100, and wavenumber ranging from 0.01 to 10, which covers the entire spectrum of operating conditions typical of industrial and scientific coating devices.

2.6. Discussion

Much can be learned about the manner and rate of spatial decay of a small, arbitrary, steady upstream disturbance in a thin film on a translating web from the foregoing analysis. What are of greatest importance are the modes which decay the most slowly, because they persist furthest downstream. Higgins (1982) has described the results when wavenumber is zero. In that limit, Higgins (1982) shows that the dominant eigenvalue, α_1 , is always real and always belongs to the same family of modes, i.e. the first and second eigenvalues, α_1 and α_2 , never swap positions because the inequality $\alpha_1 < \text{Real}(\alpha_2)$ holds for all values of Reynolds number and capillary number. The situation can be much more complicated when wavenumber is finite. To illustrate the kinds of behavior that can occur, Figures 2.7, 2.9, and 2.13 show how the first five decay rates, α_1 through

α_5 , vary with wavenumber when Reynolds number is 100 and capillary number is 100, 1, and 0.01, respectively.

Manner of Spatial Decay. When Reynolds and capillary numbers are both 100 (Figure 2.7), the first five decay rates — numbered to put the real parts in ascending order when wavenumber is zero — are real and retain the same ordering as wavenumber increases from 0.1 to 10. As wavenumber decreases, each of the spatial decay rates except α_1 approach a finite limit. α_1 approaches zero for the same reason as in the zero Reynolds number case described in Section 2.5: the mode corresponding to α_1 is primarily a transverse redistribution of liquid and as wavenumber goes to zero the transverse distance over which the film levels increases without bound. The higher modes become two-dimensional, i.e. they have no transverse velocity component or transverse gradients, in the zero wavenumber limit and therefore have finite decay rates. When the wavenumber becomes large the decay rates become large as well because the length scale over which liquid must redistribute becomes small. The minima in the curves for α_3 and α_5 are presumably due to coupling between transverse and streamwise velocity components. The real values of spatial decay rate in Figure 2.7 indicate purely exponential decay. This is illustrated further in Figure 2.8, which is a portrait of six streaklines of a flow disturbed by the most slowly decaying mode when wavenumber is unity. The streaklines, which are the loci of particles that have passed through a given point, were constructed for this steady flow by Eulerian time integration of velocity:

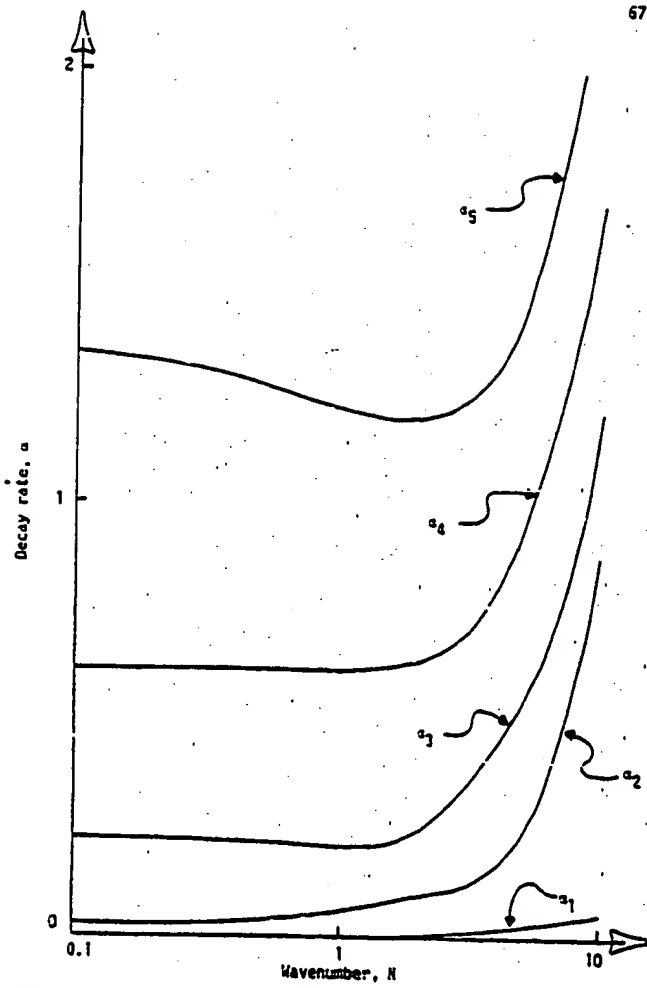


Figure 2.7. Behavior of the first five spatial decay rates, α_1 through α_5 , as wavenumber varies when $N_{Re} = 100$ and $N_{Ca} = 100$.

ORTHOGRAPHIC PROJECTION
OF STREAKLINES FOR
PARAMETER VALUES

$$N_{RE} = 100.$$

$$N_{CA} = 100.$$

$$N = 1.00$$

$$\text{ALPHA}_0 = .00123$$

$$\text{ALPHA}_1 = -0$$

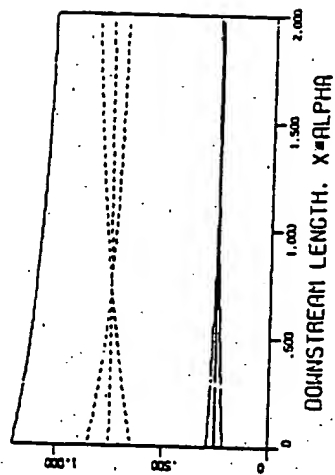
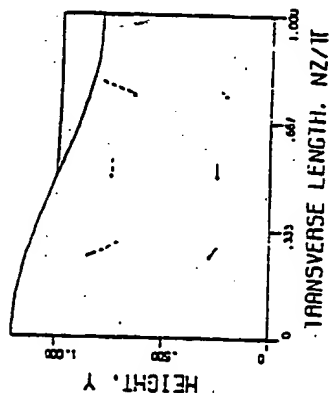
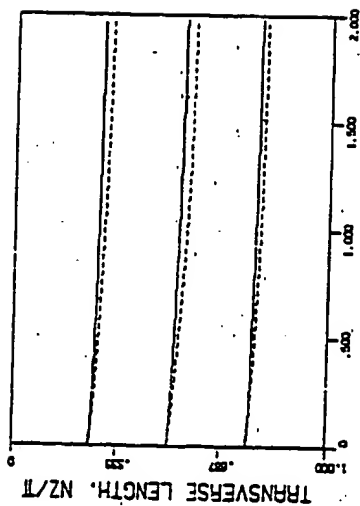


Figure 2.8. Portrait of some streaklines of the most slowly decaying disturbance in a trans-
lating liquid film.

$$\underline{x}(T) = \int_0^T \underline{u} \, dt + \underline{x}(0),$$

where $\underline{x}(T)$ is the position of a liquid particle at time T that passed through $\underline{x}(0)$ at time 0. Figure 2.8 shows monotonic decay of a sinuous free surface upstream to a nearly uniform plug flow at a distance of twice the real part of the decay rate, α_{Real} , downstream.

The situation is markedly different when capillary number is decreased from 100 to 1. The first two decay rates coalesce and form a complex pair at a wavenumber of about 0.5 as shown in Figure 2.9. For wavenumbers greater than about 7, α_3 becomes the most slowly decaying rate, α_1 , and the complex pair of decay rates, α_1 and α_2 , become α_{II} and α_{III} , respectively. This crossover of slowest decay rates occurs only at finite wavenumbers. The transition from real α_1 to complex α_1 and α_2 is shown in Figures 2.10-2.12. Figure 2.10 is a portrait of the streaklines for the mode corresponding to α_1 when wavenumber is 0.1. The decay is purely exponential and the flow pattern is similar to that shown in Figure 2.8. However, when wavenumber is unity the slowest decaying mode, corresponding to α_1 and α_2 , is oscillatory in the downstream coordinate, as shown in Figure 2.11, and the streaklines look substantially different than those in Figure 2.10. At a wavenumber of 10, the mode corresponding to α_1 and α_2 is shown in Figure 2.12 to oscillate less noticeably in streamwise coordinate than at a wavenumber of unity because the exponential decay is more rapid. Figures 2.13 and 2.14 show in more detail the flow profiles of the first two modes for selected values of wavenumber. Figure 2.13 shows the three components of velocity, scaled so that maxi-

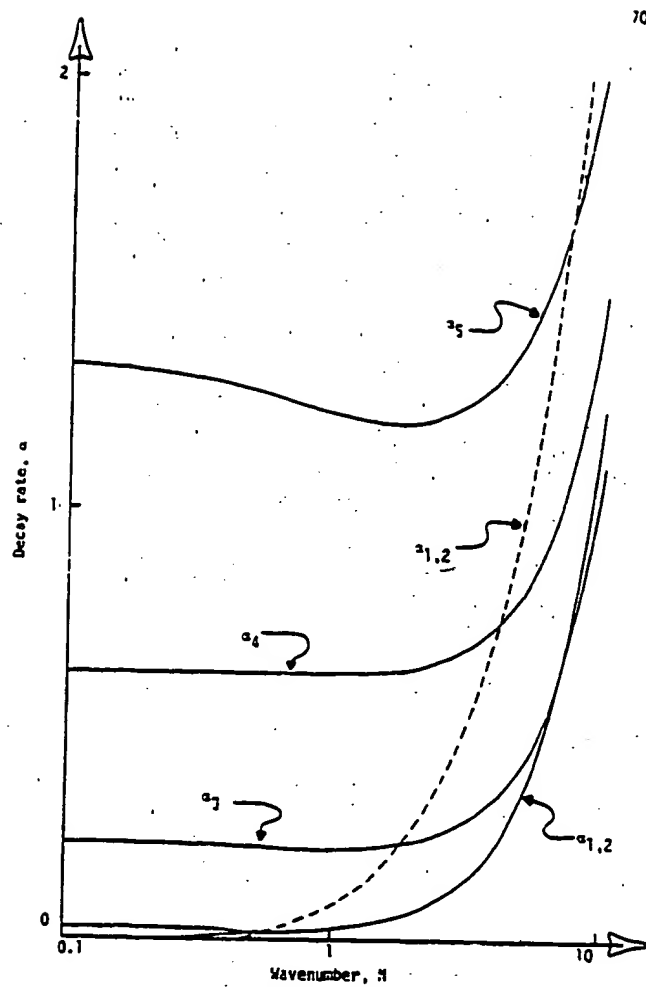


Figure 2.9. Behavior of the first five spatial decay rates, α_1 through α_5 , as wavenumber varies when $N_{Re} = 100$ and $N_{Ca} = 1$. —, real part; ----, imaginary part.

ORTHOGRAPHIC PROJECTION
OF STREAKLINES FOR
PARAMETER VALUES

$$N_{RE} = 100.$$

$$N_{CA} = 1.00$$

$$N = .100$$

$$\alpha_{PHR} = .00003$$

$$\alpha_{PHI} = 0$$

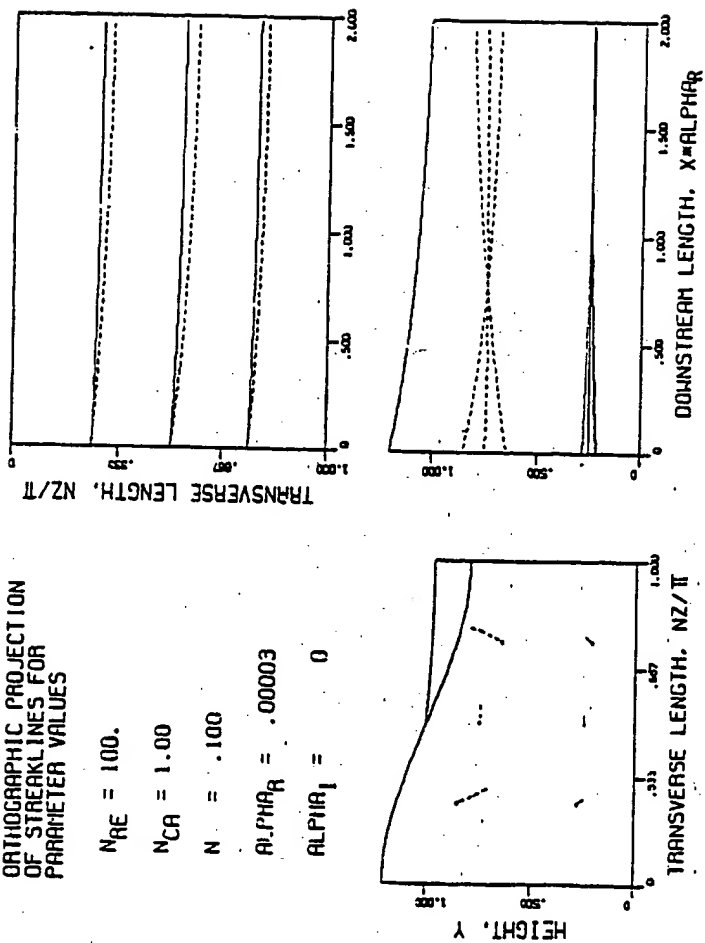


Figure 2.10. Portrait of some streaklines of the most slowly decaying disturbance in a translating liquid film.

CATHODOGRAPHIC PROJECTION
OF STREAKLINES FOR
PARAMETER VALUES

$$N_{HE} = 100.$$

$$N_{CA} = 1.00$$

$$N = 1.00$$

$$\text{ALPHA}_R = .0302$$

$$\text{ALPHA}_I = .0790$$

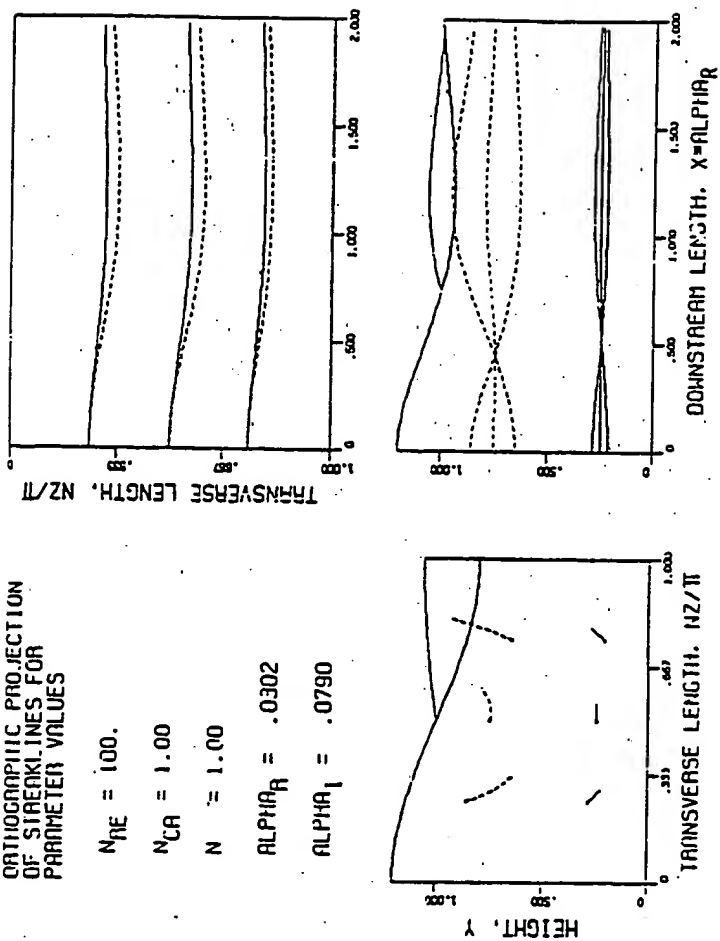


Figure 2.11. Portrait of some streaklines of the most slowly decaying disturbance in a translating liquid film.

ORTHOGRAPHIC PROJECTION
OF STREAKLINES FOR
PARAMETER VALUES

$$N_{RE} = 100.$$

$$N_{CA} = 1.00$$

$$N = 10.0$$

$$\text{ALPHA}_R = 1.25$$

$$\text{ALPHA}_I = 2.55$$

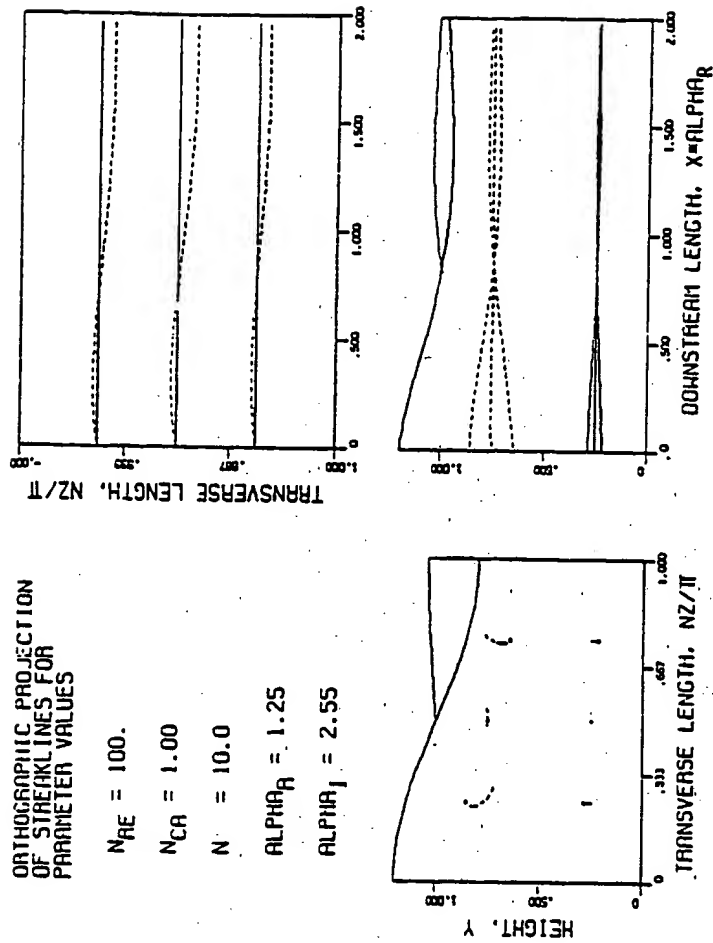


Figure 2.12. Portrait of some streaklines of the second most slowly decaying disturbance in a translating liquid film.

mum values are unity, for two wavenumbers, 0.1 and 0.398, which are below the limit at which the two decay rates coalesce. Each of the curves is nearly parabolic in form.

The situation is drastically different at higher values of wavenumber. In Figure 2.14 the imaginary parts of the three velocity component profiles are shown for wavenumbers of 0.501, 1, 2.00, 3.16, and 10, all above the limit at which the first two decay rates form a complex conjugate pair. These velocity profiles would occur at planes perpendicular to the x-axis and spaced at a distance of $2\pi/\alpha_1$ apart. The profiles become increasingly complicated as wavenumber is increased. When wavenumber is 10, the motion is confined to a thin layer near the top of the liquid film of which the thickness is about one half of the transverse wavelength, $\pi/10$. The spatially oscillatory perturbation is unable to reach the web because viscous diffusion is slight. Lamb's (1945) analysis of two-dimensional standing waves on an inviscid moving stream is analogous. His result shows that motion varies as $e^{-N(1-y)}$ when the wavelength is short compared with stream depth. Thus, the velocity disturbance at a depth π/M below the free surface is only about 4% of that at the free surface. Stokes' (1851) analysis of the flow near an oscillating flat plate is also analogous. He showed that if the wall velocity is $U_0 \cos(nt)$, the velocity of the liquid decays exponentially with distance from the wall:

$$u(y,t) = U_0 e^{-ky} \cos(nt - ky) ,$$

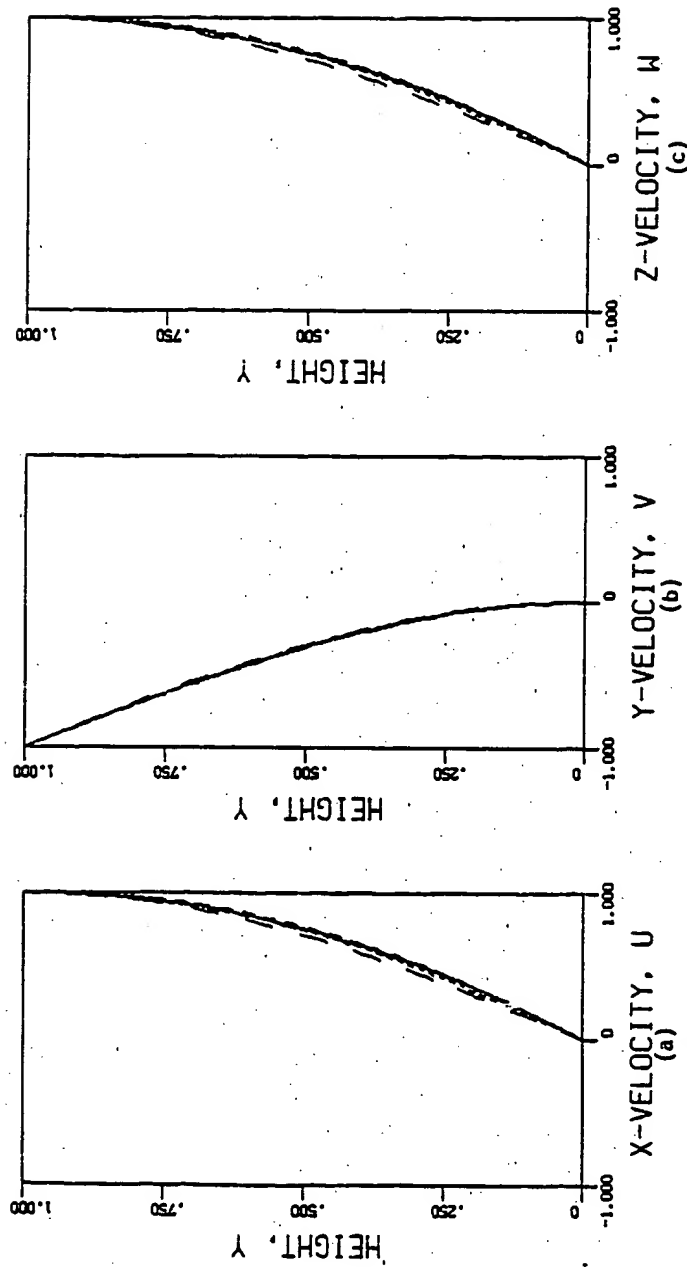


Figure 2.13. Scaled x -, y -, and z -velocity profiles for $N_{Re} = 100$ and $N_{Ca} = 1$. —, first mode when $N = 0.1$; ---, second mode when $N = 0.1$; ----, first mode when $N = 0.398$;; second mode when $N = 0.398$.

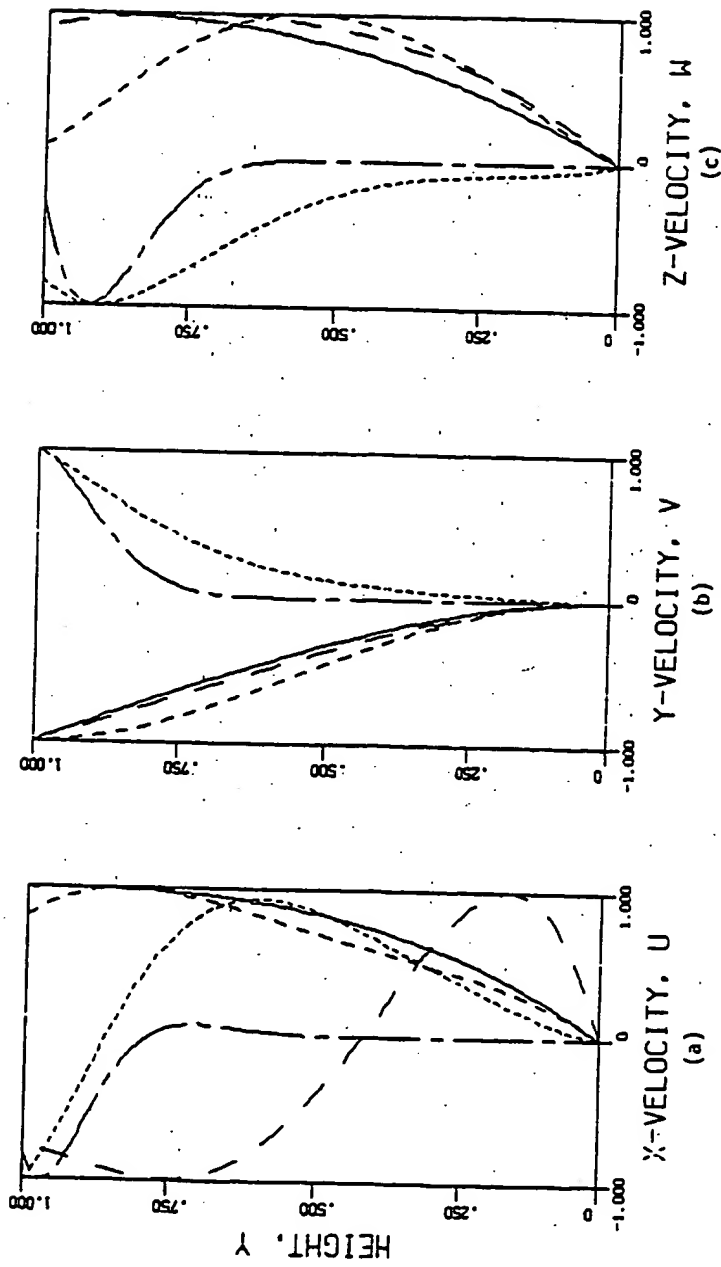


Figure 2.14. Scaled imaginary part of x-, y-, and z-velocity profiles for $N_{Re} = 100$ and $N_{Ca} = 1$.
 — first mode when $N = 0.501$; --- first mode when $N = 1$; first mode when $N = 2.00$; - - - - - first mode when $N = 3.16$; — — — — — first mode when $N = 10$.

where $k = \sqrt{n/2v}$. Thus, the liquid oscillations are confined to a boundary layer which has a thickness of about π/k (based on the 4% criterion used above).

At lower capillary number the behavior of the first two decay rates with wavenumber is even more complicated than in Figure 2.9, as shown in Figure 2.15. The first two decay rates merge and form a complex conjugate pair at wavenumber slightly greater than 0.1. At a wavenumber of about 0.5 the real part of this complex conjugate pair increases rapidly with wavenumber and soon overtakes the next three decay rates. α_3 is the dominant mode, α_1 , for wavenumbers higher than about 0.6. Figure 2.16 is a portrait of six streaklines in a flow disturbed by the first mode when wavenumber is unity. Although the decay rate is complex, the free surface elevation appears to decay monotonically with downstream distance because the half-wavelength, $\pi/\alpha_{\text{imag}} = 5.45$, is much longer than the distance necessary for the flow to become nearly solid body translation, which is a distance of about $2/\alpha_{\text{Real}} = 2.28$. However, the flow would exhibit large standing waves if wavenumber were 0.5 because $\alpha_{\text{imag}} = 0.3$ is about five times α_{Real} as shown in Figure 2.15 and therefore the half-wavelength, $\pi/\alpha_{\text{imag}} = 10.5$, is much shorter than the distance $2/\alpha_{\text{Real}} = 33$. In general it should be expected that a mode "appears" to be spatially oscillatory, i.e. to exhibit standing waves that are noticeable to the naked eye only when $\alpha_{\text{imag}}/\alpha_{\text{Real}} > 1$.

The effect of decreasing Reynolds number from 100 to 10 to 1 on the behavior of the first five spatial decay rates, α_1 through α_5 , as wavenumber varies when capillary number is 0.01 is seen by comparing Figures

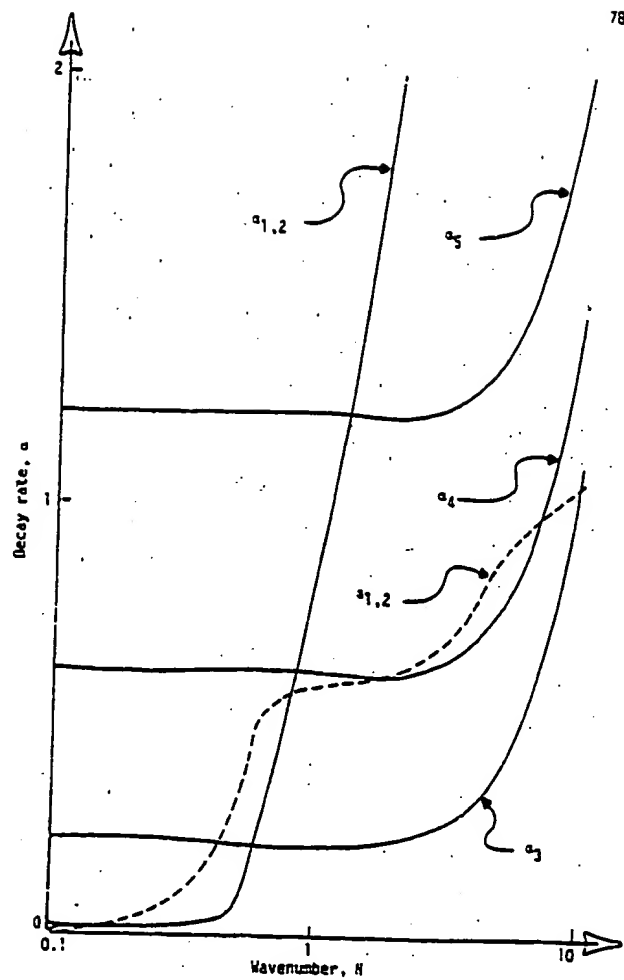


Figure 2.15. Behavior of the first five spatial decay rates, a_1 through a_5 , as wavenumber varies when $N_{Re} = 100$ and $N_{Ca} = 0.01$. —, real part; ----, imaginary part.

ORTHOGRAPHIC PROJECTION
OF STREAKLINES FOR
PINNETER VALUES

$$N_{RE} = 100.$$

$$N_{CA} = .0100$$

$$N = 1.00$$

$$\text{ALPHA}_R = .877$$

$$\text{ALPHA}_I = .576$$

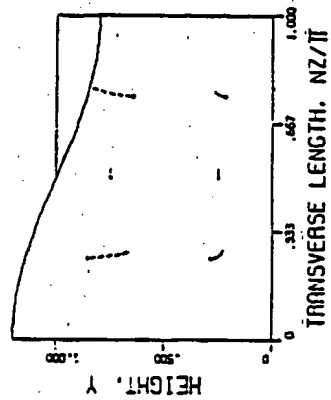
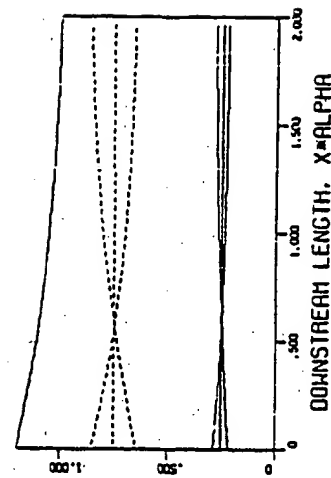
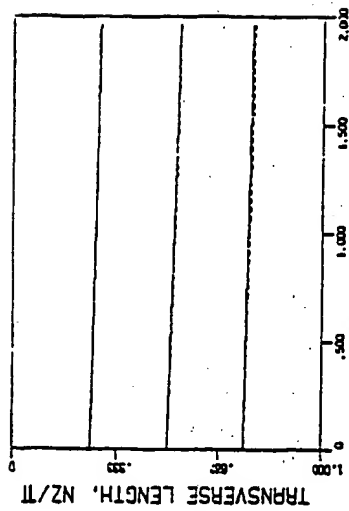


Figure 2.16. Portrait of some streaklines of the most slowly decaying disturbance in a translating liquid film.

2.15, 2.17, and 2.18. When Reynolds number is 100, Figure 2.15 shows that the dominant mode is exchanged at a wavenumber of about 0.6 as described above. This outright exchange of dominant modes evolves into a complicated pattern of merging of real decay rates into complex pairs and splitting again back to real ones when Reynolds number is decreased from 100 to 10 as shown in Figure 2.17. At even lower values of Reynolds number the complicated pattern of Figure 2.17 gives way to the simple behavior shown in Figure 2.18 for Reynolds number equal to 1.

Figures 2.7, 2.9, 2.15, 2.17, and 2.18 show that the dominant mode can exhibit "observable" spatial oscillation — as defined by the criterion above that $\alpha_{\text{imag}}/\alpha_{\text{Real}} > 1$ — only when capillary number is of order 1 or smaller and Reynolds number is of order 100 or greater. We conclude then that downstream standing waves on a coated film can be detected by the naked eye only when operating and liquid parameters are so chosen that Reynolds number is over 100 and capillary number is below 1, and furthermore the flow is disturbed by a sinuous transverse perturbation with a wavenumber of about unity (depending on capillary and Reynolds numbers), such as those generated by the ribbing instability. However, use of optical techniques such as Moré topography (see Khesghi 1982) should significantly increase the range of operating parameters for which standing waves could be seen.

Comparison of Analyses. The slowest decay rates predicted by lubrication theory in Section 2.3 and the Oseen analysis in Section 2.4 are compared in Figure 2.19. The Oseen prediction is indistinguishable from that of lubrication theory when Reynolds number is zero (as it is

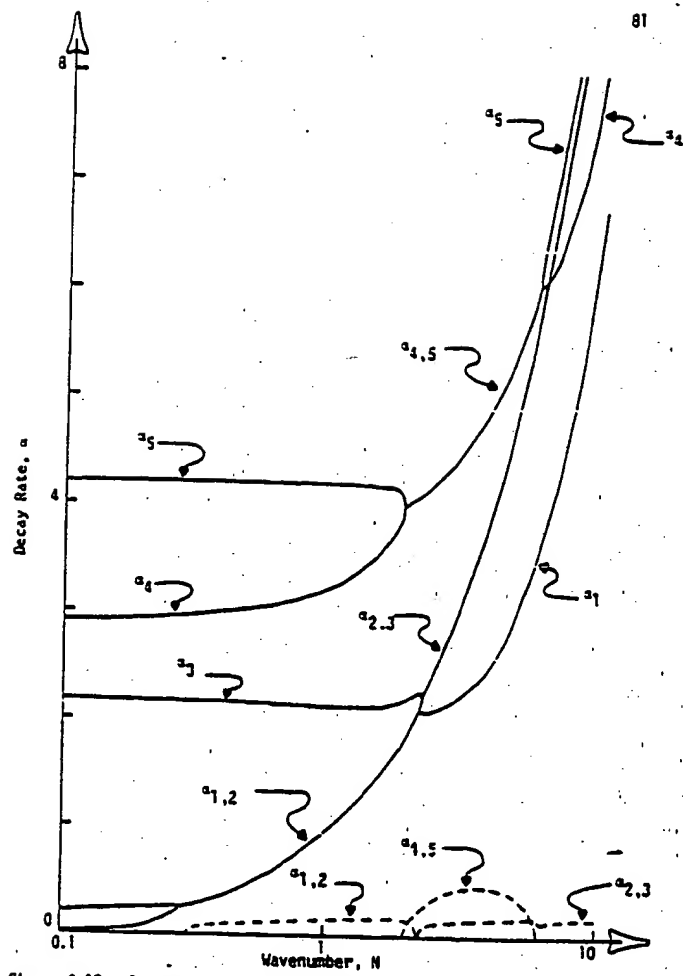


Figure 2.17. Behavior of α_1 through α_5 as wavenumber varies when $N_{Re} = 10$ and $N_{Ca} = 0.01$. —, real part; ---, imaginary part.

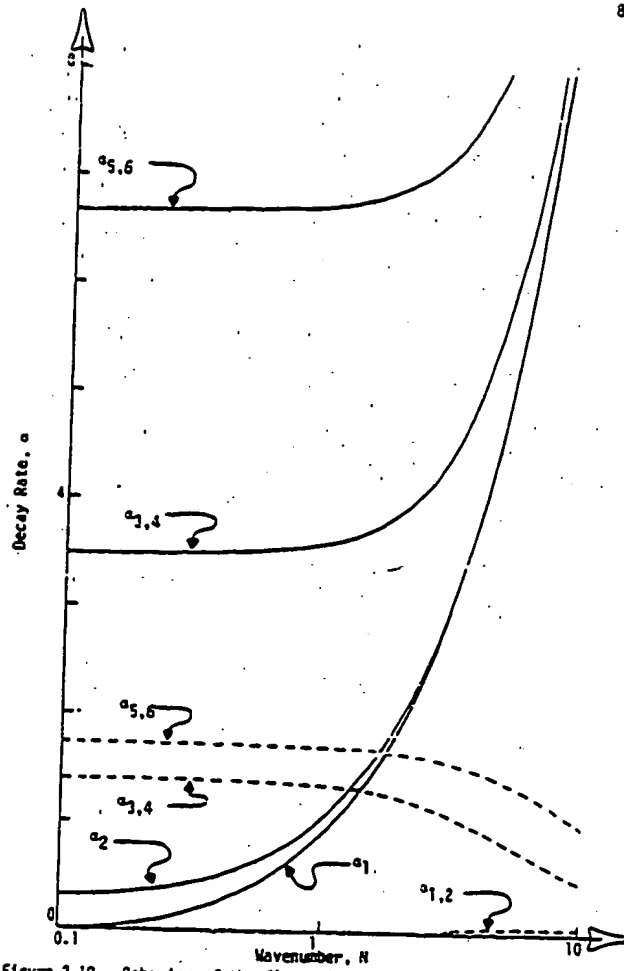


Figure 2.18. Behavior of the first six spatial decay rates, α_1 , through α_6 , as wavenumber varies when $N_{Re} = 1$ and $N_{Ca} = 0.01$. —, real part; ----, imaginary part.

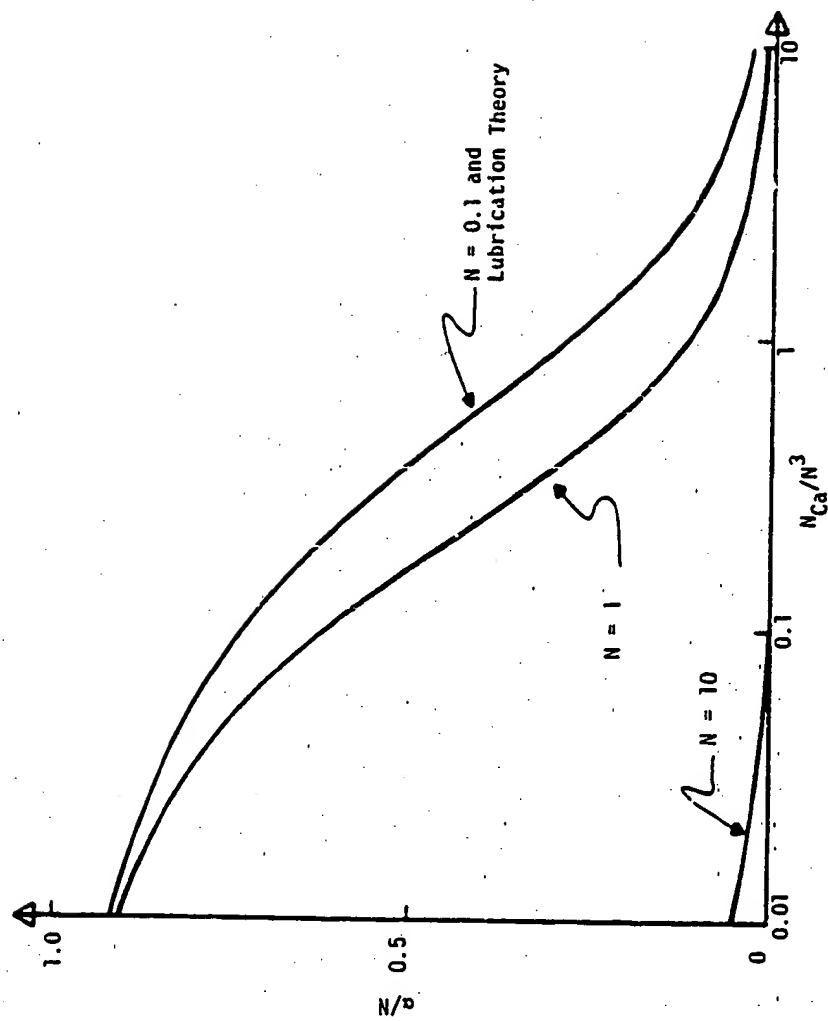


Figure 2.19. Slowest spatial decay rates of liquid film disturbances predicted by lubrication theory and by full asymptotic analysis when Reynolds number is 0. 83

in lubrication theory) and when wavenumber is 0.1 or less. At higher wavenumber the results differ markedly, the full theory predicting much slower decay rates than those of lubrication theory. Fall's (1978) solution is shown in Figure 2.4 to be in good agreement with the general lubrication result of Equation (2.3.5) only when N_{Ca}/N^3 is large, and therefore Fall's assertion that his result is valid at low capillary number is false.

Rate of Spatial Decay. The results in Tables 2.1-2.5 can readily be used to estimate downstream distance needed to achieve a certain degree of leveling of a small disturbance. Table 2.6 shows as an example the downstream distances needed for disturbances of wavenumber 0, 0.1, and 1 to decay by a factor of 10 when a coating device is operating at a Reynolds number of 1 and a capillary number of 10. As expected, long wavelength (small wavenumber) disturbances are the most dangerous and two-dimensional disturbances (wavenumber equal 0) decay the most rapidly. Disturbances with wavenumbers near unity, such as those generated by the ribbing instability (cf. Chapter 6), decay by a factor of 10 after traveling a few hundred film-thicknesses downstream, and therefore may be tolerable if there is a long enough run of the web downstream of the coating station.

Construction of Robin Boundary Condition. As mentioned in Section 2.1, the Oseen analysis of Section 2.4 can be used to construct a Robin boundary condition, i.e. a boundary condition of the third kind, for the outflow boundary in a three-dimensional finite element stability analysis of a coating flow. The equations that describe the stability of a two-

Table 2.6. Downstream distances for disturbances to decay by a factor of 10 when Reynolds number is 1 and capillary number is 10.

Wavenumber, N (film-thickness ⁻¹)	Wavelength, $2\pi/N$ (film-thickness)	Decay distance, $\ln(10)/\alpha_R$ (film-thickness)
0	∞ (2-D)	3
0.1	62.8	700,000
1	6.3	190

dimensional coating flow to three-dimensional perturbations are derived in Chapter 5. Equation 5.2.25, the Galerkin weak form of the momentum equation, contains an integral over the outflow boundary of the forming zone:

$$\int_{\partial\Omega_{OUT}} \underline{n} \cdot \underline{T}' \cdot [\phi^j(\xi, \eta) \underline{D}(Nz)] \frac{\partial y}{\partial \eta} d\eta dz \quad (2.6.1)$$

where \underline{n} is the outward pointing normal to the outflow boundary, \underline{T}' is the change in the stress tensor due to a perturbation in the velocity and pressure field, $\phi^j(\xi, \eta)$ is the j -th finite element basis function as defined in Section 4.2), \underline{D} is a tensor of Fourier basis functions as defined in Equation (5.2.10), and $\partial\Omega_{OUT}$ represents the outflow boundary of the forming zone. When the flow field at the outflow boundary is well approximated by the dominant mode of the Oseen analysis and \underline{n} is chosen to be $\underline{1}$ for convenience, the stress tensor is approximated by:

$$\underline{1} \cdot \underline{T}' \equiv \underline{A} \cdot \underline{u}' \quad (2.6.2)$$

The momentum transfer coefficient tensor is found from Equations (2.4.9) and (2.4.10) to be

$$\begin{aligned}
 \underline{A} = & \{ \underline{i} [2\partial u(N, \alpha_I) / \partial x - p(N, \alpha_I)] / u(N, \alpha_I) \\
 & + \underline{j} [\partial u(N, \alpha_I) / \partial y] / u(N, \alpha_I) + \underline{k} [\partial u(N, \alpha_I) / \partial z] / u(N, \alpha_I) \} \underline{i} \\
 & + \underline{j} [\partial v(N, \alpha_I) / \partial x] / v(N, \alpha_I) + \underline{k} [\partial w(N, \alpha_I) / \partial x] / w(N, \alpha_I) \\
 = & \{ - \underline{i} [\alpha_I + p_I(N, \alpha_I) S_I(\alpha_I) / u_{1j}^C(N, \alpha_I) S_j(\alpha_I)] \\
 & + \underline{j} [u_{1j}^C(N, \alpha_I) R_{1j}(\alpha_I) S_j(\alpha_I) / u_{1k}^C(N, \alpha_I) S_k(\alpha_I)] \\
 & - \underline{k} N \tan(Nz) \} \underline{i} - \alpha_I (\underline{i} \underline{i} + \underline{j} \underline{j} + \underline{k} \underline{k}) .
 \end{aligned} \tag{2.6.3}$$

The smaller the real part of the dominant decay rate α_I as compared with the real part of the second decay rate α_{II} , the better is the approximation in (2.6.2). Fortunately, the real part of the dominant decay rate is smaller than the real part of the second decay rate by an order of magnitude or more for a wide range of the parameters in Tables 2.1-2.5. This is especially true when capillary number is greater than 0.1 as it is at the onset of the ribbing instability (see Chapter 6). Equation (2.6.2) is imposed as a natural boundary condition by replacing $\underline{n} \cdot \underline{T}'$ in (2.6.1) by $\underline{A} \cdot \underline{u}'$ as explained further in Chapter 5. Outflow boundary condition (2.6.2) can also be used in three-dimensional finite element analysis of steady flows.

2.7. Extensions of the Oseen Analysis

The methods used in this chapter to construct asymptotic solutions

in a downstream free surface zone apply equally well to an upstream free surface zone or to upstream or downstream channel zones. The analysis of an upstream free surface zone is identical to that culminating in Equations (2.4.34)-(2.4.52) except that the relevant roots of the characteristic equation (2.4.52) are ones with negative real part. The analysis of the spatial decay of three-dimensional disturbances in a channel zone with upstream or downstream distance differs from that in a free surface zone only by the boundary conditions at the upper surface. The methods of Section 2.4 therefore can be applied to extend Wilson's (1969) analysis of the spatial decay of flow disturbances in a channel to include three-dimensional disturbances. The extension is straightforward when inertia is negligible ($N_{Re} = 0$). Wilson's Equation (3.3) applies, but with $2\alpha_0$ replaced by $\beta \equiv \sqrt{\alpha^2 - N^2}$. (Here the solid boundaries are at $y = 0$ and 1 instead of $y = \pm 1$ as Wilson uses, which accounts for the factor of 2). The characteristic equation is then

$$\sin(\beta) = \pm \beta. \quad (2.7.1)$$

The first root of Equation (2.7.1) is

$$\alpha_1 = N \quad (2.7.2)$$

and higher roots can be found from Wilson's Table 1 by using the relationship

$$\alpha_{i+1} = \sqrt{(2\alpha_{0i})^2 + N^2}, \quad i = 1, 2, \dots \quad (2.7.3)$$

where α_{0i} is Wilson's i -th eigenvalue α_0 . Solutions at finite Reynolds

number could be constructed as well, but would require computer-based methods of analysis because of the parabolic baseflow, $U(y)$. The Oseen equations for this case are

$$N_{Re} \left[U(y) \frac{\partial \underline{u}}{\partial x} + v_j \frac{\partial \underline{u}}{\partial y} \right] = -\nabla p + \nabla^2 \underline{u} \quad (2.7.4)$$

$$\nabla \cdot \underline{u} = 0 \quad (2.7.5)$$

and the no-slip and no-penetration boundary conditions are:

$$\underline{u} = 0 \quad \text{at } y = 0, 1. \quad (2.7.6)$$

In this case, the methods of Section 2.4 lead to a fourth-order ordinary differential equation with non-constant coefficients for which solutions are best constructed by numerical means.

CHAPTER 3 - LUBRICATION ANALYSIS OF THE STABILITY OF SLOT AND KNIFE COATING

3.1. Introduction

The stability of steady, viscous, nearly rectilinear flows can be studied by making a set of approximations that are collectively known as the lubrication approximation. Osborn Reynolds (1886) first proposed the ideas of lubrication theory, which he used to explain some experiments on lubrication in journal bearings done by Mr. Beauchamp Tower. However, it was not until 1960 that loss of stability of thin film flows was first investigated in the context of lubrication theory. Pearson, motivated in part by the observation of so-called brush marks formed by a brush spreading paint, analyzed the onset of ribbing in a wedge-shaped spreader, i.e. a gently sloped wedge-shaped die translating perpendicular to the direction of its translational symmetry and parallel to a plane surface. Pearson found that the results of stability analysis under the lubrication approximation agreed qualitatively with his experimental findings. Pitts and Grellier (1961) applied Pearson's ideas to estimate the conditions for onset of ribbing in film splitting between two symmetric counter-rotating cylinders. Film splitting differs from spreading in that the meniscus has no point of attachment to a solid surface, i.e. has no contact line, in film splitting whereas spreading always has a static contact line. As a result, the meniscus is less constrained in film splitting which causes the flow to be less stable, as compared with spreading. Taylor (1963) performed a series of experiments on cavitation in lubrication from which he deduced the importance of capillary

number to the separation conditions near a static contact line where the premises of lubrication theory are invalid. Coyne and Elrod (1971), apparently inspired by Taylor's work, constructed an approximate set of meniscus conditions based on an ad hoc model. Later, Savage (1977) showed how Coyne and Elrod's approximate boundary conditions could be incorporated into a lubrication stability analysis in his work on cylindrical spreaders.

The chief drawback of lubrication theory when applied to partially submerged bearings, i.e. bearings in which separating contact lines occur, or to coating devices is that the boundary conditions that should be imposed at a separating contact line are not well established. Several boundary conditions have been postulated, but which, if any of them, is best remains uncertain. One of the aims of this chapter is to evaluate some of the postulated boundary conditions by calculating the stability results that they predict. The comparisons drawn here are for exponentially-shaped slot and knife coaters.

The lubrication equation and postulated boundary conditions that apply to slot and knife coating devices are laid out in Section 3.2. Integration of the lubrication equation for translationally symmetric flows is outlined in Section 3.3. Stability of the two-dimensional flows to three-dimensional ribbing disturbances is the topic of Section 3.4. Finally, the results are discussed in Section 3.5.

3.2. Lubrication Equation and Boundary Conditions

Derivation of the lubrication equation for the standard case of a flow confined between two solid surfaces is analogous to the derivation

given in Section 2.2 for the case where one bounding surface is a meniscus. Equations (2.2.11)-(2.2.16) apply here, with the exception that the shear stress condition (2.2.14) is replaced by a no-slip condition at the solid die:

$$\underline{u}_{II} = 0 \quad @ \quad y = 1 \quad (3.2.1)$$

Here \underline{u} again represents velocity and the subscript II indicates that only streamwise (x) and transverse (z) velocity components are represented. Following the same procedure as outlined in Section 2.2 to eliminate velocity in favor of pressure leads to the standard lubrication equation (see e.g. Cameron 1976):

$$\nabla_{II} \cdot (h^3 \nabla_{II} p / 12) = (\partial h / \partial x) / 2 \quad (3.2.2)$$

Equation (3.2.2) differs from the result in (2.2.19) by a factor of one-half on the left side of the equality which is due to the difference in boundary conditions at $y = 1$. Here h refers to the local gap thickness between the stationary die and the moving web and p is the pressure.

Ideally, coating flows are transversely symmetric. When this is so, Equation (3.2.2) reduces to

$$\frac{d}{dx} \left(\frac{h^3}{12} \frac{dp}{dx} \right) = \frac{1}{2} \frac{dh}{dx} \quad (3.2.3)$$

Equation (3.2.3) apparently requires two boundary conditions to specify a unique solution. Usually, one of these is at the inflow boundary. However, when the position of the downstream boundary, i.e. the separat-

ing contact line (see Figure 3.1), is unknown an additional condition is needed there. In general two conditions must relate the contact line position, the pressure there, and the pressure gradient there. When the contact line is pinned at a geometrical or compositional discontinuity, the additional boundary condition is typically that the pressure at the known contact line location is ambient minus capillary pressure. When the contact line is free to move along the die, the condition specifying contact line position is normally replaced by a condition on pressure gradient at the contact line. Models to determine capillary pressure and pressure gradient at the contact line are thus needed.

Capillary Pressure Models. The simplest way to account for capillary pressure is to approximate the meniscus profile as an arc of circle near the contact line and as a line further downstream. The contact angle is a parameter. The splice between circle and line is chosen so that free surface elevation and slope are continuous, as illustrated in Figure 3.1. The dimensionless pressure just upstream of the contact line is then

$$p = - \frac{1}{N_{ca}} \frac{1}{R} \quad (3.2.4)$$

where $N_{ca} \equiv \mu u / \sigma$ is the capillary number and R is the radius of the cylinder. The ambient pressure is absorbed into p as a datum. Equation (3.2.4) is an approximation to the normal stress boundary condition, as given in Equation (1.2.5). Normal viscous stresses are always considered negligible in the lubrication approximation, even though they may not in fact be negligible in the vicinity of the contact line where the flow

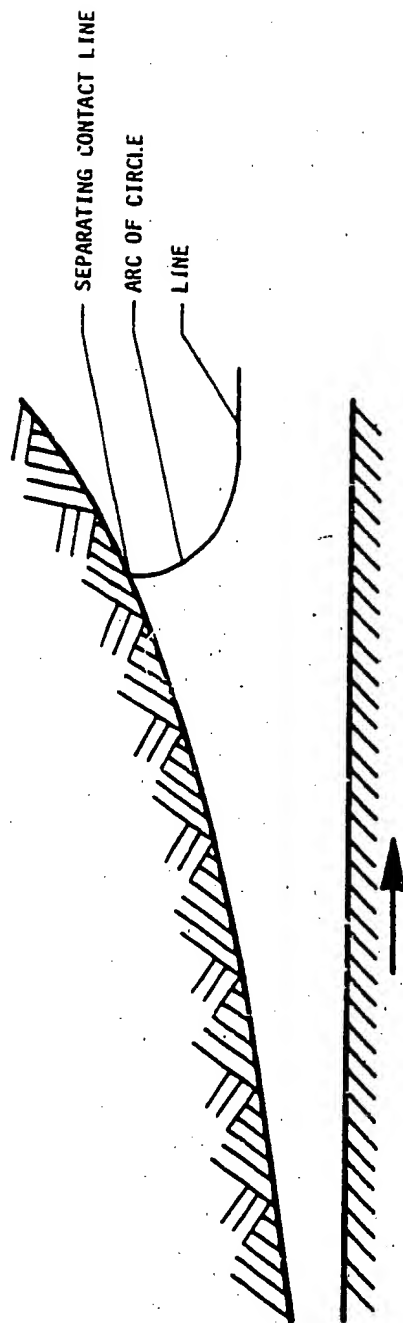


Figure 3.1. Illustration of exponential slot or knife coater and approximation to separating meniscus.

may be far from rectilinear. A more elaborate flow model is needed if the effects of normal viscous stress are to be accounted for.

Coyne and Elrod (1971) proposed an ad hoc flow model to estimate normal viscous stress as well as capillary pressure at a separating contact line. They assumed that contact angle is 90° and the velocity along spines perpendicular to the meniscus is a quadratic function of distance from the meniscus to the web. They calculated the ratios d/h_m and R/d as functions of capillary number, where d is the gap thickness h at the separating contact line. Their ratio R/d can be used in place of the arc-of-cylinder approximation in (3.2.4). Saito and Scriven (1981) showed Coyne and Elrod's results to be in surprisingly close agreement with their finite element results, thus lending credence to Coyne and Elrod's ad hoc model.

Unfortunately, Coyne and Elrod's boundary conditions are not easily used when the separating contact angle is other than 0° or 90° , the two cases for which they tabulate outcomes of their calculations, and especially when contact angle is greater than 90° because then an extrapolation of their results would be necessary. An alternative to using Coyne and Elrod's results is to calculate the ratios d/h_m and R/d by constructing finite element solutions of the exact governing equations as explained in Chapter 4. By so doing, Coyne and Elrod-like boundary conditions can be generated at all capillary numbers and contact angles.

Pressure Gradient Models. Several conditions that specify pressure gradient at the separating contact line have been proposed. Most of them stem from ad hoc arguments and so are at best of dubious validity.

They are described briefly in the following paragraphs.

Reynolds (1886) originally proposed that the pressure gradient at the separating contact line should be zero, i.e.

$$\partial p / \partial x = 0 \quad @ \quad x = c \quad . \quad (3.2.5)$$

Here c stands for the location of the separating contact line. His rationale was based on the heuristic argument that the meniscus cannot withstand a pressure gradient for it has no force of its own by which to resist (this argument neglects the action of surface tension). Later, Swift (1932) and Stieber (1933) working independently and employing different reasoning arrived at the same boundary condition as had Reynolds almost fifty years earlier. Reynolds' boundary condition predicts a pressure distribution such as that in Figure 3.2a when the die is a cylinder, i.e. it predicts that the separation line occurs at the point of incipient pressure minimum.

Prandtl (1937) and later Hopkins (1957) proposed that the separation line should be at the point of incipient reverse flow. This argument leads to the following boundary condition:

$$dp/dx = 2/h^2 \quad @ \quad x = c \quad . \quad (3.2.6)$$

This boundary condition implies that a subambient pressure zone occurs just upstream of the separating contact line, as shown in Figure 3.2b for the case of a cylindrical spreader.

Taylor (1963) was perhaps the first to realize that capillary number, which measures the relative importance of normal viscous stress at the

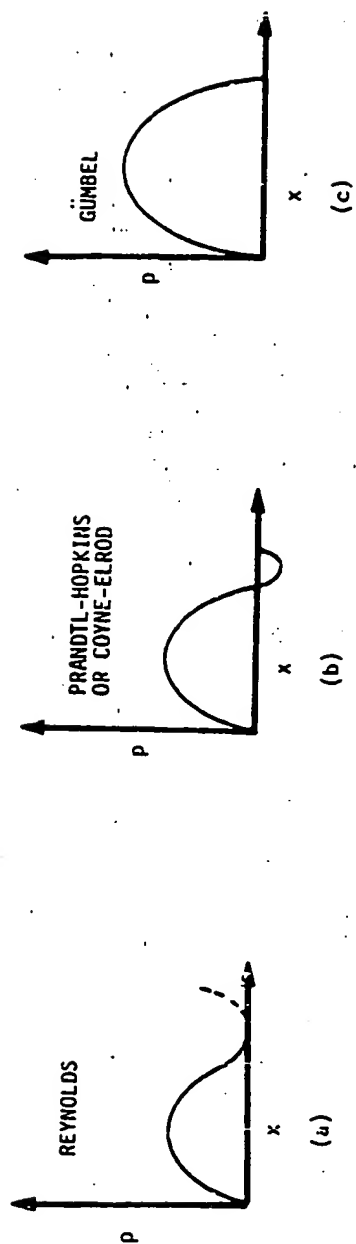


Figure 3.2. Illustration of the pressure profiles predicted by competing meniscus conditions when the die is a cylinder.

meniscus to capillary pressure, plays a significant role in determining not only the pressure but also the pressure gradient at the separating contact line. Although he did not formulate his own boundary condition, his paper appears to have motivated Coyne and Elrod's (1969) approximate analysis to account for the effects of normal viscous stress.

As already mentioned, Coyne and Elrod estimated the ratios d/h_m and R/d as functions of capillary number. The first of these ratios is a relationship between pressure gradient and contact line position. This is easily seen by integrating the lubrication equation (3.2.3) once to get:

$$-h^3(dp/dx)/12 + h/2 = q \quad (3.2.7)$$

The first term is the dimensionless flow rate per unit channel width due to Poiseuille, or pressure-driven, flow; the second term is the dimensionless flow rate per unit channel width due to Couette, or shear-driven, flow. Therefore, an overall mass balance shows that q must be the final film thickness h_m . Hence the pressure gradient at the contact line is given by:

$$dp/dx = 6(1 - 2h_m/h)/h^2 \quad (3.2.8)$$

This boundary condition predicts pressure fields similar to those predicted by the Prandtl-Hopkins condition, as illustrated in Figure 3.2b. The main distinction between the Coyne-Elrod and Prandtl-Hopkins conditions is that the former predicts a zone of recirculation just upstream of the separating contact line when the contact angle is 90° , the latter

does not.

A cruder boundary condition than the three described above is due to Gumbel (1921), but often bears the name half-Sommerfeld. Gumbel's condition states that the separating contact line is at the point of minimum gap width, and thus it applies solely to die configurations in which there is a local minimum clearance. It is used chiefly to estimate the load capacity of journal bearings. The pressure profile that Gumbel's condition predicts is illustrated in Figure 3.2c for the case of a cylindrical die.

Savage (1977) and Dowson and Taylor (1979) have reviewed each of the foregoing boundary conditions. They conclude that Coyne and Elrod's boundary condition agrees best with a collection of experimental data of the pressure distribution in bearings. However, Savage points out that Coyne and Elrod's boundary condition is in poor agreement with Smith's (1975) experimental data on the pressure distribution in a lightly loaded journal bearing, and especially so when capillary number is small.

It remains to be seen which of the boundary conditions performs best in lubrication stability analysis. Savage (1977) chose the Coyne-Elrod boundary condition in his stability analysis of a cylindrical spreader and found reasonable agreement with experimental data. However, no side-by-side evaluations of the various postulated conditions have been made. Here, three of the boundary conditions on pressure gradient, namely Reynolds', Prandtl-Hopkins', and Coyne-Elrod's conditions, are compared for slot and knife coating when the die shape is exponential. In Chapter 6, the lubrication stability results are evaluated by com-

paring with finite element stability results.

Inflow Conditions. Three linear inflow conditions can be imposed at an inflow boundary. Of these, the first is most commonly used. The three choices are described in the following paragraphs.

The first is to specify pressure at an inflow boundary:

$$p = p_I \quad \text{at} \quad x = b \quad (3.2.9)$$

This boundary condition is typically used in problems where the flow is not premetered.

The second alternative is to specify the pressure gradient at the inflow boundary, which is equivalent to specifying the flow rate (see Equation (3.2.8)):

$$dp/dx = p'_I \quad \text{at} \quad x = b \quad (3.2.10)$$

This boundary condition is useful when the flow is premetered, as it is in many coating devices.

The third alternative is to specify pressure gradient as being proportional to the difference between an external pressure and the pressure at the inflow boundary, i.e. the Robin condition

$$dp/dx = \alpha (p_0 - p) \quad (3.2.11)$$

Here α is a constant of proportionality and p_0 is the external pressure. Equation (3.2.11) is analogous to the heat flux boundary condition used in heat conduction problems which presumes that the heat flux at a solid/gas boundary is proportional to the difference between boundary

and ambient temperatures, the constant of proportionality being the heat transfer coefficient. Here the proportionality constant α is in effect a momentum transfer coefficient.

In the following analysis pressure is specified at the inflow boundary. A comparison given in Section 6.5 of lubrication stability analysis and finite element stability analysis is for pressure gradient specified asymptotically far upstream. The Robin condition (3.2.11), while being perhaps the most physically realistic of the three alternatives, is not considered further here. However, the pressure and pressure gradient inflow conditions can be thought as limiting cases of the Robin inflow condition as α increases without bound and goes to zero, respectively.

3.3. Two-Dimensional Base Flows

Two-dimensional solutions of the lubrication equations are found by integrating equation (3.2.8). The standard solution is (see e.g. Cameron 1976):

$$p = \int_b^x [6(1 - 2h_w/h)/h^2] dx + p(b) \quad (3.3.1)$$

Equation (3.3.1) contains two unknown constants which have to be determined, i.e. the final film thickness h_w and the inflow pressure $p(b)$. Furthermore, the position of the contact line c is unknown. There are determined by choosing an inflow condition and two conditions at the separating contact line, as explained in Section 3.2.

Here the case of an exponentially diverging channel is considered, i.e.

$$h = e^{x/B} \quad (3.3.2)$$

The constant $1/B$ determines the characteristic slope in the channel and the inflow boundary is chosen to be at $x = 0$. For this die configuration, Equation (3.3.1) gives:

$$p = 3B(1 - e^{-2x/B}) - 4Bh_0(1 - e^{-3x/B}) + p(b) \quad (3.3.3)$$

If the inflow pressure is given by (3.2.9) then $p(b)$ is known; if on the other hand inflow pressure gradient is given by (3.2.10) then h_0 is determined by (3.2.8). The contact line position c and either the inflow pressure $p(b)$ or the final film thickness h_0 are specified by choosing two conditions at the separating contact line.

The Reynolds condition (3.2.5) implies that

$$h_0 = \frac{1}{2} h(c) \quad (3.3.4)$$

as seen from the integrated lubrication equation in (3.2.8). Likewise, Prandtl-Hopkins' condition (3.2.6) implies that

$$h_0 = \frac{1}{3} h(c) \quad (3.3.5)$$

These conditions are imposed here in conjunction with the arc-of-circle approximation to the meniscus profile at the contact line. For ease of comparison with the Coyne-Elrod boundary condition, contact angle is chosen to be 90° . The pressure at the contact line is given by (3.2.4) and the radius of curvature R is $h(c) - h_0$ so that

$$p = - \frac{1}{N_{ca}} \frac{1}{h(c) - h_w} \quad @ \quad x = c \quad (3.3.6)$$

Coyne and Elrod's boundary condition is imposed similarly to those of Reynolds and Prandtl-Hopkins. Coyne and Elrod's ratios

$$a \equiv h_w/h(c) \quad , \quad b \equiv R/h(c) \quad (3.3.7)$$

tabulated as functions of capillary number, are used to eliminate the final film thickness, h_w from (3.3.3) and R from boundary condition (3.2.4).

The contact line positions predicted by the three alternative boundary conditions are compared in Figure 3.3 for the case where the inflow pressure is specified to be zero and the characteristic slope $1/B$ is 0.1. Reynolds' and Prandtl-Hopkins' conditions predict similar separating contact line positions, and especially so when capillary number is small. The Coyne-Elrod boundary condition predicts that the separating contact line should lie significantly further downstream than the other two conditions, except at capillary numbers near unity where Coyne-Elrod and Prandtl-Hopkins conditions agree closely.

3.4. Stability of Base Flows

Pearson (1960) estimated the stability of a lubrication flow under a wedge-shaped spreader by: (1) assuming a small disturbance to the pressure field and to the meniscus shape; (2) using a Fourier normal mode representation so that disturbances of individual wavenumber could be singled out; and (3) evaluating stability by means of an integral mass

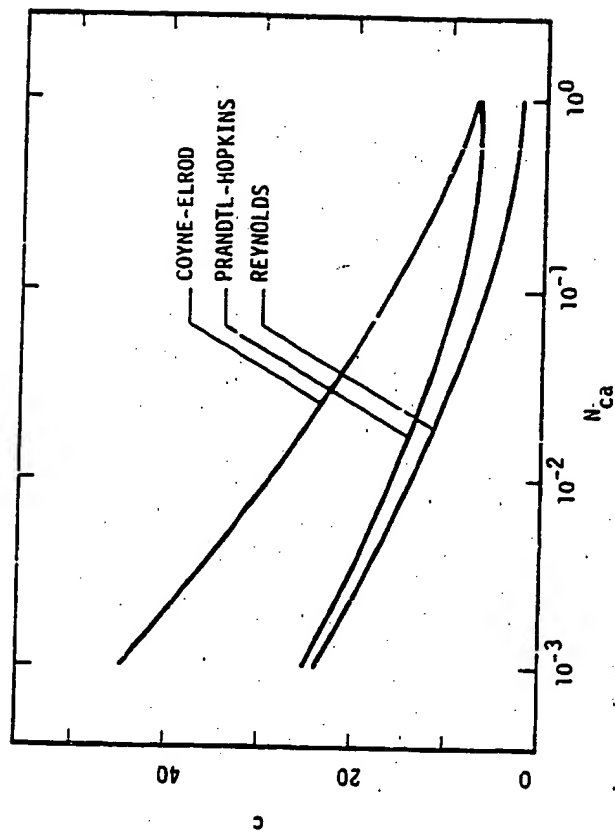


Figure 3.3. Comparison of the separating contact line location c predicted by Reynolds', Prandtl-Hopkins', and Coyne-Elrod's meniscus conditions in an exponential slot or knife coater when the characteristic slope $1/B$ is 0.1.

balance around the separation line, i.e. relating the rate of change in contact line position to the difference of inflow rate just upstream of the contact line and outflow rate just downstream of the contact line. The method used here is nearly identical to Pearson's. However, the analysis here is carried out by using the same three boundary conditions as in Section 3.3., whereas Pearson resorted to experimental data to determine the position of the contact line.

If the pressure field and contact line position are perturbed slightly they will either return to their undisturbed states or continue to move away from them. If they return the flow is said to be stable; otherwise it is said to be unstable. Here, the stability of a base flow to disturbances of the form

$$p' = e\phi(x) \cos(Nz) \quad (3.4.1)$$

$$c' = c \cos(Nz) \quad (3.4.2)$$

is considered where p' and c' are small perturbations to the pressure field and separating contact line position so that

$$\bar{p} = p + p', \quad (3.4.3)$$

$$\bar{c} = c + c'. \quad (3.4.4)$$

\bar{p} and \bar{c} represent the perturbed pressure field and separating contact line position, respectively. A small disturbance to the pressure field satisfies the homogeneous form of the lubrication equation (3.2.2):

$$\nabla_{II} \cdot (h^3 \nabla_{II} p') = 0 \quad (3.4.5)$$

For p' given by (3.4.1), this reduces to an ordinary differential equation in ϕ :

$$d^2\phi/dx^2 + (3h_x/h)d\phi/dx - N^2\phi = 0 \quad (3.4.6)$$

Finally, replacing h by the exponential form given in (3.3.2) results in

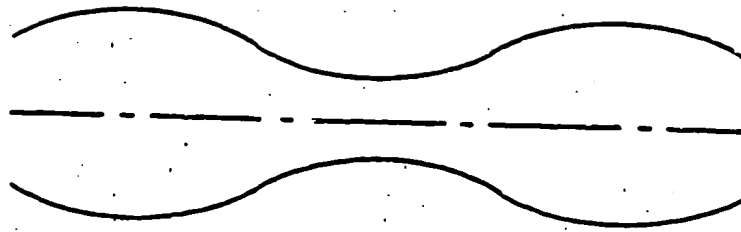
$$d^2\phi/dx^2 + (3/8) d\phi/dx - N^2\phi = 0 \quad (3.4.7)$$

At the inflow boundary, ϕ must be zero in order to satisfy the condition that pressure be zero there. The boundary condition at the separating contact line depends on how the curvature there changes with the parameter c .

A model is needed to determine how the disturbance to the contact line affects meniscus curvature. Figure 3.4 illustrates the two types of meniscus disturbances that are considered here. The first is a varicose deformation in which the radius of the cylinder is perturbed by a sinusoidal function of the axial coordinate. The second is a sinuous deformation in which the cylindrical axis is perturbed as a sinusoidal function of the axial coordinate. The change in curvature due to the superposition of these two meniscus deformations when contact angle is 90° is

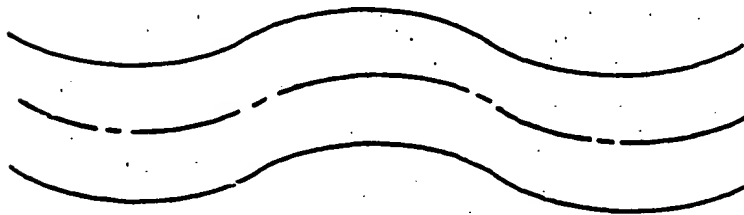
$$2H' = \epsilon \cos(Nz) \left[-N^2 + \frac{1}{R} \left(\frac{r}{r+1} \right) \right] \quad (3.4.8)$$

Here H' is the change in mean curvature at the separating contact line due to a disturbance given by (3.4.2) when the relative amplitude of



VARICOSE DEFORMATION

$$\bar{R} = R + R_1 \cos(Nz)$$



SINUOUS DEFORMATION

$$\bar{R} = R + R_2 \cos(Nz) \cos(\theta)$$

Figure 3.4. Illustration of varicose and sinuous deformations to a cylindrical meniscus due to three-dimensional disturbance.

varicose to sinuous deformation is given by Γ . The pressure disturbance p' must therefore satisfy the boundary condition:

$$p' = \epsilon \cos(Nz) \left[-N^2 + \frac{1}{R} \left(\frac{\Gamma}{\Gamma+1} \right) \right] / N_{ca} - \epsilon \cos(Nz) \frac{dp(c)}{dx} \quad \text{at } x = c \quad (3.4.9)$$

The last term is due to the displacement of the contact line through the pressure field of the base flow. The boundary condition on $\phi(x)$ is:

$$\phi = \left[-N^2 + \frac{1}{R} \left(\frac{\Gamma}{\Gamma+1} \right) \right] / N_{ca} - \frac{dp(c)}{dx} \quad \text{at } x = c. \quad (3.4.10)$$

The solution of (3.4.7) that goes to zero at the upstream boundary and satisfies (3.4.10) is

$$\phi = \left[\left(-N^2 + \frac{1}{R} \left(\frac{\Gamma}{\Gamma+1} \right) \right) / N_{ca} - \frac{dp(c)}{dx} \right] e^{A_1(c-x)} \frac{\sinh(A_2 x)}{\sinh(A_2 c)}, \quad (3.4.11)$$

where $A_1 \equiv -3/2B$ and $A_2 \equiv \sqrt{A_1^2 + N^2}$.

The ratio of varicose to sinuous meniscus deformation has yet to be specified. The lubrication approximations breaks down near the separating contact line because of the steep slopes there, and so lubrication theory cannot be used to estimate the meniscus profile there. Pearson (1960) was the first to realize the uncertainty in the change of meniscus curvature due to a contact line disturbance. For lack of information, he was forced to make an ad hoc choice of how the meniscus deforms. He compared two choices and found that his stability results were nearly the same for both. His first choice was to allow only the sinuous deformation, which is to set $\Gamma = 0$. The second was to so choose the relative

amplitude of sinuous to varicose deformation that the meniscus profile in every x-y plane is geometrically similar, which is to set

$$\frac{r}{r+1} = -\frac{R}{B} \quad (3.4.12)$$

Savage's (1977) choice was also equivalent to (3.4.12). Equation (3.4.12) is used in this analysis as well.

The final step in stability analysis in the lubrication approximation is to devise a criterion for judging whether a flow is stable or unstable to a specific disturbance. The criterion used here is identical to the one proposed by Pearson (1960). It is that a change in location of the contact line can only be due to a net accumulation (or loss) of mass near the contact line, which in turn must be caused by an increase (or decrease) in inflow rate just upstream of the meniscus minus the outflow rate just downstream of the meniscus. In other words, the criterion is based on an integral mass balance around the separating contact line, which is

$$\frac{d}{dt} [c'h(c)] = -\frac{h^3(c)}{12} \frac{\partial p'}{\partial x} - h'_0 \quad (3.4.13)$$

The term to the left of the equal sign represents the accumulation of mass on account of motion of the contact line; the terms to the right of the equal sign represent the respective changes in inflow and outflow rates due to the perturbation. Here h'_0 is the change in local final film thickness due to the disturbance, and is determined by the meniscus deformation:

$$h_0' = \epsilon \cos(Nz) [h(c)/B + r/(r+1)] \quad (3.4.14)$$

The first term in the square brackets represents the increase in gap width at the contact line because of the disturbance; the second term represents the decrease in radius of curvature in the x-y plane because of the disturbance. Small disturbances from the steady base flow either grow or decay exponentially in time,

$$\epsilon = \epsilon_0 e^{\lambda t} \quad (3.4.15)$$

Combining (3.4.13)-(3.4.15) and (3.4.2) gives the following expression for exponential growth rate:

$$\lambda = -\frac{h^2(c)}{12} \frac{d\phi}{dx} - [h(c)/B + r/(r+1)]/h(c) \quad (3.4.16)$$

When exponential growth rate λ is greater than zero the base flow is unstable; otherwise it is stable.

Figure 3.5 shows the stability results for exponential slot or knife coating as predicted by (3.4.16) when Reynolds, Prandtl-Hopkins and Coyne-Elrod boundary conditions are used. The results show how growth rate varies with wavenumber at four values of capillary number. The results predicted by the three boundary conditions are strikingly different. Each predicts that the fastest growing disturbance occurs at a nonzero wavenumber, but the maximum value of growth rate predicted at a given capillary number varies widely with meniscus condition. The most important distinction is that the Coyne-Elrod condition predicts

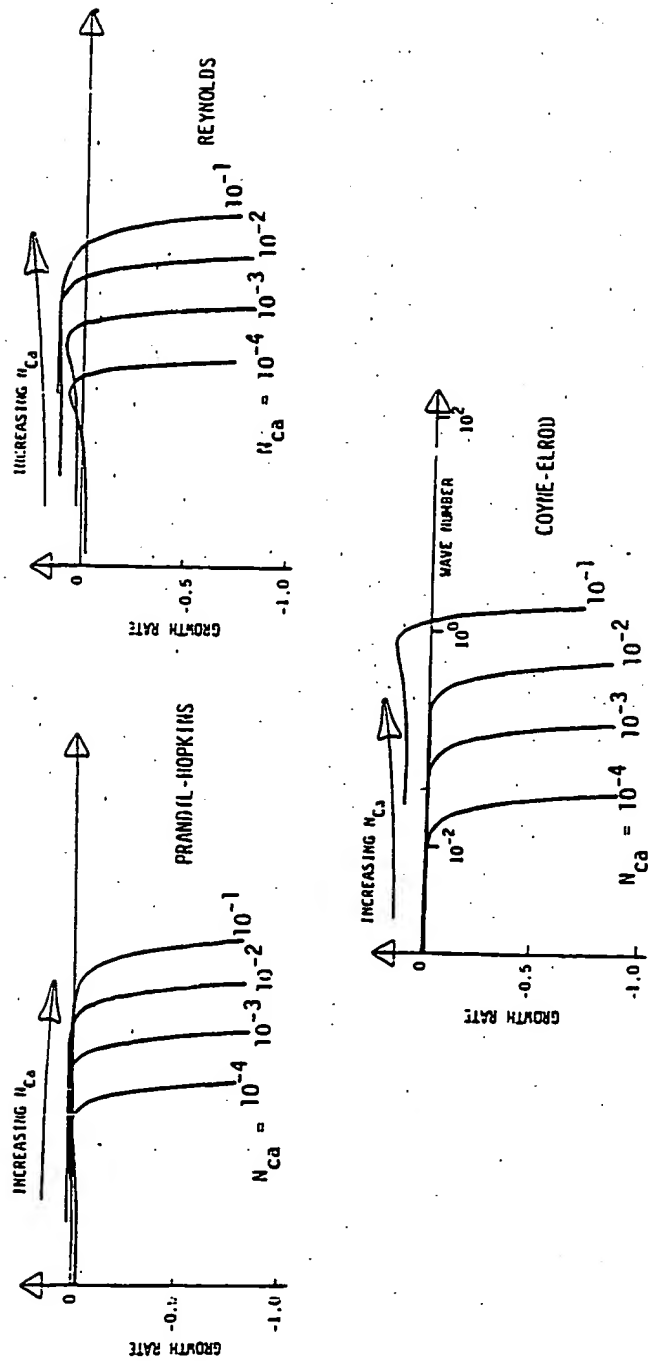


Figure 3.5. Comparison of stability results of exponential slot or knife coating for three meniscus conditions and over four orders of magnitude in capillary number.

that the flow is unstable only at the highest capillary number while the others predict instability even at the smallest capillary number.

3.5. Discussion

Several researchers, most notably Pearson (1960), Pitts and Greiller (1961), and Savage (1977), have shown that lubrication stability predictions are in some cases in qualitative agreement with experimental results and they have concluded that the mechanism of ribbing can be explained by lubrication theory. However, there are several uncertainties in the lubrication model, not the least of which are the appropriate boundary conditions to choose at the separating contact line, which strongly affect the stability predictions. As shown in Chapter 6, the uncertainties are most likely due to failure of the lubrication assumptions in the vicinity of contact line where the flow is generally far from rectilinear. These uncertainties force the practitioner to resort to guesses as to the conditions that apply there. The uncertainties grow particularly severe when a three-dimensional disturbance to a base flow is considered because little or nothing can be determined about the manner in which the meniscus is deformed by lubrication theory alone.

The apparent deficiencies of stability analysis in the lubrication approximation can perhaps best be overcome by solving the exact equations of motion, as given in Section 1.2, and then analyzing the stability of those solutions. This is done by the Galerkin/finite element method in Chapters 4 and 6. The results of the finite element stability analysis of exponential slot and knife coating reported in Chapter 6 are strikingly different than those of lubrication theory using Coyne and Elrod's bound-

any condition, as shown in Figure 6.12. One must conclude therefore that lubrication stability results are unreliable, and especially so when experimental or other data is unavailable to guide in the selection of conditions at a separating contact line.

CHAPTER 4 - ANALYSIS OF STEADY TWO-DIMENSIONAL SLOT AND KNIFE COATING FLOWS

4.1. Introduction

Slot and knife coating devices are among the most commonly used by coatings industries to apply thin liquid layers onto moving webs, i.e. flexible sheets. A typical slot or knife coater consists of a solid die which may be parallel or inclined to a moving web supported on the opposite side by a back-up roll, or in some cases stretched between two rolls not far apart. Figure 4.1 shows a knife coating device in which the die and web form a channel which has both parallel and diverging sections. This chapter is devoted to finding steady two-dimensional solutions to the equations that govern slot and knife coating flows, as laid out in Chapter 1. The stability of these flows to two- and three-dimensional disturbances is investigated in Chapter 6.

The flows considered here are of Newtonian liquids with uniform properties. The physical properties of the liquid and the operating parameters can be conveniently expressed in terms of five dimensionless parameters: (1) Reynolds number, $Re \equiv Ud/\nu$, indicates the relative importance of inertia as compared with viscous forces; (2) flow rate, $Q \equiv h_w/d$, is essentially a draw-down ratio; (3) Stokes number, $St \equiv gd^2/\nu U$, expresses the relative magnitude of gravity as compared with viscous forces; (4) capillary number, $Ca \equiv \mu U/\sigma$, is the ratio of a characteristic normal viscous stress to a characteristic capillary pressure; and (5) the three-phase contact angle that the liquid makes with the upper solid die, or equivalently, the position of the contact line. The first three of these parameters are associated with the flow field;

the last two are associated with the interface. Here, U is web speed, d is upstream gap thickness; ν is kinematic viscosity; h_∞ is the liquid film thickness far downstream from the slot or knife coater; g is the acceleration of gravity; μ is dynamic viscosity; and σ is surface tension. The effects of gravity are usually inconsequential in slot and knife coating and so Stokes number is usually much smaller than unity. Here it is taken to be negligibly small.

Figure 4.1 shows that slot and knife coating flows, like many other coating flows, contain three more or less distinct flow zones. In the upstream channel zone the flow departs only asymptotically from rectilinear flow, so that the governing equations are the momentum and mass conservation equations linearized about the rectilinear regime that prevails far upstream. Likewise, in the downstream free surface zone the flow departs only slightly from rectilinear motion — in this case plug flow, i.e. solid body translation — and so the linearized form of the governing equations apply there as well. However, in the intermediate region, here called the forming zone, the flow field rapidly evolves from channel to free surface flow and the full nonlinear form of the governing equations must be retained.

The strategy for analyzing the steady two-dimensional flow field in slot or knife coating is illustrated in Figure 4.2. Asymptotic solutions that describe the flow fields in the channel and free surface zones were constructed by Wilson (1969) and Higgins (1982), respectively both by means of perturbation analysis. Flow-fields in the forming zone are constructed by Galerkin/finite element analysis, a method which relies

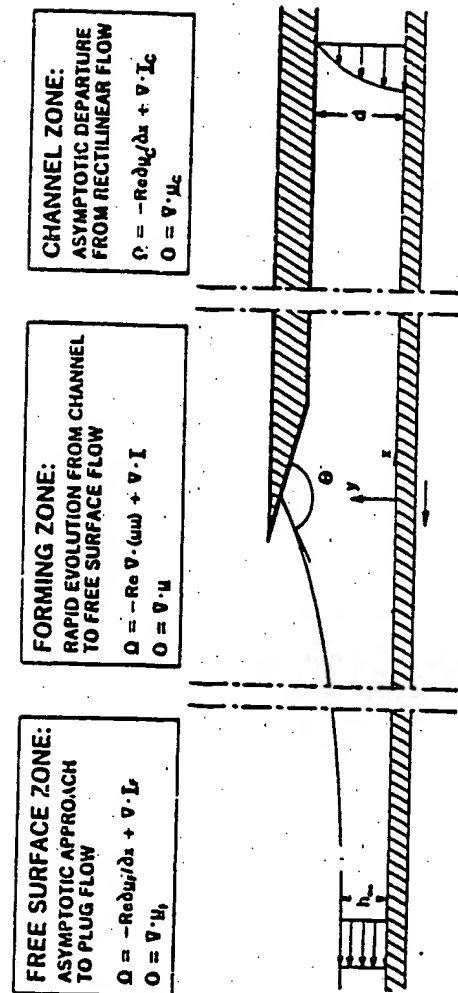


Figure 4.1. Three flow zones in slot and knife coating.

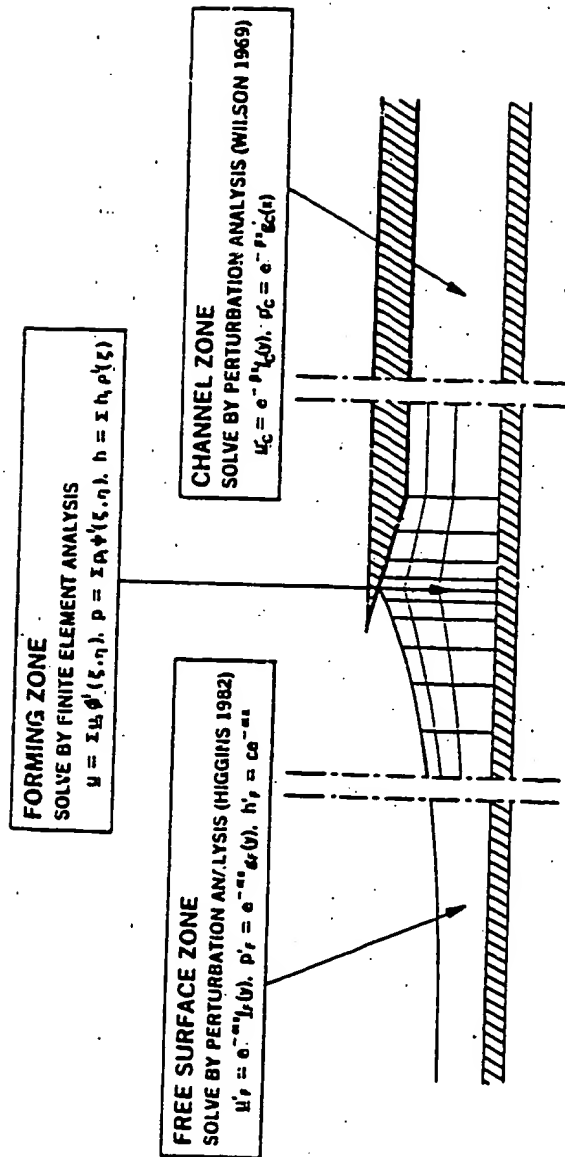


Figure 4.2. Strategy to solve the equations governing slot and knife coating flows.

on the modern digital computer to overcome what would otherwise be an insurmountable algebraic problem. Earlier theses by Orr (1976) and Silliman (1979) demonstrate that the Galerkin/finite element method is ideally suited to handle viscous free surface flow problems with irregular boundaries; this is further documented in articles by Silliman and Scriven (1980), Saito and Scriven (1981), and Kistler and Scriven (1982).

Two important considerations are the following: (1) Where should the inflow and outflow boundaries of the forming zone be placed? (2) What boundary conditions should be imposed there? The first question arises because open-flow boundary conditions are known only asymptotically, yet when a computer-based method such as Galerkin/finite elements is used the inflow and outflow boundaries must be located at finite rather than asymptotically large distances. The second question is one of choosing the boundary conditions that best approximate the interactions that the forming zone has with the surrounding zones. The choices considered here are the three general types of linear boundary conditions: (1) a Dirichlet condition, i.e. setting the dependent variables, would require that the asymptotic velocity profile already be attained at a finite location; (2) a Neumann condition, i.e. setting gradients of the dependent variables, would require that some final flow state (not necessarily the actual one) be attained at a finite location; and (3) a Robin boundary condition, i.e. choosing a proportionality between dependent variables and their gradients, would require only that at a finite location the flow decay towards the final regime at the asymptotic rate. The issues of choice and location of open-flow boundary conditions are

investigated here in two examples: developing plane Couette flow; and film formation on a moving web downstream of a slot or knife coater. The results of the first example have implications for the inflow boundary of slot and knife coating flows.

In section 4.2 the Galerkin/finite element forms of the equations governing viscous free surface flows are laid out and alternative open-flow boundary conditions are displayed. Section 4.3 focusses on how the choice and location of the outflow boundary condition affects the accuracy of the results in the examples of developing plane Couette flow and film formation on a moving web. The main findings are summarized and discussed in Section 4.4.

4.2. Galerkin/Finite Element Formulation

Equations (1.2.1)-(1.2.7) govern viscous free surface flows when liquid properties are uniform. These equations are solved here by the Galerkin/finite element method. The procedure is: (1) the unknown velocity, pressure, and free surface elevation are expanded in terms of finite element basis functions, each of which is nonzero only over a small subdomain; (2) the weak forms of the governing equations are constructed by choosing the basis functions as weighting functions and integrating over the domain; (3) the divergence theorem is applied to the governing equations wherever it is advantageous to reduce the order of the highest derivatives, in this case from second-order to first-order; (4) natural boundary conditions, i.e. ones that involve derivatives of the unknown variables, are introduced into the boundary integral that results from application of the divergence theorem; and (5) essen-

tial boundary conditions are imposed by replacing the equations weighted by trial functions associated with boundary nodes by the respective boundary conditions that apply there. Each of these steps is standard in finite element theory (see Strang and Fix 1973); the following paragraphs explain them in greater detail.

Basis Function Expansions. The unknown velocity, pressure, and free surface elevation are each expanded in a set of finite element basis functions. Each basis function is nonzero only on a small subdomain of the entire flow domain, and is expressed as a simple polynomial of the isoparametric coordinates ξ and η which act as local stand-ins for the global rectangular coordinates shown in Figure 4.1. Basis functions are defined not only by choosing the order of the polynomial by which they are expressed, but also by choosing the manner in which the domain is subdivided into elements, for this latter choice determines the subdomain over which each trial function is nonzero.

The flow field unknowns are expanded in basis functions:

$$\underline{u} = \underline{u}_i \phi^i(\xi, \eta) \quad (4.2.1)$$

$$p = p_i \psi^i(\xi, \eta) \quad (4.2.2)$$

$$h = h_i \rho^i(\xi, \eta) \quad (4.2.3)$$

Here \underline{u} is velocity, p is pressure, h is free surface elevation. ϕ^i , ψ^i , and ρ^i are finite element basis functions as specified below; u_i , p_i , and h_i are unknown coefficients which determine the velocity and pressure fields and the free surface elevation in the finite element approx-

imation; and (ξ, η) are isoparametric coordinates which are defined on each element by an isoparametric transformation:

$$(x, y) = (x_0, y_0)_i \phi^i(\xi, \eta), \quad (4.2.4)$$

where $(x_0, y_0)_i$ is the location of the i -th node. The purpose of the isoparametric transformation is to map deformed elements into standard squares as shown in Figure 4.3, which facilitates evaluation of the integrals below. The standard procedure of mixed interpolation (see, e.g., Huyakorn et al.) is adhered to in this analysis, i.e. velocity basis functions are chosen to be higher order than pressure basis functions. Here, velocity basis functions are standard biquadratics and pressure basis functions are standard bilinears (see Strang and Fix 1973). Tessellation of the domain into elements is illustrated in Figure 4.2. The location of velocity and pressure nodes in an element is illustrated in Figure 4.3. Free surface elevation basis functions are chosen to be standard Hermite cubics (Strang and Fix 1973).

Galerkin/Finite Element Residual Equations. Residual equations of the momentum conservation equation are formed by weighting Equation (1.2.1) by the velocity trial functions, integrating over the domain, and applying the divergence theorem to the stress term. The result is:

$$\begin{aligned} R_1^M = & \int_{\Omega} \{ \text{Re } \nabla \cdot (\underline{uu}) \phi^i(\xi, \eta) + \underline{T} \cdot \nabla \phi^i(\xi, \eta) \} \frac{\partial(x, y)}{\partial(\xi, \eta)} d\xi d\eta \\ & - \int_{\partial\Omega} \underline{n} \cdot \underline{T} \phi^i(\xi, \eta) \frac{\partial s}{\partial \gamma} d\gamma \end{aligned} \quad (4.2.5)$$

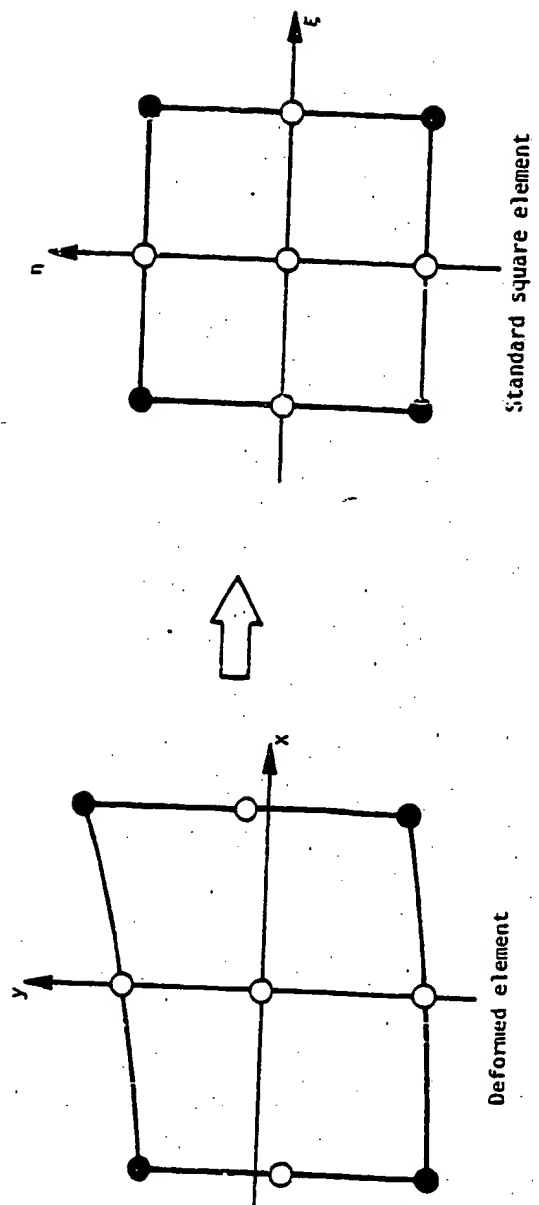


Figure 4.3. Illustration of isoparametric mapping of a deformed element into a standard square reference element. Open circles are nodes of velocity basis functions; closed circles are nodes of both velocity and pressure basis functions.

Here R_i^M is the i -th momentum residual equation; \underline{T} is the stress tensor, and under the conditions here that the liquid is Newtonian and has uniform properties it is given by $\underline{T} = \nabla \underline{u} + (\nabla \underline{u})^T - p(\underline{1}\underline{1} + \underline{j}\underline{j})$; $\partial(x,y)/\partial(\xi,\eta)$ is the Jacobian of the isoparametric transformation; s represents arc-length along the interface; γ is a parameter representing either ξ or η ; and Ω and $\delta\Omega$ are the flow domain and its boundary, respectively. Residual equations of the mass conservation equation are formed by weighting Equation (1.2.2) by the pressure basis functions and integrating over the domain. The result is

$$R_i^C = \int_{\Omega} \{(\nabla \cdot \underline{u})\phi^i(\xi,\eta)\} \frac{\partial(x,y)}{\partial(\xi,\eta)} d\xi d\eta. \quad (4.2.6)$$

Here R_i^C is the i -th continuity residual. Area integrals in Equations (4.2.5) and (4.2.6) are evaluated by standard three-by-three point Gaussian quadrature in the standard square reference element shown in Figure 4.3; the boundary integral in (4.2.5) is evaluated by standard three-point Gaussian quadrature along one of the edges of the square reference element.

Adherence Boundary Conditions. Adherence boundary conditions are imposed by setting the velocity coefficients corresponding to nodes which lie on solid boundaries so that local liquid velocity is the same as local boundary velocity, as illustrated in Figure 4.4. The web velocity is -1 , so

$$\underline{u}_i = -1 \quad (4.2.7)$$

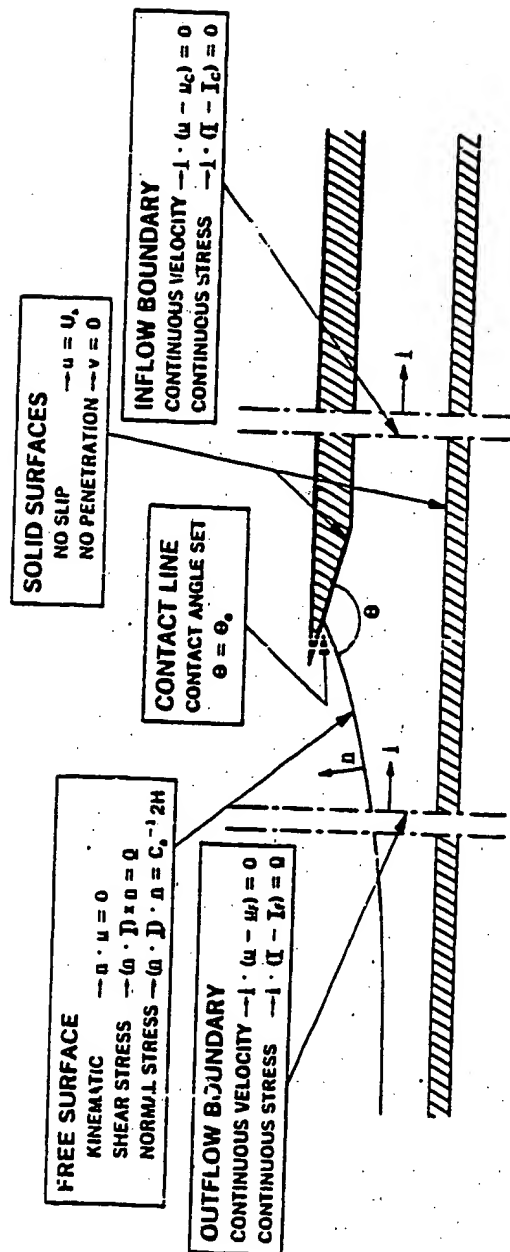


Figure 4.4. Boundary conditions on the forming zone.

for each node on the web. Likewise, the upper solid die is stationary; thus

$$\underline{u}_1 = \underline{0} \quad (4.2.8)$$

for each node on the die. Equations (4.2.7) and (4.2.8) replace the momentum residuals (4.2.5) at nodes along solid boundaries.

Free Surface Boundary Conditions. Balance of normal and shear stresses and lack of normal velocity component at the liquid/gas interface impose three boundary conditions there, as described in Section 1.2. Here, the gas phase is approximated as being inviscid and is assigned a datum pressure of zero. The shear stress balance is imposed as a natural boundary condition by replacing the boundary integral term in the momentum residual equation (4.2.5) by

$$\int_{\delta\Omega_{FS}} \underline{nn} : \underline{T} \phi^1(\xi, \eta) \frac{\partial \phi}{\partial \xi} d\xi. \quad (4.2.9)$$

Here, $\delta\Omega_{FS}$ indicates the free surface portion of the boundary and \underline{n} is the outward-pointing unit normal to the interface. The normal stress balance is imposed as an independent equation:

$$\begin{aligned} R_1^{NS} = & \int_{\delta\Omega_{FS}} \{ \underline{nn} : \underline{T} \phi^1(\xi, \eta) + [Ca^{-1} h_x / (1+h_x^2)^{1/2}] \partial \phi^1(\xi, \eta) / \partial x \} \frac{\partial x}{\partial \xi} d\xi \\ & - \{ \phi^1(\xi, \eta) Ca^{-1} h_x / (1+h_x^2)^{1/2} \}_{\delta\Omega_{OUT}}^{\delta\Omega_{CL}} \end{aligned} \quad (4.2.10)$$

$\delta\Omega_{OUT}$ and $\delta\Omega_{CL}$ refer to the intersection of the free surface with the outflow boundary and to the contact line, respectively. The last term

of Equation (4.2.10) is dealt with below. The third boundary condition, which expresses the impenetrability of the interface, i.e. the kinematic boundary condition, is imposed as an essential condition:

$$R_i^K = \underline{n} \cdot \underline{u}_i \quad (4.2.11)$$

for each node on the free surface. Equation (4.2.11) replaces the y-component of the momentum residual (4.2.5) for each i corresponding to a free surface node.

Contact Line Boundary Condition. Two alternative contact line boundary conditions are considered here. The simpler is to prescribe the contact line position as an essential condition, which corresponds to the situation when a meniscus is pinned at a geometric or compositional discontinuity. In this case the boundary condition is

$$h_i = h_{ss}(x_i) \quad (4.2.12)$$

for node i at the contact line, $h_{ss}(x_i)$ being the elevation of the upper solid surface there. The second alternative is to prescribe the angle that the interface makes with the upper solid die, denoted here as θ and defined by the angle between the outward pointing normals to the liquid and the solid die at the contact line. This is done using

$$\frac{dh}{dx} = \tan \left[180^\circ + \tan^{-1} \left(\frac{dh_{ss}}{dx} \right) - \theta \right] \quad (4.2.13)$$

to replace dh/dx in the last term of Equation (4.2.10) at the contact line.

Which of the two contact line boundary conditions, Equation (4.2.12) or (4.2.13), is selected makes little difference in a steady two-dimensional flow calculation, for given a contact line position there corresponds a contact angle and vice versa. On the other hand, it is convenient to be able to specify directly a contact angle when it is the known quantity, rather than iteratively choosing a contact line position until the one is found that satisfies the desired contact angle. However, the most important difference between prescribing contact angle and contact line is in the stability of the resulting flow, as described in Chapter 6.

Open-Flow Boundary Conditions. The slot or knife coating flows that are considered here are mathematical idealizations because the domain is taken to be unbounded in both the upstream and downstream directions. In reality liquid is supplied at some finite distance upstream and the coated liquid eventually solidifies at some finite distance downstream because it is chilled, polymerized, or dried. Nevertheless, these distances are often large enough that the mathematical idealizations are justified. However, the Galerkin/finite element scheme relies heavily on the digital computer, which is limited in speed and capacity, and hence the unbounded domain must be shrunk back to a finite size. One way to view the shrunk domain, i.e. shrunk from the unbounded domain of the mathematical idealization, is illustrated in Figure 4.2. Finite element basis functions are used to expand the flow field unknowns in the forming zone. Upstream and downstream of the forming zone are respectively the channel zone and the free surface zone. Flow in the

channel zone can be made as nearly rectilinear as desired by choosing the inflow boundary, i.e. the boundary between channel and forming zones, far enough upstream. Likewise, flow in the free surface zone can be made as nearly plug-like as desired by choosing the outflow boundary, i.e. the boundary between free surface and forming zones, far enough downstream. How far is far enough has to be tested. Furthermore, the conditions to be imposed at these stand-in boundaries should represent as accurately as conveniently possible the interactions of the flow interior and exterior to the boundaries. The more accurately they represent the internal/external flow interactions, the smaller need be the finite element domain. This is the criterion that is used to judge among possible boundary conditions: that boundary condition is "best" which allows the forming zone to be the smallest given the accuracy desired.

Each of the three types of linear boundary conditions are considered. The first is a Dirichlet condition in which the asymptotic velocity profile and free surface elevation are specified at the open-flow boundary nodes:

$$\underline{u} - \underline{u}_\infty = 0 \quad (4.2.14)$$

$$h - h_\infty = 0 \quad (4.2.15)$$

Here \underline{u}_∞ and h_∞ represent the asymptotic velocity profile and free surface elevation, respectively. Equations (4.2.14) and (4.2.15) are imposed as essential boundary conditions. The second is a Neumann condition in which the asymptotic normal traction and free surface elevation gradient is specified at the open-flow boundary nodes:

$$\underline{\underline{t}} \cdot [\underline{\underline{T}} - \underline{\underline{T}}_p] = \underline{\underline{0}} \quad (4.2.16)$$

$$dh/dx = 0 \quad (4.2.17)$$

Equations (4.2.16) and (4.2.17) are imposed as natural boundary conditions by using them to replace the normal traction term at the outflow boundary in the momentum residuals (4.2.5) and free surface gradient term at the intersection of the free surface and the outflow boundary in the normal stress residuals (4.2.10), respectively. An alternative to Equation (4.2.16) is to impose the asymptotic normal velocity gradient at the open-flow boundary:

$$\underline{\underline{t}} \cdot [\nabla \underline{\underline{u}} - \nabla \underline{\underline{u}}_p] = \underline{\underline{0}} \quad (4.2.18)$$

Equation (4.2.18) would be the appropriate boundary condition if only the Laplacian of velocity had been integrated by parts in forming the momentum residuals. The third is a Robin condition in which normal traction is taken to be proportional to velocity and free surface elevation gradient is taken to be proportional to free surface elevation:

$$-\underline{\underline{t}} \cdot [\underline{\underline{T}} - \underline{\underline{T}}_p] = \underline{\underline{A}} \cdot [\underline{\underline{u}} - \underline{\underline{u}}_p] \quad (4.2.19)$$

$$-dh/dx = c[h - h_p] \quad (4.2.20)$$

Here $\underline{\underline{A}}$ is a dyadic, a second-rank tensor which depends on no more than the filmwise coordinate y , and c is a constant. $\underline{\underline{A}}$ and c should be chosen so that velocities and tractions are as nearly continuous as possible at the open-flow boundaries, as indicated in Figure 4.4. Equations (4.2.19)

and (4.2.20) are imposed as natural boundary conditions in the same way as the Neumann condition in Equations (4.2.16) and (4.2.17). An alternative to Equation (4.2.19) is

$$-\underline{I} \cdot [\nabla \underline{u} - \nabla \underline{u}_\infty] = \underline{B} \cdot [\underline{u} - \underline{u}_\infty] \quad (4.2.21)$$

The asymptotic analyses of Higgins (1982) and Wilson (1969) show how small perturbations from final (initial) flow states decay to zero with distance downstream (upstream) for the cases of film formation on a moving web and developing plane rectilinear flow, respectively. The results of these analyses can be used to choose the dyadic \underline{A} (or \underline{B}) and the constant C . Both asymptotic solutions have a series form: each successive term in the series represents an increasingly complicated flow mode which has its own decay rate. The most important modes are the ones which decay most slowly with distance, because they persist furthest from the forming zone. When a single mode decays much more slowly than any of the others — and this is usually the case in film formation on a moving web — the dominant mode can be used to construct the dyadic \underline{A} (or \underline{B}) and the constant C , for example:

$$\underline{A} \equiv \underline{I} \{ [2\partial u_1^* / \partial x - p_1^*] / u_1^* \} + \underline{J} \{ [(\partial u_1^* / \partial y) / u_1^*] + \underline{J} \{ [(\partial v_1^* / \partial y) / v_1^*] \} \quad (4.2.22)$$

$$C \equiv [(h_1^* / dx) / h_1^*] \quad , \quad (4.2.23)$$

or if the alternative formulation is used so that only velocity gradients appear in the boundary integral:

$$\begin{aligned} \underline{B} &\equiv \underline{ii}[(\partial u_1^*/\partial x)/u_1^*] + \underline{jj}[(\partial v_1^*/\partial x)/v_1^*] \\ &= (\underline{ii} + \underline{jj}) [\alpha] \end{aligned} \quad (4.2.24)$$

Here, u_1^* and v_1^* are the velocity components of the dominant mode from the asymptotic analysis; p_1^* is the pressure field of the dominant mode; $h_\infty + h_1^*$ is the free surface elevation of the dominant mode; and α is the exponential spatial decay rate of the dominant mode. The quantities in Equations (4.2.22)-(4.2.23) have been so chosen that boundary conditions (4.2.19)-(4.2.21) would be satisfied identically if the dominant mode of the asymptotic analysis exactly described the flow field at the open-flow boundary.

Wilson's (1969) analysis of developing rectilinear channel flows at low Reynolds number shows that there are two dominant modes that decay spatially at the same exponential rate, but they are modulated by sinusoidal spatial oscillations that are 90° out of phase. Therefore, both modes are needed to construct the dyadic \underline{A} and constant C . The method used here is to select coefficients a_1 and a_2 so that the vector equation

$$\underline{u} - \underline{u}^\infty = a_1 \underline{u}_1^* + a_2 \underline{u}_2^* \quad (4.2.25)$$

is satisfied locally. Then, Equation (4.2.19) is replaced by

$$-\underline{i}[\underline{T} - \underline{T}^\infty] = a_1 \underline{A}_1 \cdot \underline{u}_1^* + a_2 \underline{A}_2 \cdot \underline{u}_2^* \quad (4.2.26)$$

where \underline{A}_1 and \underline{A}_2 are defined by (4.2.21) for \underline{u}_1^* and \underline{u}_2^* , respectively. The same method can be used when boundary condition (4.2.21) is applicable.

Newton's Iteration. Newton's iteration procedure was used to solve the finite element residual equations (4.2.5)-(4.2.20). Newton's method and its theory are described in a number of books on numerical methods for solving systems of equations, among which those by Traub (1964), Isaacson and Keller (1966), Oden (1972), and Ortega and Rheinboldt (1970) are especially useful. The basis of this method is simply a Taylor expansion of the set of residual equations, the i -th of which is denoted here as R_i as defined by:

$$\{R_i\} \equiv \{R_1^{Mx}, \dots, R_n^{Mx}, R_1^{My}, \dots, R_n^{My}, R_1^C, \dots, R_m^C, R_1^K, \dots, R_s^K\} \quad (4.2.27)$$

Here R_i^{Mx} and R_i^{My} are respectively the x - and y -components of the momentum residual R_i^M ; n is the number of velocity nodes; m is the number of pressure nodes; s is the number of free surface elevation unknowns. If β_i^j is the i -th nodal unknown, as defined by

$$\{\beta_i\} \equiv \{u_1, \dots, u_n, v_1, \dots, v_n, p_1, \dots, p_m, h_1, \dots, h_s\} \quad (4.2.28)$$

then Newton's iteration is defined by

$$J_{ji}^{(n)} (\beta_i^{(n+1)} - \beta_i^{(n)}) = R_j^{(n)} \quad (4.2.29)$$

Here, the superscript indicates the iteration number and J_{ji} is the ji -th entry in the Jacobian matrix, as defined by:

$$J_{ji}^{(n)} \equiv \partial R_j^{(n)} / \partial \beta_i \quad (4.2.30)$$

The system of linear equations expressed by (4.2.29) was solved by using Hood's (1976) subroutine FRONT. Silliman (1979) used the same iteration procedure as (4.2.29) in his investigation of extrusion coating. However, he did not correctly evaluate the derivatives of the residual equations with respect to the free surface elevation unknowns. Saito and Scriven (1981) later showed how those derivatives could be evaluated in the reference domain of the isoparametric mapping. Saito and Scriven also demonstrated that their convergence rates were asymptotically quadratic, as theory predicts, whereas Silliman's convergence rates were only linear due to the errors in his Jacobian. Asymptotic quadratic convergence was also attained in this work, verifying that the Jacobian matrix was evaluated correctly.

Initial approximations, $\beta_1^{(0)}$, to start up Newton iteration were generated in two ways: (1) velocities were set to zero everywhere except at the moving web where the adherence boundary condition was imposed, and the free surface profile was chosen to be a straight line that passed through the contact line and a point lying on the outflow boundary at $y = h_w$; and (2) a previous solution was used as the initial guess. The first method was used chiefly for start-up. It usually required from 5 to 7 Newton iterations to converge when the criterion was

$$\max_i |R_i| < 10^{-4} \quad (4.2.31)$$

The second method was used for continuation once the first solution had been attained and normally required 3 to 4 Newton iterations. Each Newton iteration required only about 5.4 central processor seconds on

the University of Minnesota Cyber 74, and thus the computations were relatively inexpensive (typically \$4.00 for one solution).

4.3. Comparison of Outflow Boundary Conditions

Figure 4.5 illustrates the basis used here to compare the contending boundary conditions. Four domain lengths were chosen in each situation: for the channel, lengths of 8, 6, 4, and 2 channel widths were chosen; for the slot or knife coater, lengths measured downstream of the contact line were 12, 8, 6, and 4 channel widths. In both cases shorter domains were formed by chopping off elements from the longer ones. Therefore, the shorter the domain the fewer the degrees of freedom and consequently the cheaper the computations. It was found that computation costs were nearly a linear function of the number of elements used. Dirichlet inflow conditions were used in both cases.

The standard of comparison was always chosen to be the solution with the Robin condition and the longest domain. This might seem to bias the results in favor of the Robin condition, but in fact did not because the three types of boundary conditions generally agreed closely on the longest domain. In order to test the influence that the boundary condition has on the flow further upstream, comparisons were limited to the shaded portion of the domains in Figure 4.5, four comparisons in all. These are as follows: (1) maximum difference in the streamwise velocity component, u ; (2) maximum difference in the cross-stream velocity component, v ; (3) maximum difference in pressure; and (4) difference in free surface elevation at the downstream edge of the shaded region (knife coater geometry only).

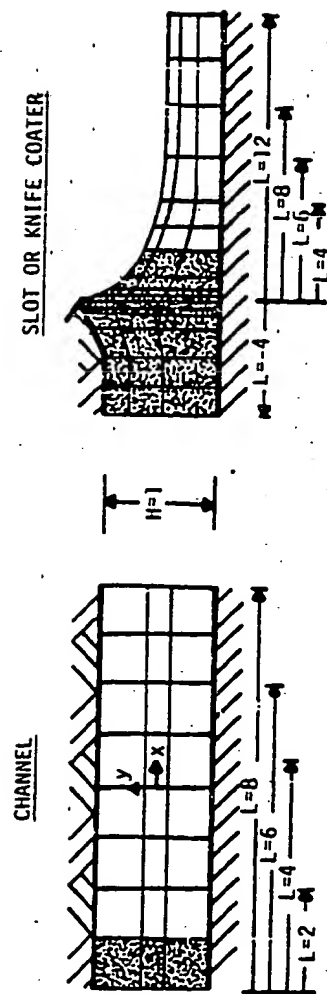


Figure 4.5. Basis for comparison of alternative boundary conditions on four domain lengths in developing channel flow and in film formation downstream of a slot or knife coater. Comparisons were made in shaded portions of each domain.

Figure 4.6 shows the results for developing plane Couette flow when inertia is negligible, i.e. Reynolds number is negligibly small. All three boundary conditions give comparable accuracy in velocity components, but the Dirichlet condition gives 1 to 1.5 fewer decimals of accuracy in pressure. Thus for developing plane Couette flow, in which disturbances decay rapidly, the Robin and Neumann conditions are superior, and competitive with each other.

The ordinates in Figure 4.6 (also Figures 4.7 and 4.8) represent the number of digits to the right of the decimal point which are in agreement with the standard, i.e. the solution with the Robin condition on the longest domain. The ordinate values were calculated by taking the negative of the base-ten logarithm of the difference or maximum difference of a property at corresponding node points of the two solutions being compared.

In film formation on a moving web the Robin condition gives the best accuracy when capillary forces dominate, i.e. when capillary number is small as shown in Figure 4.7. The increase in accuracy with the Robin condition over the others is about 2 decimals for velocity components, 1 to 2 decimals for pressure, and 0.5 to 2 decimals for free surface elevation. These are significant improvements in accuracy, and so the Robin condition is to be preferred in these circumstances.

Figure 4.8 shows that when inertial forces dominate over viscous forces, i.e. when Reynolds number is appreciably greater than unity, the situation changes dramatically. Here the Dirichlet condition has been discarded from the comparison because it led to solutions with large un-

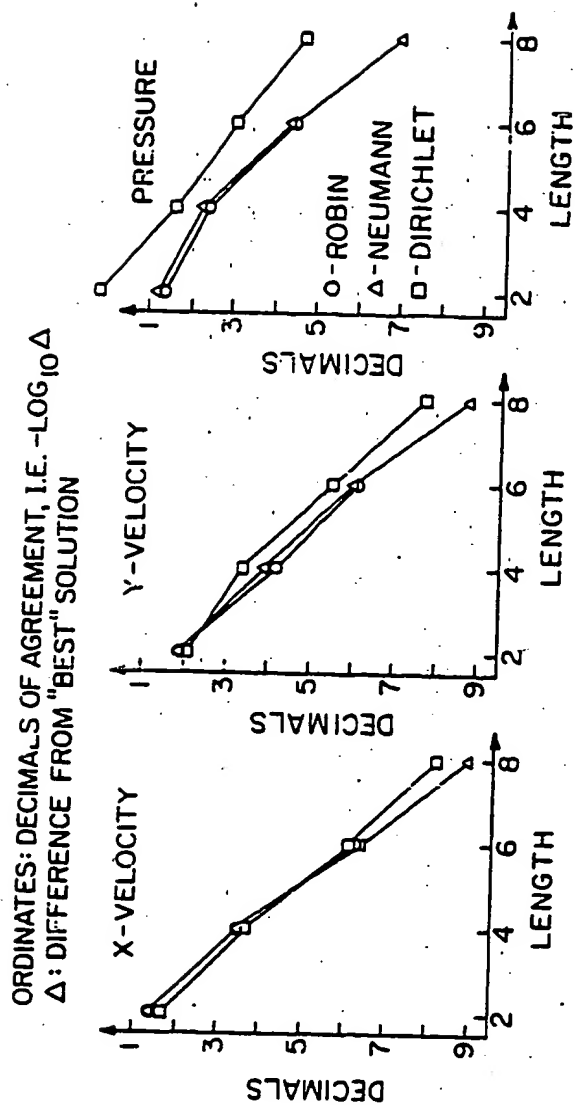


Figure 4.6. Comparisons of solution accuracy in developing channel flow when Reynolds number is negligibly small.

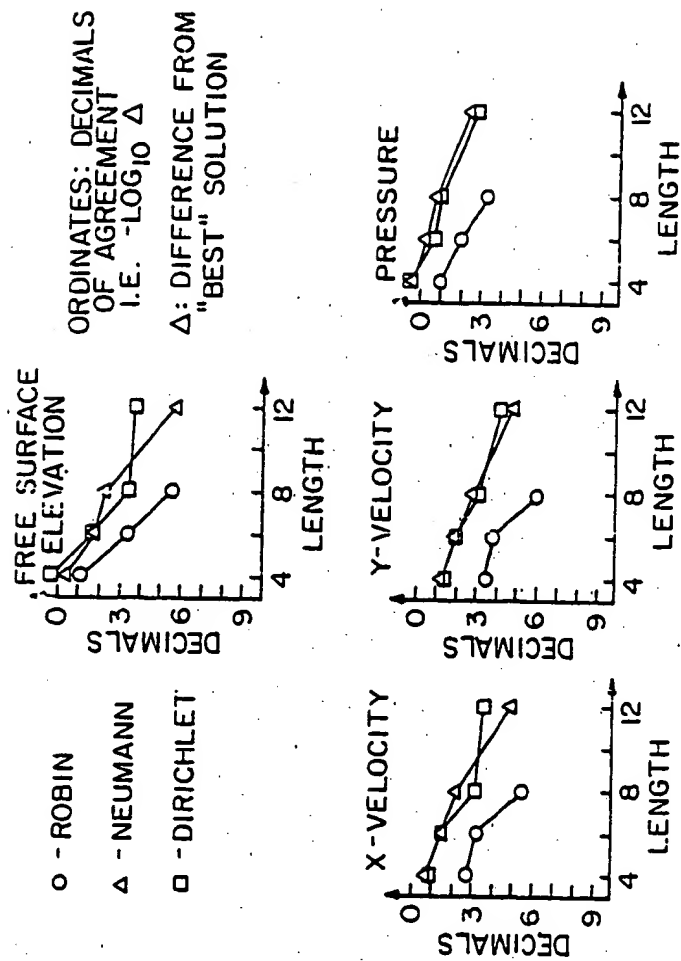


Figure 4.7. Comparisons of solution accuracy in film formation on a moving web when Reynolds number is 2 and capillary number is 0.01.

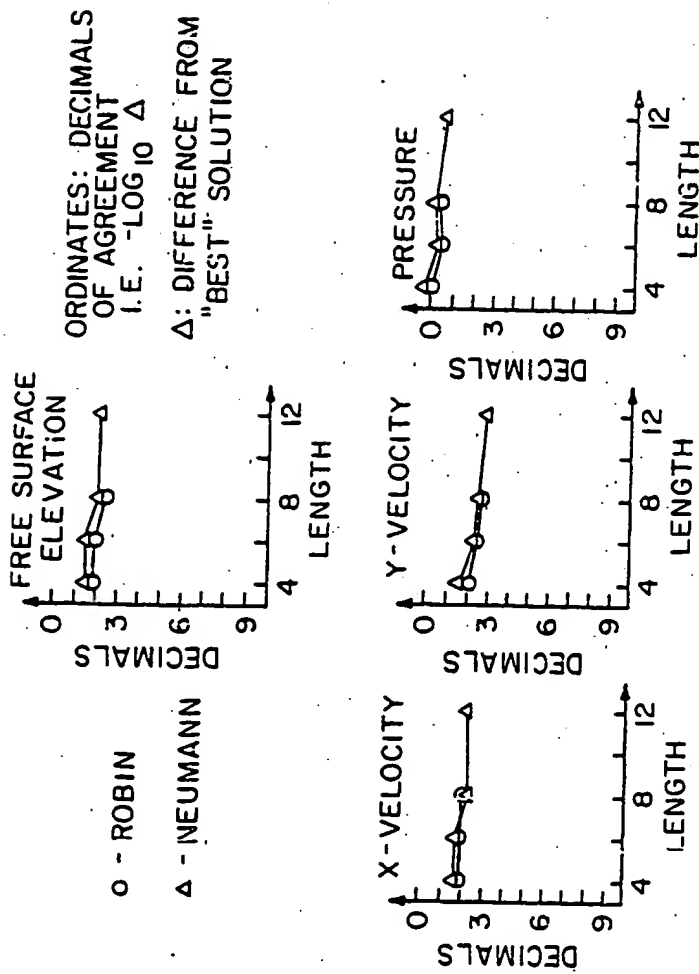


Figure 4.8. Comparisons of solution accuracy in film formation on a moving web when Reynolds number is 200 and capillary number is 0.01.

physical standing waves and furthermore the convergence rate of Newton's iteration was slow when it was used. The other boundary conditions, Robin and Neumann, are competitive, the Robin condition having a slight edge. The reason that the two are close is clear: the spatial decay rate of the most slowly decaying mode decreases nearly to zero as the inertia effect grows large. This is because viscosity provides the sole mechanism for transporting momentum from the liquid to the moving web, and the effect of viscosity becomes relatively small when Reynolds number becomes large. As a result, the constants of proportionality in the Robin condition become very small at large Reynolds number, causing it to degenerate almost all the way to a Neumann condition, which is the limiting case. Thus, it is not unexpected that the two results should be similar.

The chief advantage of the Robin condition is not that it improves accuracy at a given domain length, but that shorter domain lengths can be used without loss of accuracy. For example, if two-decimal accuracy is sought in the velocity components and free surface elevation for the case of film formation on a moving web, the minimum domain length needed when each of the three boundary conditions is used can be compared. Figure 4.9 shows that, as expected, the Robin condition allows shorter domain lengths to be used — about a factor of 2 shorter when inertia is a small to moderate effect, but decreasing to about a factor of $1\frac{1}{3}$ when inertia is large.

Figure 4.10 shows the performance of the three boundary conditions at vanishing Reynolds number as the ratio of capillary to viscous forces

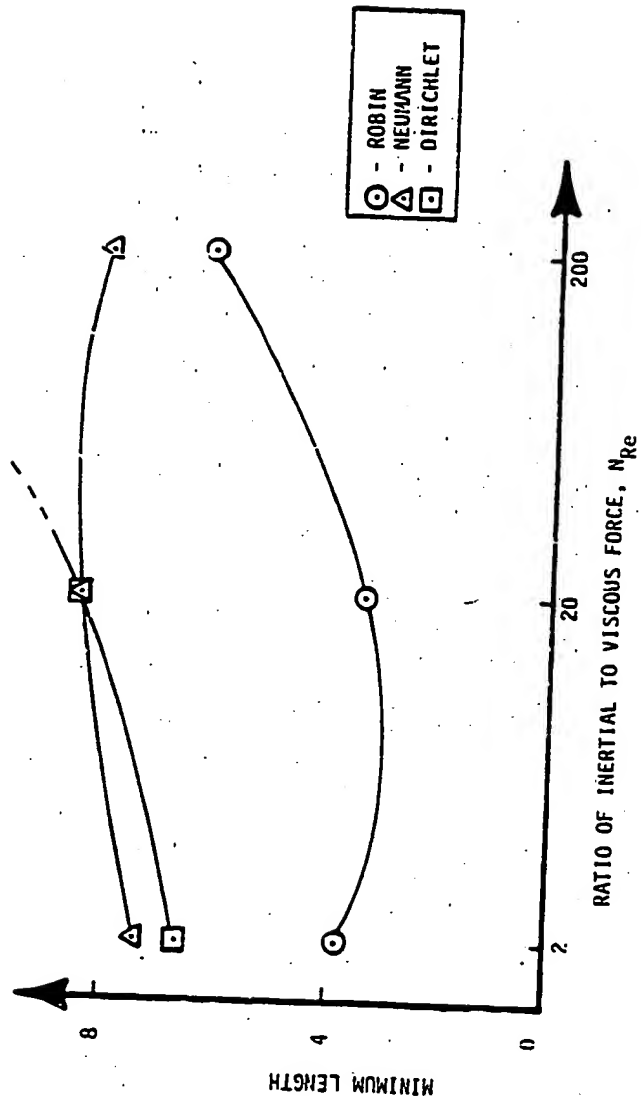


Figure 4.9. Minimum domain lengths necessary to maintain two-decimal accuracy of velocity components and free surface elevation in film formation on a moving web when capillary number is 0.01.

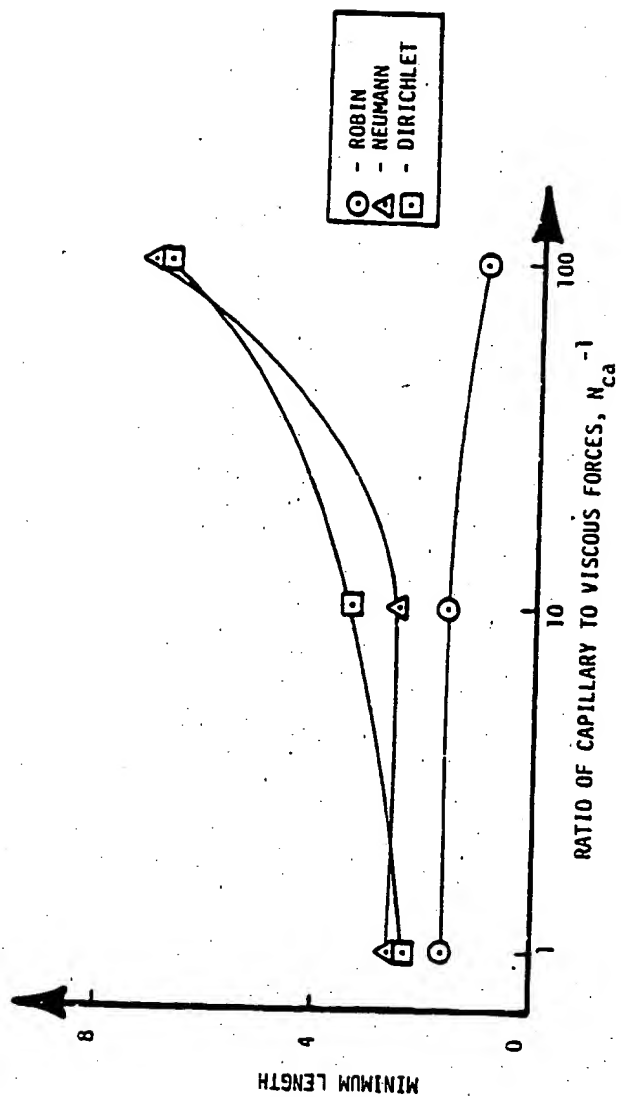


Figure 4.10. Minimum domain lengths necessary to maintain two-decimal accuracy of velocity components and free surface elevation in film formation on a moving web when Reynolds number is negligibly small.

is varied. Again, two-decimal accuracy in the velocity components and free surface elevation is sought. In this case the Robin condition allows more than a four-fold decrease in domain length compared with the other two conditions. This factor, however, falls rapidly when viscous forces rise and it levels off at about 1.25. The results in Figures 4.9 and 4.10 indicate that the Robin condition always allows shorter domain lengths to be used for the given accuracy specified, but that the advantage is greatest when capillary forces dominate over both inertial and viscous forces.

4.4. Discussion

The results of Section 4.3 show that a Robin outflow condition is superior to Dirichlet or Neumann conditions in developing channel flow and film formation on a moving web, but the degree to which it is superior varies widely with the circumstances. In developing channel flow the advantage of a Robin condition over a Neumann condition is marginal, both being superior to a Dirichlet outflow condition. In film formation on a moving web the advantage of a Robin condition is greatest when capillary forces dominate over viscous and inertial forces. One major advantage of a Robin outflow condition is that the degree to which the domain needs to be shrunk or expanded to obtain maximum computational efficiency without loss of accuracy as parameters are changed is moderated in comparison with the situation when a Neumann or Dirichlet condition is used. For example, Figure 4.10 shows that the domain length measured downstream of the contact line can be maintained at about 2 gap thicknesses when a Robin condition is used and capillary number is varied

over two orders of magnitude. By comparison, the domain length would have to vary by about a factor of about three if Neumann or Dirichlet conditions were used.

The question of which boundary condition is "best" at the inflow boundary of slot or knife coating has not been addressed directly, but some conclusions can be drawn from the foregoing results. The inflow boundary of slot and knife coating flows is analogous to the outflow boundary in developing channel flow, and especially so at low Reynolds number when momentum convection is not important. This suggests that the type of inflow boundary condition plays only a minor role in affecting accuracy of computations. Moreover, when Reynolds number is not negligible the upstream influence of a downstream departure from rectilinear flow is less than it would be at negligible Reynolds number. A Dirichlet inflow boundary condition is likely "best", and especially so at moderate to high Reynolds numbers.

Figure 4.11 shows the results of two flow field calculations when contact angle is specified. The arrows show the relative magnitude and direction of local velocity. The inflow condition is Dirichlet and the outflow condition is Robin. In neither case has the flow profile reached solid body translation at the outflow boundary, yet the arrows representing the local velocities near the outflow boundary appear to be smoothly approaching the asymptotic state. This demonstrates the power of the Robin outflow condition as given in Equations (4.2.19) and (4.2.20).

Figure 4.11 also shows the sensitivity of contact line position to capillary number. As capillary number increases (here by a factor of

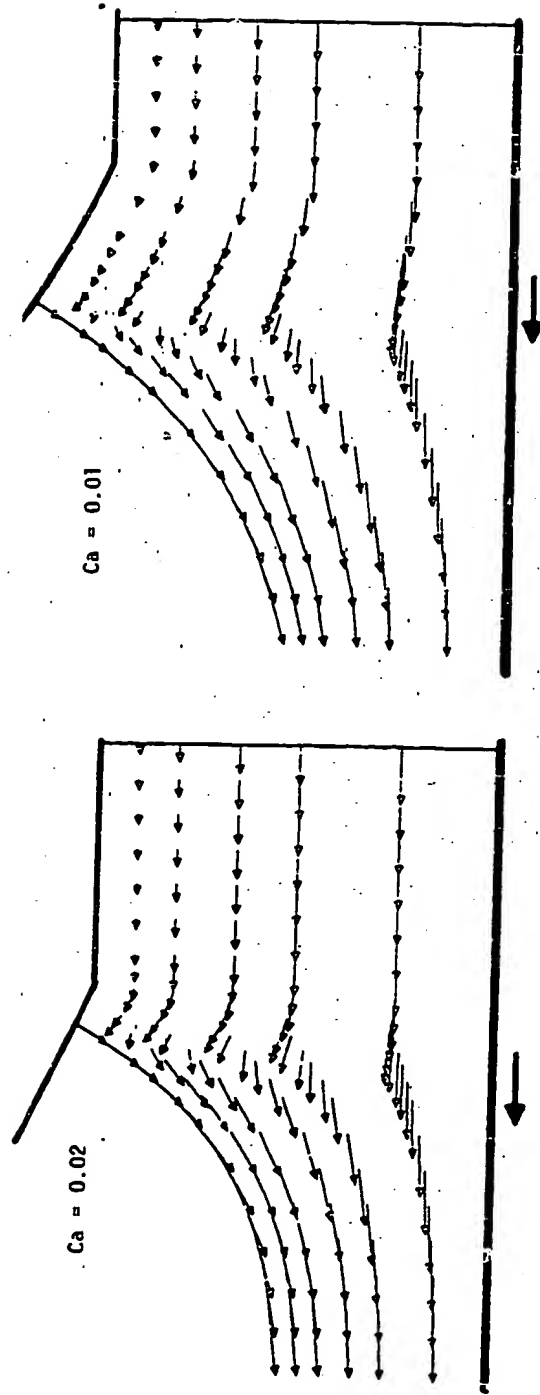


Figure 4.11. Velocity field in slot or knife coating when Reynolds number is negligibly small, contact angle is 157.5° , and outflow condition is a Robin condition. Vertical scale is exaggerated by factor of 6.

2), the contact line invades further upstream. Furthermore, the meniscus curvature increases with capillary number. These features of the flow are discussed further in Chapter 6 in connection with the stability of slot and knife coating.

Figure 4.12 shows some streamline contours of a similar flow but on a longer domain. The streamlines are parallel and quadratically spaced at the upstream boundary, indicating plane Couette flow. At the outflow boundary the streamlines are parallel and evenly spaced, indicating solid body translation. The streamlines fan out slightly in the diverging portion of the channel, rapidly converge as the meniscus forms, then converge more and more gradually, finally approaching parallel and evenly spaced asymptotes. Although this flow appears innocuous, it is shown in Chapter 6 to be unstable to a ribbing disturbance.

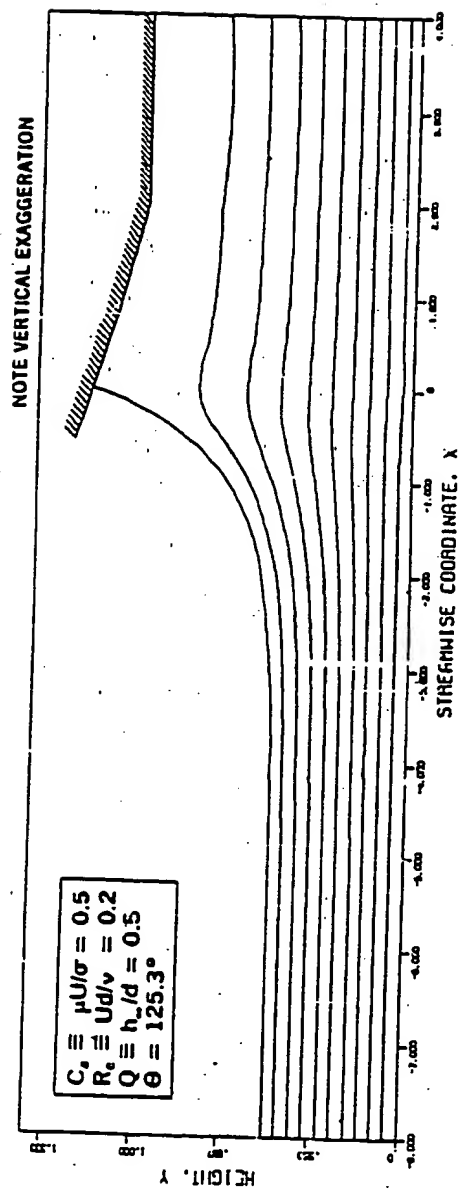


Figure 4.12. Some streamline contours in slot or knife coating. Stability of this flow is considered in Chapter 6.

CHAPTER 5 - FINITE ELEMENT ANALYSIS OF COATING INSTABILITIES

5.1. Introduction

Previous analyses of the fluid mechanics of coating flows have been incomplete. The existence of steady two-dimensional flows has been demonstrated, but not their stability or uniqueness. The stability and uniqueness of static equilibria, gyrostatic equilibria, and simple rectilinear flows have been addressed (see Brown 1979, Brown and Scriven 1980a,b, and Drazin and Reid 1981, for examples), but not of complicated two-dimensional flows like those typical in the deposition of a coating onto a moving web. These flows have become amenable to analysis only in recent years by virtue of the advent of the modern digital computer and sophisticated computer-based schemes for handling elliptic partial differential equations — primarily the finite element method. How to harness the finite element method to undertake the stability analysis of these flows is only now coming into focus. The origins of finite element stability analysis in fluid dynamics date back to Orr's (1976) thesis research; analysis began with Brown's investigations of the shape and stability of static menisci as recorded in his thesis (1979) and paper by Brown and Scriven (1980a). The analysis then turned to shape stability of rotating drops (Brown and Scriven 1980b). Brown's stability analysis of simple static and gyrostatic "flows" depended on an energy minimization principle, and thereby his analysis resulted in a symmetric eigenproblem. On the other hand, "dynamic" free surface flows usually have no minimization principle because they are not conservative, and thereby the study of their stability leads to an asymmetric eigenproblem.

Although the ideas and methods of finite element stability analysis carry over from "static" or "gyrostatic" flows to "dynamic" flows, the methods to perform the eigenanalysis do not. Because techniques to solve asymmetric eigenproblems are not well developed at present, finding means of eigenanalysis necessary to determine the stability of a free surface flow was one of the major challenges of this research.

Pioneers in finite element stability analysis and undamped vibrations in mechanical structures were Gallagher and Padlog (1963), Martin (1965), Kapur and Harty (1966), Anderson et al. (1968), Carson and Newton (1969), Gupta (1969, 1970, 1972, 1973), Jennings and Orr (1971), Dong et al. (1972), and Bathe and Wilson (1972, 1973). These early analyses concentrated on solving a symmetric generalized eigenproblem, i.e. an eigenproblem of the form

$$J_{ij}X_j = \lambda M_{ij}X_j, \quad (5.1.1)$$

where J_{ij} and M_{ij} are the respective components of symmetric stiffness and mass matrices, X_j is the j -th component of an eigenvector, and λ is the corresponding eigenvalue. The stiffness matrix, also called the Jacobian matrix, is an array of sensitivities of residuals to changes in the nodal parameters, and the mass matrix represents time variation of residuals. A solution of (5.1.1) is a possible disturbance or vibration mode, the matrix vector X , and the corresponding decay or vibration rate squared, λ . These early works also began fueling interest in the asymmetric variety of (5.1.1) which arises when damped vibrations are considered. The convention that repeated indices be summed is adopted in

Equation (5.1.1) and below.

The first notable step toward an effective strategy for handling large asymmetric eigenproblems with the digital computer was by Bauer in 1957. He devised a scheme in which both dominant eigenvectors — i.e. eigenvectors for which the corresponding eigenvalues are largest in magnitude — and dominant adjoint eigenvectors — i.e. dominant eigenvectors of the adjoint eigenproblem

$$J_{ij}^T x_j^* = \lambda^* M_{ij}^T x_j^* ,$$

where x_i^* is the i -th component of an adjoint eigenvector and λ^* is the corresponding eigenvalue — were constructed simultaneously and the well-known property of biorthogonality (see e.g. Friedman 1956) was exploited. Bauer's method was the first to use simultaneous iteration to find the dominant subspace of an asymmetric eigenproblem. The dominant subspace is the subspace spanned by the dominant eigenvectors. However, his method has two major shortcomings. The first is that the computational work is doubled by tracking both eigenvectors and adjoint eigenvectors. The second is that eigenvectors may be nearly parallel and as a result, there can be problems of numerical instability (Stewart 1976). Some of the practical aspects of Bauer's method and additional improvements were later discussed by Clint and Jennings (1971).

Work on another computational strategy which would find all the eigenvalues and optionally all the eigenvectors of an asymmetric matrix had begun somewhat earlier. Von Neumann and Goldstein (1947) first proposed that the method of Jacobi (1846) should be extended for the reduc-

tion of a general matrix to triangular form. Interest in this idea did not spring up until about ten years later, when Rutishauser (1955, 1958, 1960, 1963) developed the LR algorithm, which is based on repeated factorization of a matrix into the product of a lower-triangular (L) matrix and upper-triangular (R) matrix. Francis (1961, 1962) improved Rutishauser's algorithm markedly in the development of the well-known QR algorithm, which is based on repeated factorization into the product of an orthogonal (Q) matrix and an upper-triangular (R) matrix (see Stewart 1973 for a detailed description). Wilkinson (1965) has called the QR algorithm "the most effective of known methods for the solution of general algebraic eigenvalue problems." It remains today the most popular and effective method for finding all the eigenvalues of a matrix. Furthermore, it plays a significant role in many computational strategies which seek only the dominant subspace.

With these two pieces in place, i.e. Bauer's and Francis's works, the time was right to build up better computational strategies for tracking dominant subspaces of asymmetric matrices. In a series of papers Stewart (1969, 1975, 1976, 1978) developed a method, referred to here as Stewart's algorithm, for calculating the dominant subspace of a real matrix. He drew heavily from Rutishauser's published algorithm (1970) for solving the symmetric eigenproblem, and he incorporated Francis's QR algorithm as well. The details of Stewart's algorithm are explained more fully in Appendix A. This algorithm is used here to solve the eigenproblem which arises from the stability analysis. Alternatives are discussed in Section 5.3 and further ideas in Section 5.4.

Before proceeding it is essential to define the stability problem to be solved in a precise and mathematical way by addressing two issues. What class of perturbations are to be allowed? What criterion should be used to judge whether a flow is stable or unstable to that class of perturbations? The class of allowable perturbations is limited here by four restrictions: (1) they are to be small in amplitude in comparison with the base flow; (2) they must satisfy all physical constraints, which are local conservation of mass, no slip and no penetration boundary conditions, and balance of normal stress at a free surface; (3) they must be representable in a set of basis functions which are products of finite element and Fourier basis functions, as described in Section 5.2.; and (4) they must disappear far upstream and downstream of the forming zone. The first restriction removes the possibility of considering the interactions of a perturbation with itself due to self-convection and to coupling between free surface elevation and stress components at the free surface, but so doing allows great simplification in the mathematics. In particular, small perturbations have the following properties: 1) they grow or decay exponentially in time; 2) they obey the property of superposition; and 3) therefore may be decomposed into Fourier normal modes in the transverse direction z . The second restriction is self-evident: perturbations must conserve mass and satisfy essential boundary conditions. The third restriction is a convenient choice of perturbation representation to make manageable the stability analysis on a digital computer. Furthermore, it is consistent to use the same set of finite element basis functions to represent the perturbation as was used

to represent the base flow; otherwise the stability analysis might show the base flow to be unstable to a mode which the base flow analysis did not permit. The fourth restriction is to eliminate from the stability analysis consideration of possible modes which originate far upstream or downstream of the forming zone. The criterion for judging stability of a flow to the class of disturbances defined above is that of asymptotic stability, i.e. a base flow is considered to be stable if and only if all allowable perturbations decay as time increases. It will be shown in Section 5.2 that a baseflow is stable whenever all the eigenvalues of a certain eigenproblem have positive real part.

Sections 5.2 and 5.3 respectively show how to formulate the stability problem in terms of an eigenproblem and how to solve the eigenproblem. The ideas are summarized and compared with some ongoing work of Ruschak and of Brown in Section 5.4. A promising variant of Brown's method is being investigated by Basaran and Benner.

5.2. Formulation of the Stability Problem

Here the equations governing a small unsteady three-dimensional perturbation to a steady two-dimensional base flow are set out and the Galerkin weak form of these equations is constructed. The superposition of a small perturbation and a steady two-dimensional base flow can be represented by the perturbed velocity and pressure fields:

$$\bar{u}(c) \equiv \underline{u}(x,y) + \epsilon \underline{u}'(x,y,z,t) \quad (5.2.1)$$

$$\bar{p}(c) \equiv p(x,y) + \epsilon p'(x,y,z,t) \quad (5.2.2)$$

The shape of the domain changes because the free surface elevation is

also perturbed:

$$\bar{h}(\epsilon) \equiv h(x) + \epsilon h'(x, z, t) . \quad (5.2.3)$$

Here overbars indicate a perturbed field or quantity, primes indicate perturbations to the baseflow, and ϵ is a small parameter which is proportional to the amplitude of the perturbation. Because ϵ is small, only terms that are linear in it need be retained, for higher-order terms are negligible by comparison. Formally, linearizing in ϵ is equivalent to taking the first derivative of the governing equations and boundary conditions with respect to ϵ and then setting ϵ to zero. The strategy illustrated in Figure 4.1 to solve the steady base flow, i.e. dividing the flow domain into three zones, is also used to solve the three-dimensional unsteady perturbed flow, and thus the equations have to be linearized in each of the three zones.

Figure 5.1 illustrates the three-zone strategy for analyzing the perturbed flow. Linearization of the governing equations, (1.2.1) and (1.2.2), leads to the result:

$$\text{Re} \frac{\partial \underline{u}'}{\partial t} = - \text{Re} \nabla \cdot (\underline{u} \underline{u}' + \underline{u}' \underline{u}) + \nabla \cdot \underline{T}' \quad (5.2.4)$$

$$0 = \nabla \cdot \underline{u}' . \quad (5.2.5)$$

Here the stress tensor is $\underline{T}' = (\nabla \underline{u}' + \nabla \underline{u}'^T) - \nabla p'$ because the liquid is Newtonian and incompressible and $\text{Re} \equiv Ud/\nu$ is again Reynolds number, U is web speed, d is the upstream gap thickness as illustrated in Figure 4.1, and ν is the kinematic viscosity. In the forming zone the base

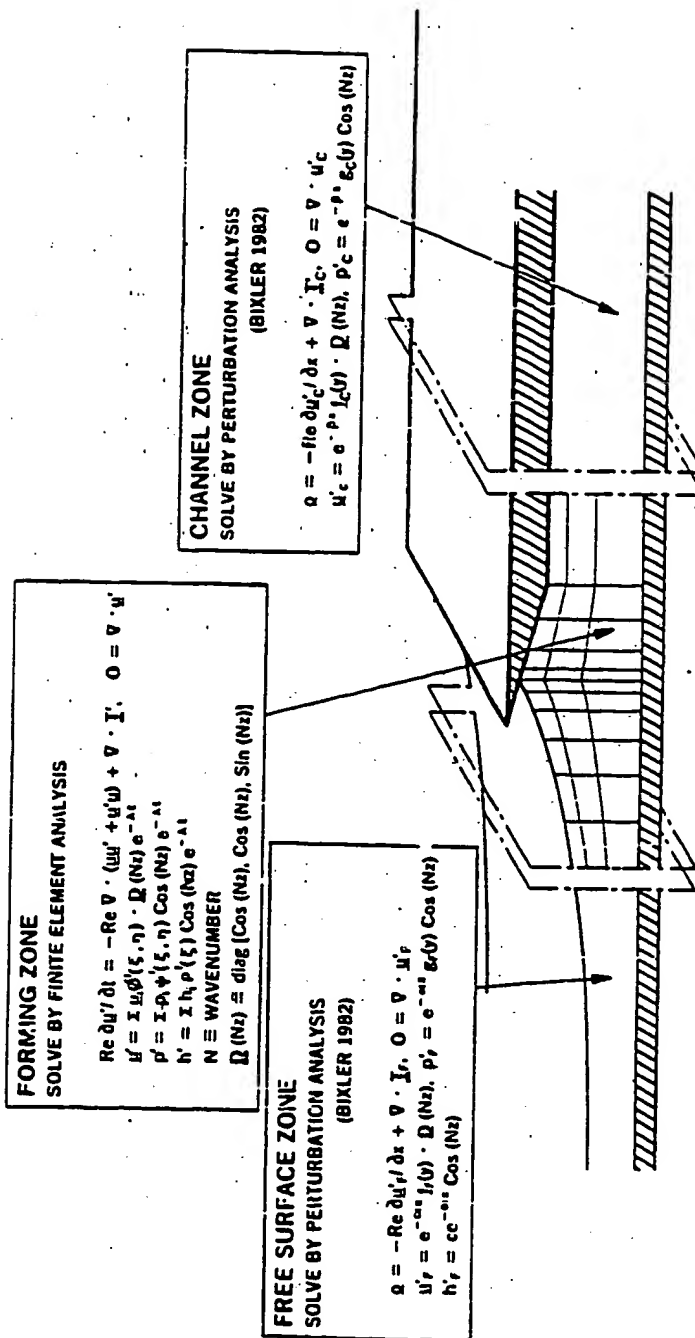


Figure 5.1. Strategy for solving the three-dimensional unsteady perturbed flow.

flow velocity, \underline{u} , is known as an expansion in finite element basis functions from the analysis of Chapter 4. In the asymptotic free surface and channel zones the base flow velocities are solid body translation and parabolic, respectively. The acceleration terms in these asymptotic zones have been set to zero as an approximation, as indicated in Figure 5.1. This approximation is justified in the vicinity of a neutral stability point when the neutrally stable disturbance does not oscillate temporarily. Asymptotic solutions were constructed by perturbation analysis for these two flow zones in Chapter 2. These solutions are used below to construct boundary conditions at the inflow and outflow boundaries of the forming zone.

To expand the velocity and pressure perturbations in three-dimensional finite element basis functions in the forming zone would be prohibitively expensive for reasonably fine meshes (e.g., a $3 \times 13 \times 5$ element mesh would involve about 6500 unknowns). Instead, the device of employing Fourier normal mode analysis in the transverse coordinate used previously in Chapter 2 is applied here as well, and this results in a tenfold decrease in the number of unknowns. Perturbations are represented by basis functions which are products of the same two-dimensional finite element basis functions that were used to approximate the base flow in Chapter 4 and Fourier basis functions. Furthermore, because the governing equations (and boundary conditions to appear below) are linear in the perturbation, time behavior is exponential. Therefore, a perturbation of single wavenumber has the following representation:

$$\underline{u}'(x,y,z,t) = \underline{u}_i' \phi^i(\xi,n) \cdot \underline{D}(Nz) e^{-\lambda t} \quad (5.2.6)$$

$$p'(x,y,z,t) = p_i' \psi^i(\xi,n) \cos(Nz) e^{-\lambda t} \quad (5.2.7)$$

$$h'(x,z,t) = h_i' \rho^i(\xi) \cos(Nz) e^{-\lambda t} , \quad (5.2.8)$$

where \underline{u}_i' , p_i' , and h_i' are coefficients which determine the form of the velocity, pressure, and free surface elevation perturbations, respectively; ϕ^i , ψ^i , and ρ^i are the same finite element basis functions defined in Chapter 4; the isoparametric coordinates (ξ,n) represent the spatial coordinates (\bar{x},\bar{y}) as defined by the isoparametric transformation:

$$[\bar{x}(\epsilon), \bar{y}(\epsilon)] = [(x_0, y_0) + \epsilon(x_0', y_0')]_i \phi^i(\xi,n) . \quad (5.2.9)$$

Here $[\bar{x}_0(\epsilon), \bar{y}_0(\epsilon)]_i$ are the perturbed coordinates of node i which must move with the free surface whenever node i lies beneath the free surface; N is the transverse wavenumber and is inversely proportional to the transverse wavelength, $2\pi/N$; $\underline{D}(Nz)$ is a specially constructed tensor which serves the same purpose as the vector $\underline{D}(Nz)$ defined in Equation (2.4.9),

$$\underline{D}(Nz) = \cos(Nz) (\underline{ii} + \underline{jj}) + \sin(Nz) \underline{kk} ; \quad (5.2.10)$$

and λ is the exponential decay rate. Summation over the repeated index i is implied. The exponential decay rate, λ , may be complex in the general case. The real part of λ , λ_R , is the temporal decay or growth rate; the imaginary part, λ_I , is the temporal oscillation rate. When λ is real the perturbation grows or decays in a purely exponential manner;

when it is complex the exponential behavior is modulated by temporal oscillation. The crucial characteristic of λ in stability analysis is whether its real part is larger than zero, in which case the flow is stable to the corresponding perturbation, less than zero, in which case the flow is unstable to the corresponding perturbation, or equal to zero, in which case the flow is neutrally stable to the corresponding perturbation, i.e. the perturbation neither grows nor decays in time.

Boundary conditions for perturbations in the forming zone are analogous to those for the steady base flow, as shown in Figure 5.2 (cf. Figure 4.3). At the inflow and outflow boundaries, velocity and stress are required to be continuous. At solid surfaces neither slip nor penetration is allowed, except near the contact line where slip must be admitted if the contact line can move. Huh and Scriven (1971) showed that no slip at a contact line is physically inconsistent with movement of that contact line. Silliman and Scriven (1978) showed that allowing some slip near a contact line, either by prescribing a slip coefficient or slip velocity profile, removes the stress singularity which would otherwise result. When a contact line can be perturbed, i.e. when it is not pinned at a geometric or compositional discontinuity, it is necessary to permit some slip. This is done here by prescribing a slip velocity profile that is convenient in the finite element formulation. Boundary conditions at the free surface are the following: (1) the kinematic boundary condition states the free surface must deform at a rate consistent with the arrival or departure of liquid there; (2) because the gas phase is considered inviscid as in Chapter 4, the shear stress boundary

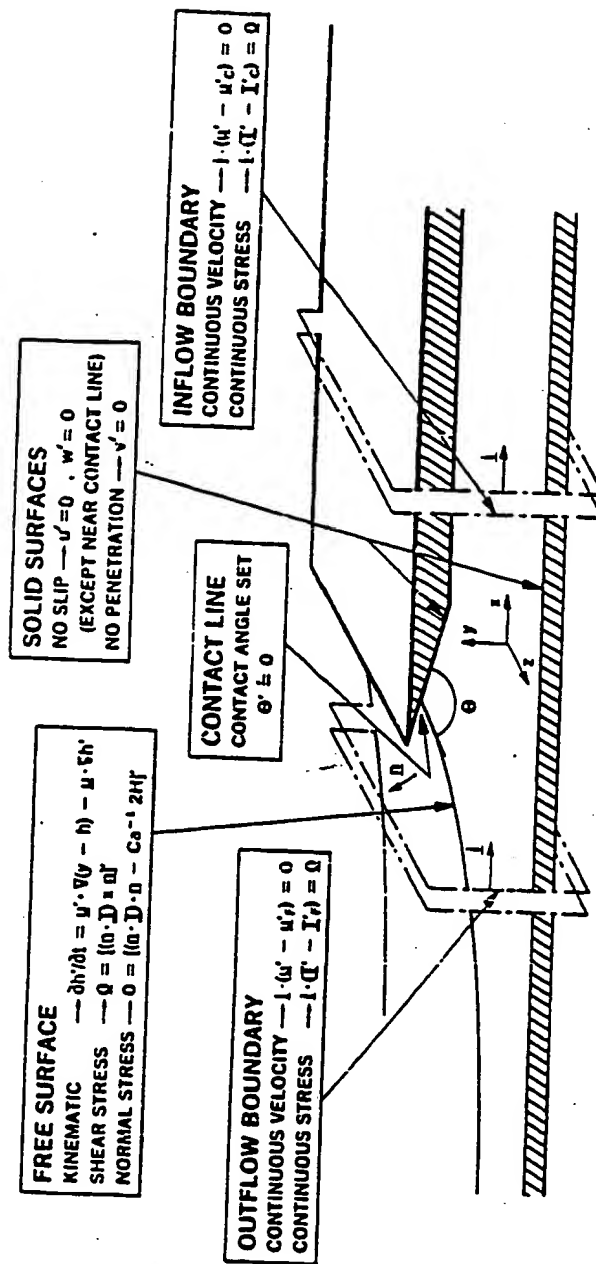


Figure 5.2. Forming zone boundary conditions for the three-dimensional unsteady perturbed flow.

condition states that a perturbation of velocity and free surface elevation must maintain zero shear at the interface; and (3) the normal stress boundary condition states that change in the normal viscous stress and pressure at the interface must be balanced by a change in the capillary force due to the mean curvature, H . Additional boundary conditions at the perimeter of the free surface are that the interface be continuous at the outflow boundary, both in elevation and slope, and that either the contact line or the contact angle not be disturbed. The boundary conditions at the contact line correspond respectively to cases where the contact line is pinned or free to slide along the solid boundary. The free contact line case is developed here; the pinned contact line case is identical except that the free surface elevation at the contact line is an essential boundary condition, and thus the contact line term in Equation (5.2.33) below can be omitted. Boundary conditions at the edge surfaces, i.e. planes of constant z , need not be written explicitly because the domain is chosen to be one wavelength, $2\pi/N$, in the transverse dimension so that periodicity conditions apply. The boundary terms at the two edge boundaries cancel each other as shown below. The set of boundary conditions described above is:

$$\underline{1} \cdot (\underline{u}' - \underline{u}_F') = 0 \quad (5.2.11)$$

$$\underline{1} \cdot (\underline{T}' - \underline{T}_F') = 0 \quad (5.2.12)$$

$$h' - h_F' = 0 \quad \text{Outflow boundary} \quad (5.2.13)$$

$$d(h' - h_F')/dx = 0 \quad (5.2.14)$$

$$\underline{i} \cdot (\underline{u}' - \underline{u}'_{CL}) = 0 \quad (5.2.15)$$

$$\underline{i} \cdot (\underline{T}' - \underline{T}'_{CL}) = 0 \quad \text{Inflow boundary} \quad (5.2.16)$$

$$\underline{u}' \times \underline{n} = 0 \quad (5.2.17)$$

$$\underline{u}' \cdot \underline{n} = 0 \quad \text{Solid surfaces} \quad (5.2.18)$$

$$\underline{u}' \times \underline{n} = -\underline{u}'_{CL} Q(\xi) \underline{k} \quad \text{Solid surfaces} \quad (5.2.19)$$

$$\underline{u}' \cdot \underline{n} = 0 \quad \text{near contact line} \quad (5.2.20)$$

$$\partial h' / \partial t = \underline{u}' \cdot \nabla (y-h) - \underline{u} \cdot \nabla h' \quad (5.2.21)$$

$$\underline{0} = [(\underline{n} \cdot \underline{T}) \times \underline{n}]' \quad \text{Free surface} \quad (5.2.22)$$

$$0 = [(\underline{n} \cdot \underline{T}) \cdot \underline{n}]' - C_a^{-1} 2H' \quad (5.2.23)$$

$$\theta' = 0 \quad \} \text{Contact line} \quad (5.2.24)$$

The unit normal \underline{n} at the boundary is illustrated in Figure 5.2. \underline{u}'_{CL} is the slip velocity at the contact line and $Q(\xi)$ is a quadratic function of the isoparametric coordinate ξ , as explained below. $Ca = \mu U / \sigma$ is again the capillary number, μ is dynamic viscosity, U is web speed, σ is surface tension, and H' is the change in the mean curvature due to a perturbation of the meniscus elevation, h' . This set of boundary conditions, Equations (5.2.11)–(5.2.24), applies generally to small perturbations to coating flows. However, the physics governing the immediate vicinity of a wetting line, i.e. the contact angle and the flow nearby, is not yet firmly established and thus Equations (5.2.19) and (5.2.24) may be modified or replaced as understanding increases.

The Galerkin weak forms of the unsteady governing equations were derived in Section 4.2. Galerkin's method requires that the basis functions which appear in Equations (5.2.6)-(5.2.8) be chosen as weighting functions, and thus the weighted residual equations for the perturbed flow field are:

$$\begin{aligned}
 & - \int_{\Omega} \text{Re} \frac{\partial \underline{u}(\epsilon)}{\partial t} \cdot [\phi^J(\epsilon, n) \underline{D}(Nz)] \frac{\partial [\overline{x}(\epsilon), \overline{y}(\epsilon)]}{\partial (\epsilon, n)} d\epsilon dn dz \\
 & = \int_{\Omega} \{ \text{Re } \nabla \cdot [\underline{u}(\epsilon) \underline{u}(\epsilon)] \cdot [\phi^J(\epsilon, n) \underline{D}(Nz)] \\
 & + \overline{T}(\epsilon) : \nabla [\phi^J(\epsilon, n) \underline{D}(Nz)] \frac{\partial [\overline{x}(\epsilon), \overline{y}(\epsilon)]}{\partial (\epsilon, n)} d\epsilon dn dz \\
 & - \int_{(\delta\Omega - \delta\Omega_{\text{EDGES}})} \underline{n}(\epsilon) \cdot \overline{T}(\epsilon) \cdot [\phi^J(\epsilon, n) \underline{D}(Nz)] \frac{\partial \overline{s}(\epsilon)}{\partial \gamma} d\gamma \frac{\partial \overline{\zeta}(\epsilon)}{\partial z} dz \\
 & - \int_{\delta\Omega_{\text{EDGES}}} \underline{n}(\epsilon) \cdot \overline{T}(\epsilon) \cdot [\phi^J(\epsilon, n) \underline{D}(Nz)] \frac{\partial [\overline{x}(\epsilon), \overline{y}(\epsilon)]}{\partial (\epsilon, n)} d\epsilon dn dz \quad (5.2.25)
 \end{aligned}$$

$$0 = \int_{\Omega} \nabla \cdot \underline{u}(\epsilon) \phi^J(\epsilon, n) \text{ c.c.} \frac{\partial [\overline{x}(\epsilon), \overline{y}(\epsilon)]}{\partial (\epsilon, n)} d\epsilon dn dz, \quad (5.2.26)$$

where Ω represents the three-dimensional domain, $\delta\Omega$ represents the boundary of Ω and has five distinct parts:

$$\delta\Omega = \delta\Omega_{\text{SS}} + \delta\Omega_{\text{FS}} + \delta\Omega_{\text{IN}} + \delta\Omega_{\text{OUT}} + \delta\Omega_{\text{EDGES}} \quad (5.2.27)$$

These respective parts are solid surfaces, free surface, inflow boundary, outflow boundary, and edge boundaries, i.e. planes of constant transverse coordinate z as illustrated in Figure 5.2; $\overline{s}(\epsilon)$ is the perturbed arc-length along the boundary at a plane of constant z ; $\overline{\zeta}(\epsilon)$ is the per-

turbed arc-length along the boundary at a plane of constant streamwise coordinate x ; and $\partial[\bar{x}(\epsilon), \bar{y}(\epsilon)]/\partial(\xi, \eta)$ is the Jacobian of the isoparametric map. As mentioned above, a convenient choice of domain width is $\Delta z = 2\pi/N$, one wavelength, because the boundary integral over the edge boundaries in Equation (5.2.25) drops out by cancellation of the terms at opposing edges.

The next step in the derivation is to linearize the governing equations, (5.2.25) and (5.2.26), in the parameter ϵ . This is a complicated step because the nodal parameters, \bar{u}_i , \bar{p}_i , and \bar{h}_i , and the nodal coordinates $(\bar{x}_0, \bar{y}_0)_i$ all depend on ϵ . The nodal coordinates do so because as the free surface deforms, the mesh lying beneath also deforms. This affects the acceleration term in Equation (5.2.21) because points of constant ξ and η are convected through space and therefore (cf. Kheshgi 1982)

$$\left. \frac{\partial u(\epsilon)}{\partial t} \right|_{\xi, \eta} = \left. \frac{\partial \bar{u}(\epsilon)}{\partial t} \right|_{x, y} + \frac{\partial \bar{h}_j(\epsilon)}{\partial t} \frac{\partial \bar{x}_{-0j}(\epsilon)}{\partial \bar{h}_j(\epsilon)} \cdot \frac{\partial \bar{x}(\epsilon)}{\partial \bar{x}_{-0k}(\epsilon)} \bigg|_{\xi, \eta} \cdot \nabla u(\epsilon). \quad (5.2.28)$$

The last term in this equation is evaluated as follows: (1) the first factor is the rate of change of the free surface elevation parameters; (2) the second factor, a vector, is the rate of change of the nodal coordinates with the free surface elevation parameters, which depends entirely on the mesh construction; (3) the third factor, a tensor, is the rate of change of global coordinates, (x, y) , with nodal coordinates at fixed isoparametric coordinates, (ξ, η) , as determined by Equation

(5.2.9); and (4) the last factor, a tensor, is the gradient of the velocity vector. Linearizing and solving for $\frac{\partial \underline{u}'}{\partial t} \Big|_{x,y}$ leads to

$$\frac{\partial \underline{u}'}{\partial t} \Big|_{x,y} = \frac{\partial \underline{u}'}{\partial t} \Big|_{\xi,n} + \lambda \cos(Nz) h_j^i \frac{\partial x'_{0k}}{\partial h_j^i} \cdot \frac{\partial x'}{\partial x'_{0k}} \Big|_{(\xi,n)} \cdot \nabla \underline{u} \quad (5.2.29)$$

The gradient terms in Equations (5.2.25) and (5.2.26) also depend on both nodal parameters and nodal coordinates. This is more easily seen from the equation for the gradient in terms of the isoparametric coordinates, viz.

$$\begin{aligned} \nabla &= \frac{\partial}{\partial x} \underline{i} + \frac{\partial}{\partial y} \underline{j} + \frac{\partial}{\partial z} \underline{k} \\ &= \left(\frac{\partial \xi}{\partial x} \frac{\partial}{\partial \xi} + \frac{\partial \eta}{\partial x} \frac{\partial}{\partial \eta} \right) \underline{i} + \left(\frac{\partial \xi}{\partial y} \frac{\partial}{\partial \xi} + \frac{\partial \eta}{\partial y} \frac{\partial}{\partial \eta} \right) \underline{j} + \frac{\partial}{\partial z} \underline{k} \\ &= \left(\frac{\partial [\bar{x}(\epsilon), \bar{y}(\epsilon)]}{\partial (\xi, \eta)} \right)^{-1} \left[\left(\frac{\partial \bar{y}(\epsilon)}{\partial \eta} \frac{\partial}{\partial \xi} - \frac{\partial \bar{y}(\epsilon)}{\partial \xi} \frac{\partial}{\partial \eta} \right) \underline{i} \right. \\ &\quad \left. + \left(-\frac{\partial \bar{x}(\epsilon)}{\partial \eta} \frac{\partial}{\partial \xi} + \frac{\partial \bar{x}(\epsilon)}{\partial \xi} \frac{\partial}{\partial \eta} \right) \underline{j} \right] + \frac{\partial}{\partial z} \underline{k} \end{aligned} \quad (5.2.30)$$

The last equality results from the inverse of the isoparametric map. Equation (5.2.9) is needed to evaluate the derivatives of global coordinates, $[\bar{x}(\epsilon), \bar{y}(\epsilon)]$, with respect to the isoparametric coordinates, (ξ, η) . The linearized form of (5.2.30) is fairly complicated, and fortunately need not be computed because the inverse Jacobian of the isoparametric map in (5.2.30) cancels the Jacobian in (5.2.25) and (5.2.26). The linearized form of the Jacobian times the gradient is (Saito and Scriven 1981):

$$\begin{aligned} \left(\frac{\partial [x(\xi), y(\xi)]}{\partial (\xi, \eta)} \right) \nabla = & \left(\frac{\partial y}{\partial \eta} \frac{\partial}{\partial \xi} - \frac{\partial y}{\partial \xi} \frac{\partial}{\partial \eta} \right) \underline{i} + \left(-\frac{\partial x}{\partial \eta} \frac{\partial}{\partial \xi} + \frac{\partial x}{\partial \xi} \frac{\partial}{\partial \eta} \right) \underline{j} + \frac{\partial}{\partial z} \underline{k} \\ & + c \left[\left(\frac{\partial y'}{\partial \eta} \frac{\partial}{\partial \xi} - \frac{\partial y'}{\partial \xi} \frac{\partial}{\partial \eta} \right) \underline{i} + \left(-\frac{\partial x'}{\partial \eta} \frac{\partial}{\partial \xi} + \frac{\partial x'}{\partial \xi} \frac{\partial}{\partial \eta} \right) \underline{j} \right]. \quad (5.2.31) \end{aligned}$$

Equations (5.2.25) and (5.2.26) can be linearized with the aid of Equations (5.2.29) and (5.2.31). The results are exemplified by the derivative of the j -th x -momentum equation with respect to the i -th x -velocity unknown, u_i' , when the element that contains u_i' borders on the free surface:

$$\begin{aligned} 0 = & -\operatorname{Re} \lambda \int_{\Omega} \phi^i \phi^j \cos^2(Nz) \left[\partial(x, y) / \partial(\xi, \eta) \right] d\xi d\eta dz \\ & + \int_{\Omega} \left[\operatorname{Re} \left[\phi^i \partial u / \partial x + u \partial \phi^i / \partial x + v \partial \phi^i / \partial y \right] \phi^j \right. \\ & + \left[(2 \partial \phi^i / \partial x) (\partial \phi^j / \partial x) + (\partial \phi^i / \partial y) (\partial \phi^j / \partial y) \right. \\ & \left. \left. - N^2 \phi^i \phi^j \right] \right] \cos^2(Nz) \left[\partial(x, y) / \partial(\xi, \eta) \right] d\xi d\eta dz \\ & - \int_{\partial \Omega_{FS}} \left[\underline{n} \cdot \left[2 \underline{i} \partial \phi^i / \partial x + \underline{j} \partial \phi^i / \partial y \right] \cos^2(Nz) (\partial s / \partial \xi) \right] d\xi dz \quad (5.2.32) \end{aligned}$$

The boundary conditions are administered in the same way as in Chapter 4. The adherence boundary conditions in (5.2.17)-(5.2.20) take the place of the momentum equations (5.2.21) weighted by basis functions associated with boundary nodes, and thus the surface integral over $\partial \Omega_{SS}$ need not be evaluated because each trial function associated with all other than solid boundary nodes is identically zero at the solid boundaries. Equations (5.2.17) and (5.2.18) are used everywhere along the solid surfaces except in the element adjoining the contact line, where

(5.2.19) and (5.2.20) are prescribed and $Q(\xi)$ is chosen so that it is unity at the contact line and it and its first derivative disappear at the upstream edge of the element. The shear stress boundary condition, Equation (5.2.22), is imposed as a natural boundary condition in Equation (5.2.25) by setting

$$\underline{\underline{n}} \cdot \underline{\underline{T}} = \underline{\underline{n}} \underline{\underline{n}} \underline{\underline{n}} : \underline{\underline{T}} \quad (5.2.33)$$

in the free surface boundary integral. The y component of each momentum residual, \underline{j} dotted into (5.2.25), is replaced at free surface nodes by the kinematic equation, (5.2.21). The linearized normal stress equation is enforced along the free surface:

$$\begin{aligned} 0 = & \int_{\delta\Omega_{FS}} \{ [2\underline{\underline{n}}' \underline{\underline{n}} : \underline{\underline{T}} + \underline{\underline{n}} \underline{\underline{n}} : \underline{\underline{T}}'] \cos(Nz) \rho^f(\xi) + Ca^{-1} \underline{\underline{n}}' \cdot \nabla [\cos(Nz) \rho^f(\xi)] \} \frac{\partial x}{\partial \xi} d\xi dz \\ & + \int_{\delta\Omega_{FS}} \{ \underline{\underline{n}} \underline{\underline{n}} : \underline{\underline{T}} \cos(Nz) \rho^f(\xi) + Ca^{-1} \underline{\underline{n}} \cdot \nabla [\cos(Nz) \rho^f(\xi)] \} \frac{\partial x'}{\partial \xi} d\xi dz \\ & - Ca^{-1} \oint_{\delta\delta\Omega_{FS}} [\underline{\underline{n}}' \cdot \underline{\underline{m}} \cos(Nz) \rho^f(\xi)] ds, \end{aligned} \quad (5.2.34)$$

The last term is the line integral around the perimeter of the free surface boundary and \underline{m} is the outward pointing normal to the base plane, i.e. xz -plane. The line integrals along the two edges of constant transverse coordinate z cancel each other and thus the last term simplifies to

$$- Ca^{-1} \oint_{\delta\delta\Omega_{FS}} [\underline{\underline{n}}' \cdot \underline{\underline{m}} \cos(Nz) \rho^f(\xi)] ds = - Ca^{-1} \oint_{\delta\delta\Omega_{FS}} [\underline{\underline{n}}' \cdot \underline{\underline{t}} \cos(Nz) \rho^f(\xi)]_{OUT}^{CL} dz$$

where CL and OUT refer to the contact line and outflow boundary, respectively; the normal to the free surface is

$$\bar{n} \equiv n + \epsilon n' + \dots$$

$$\equiv \frac{-i h_x + j}{\sqrt{1 + h_x^2}} + \epsilon \frac{-h'_x(-i h_x + j) \cos(Nz) + N(1 + h_x^2) h' \sin(Nz) k}{(1 - h_x^2)^{3/2}} \quad (5.2.36)$$

Boundary conditions (5.2.13) and (5.2.14) combine to form a Robin condition at the outflow boundary:

$$n' \cdot j^{OUT} = -\alpha(N) h' / [1 + \alpha^2(0)(h - h_w)^2]^{3/2} \quad (5.2.37)$$

Here $\alpha(0)$ and $\alpha(N)$ are the slowest decay rates for perturbations in the asymptotic free surface zone when wavenumber is 0 and N , respectively, as calculated in Chapter 2. Equation (5.2.38) is substituted in Equation (5.2.35). Equation (5.2.24) with the aid of the trigonometric relationship

$$\bar{\theta} = 180^\circ - \tan^{-1} \bar{h}_x - \tan^{-1} h_x^S \quad (5.2.38)$$

is also imposed as a natural boundary condition in Equation (5.2.35). Here h^S is the elevation of the solid die above the web. Boundary conditions (5.2.15) and (5.2.16) combine to give a Robin condition at the inflow boundary and (5.2.11) and (5.2.12) combine to give a Robin condition at the outflow boundary. These are imposed as natural boundary conditions in the linearized form of (5.2.25):

$$\begin{aligned} \int_{\partial\Omega_{IN}} \underline{1} \cdot \underline{T}' \cdot \underline{D}(Nz) \phi^1(\xi, \eta) \frac{dy}{d\eta} d\eta dz \\ = \int_{\partial\Omega_{IN}} \underline{B} \cdot \underline{u}' \cdot \underline{D}(Nz) \phi^1(\xi, \eta) \frac{dy}{d\eta} d\eta dz \quad (5.2.39) \end{aligned}$$

$$\begin{aligned}
 & - \int_{\delta\Omega_{OUT}} \underline{i} \cdot \underline{T}' \cdot \underline{D}(Nz) \phi^1(\xi, \eta) \frac{dy}{dn} dndz \\
 & = \int_{\delta\Omega_{OUT}} \underline{A} \cdot \underline{u}' \cdot \underline{D}(Nz) \phi^1(\xi, \eta) \frac{dy}{dn} dndz, \quad (5.2.40)
 \end{aligned}$$

$$\begin{aligned}
 \underline{B} \equiv & \left\{ \left[\left(1(2) \frac{\partial u'}{\partial x} - p' \right) / u' + j \frac{\partial u'}{\partial y} / u' + k \frac{\partial u'}{\partial z} / u' \right] \underline{i} \right. \\
 & \left. + j \left[\frac{\partial v'}{\partial x} / v' + k \frac{\partial w'}{\partial x} / w' \right] \underline{j} \right\}_C \quad (5.2.41)
 \end{aligned}$$

$$\begin{aligned}
 \underline{A} \equiv & \left\{ \left[\left(1(2) \frac{\partial u'}{\partial x} - p' \right) / u' + j \frac{\partial u'}{\partial y} / u' + k \frac{\partial u'}{\partial z} / u' \right] \underline{i} \right. \\
 & \left. + j \left[\frac{\partial v'}{\partial x} / v' + k \frac{\partial w'}{\partial x} / w' \right] \underline{j} \right\}_F \quad (5.2.42)
 \end{aligned}$$

Subscripts C and F indicate that the quantities inside the brackets pertain respectively to the upstream channel and downstream free surface zones. Chapter 4 demonstrates that a Robin condition is better than Neumann or Dirichlet conditions at an open-flow boundary (especially at an outflow boundary) for the two-dimensional flows considered there. The Robin conditions in Equations (5.2.39)–(5.2.42) are three-dimensional analogues of the one in Equations (4.2.19) and (4.2.22), and so they extend from two-dimensional flows to three-dimensional ones the idea of matching asymptotic zones to forming zone.

The final step in the derivation of the equations governing a perturbation to a steady two-dimensional flow is to integrate over the transverse coordinate, z . This turns out to be trivial because every term in the governing equations, (5.2.25) and (5.2.26), and in the normal stress equation, (5.2.34), is weighted by either $\cos^2(Nz)$ or $\sin^2(Nz)$ (cf. Equation (5.2.32)) and these both integrate to the same constant.

The final form of the resulting equation set is an asymmetric generalized eigenproblem,

$$J_{ki} q_i = \lambda M_{ki} q_i \quad (5.2.43)$$

as exemplified by Equation (5.2.32) and illustrated by Figure 5.3. The symbols in Figure 5.3 are defined as follows:

R_i^{Mx} \equiv Right side of i -th x -momentum equation, \underline{i} • (5.2.25)

R_i^{My} \equiv Right side of i -th y -momentum equation, \underline{j} • (5.2.25)

R_i^{Mz} \equiv Right side of i -th z -momentum equation, \underline{k} • (5.2.25)

R_i^K \equiv Right side of the i -th kinematic equation, (5.2.21)

R_i^C \equiv i -th continuity equation, (5.2.26)

R_i^{NS} \equiv i -th normal stress boundary condition, (5.2.32)

M_{ij}^I \equiv ij -th element of inertial mass matrix, i.e. the derivative of the i -th left side of the x -momentum equation, \underline{i} • (5.2.25), with respect to u_j^i

M_{ij}^{Cx} \equiv ij -th element of x -convective mass matrix, i.e. the derivative of the i -th left side of the x -momentum equation, \underline{i} • (5.2.25), with respect to h_j^i

M_{ij}^{Cy} \equiv ij -th element of y -convective mass matrix, i.e. the derivative of the i -th left side of the y -momentum equation, \underline{j} • (5.2.25), with respect to h_j^i

M_{ij}^K \equiv ij -th element of kinematic mass matrix, i.e. the derivative of the i -th left side of the kinematic equation, (5.2.21), with respect to h_j^i

The adherence boundary conditions, (5.2.17) and (5.2.18), result in the

[illegible]

Figure 5.3. Entries in the generalized asymmetric eigenproblem of Equation (5.2.43).

Kronecker delta entries in Figure 5.3. The eigenvector in Equation (5.2.43), the i -th element of which is denoted by q_i , represents the velocity, pressure, and free surface unknowns, i.e.

$$[q_i] \equiv [u_1, \dots, u_n, v_1, \dots, v_n, w_1, \dots, w_n, p_1, \dots, p_m, h_1, \dots, h_l]^T.$$

Here n is the number of velocity nodes, m is the number of pressure nodes, and l the number of free surface elevation unknowns. Each eigen-solution is a possible perturbation mode and its decay rate. A base flow is therefore stable if each possible mode has a positive decay rate at every value of wavenumber, N . Means to solve this problem are the topic of Section 5.3.

Ruschak (1980) and more recently Kistler and Scriven (1982) have described an alternative method for introducing the boundary conditions at the free surface. They suggest that both normal and shear stress conditions should be used as natural boundary conditions for the weak form of the momentum equations. In their formulation, the free surface boundary integral in Equation (5.2.25) would be replaced by

$$\begin{aligned} & \int_{\partial\Omega_{FS}} \bar{n} \cdot \bar{T} \cdot \underline{D}(Nz) \phi^i(\xi, n) \frac{\partial \bar{S}}{\partial \xi} d\xi \frac{d\bar{C}}{dz} dz \\ &= Ca^{-1} \int_{\partial\Omega_{FS}} 2H \bar{n} \cdot \underline{D} \cos(Nz) \phi^i(\xi, n) \frac{\partial \bar{S}}{\partial \xi} d\xi \frac{\partial \bar{C}}{\partial z} dz. \end{aligned} \quad (5.2.44)$$

The surface divergence theorem (Weatherburn 1927) can be applied to the right side to get:

$$\begin{aligned}
& \int_{\delta\Omega_{FS}} 2H \bar{\underline{n}} \cdot \underline{D} \cos(Nz) \phi^i(\xi, n) \frac{\partial \bar{S}}{\partial \xi} d\xi \frac{\partial \bar{C}}{\partial z} dz \\
& = - \int_{\delta\Omega_{FS}} \bar{\underline{\nabla}}_s \cdot [\underline{D}(Nz) \phi^i(\xi, n) \frac{\partial \bar{S}}{\partial \xi} d\xi \frac{\partial \bar{C}}{\partial z} dz \\
& + \oint_{\delta\Omega_{FS}} \bar{\underline{m}} \cdot \underline{D}(Nz) \phi^i(\xi, n) ds .
\end{aligned} \tag{5.2.45}$$

Here $\bar{\underline{\nabla}}_s$ is the perturbed surface gradient and $\bar{\underline{m}}$ is the perturbed outward pointing tangent on the perimeter of the free surface. Evaluation of the last term in this equation is analogous to evaluation of the perimeter integral of the normal stress condition in (5.2.35). The surface divergence term is evaluated by using the definition of the surface divergence (Weatherburn 1927).

5.3. Methods of Eigenanalysis for the Stability Problem

The features of the eigenproblem defined in the previous section are the following: (1) the matrices are large in size, about 650 by 650 for the mesh used in Chapter 6, but are sparse and banded; (2) both the Jacobian and mass matrices are asymmetric; (3) the mass matrix is singular because continuity, solid wall velocity, and normal stress constraints on the perturbation contain no time derivatives (see Figure 5.3). These features are crucial to the choice of an algorithm to solve the eigenproblem. The first feature rules out as too costly any algorithm which computes the eigenvalues or requires full matrix storage. The second precludes most of the available algorithms because they cannot handle the asymmetric eigenproblem. The third feature, that the mass matrix is singular, eliminates the possibility of inverting that matrix. Thus it

is not possible to reduce the generalized eigenproblem to a simple eigenproblem of the form:

$$M_{kj}^{-1} J_{ji} q_i = \lambda q_k .$$

Because of the above restrictions there are only a few viable methods to perform the eigenanalysis. Three possibilities are worthy of consideration: (1) Newton's method; (2) inverse iteration; and (3) inverse subspace iteration. The pros and cons of these methods are described in the following paragraphs.

Newton's method is the method of choice for solving the nonlinear problem of Chapter 4, i.e. solving the two-dimensional steady baseflow, and therefore it would seem to be a worthy candidate here as well. To apply Newton's method, Equation (5.2.41) is rewritten as a set of residual equations:

$$R_j = (J_{j1} - \lambda M_{j1}) q_1, \quad j = 1, \dots, L, \quad (5.3.1)$$

where L is the number of degrees of freedom in the basis set. An additional constraint is needed to normalize the components of the eigenvector, q_1 . A convenient choice is:

$$R_{L+1} = \frac{1}{2} (1 - q_1 q_1) \quad (5.3.2)$$

Applied to Equations (5.3.1) and (5.3.2), Newton's method gives the following iteration formula:

$$\left[\begin{array}{c|c} J_{j1} - \lambda^{(k)} M_{j1} & -M_{j1} q_1^{(k)} \\ \hline -q_1^{(k)} & 0 \end{array} \right] \begin{bmatrix} q_1^{(k+1)} - q_1^{(k)} \\ \lambda^{(k+1)} - \lambda^{(k)} \end{bmatrix} = \begin{bmatrix} R_j^{(k)} \\ R_{L+1}^{(k)} \end{bmatrix},$$

$$k = 1, 2, \dots, \quad (5.3.3)$$

where k is the iteration count and $q_1^{(0)}$ and $\lambda^{(0)}$ is an initial guess. Newton's method has the advantage of quadratic convergence of the update vector, $(\delta q_1^{(k)}, \delta \lambda^{(k)})$, to zero with iteration count k . However, the drawbacks to using Newton's method to perform the eigenanalysis are many and serious: (1) the linear system of equations in (5.3.3) would have to be solved several times to find each eigenpair; (2) complex arithmetic would have to be used extensively if a complex eigenpair were sought, and this would double the memory requirement for Jacobian and eigenvectors and thereby increase computation costs significantly; and (3) the eigenpair found at convergence of Newton's method would depend strongly on the initial guess. The last point is the most severe drawback because the goal of the analysis is to find the most dangerous modes, i.e. the ones which decay most slowly or grow most rapidly in time. With Newton's method there is no assurance that the eigenpair found is the most dangerous unless a very good initial guess is known.

The second candidate, inverse iteration, is simpler to implement than Newton's method. At each stage of the iteration the linear set of equations defined by

$$J_{j1} \bar{q}_1^{(k+1)} = M_{j1} \bar{q}_1^{(k)}, \quad k = 1, 2, \dots, \quad (5.3.4)$$

where $q_i^{(1)}$ is again an initial guess and $\bar{q}_i^{(k+1)}$ is the $(k+1)$ -th iterate prior to normalization, i.e.

$$q_i^{(k+1)} = \bar{q}_i^{(k+1)} / \| \bar{q}_i^{(k+1)} \| \quad (5.3.5)$$

where $\| \cdot \|$ is a convenient norm. The corresponding eigenvalue is given by

$$\lambda_i^{(k+1)} = \| \bar{q}_i^{(k+1)} \|^{-1} \quad (5.3.6)$$

This algorithm has been shown to converge linearly to the eigenpair which has smallest absolute value, provided one exists (Stewart 1973). The chief advantage of inverse iteration over Newton's method is that inverse iteration is more likely to converge to the dominant mode, but on the other hand it may converge slowly or not at all depending on the spectrum of the problem, i.e. the distribution of eigenvalues (see Appendix A for further discussion). An additional advantage of inverse iteration (also inverse subspace iteration) over Newton's method is that Hood's method (1976), which is used to solve the base flow equations as described in Chapter 4, can be used to solve (5.3.4).

The third candidate, simultaneous inverse iteration, is like simple inverse iteration except that several eigenvectors are tracked simultaneously. Algorithms to perform simultaneous inverse iteration are of necessity more complicated than algorithms for simple inverse iteration, but they offer improvements. Some of these are: (1) the convergence rate can be markedly increased (see Appendix A for details); (2) complex

eigenpairs can be found easily without need for explicit complex arithmetic; (3) dominant modes can be found simultaneously instead of sequentially as in the simple inverse iteration scheme. The algorithm of Stewart (1976, 1978) is the most elegant of the alternative simultaneous inverse iteration algorithms for asymmetric matrices (see Bauer 1957, Clint and Jennings 1971, and Dong 1977). Appendix A discusses at length Stewart's algorithm and its implementation.

Inverse subspace iteration may not always find the most dangerous modes, however. It finds the smallest set of eigenvalues in absolute value, i.e. the ones for which $|\lambda| = \sqrt{\lambda_R^2 + \lambda_I^2}$ is the smallest. But the most dangerous modes are the ones for which λ_R is least, i.e. λ_R is most negative. At some safe parameter values the flow should be stable and thus each λ_R should be greater than zero. When marginal stability is approached, for example by increasing capillary number (see Chapter 6), one or more of the λ_R becomes nearly zero. If λ_R passes through zero and becomes negative, then the solution bifurcates and loses stability. If the eigenvalue passing through zero is real, i.e. $\lambda_I = 0$, then inverse subspace iteration cannot miss the bifurcation point because $|\lambda| = 0$ there. But, the bifurcation point would be missed if λ_I were large in comparison with the magnitudes of other eigenvalues, i.e. if the dominant mode had a high temporal frequency. Computation of the onset of high frequency modes of instability requires a special trick from the methods of conformal mapping. The bilinear transformation is known to transform generalized circles in one complex plane into generalized circles in another complex plane (Churchill et al. 1974). By choosing

the parameters of the mapping appropriately, a line can be transformed into a circle, and the half-plane to the left of the line into the interior of the circle, as illustrated in Figure 5.4. A bilinear transformation that does this is

$$\mu = \frac{\lambda}{2d - \lambda} \quad , \quad (5.3.7)$$

where d is the x -intercept of the vertical line shown in Figure 5.4.

The inverse transformation, also bilinear, is

$$\lambda = \frac{2d\mu}{1 + \mu} \quad . \quad (5.3.8)$$

Replacing the eigenvalue λ in Equation (5.2.40) by (5.3.8) and rearranging gives

$$J_{j1}q_1 = \mu(2d M_{j1} - J_{j1})q_1 \quad , \quad (5.3.9)$$

which is another generalized eigenproblem, but with μ as eigenvalue. By choosing d carefully, the most dangerous modes can be found by solving (5.3.9). However, the choice of d is crucial; it must be so chosen that the number of eigenvalues in the half-plane to the left of d is exactly the same number as those sought in the eigenanalysis. If more are present, the ones found by the eigenanalysis would not necessarily be the most dangerous; if fewer are present, inverse subspace iteration would not be likely to converge. Convergence would be lost because of the structure of the spectrum in the μ -plane. The distance of each eigenvalue from the origin in the μ -plane is found from Equation (5.3.7) to be

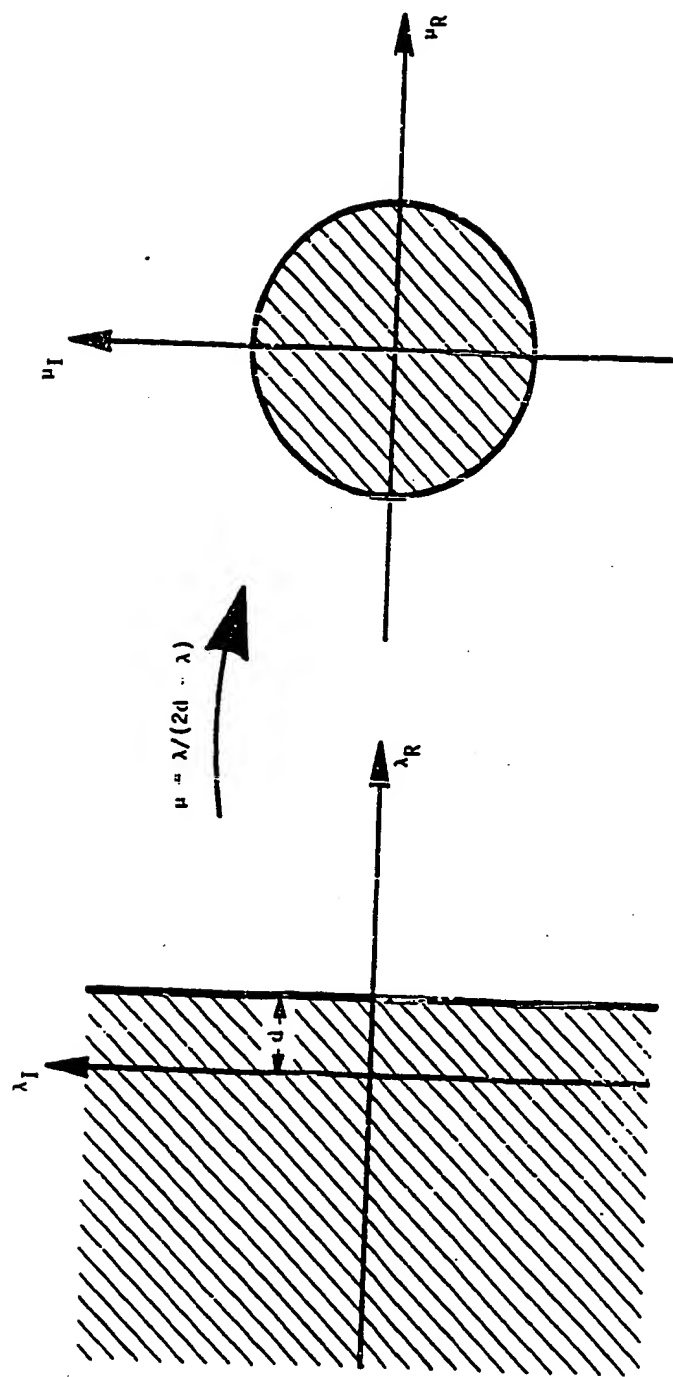


Figure 5.4. Bilinear map to capture high frequency modes.

$$|\mu| = |\lambda| / \sqrt{(\lambda_R - 2d)^2 + \lambda_I^2} . \quad (5.3.10)$$

Eigenvalues at infinity in the λ -plane are mapped into ones which are at a distance of unity from the origin in the μ -plane. Unfortunately, many such eigenvalues exist, one for each continuity, adherence, and normal stress constraint on the perturbation. As explained in Appendix A, inverse subspace iteration does not converge when the dominant subspace is not uniquely determined. Furthermore, even if d were chosen properly, inverse subspace iteration might converge more slowly for the mapped eigenproblem in (5.3.9) than for the original eigenproblem in (5.2.43) because large eigenvalues in the λ -plane would lie near the unit circle in the μ -plane, as seen from Equation (5.3.10). (The effect of the spectrum on the convergence rate of inverse subspace iteration is quantified in Appendix A.) The bilinear mapping, then, should be used only with caution and when temporally oscillatory modes of instability are sought.

Because inverse subspace iteration is an iterative technique for solving a nonlinear problem, an initial guess is needed. The best way to choose an initial guess is to use information from nearby solutions, provided one or more are available. If the dominant subspace has been calculated at an old set of parameters, that subspace can be chosen as an initial guess of the dominant subspace at new parameter values, a technique known as zeroth-order continuation. A better initial guess can be constructed by using first-order continuation, in which the rate of change of the dominant subspace with respect to the parameter or

parameters to be changed is calculated at the old point and used to construct an extrapolation in Euler-like fashion to a new point. However, first-order continuation is more difficult and more costly to implement than zeroth-order continuation, and is therefore preferred only when the savings gained in the iteration process because of improvement of the initial guess outweighs the additional cost needed to construct the initial guess. In the case of the generalized asymmetric eigenproblem, the advantage of first-order continuation is doubtful. For example, to calculate the rate of change of one eigenvector to a parameter, say s , the derivative of Equation (5.2.41) with respect to s is calculated:

$$(\partial J_{j1}/\partial s - 2\lambda/2s M_{j1})q_1 + (J_{j1} - \lambda M_{j1})\partial q_1/\partial s = 0. \quad (5.3.11)$$

The derivative of the Jacobian matrix with respect to the parameter, $\partial J_{j1}/\partial s$, has to be calculated and the Equation (5.3.11) used to find $\partial q_1/\partial s$ and $\partial \lambda/\partial s$. If the eigenproblem were symmetric, $\partial \lambda/\partial s$ could be found first by taking the inner product of Equation (5.3.11) with the eigenvector and taking advantage of the fact that

$$(J_{j1} - \lambda M_{j1}) (\partial q_1/\partial s)q_j = (J_{j1} - \lambda M_{j1})q_1 (\partial q_j/\partial s) = 0, \quad (5.3.12)$$

so that

$$\partial \lambda/\partial s = (\partial J_{j1}/\partial s)q_1 q_j / M_{j1} q_1 q_j. \quad (5.3.13)$$

When the eigenproblem is asymmetric this simplification could be made only if the adjoint eigenvector were found, an uneconomical option. The other possibility is to solve (5.3.11) plus an additional constraint, say

$$q_1(\partial q_1/\partial s) = 0 \quad , \quad (5.3.14)$$

simultaneously for $\partial q_1/\partial s$ and $\partial \lambda/\partial s$. This also would be difficult because the system of equations to be solved would not be banded and therefore subroutine FRONT (Hood 1976) could not be used to find $\partial q_1/\partial s$ and $\partial \lambda/\partial s$. Zeroth-order continuation is therefore preferred to generate an initial guess, or when several steps in the same parameter are taken, a secant extrapolation could be used.

5.4. Discussion

A general method for finding the stability of a steady, two-dimensional, viscous free surface flow has been described. Furthermore, the dominant eigenvectors represent the most dangerous disturbance modes, and thus both the onset and mode of instability can be predicted. Although the derivation of the stability equations has been aimed toward coating flows in particular, the methods and strategies have obvious generalizations to practically any steady two-dimensional viscous flow, with or without a free surface. Allowable perturbations are two-dimensional ($N=0$) or three-dimensional, the basic restriction being that they must be representable in basis functions which are products of finite element and Fourier bases. The methods for solving the resulting eigenproblem are general in the sense that any mode of disturbance, even if it is time oscillatory, can be tracked.

Ruschak (1982) has recently developed an approximate method that should be useful for creeping flows, i.e. for flows when Reynolds number

is sufficiently small, or for predicting the onset of instability to disturbances that do not oscillate in time. He assumes that acceleration is negligible in the momentum equations, i.e. he makes the quasi-steady assumption, an assumption that is entirely justified only when Reynolds number is sufficiently small. This assumption allows him to eliminate each of the velocity and pressure unknowns from the eigenproblem, and thus to "statically condense" the original eigenproblem to a much smaller one. The small eigenproblem can then be solved efficiently by the QZ algorithm (Holer and Stewart 1973), for which IMSL and EISPACK subroutines are available. Ruschak's approximation is quite attractive for low Reynolds number flows, but it is not reliable at even moderate Reynolds number, in contrast to the one used here.

Brown (1982) has investigated the loss of stability of stagnant liquid between two discs heated from below, a Rayleigh-Jeffreys problem (sometimes mistakenly called a Bénard problem) by finite element analysis. He considered only axisymmetric disturbances, however, and thus needed no more than a two-dimensional representation. It is well known that the stagnant liquid layer goes unstable to disturbance modes in which convective cells form as adverse temperature gradient is increased (Chandrasekhar 1961). Furthermore, Chandrasekhar (1961) proved that the convective cells at onset are steady rather than time periodic because the decay or growth rate of each disturbance mode is real, i.e. the eigenvalues are all real. Finite element stability analysis of the Rayleigh-Jeffreys problem leads to an eigenproblem of the same form as (5.2.43). Because the Jacobian matrix in this eigenproblem has only

real eigenvalues, Brown is able to detect the onset of an instability by examining the sign of the determinant of his Jacobian matrix. By doing so he avoids the unpleasant task of solving the eigenproblem. However, his method could fail if applied to problems for which the eigenvalues are not known a priori to be real. Furthermore, Brown's method might have difficulty in resolving closely spaced eigenvalues as they cross the imaginary axis.

It is unlikely that the ultimate methods for computer-based stability analysis have yet been found. The work presented here is the first of its kind, although it is paralleled by those of Ruschak and Brown. Furthermore, good computational strategies for handling asymmetric eigenproblems have only recently been devised, and even these are still in their infancy. Giant steps in improvement of numerical and analytic techniques are almost certain to be made in the future, and will enable coating flow stability analysis to be done with much more ease and simplicity than at present.

CHAPTER 6 — STABILITY OF SLOT AND KNIFE COATING

6.1. Introduction

The methods described in Chapter 5 were designed to analyze the stability of steady, two-dimensional, viscocapillary flows, and furthermore to understand the most dangerous disturbance modes, i.e. the patterns of flow that decay most slowly or grow most rapidly. In this chapter, the power of these methods is illustrated by analyzing the stability of slot and knife coating.

Steady two-dimensional slot and knife coating flows were treated in Chapter 4 by the Galerkin/finite element method. As discussed in Chapters 1 and 3, it is well-known that these flows can be unstable to three-dimensional disturbances that are transversely periodic, an instability that is commonly known as ribbing. The parameters that determine the stability of the base flow are capillary number, $Ca \equiv \mu U/\sigma$; Reynolds number, $Re \equiv Ud/\nu$; dimensionless flow rate, $Q \equiv h_0/d$; die shape as determined by the exponential factor $1/8$ defined in Section 4.2; and contact line physics, i.e. whether the contact line is pinned at a geometric or compositional discontinuity or free to move along the die with some prescribed contact angle θ . The operating parameters and liquid properties are as follow: μ is the dynamic viscosity of the liquid; U is the web speed; σ is the surface tension of the liquid/gas interface; h_0 is the final uniform film thickness; and d is the upstream gap width between the stationary die and moving web. The effect of gravity is considered to be negligible in comparison with the effects of viscous stress.

Particulars of the method of stability analysis are described in

Section 6.2. The influence of liquid and operating parameters on the stability of knife coating is investigated in Section 6.3. In Section 6.4 the results are summarized and compared with the approximate results based on lubrication theory which were described in Chapter 3.

6.2. Stability Analysis

This section describes the particulars of applying the methods of Chapter 5 to the stability of steady two-dimensional slot and knife coating flows similar to those investigated in Chapter 4. Attention is concentrated on the issues which were not considered in Chapter 5, namely the subdivision of the domain into elements, startup and continuation strategy, and approximate computation costs.

The domain is tessellated into elements in exactly the same way as in Chapter 4, i.e. by erecting spines orthogonal to the moving web along which nodes are placed according to preassigned weighting factors. The node locations define element shapes through the isoparametric mapping set out in Equation (4.2.4) and illustrated in Figure 4.3. Thus, nodes lying on or beneath the free surface adjust in proportion to the local free surface elevation. Furthermore, the node at the three-phase contact line is free to move along the solid die when the contact line is not pinned. Thereby, the spine which intersects the contact line is required to move upstream or downstream with the contact line. The two spines immediately upstream and downstream of the contact line are required to maintain a position midway between their nearest neighbors. Because only small amplitude disturbances are considered, the contact line moves only infinitesimally so that no overtaking of spines by other

spines is possible. If spines were allowed to cross, elements which have negative areas would be created!

Eigenanalysis was started up by generating a random guess to the dominant subspace, and then using Stewart's inverse subspace iteration algorithm (described in Appendix A) until the maximum error in the eigenproblem residuals was less than 10^{-8} . Once an eigensolution of the startup case was generated, zeroth-order continuation was used (as described in Chapter 5) to track the dominant subspace as a parameter was varied. First, a point of neutral stability, i.e. a point at which the dominant decay rate was zero, was sought by using secant extrapolation to vary capillary number, all other parameters being fixed. Then the parameters were varied one-by-one to explore their effect on stability. Whenever a new set of parameters was investigated, the following procedure was used: (1) a base flow was calculated; (2) the Jacobian and mass matrices were computed for a specified wavenumber and Hood's (1976) subroutine FRONT was used to execute the forward elimination part of Gaussian elimination; (3) Stewart's algorithm in conjunction with Hood's (1976) subroutine RESOL was used to find the dominant subspace for the given wavenumber; and (4) steps (2) and (3) were repeated for several different wavenumbers. Usually, the dominant subspace was calculated for five wavenumbers so that growth rate curves could be fared in by eye (with a French curve).

The cost of calculating one stability point, i.e. finding the dominant subspace at a given set of parameters, ranged from about one to more than ten times the cost of a base flow calculation, i.e. from about

55 to 1000 cpu seconds on the University of Minnesota Cyber 730 (equivalent to 35 to 600 seconds on the University of Minnesota Cyber 74). The cost was relatively small whenever the ratio of the magnitude of the second eigenvalue to the magnitude of the first eigenvalue was of order 10 or larger; it was relatively large when the same ratio was of order unity, and especially at start-up when no previously calculated dominant subspace was available for continuation. To cut down on computation costs, it was therefore necessary to use a continuation strategy and to follow neutral stability curves.

6.3. Stability of Slot and Knife Coating

Figure 4.12 shows a set of streamline contours for a knife coating flow at values of the operating parameters which are typical of industrial coating devices and for the case where the contact line is free to slide along the solid boundary.

Some streamline contours of the most dangerous two-dimensional mode of disturbance to the flow illustrated in Figure 4.12 are shown in Figure 6.1. This disturbance decays in time, and thus the base flow is stable to it. The streamlines have an eddy-like appearance, except that they terminate at the free surface. (Though one end of each streamline appears to intersect the upper solid die, this is an error in the plotting routine caused by insufficient resolution. In reality, they intersect the free surface close to the contact line.) The intersection of the streamlines with the free surface indicate flow normal to the interface, and therefore the interface location must be changing with time. The recirculatory pattern accompanies displacement of the contact line.

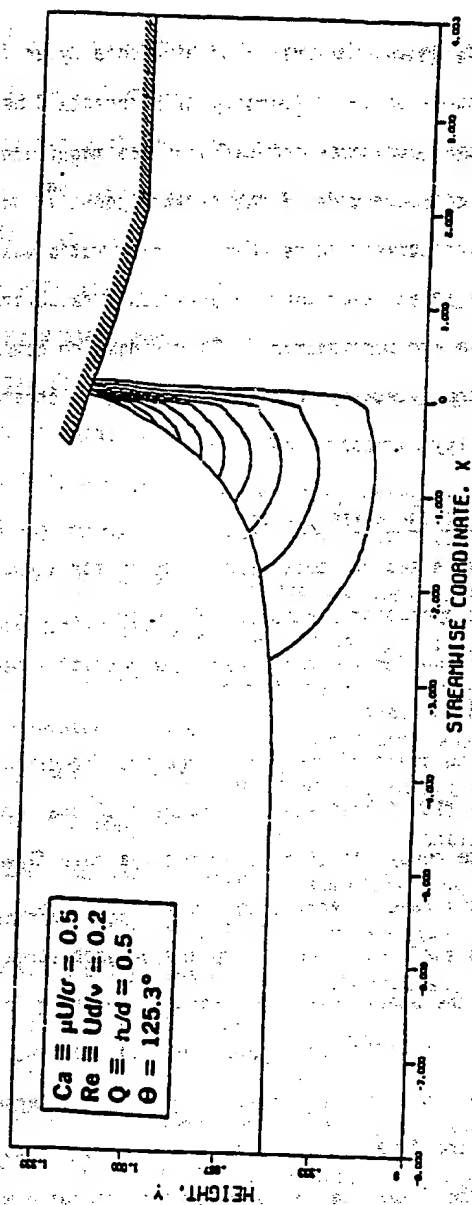


Figure 6.1. Representative streamline contours of the most dangerous two-dimensional disturbance made in a slot or knife coater.

For example, if the contact line is moving tangent to the die in the upstream direction, liquid upstream of the contact line must be displaced. Because the upstream flow rate is specified, the displaced liquid in order to conserve mass, must move downstream of the contact line and thereby increase the flow rate just downstream of the contact line. The result is that the meniscus must bulge outward.

Figure 6.2 shows how the decay rate of the most dangerous three-dimensional disturbance varies with the wavenumber of the disturbance, i.e. with 2π divided by its dimensionless wavelength. The two-dimensional disturbance portrayed in Figure 6.1 corresponds to the limit as wavenumber approaches zero, i.e. as transverse wavelength increases without bound. Disturbances become increasingly three-dimensional as wavelength decreases and wavenumber increases from zero, i.e. from the two-dimensional limit. Figure 6.2 shows that decay rate passes through a minimum, and therefore that the slowest decaying (fastest growing) disturbance is at a finite wavenumber. Furthermore, in the range of wavenumbers where the decay rate is negative, as denoted by the shaded region of Figure 6.2, there are disturbances to which the flow is unstable, i.e. there are disturbances which grow with time. Therefore, this flow is unstable. The wavenumber of the fastest growing disturbance, in this case about 0.54, approximates that of a finite amplitude disturbance whenever wavenumber is a weak function of disturbance amplitude, an assumption for which there is no a priori justification but which is commonly made nonetheless. The dominant decay rates in Figure 6.2, and also in the figures to follow, are real-valued, and thereby

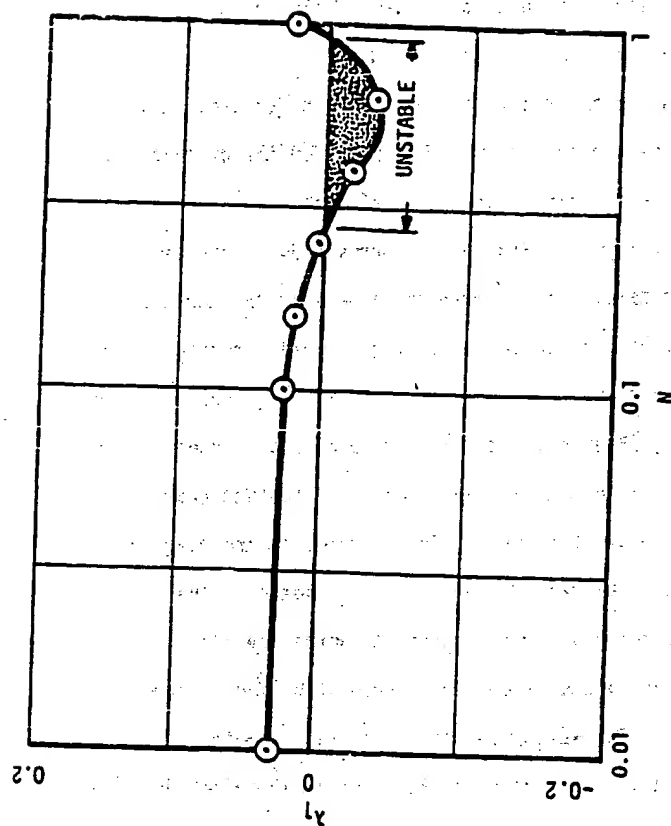


Figure 6.2. Dominant decay rate versus wavenumber for exponential slot or knife coater when capillary number is 0.5, Reynolds number is 0.2, flow rate is 0.5, and contact angle is 125.3° .

signify exponential decay or growth of the associated disturbance.

The influence of the flow parameters on stability is readily examined. Figure 6.3 shows the effect of changing the capillary number. When the capillary number is decreased from 0.50 to 0.45, a relative change of 10%, the flow becomes stable to disturbances of every wavenumber, as demonstrated by the upward translation (accompanied by some deformation) of the decay rate curve. Increasing capillary number by 10% has the opposite effect; the base flow becomes stable over the whole range of wavenumbers shown in Figure 6.3. This clearly demonstrates that capillary forces are stabilizing and viscous forces are destabilizing. The free surface profiles of the base flow at the same three values of capillary number, i.e. 0.45, 0.50, and 0.55, are also shown in Figure 6.3. The contact line and consequently the meniscus too move upstream as capillary number increases. However, the meniscus position is much less sensitive to capillary number than is the decay rate.

It is clear from Figure 6.3 that at some capillary number between 0.45 and 0.5 a decay rate curve would just touch the zero decay rate axis. That value of capillary number is the maximum at which a stable two-dimensional flow could exist, all other parameters being held constant.

Flow rate also affects strongly the stability of slot and knife coating, as shown in Figure 6.4. Reducing the flow rate for 0.5 by 10% leads to a dramatic destabilization of the base flow. Increasing flow rate has the opposite effect. Comparison of Figures 6.3 and 6.4 shows that changes in flow rate affect the meniscus position and curvature

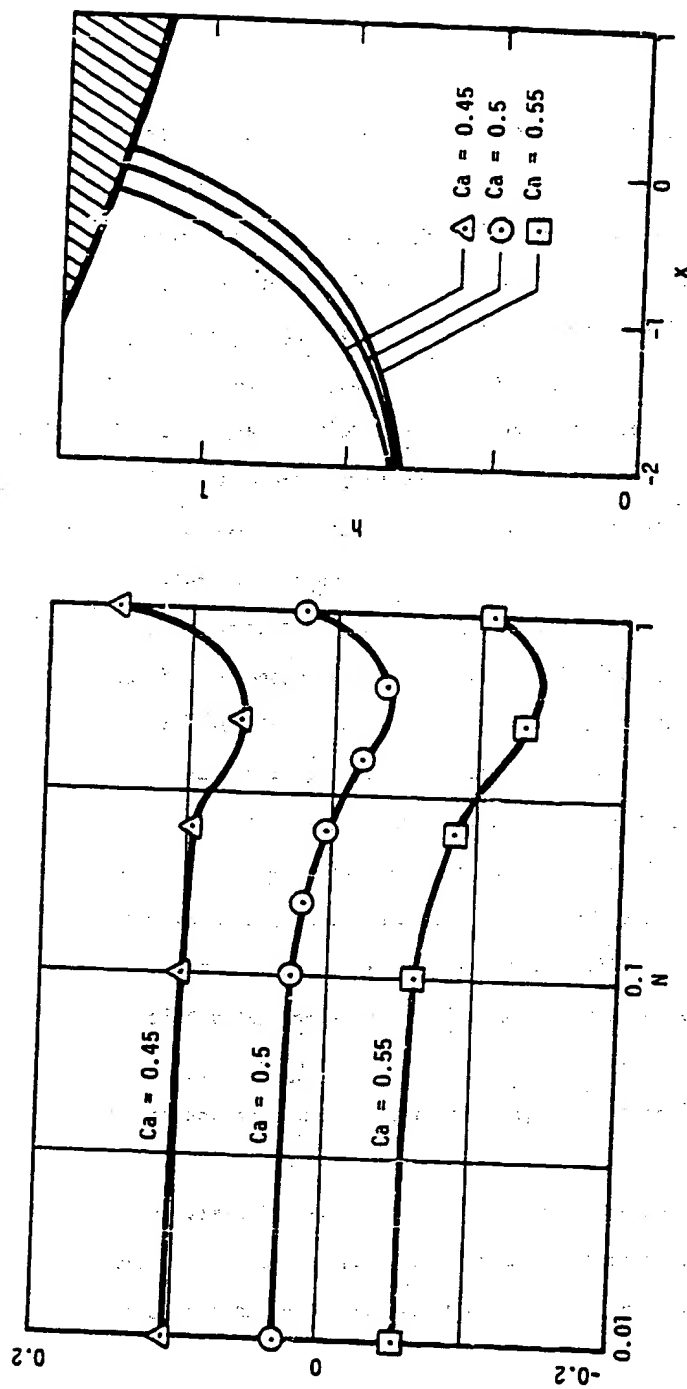


Figure 6.3. Influence of capillary number on dominant decay rate and meniscus profile for exponential slot or knife coater when Reynolds number is 0.2, flow rate is 0.5, and contact angle is 125.3° .

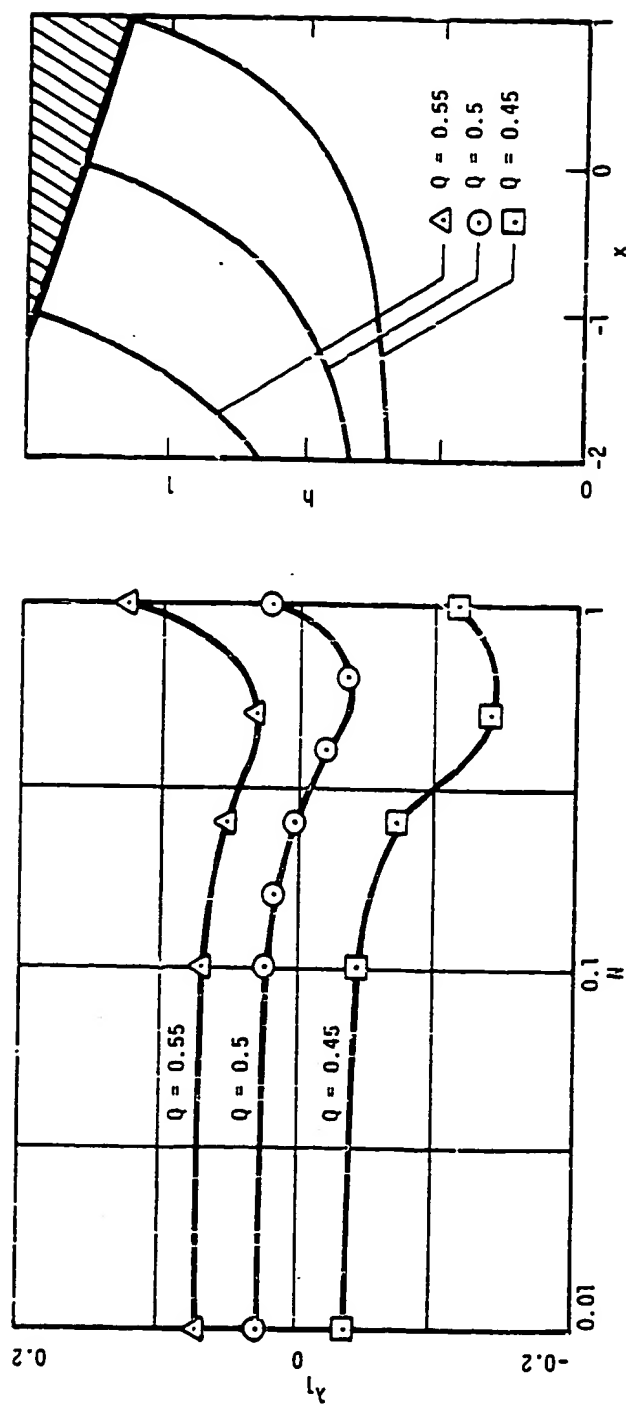


Figure 6.4. Influence of flow rate on dominant decay rate and meniscus profile for exponential slot or knife coater when capillary number is 0.5, Reynolds number is 0.2, and contact angle is 125.3° .

more than does capillary number, and this may explain the influence of flow rate on stability. One result of the dependence of meniscus position on flow rate is that no stagnation line appears on the meniscus due to a recirculation zone near the upper solid die before the contact line reaches the parallel section of the channel. For this reason the influence of a stagnation line on stability behavior is not considered.

Figure 6.5 shows that inertia plays a stabilizing role in slot and knife coating. Decreasing Reynolds number from 0.2 to 0.02, an order of magnitude, does little to affect either the meniscus profile or the decay rate curve, which shows that inertia is inconsequential in this range. However, increasing Reynolds number by an order of magnitude stabilizes the flow significantly. This demonstrates that ribbing is indeed a viscocapillary instability. Inertia plays a role only when it is at least comparable with viscous forces, and then it is a stabilizing force.

The effects of channel divergence angle and contact angle on meniscus profile and stability are demonstrated respectively in Figures 6.6 and 6.7. The meniscus profile changes little, aside from being translated upstream or downstream, as channel divergence angle is varied, while varying contact angle markedly affects the meniscus profile. However, both parameters influence the flow stability; increasing channel divergence angle and decreasing contact angle have stabilizing effects.

6.4. Mechanism of Instability

A simple and somewhat heuristic rationale of ribbing instability was proposed by Pitts and Greiller (1961) and reiterated by Savage (1976). They derived a criterion which is based on a force balance at

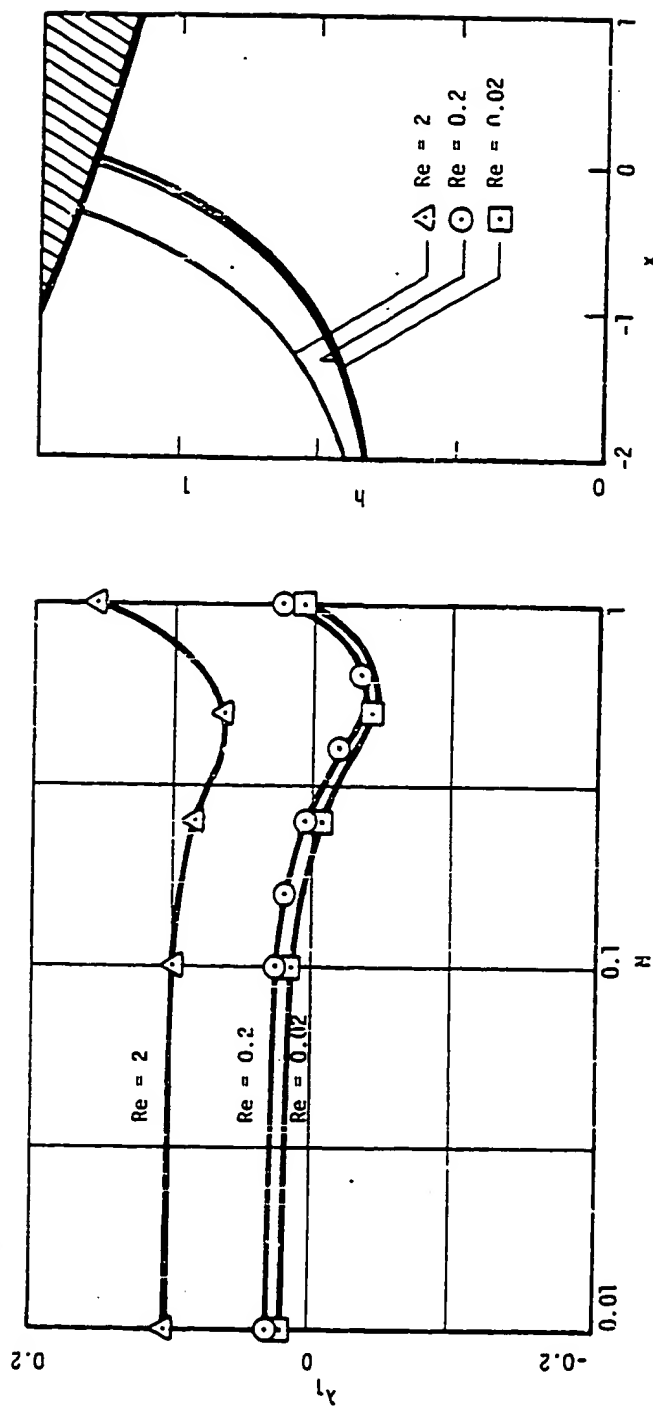


Figure 6.5. Influence of Reynolds number on dominant decay rate and meniscus profile for exponential slot or knife coater when capillary number is 0.5, flow rate is 0.5, and contact angle is 125.3° .

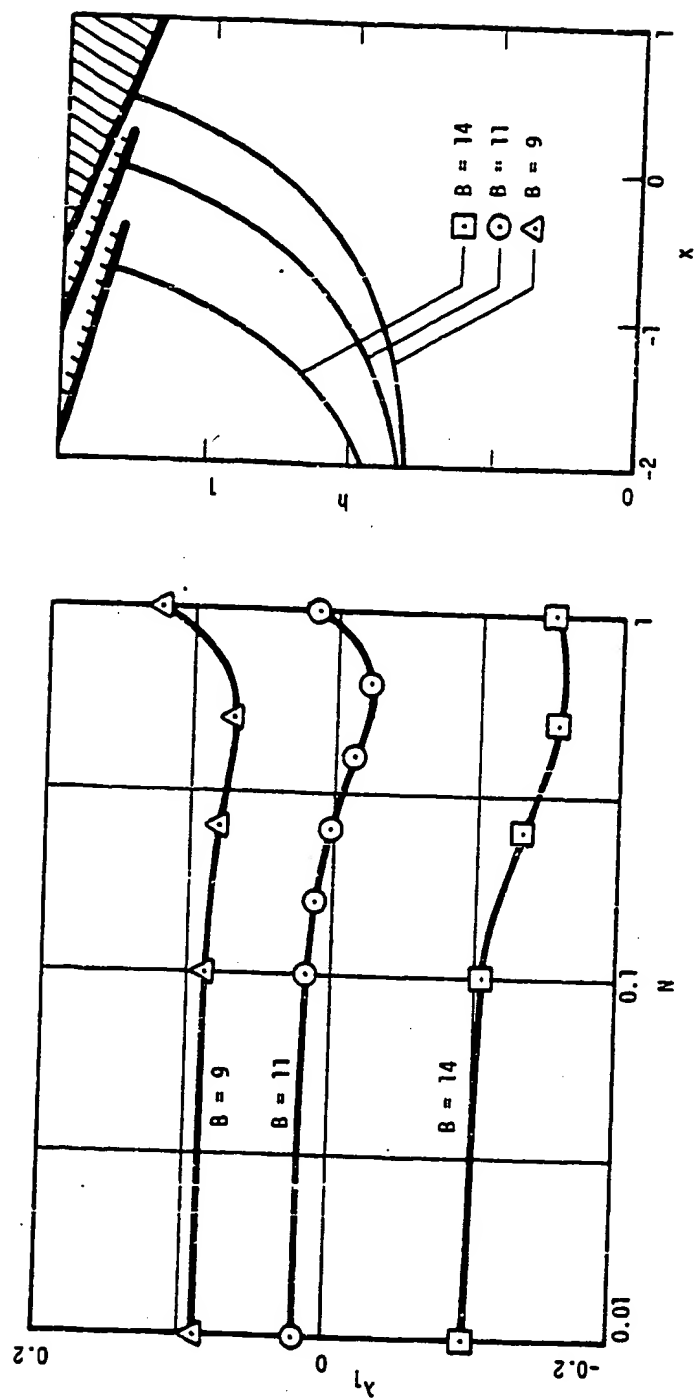


Figure 6.6. Influence of channel divergence angle on dominant decay rate and meniscus profile for exponential slot and knife coater when capillary number is 0.5, Reynolds number is 0.2, flow rate is 0.5, and contact angle is 125.3° .

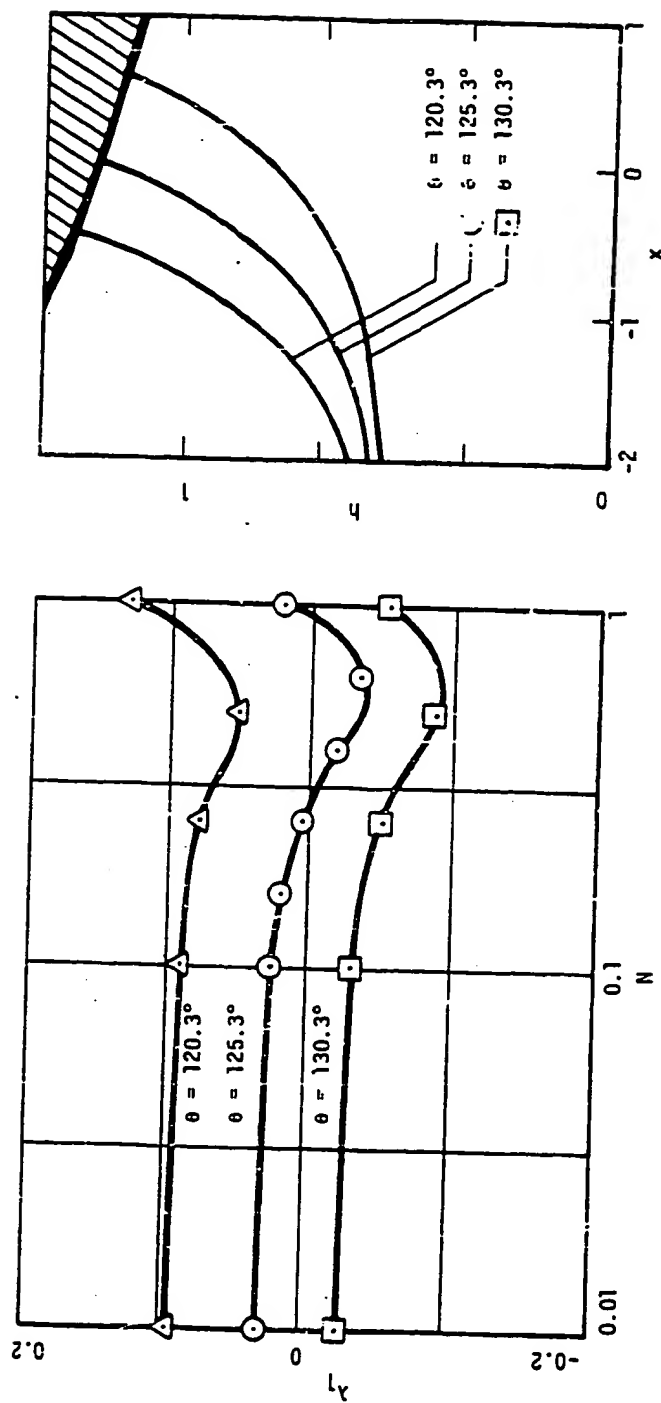


Figure 6.7. Influence of contact angle on dominant decay rate versus wavenumber curves and meniscus profile for exponential slot or knife coater when capillary number is 0.5, Reynolds number is 0.2, and flow rate is 0.5.

the meniscus and on the ideas of lubrication theory. However, they overlooked two important considerations: the effects of normal viscous stress at the meniscus and the three-dimensional nature of a ribbing disturbance. To understand better the importance of these issues and how they relate to the mechanism of the ribbing instability, it is useful to consider the complete force balance at the meniscus, which is the normal stress balance as recorded in Equation (5.2.34). The terms that enter that equation can be classified into three categories: (1) those which represent the change in the action of pressure on the meniscus due to a disturbance; (2) those which represent the change in the action of normal viscous stress on the meniscus due to a disturbance; and (3) those which represent the change in the action of capillary force on the meniscus due to a disturbance. In lubrication theory the first and third of these contributions can be only crudely approximated, and the second has to be omitted entirely. Here, each of the contributions to the normal stress balance can be evaluated from the finite element basis function expansions of the base flow and the eigenvector associated with the dominant mode of instability.

The changes in the contributions to the normal stress balance due to the onset of a disturbance are computed here by integrating the weighted normal stress equation, i.e.

$$0 = \int_{\delta\Omega_{FS}} \left[2 \frac{\partial \bar{u}_n}{\partial n} - \bar{p} - Ca^{-1} 2\bar{H} \right] \cos(\bar{n}z) \phi(\xi) \frac{\partial \bar{x}}{\partial \xi} d\xi dz \quad (6.3.1)$$

over a portion of the meniscus just downstream of the contact line, the

portion where most of the action occurs (see Figure 6.1). Here \bar{u}_n represents the perturbed velocity component normal to the meniscus, n represents distance normal to the meniscus, \bar{p} is the perturbed pressure, $Ca \equiv \mu U / \sigma$ is capillary number, μ being dynamic viscosity, U being web speed, and σ being surface tension, \bar{H} is the perturbed mean curvature, N is wavenumber and ξ is an isoparametric coordinate (see Figure 5.3). The normal tractions are evaluated by integrating each of the weighted normal stress contributions from the contact line to a point lying 0.2 gap thicknesses downstream, which is the distance to the node that divides the second and third free surface elements. The weighting function $\phi(\xi)$ in Equation (6.3.1) is chosen to be the sum of two Hermite cubic basis functions, two of the same basis functions which served as weighting functions in the normal stress equation (5.2.34), so that ϕ is unity over the first element downstream of the contact line and goes to zero at the downstream edge of the second free surface element. The magnitudes of the normal stress terms are set by choosing the maximum film-wise displacement of the contact line due to the disturbance to be unity. The sign preceding the normal viscous stress term in (6.3.1) is positive so that when $\partial \bar{u}_n / \partial n$ is positive, stress is in the direction of the inward pointing normal to the meniscus; on the other hand, the sign preceding the pressure and capillary terms in (6.3.1) are negative so that when \bar{p} or $Ca^{-1} \bar{H}$ are positive, stress is in the direction of the outward pointing normal to the meniscus.

The normal stress components of the baseflow integrated over the first two free surface elements are shown in Table 6.1. The curvature

Table 6.1. Normal tractions on the meniscus rear the contact line of the slot or knife coating flow shown in Figure 4.11.

Traction	Contribution
Capillary (outward)	0.628
Pressure (outward)	- 0.383
Normal Viscous (inward)	0.245

Table 6.2. Changes in normal tractions on the meniscus near the contact line of the slot or knife coating flow shown in Figure 4.11 due to the dominant two-dimensional disturbance shown in Figure 6.1.

Traction	Contribution
Capillary (outward)	- 0.779
Pressure (outward)	- 0.597
Normal Viscous (inward)	- 1.477

is positive so that the net capillary force is acting in the direction of the outward pointing normal to the free surface. The net forces due to pressure and viscous stress acts in the opposite direction and counterbalance the capillary force. It is clear from Table 6.1 that normal viscous stress near the contact line in this flow is of the same order of magnitude as pressure, a feature that is missing in lubrication theory.

Table 6.2 shows how these meniscus tractions are changed by the dominant two-dimensional disturbance mode when the meniscus moves downstream. The changes are per unit displacement of the contact line in the filmwise direction. Each of the normal tractions is decreased by the disturbance and this leads to the following consequences: (1) the capillary traction on the meniscus in the direction of the outward pointing normal to the free surface is decreased; (2) the traction exerted by pressure in the direction of the inward pointing normal to the free surface is increased; (3) the normal viscous traction, acting in the same direction as pressure, is decreased. These three changes occur in concert so that the overall balance of forces on the meniscus is maintained, as it must be. Table 6.2 shows that the change in normal viscous stress along the meniscus due to the dominant two-dimensional disturbance mode is of the same order of magnitude as the change in pressure, a feature that is not included in lubrication analysis of stability. The relationship between the changes in the normal stress components and the stability of the flow is discussed further in the following paragraphs.

Figures 6.8 and 6.9 show how the changes in the components of normal traction due to the dominant two-dimensional disturbance mode depends on the flow parameters (excluding Reynolds number). The ordinate values are differences from the values given in Table 6.2. Comparison of Figures 6.8 and 6.9 with the growth rate curves contained in Figures 6.3-6.7 shows that the changes in the three normal tractions always turn more negative as the flow becomes less stable. (The trend as Reynolds number changes agrees with this observation as well.) Thus, two-dimensional disturbances are least stable when they reduce capillary force (outward), increase pressure force (inward), and decrease normal viscous force (inward, i.e. normal viscous force is tensile). How these trends account for the loss of stability of the base flow to a two-dimensional disturbance can be explained as follows. For the contact line to move downstream along the solid die, liquid must be driven from downstream of the contact line to immediately upstream of it, as shown in Figure 6.1. The more negative pressure becomes near the contact line as it moves downstream, the greater is the driving force for liquid to be delivered there. Normal viscous force plays a role as well. The more negative the normal viscous force (i.e. the less tensile) on the meniscus, the greater the driving force for liquid to be delivered there. This last point can be understood by considering an extensional flow such as an accelerating liquid curtain. At the midplane of the curtain the normal viscous stress along the midplane is tensile, consequently the normal viscous stress perpendicular to the midplane is compressive. The compressive (negative) viscous stress normal to the midplane corresponds to

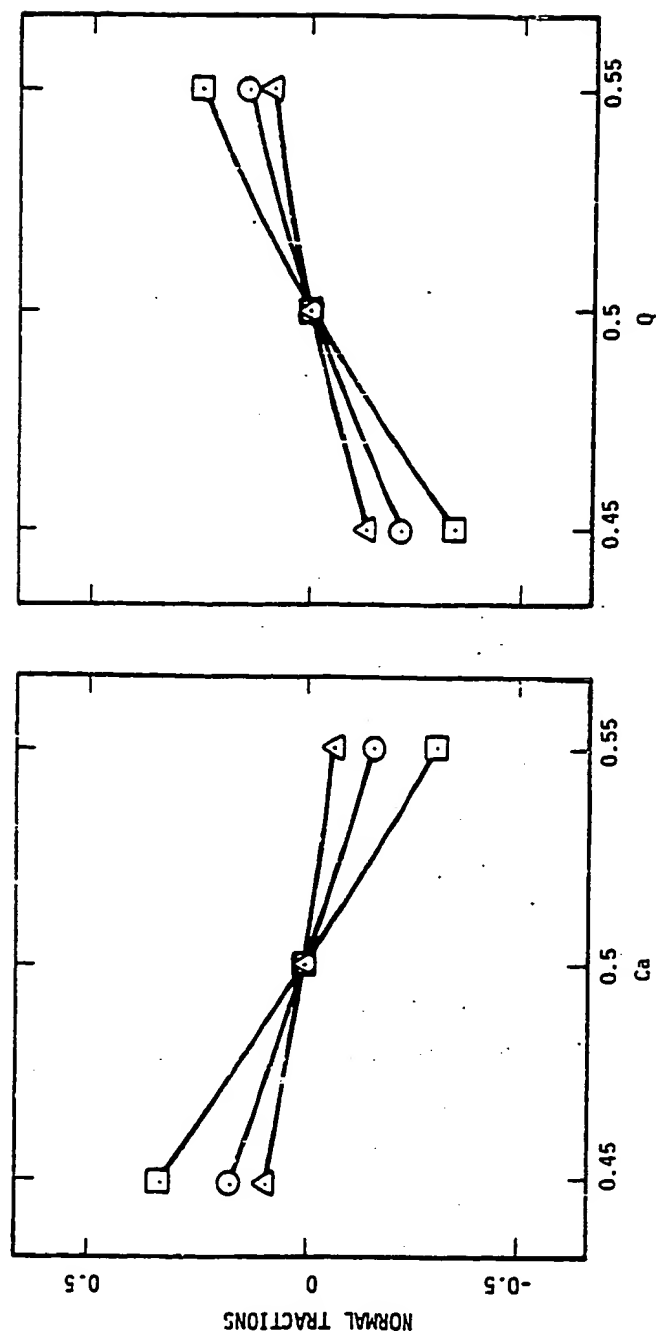


Figure 6.8. Changes in normal tractions due to the dominant two-dimensional disturbance integrated over the first two elements downstream of the contact line. Ordinates are differences from the values in Table 2.2. The symbols are: \circ , pressure force; \triangle , normal viscous force; and \square , capillary force.

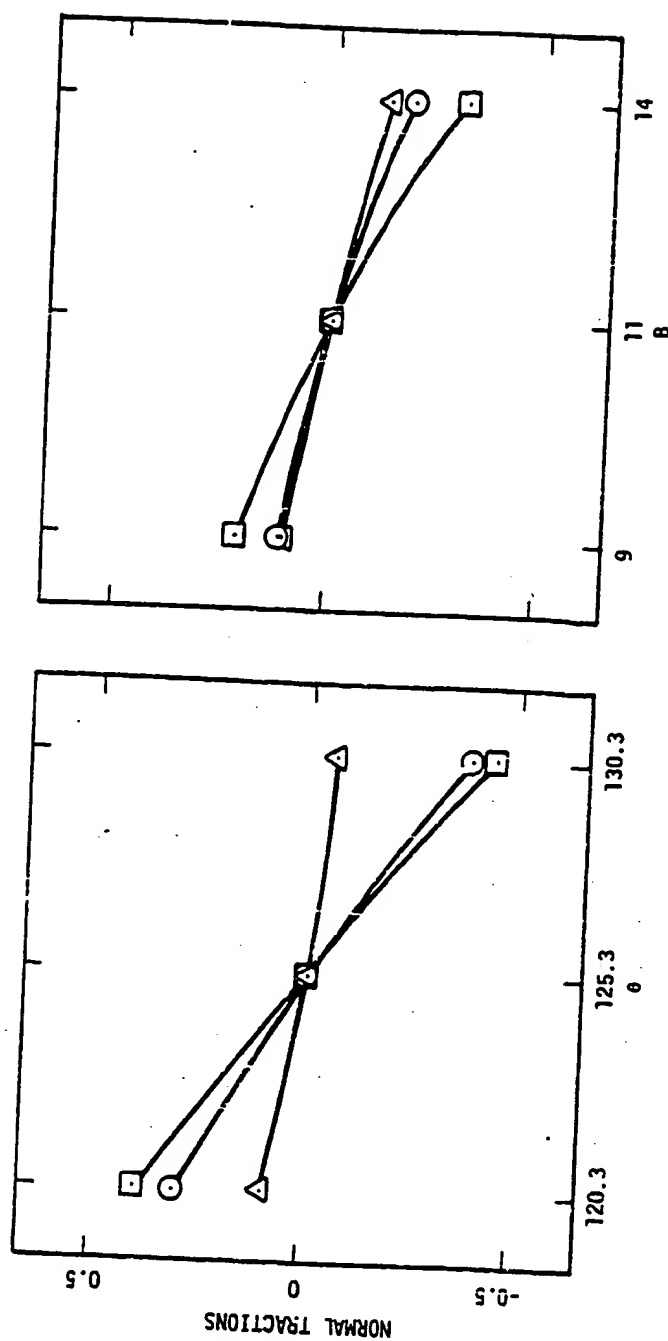


Figure 6.9. Changes in normal tractions due to the dominant two-dimensional disturbance integrated over the first two elements downstream of the contact line. Ordinates are differences from the values in Table 2.2. The symbols are: θ , pressure force; Δ , capillary force; D , normal viscous force.

liquid flowing toward it. The same is true at the meniscus in slot and knife coating. Thus, two-dimensional disturbances are least stable when they decrease pressure and normal viscous stress at the meniscus as the contact line moves downstream.

An identification of the mechanism of instability in slot and knife coating must also account for the fact that the fastest growing disturbance mode is always three-dimensional, as shown in Figures 6.3-6.7. Three-dimensional disturbances are characterized by wavenumber greater than zero, and are represented by Fourier basis functions in the transverse coordinate (see Chapter 5). Therefore, three-dimensional disturbances of a given wavenumber N are transversely periodic and have wavelength $2\pi/N$. Whatever the changes in normal stress components due to a three-dimensional disturbance at a plane of specified transverse coordinate, the changes are of opposite sign at a parallel plane separated by a distance of a half-wavelength. Likewise, whatever the change in meniscus profile at a plane of specified transverse coordinate, the change is of opposite sign at a parallel plane separated by a half-wavelength. It is enough therefore to consider how a three-dimensional disturbance changes the base flow in one plane perpendicular to the transverse coordinate axis, say at a plane that intersects the contact line where it protrudes downstream the furthest, for the changes at every other plane parallel to the first could be constructed from the Fourier representation.

Figure 6.10 shows how changes in normal stress forces on the meniscus due to the dominant disturbance mode depend on wavenumber for the

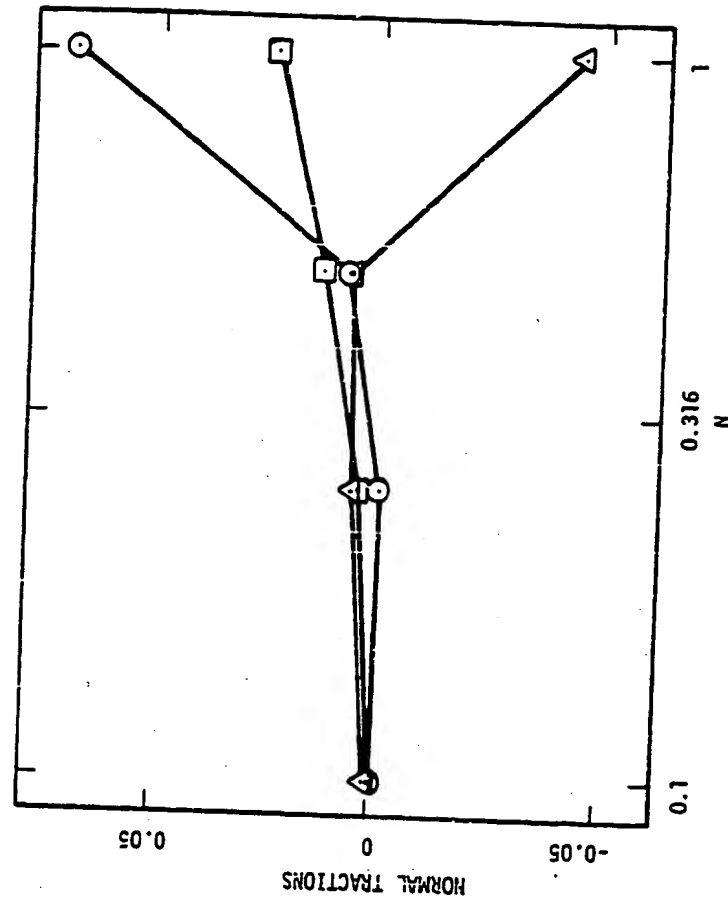


Figure 6.10. Changes in normal tractions due to the dominant three-dimensional disturbance of wavenumber N integrated over the first two elements downstream of the contact line. Ordinates are differences from the values in Table 2.2. The symbols are: ○, viscous force; □, pressure force; △, capillary force.

flow illustrated in Figure 4.11. The ordinate values for each of the tractions are again differences from the corresponding values in Table 6.2, which are for the two-dimensional limit. The following trends can be observed as wavenumber increases: (1) the change in pressure force on the meniscus due to the dominant disturbance mode first decreases slowly, then increases rapidly; (2) the change in normal viscous force increases monotonically; and (3) the change in capillary force — which equals the change in total force on the meniscus, i.e. viscous plus pressure force — reaches a maximum then decreases again. The maximum is of tensile force on the meniscus and corresponds approximately to the same value of wavenumber as does the fastest-growing disturbance mode. The above trends hold at transverse coordinate planes where the contact line protrudes furthest downstream; the opposite trends hold at transverse coordinate planes where the contact line invades furthest upstream. Thus, the fastest growing disturbance occurs at the wavenumber which maximizes the difference in tensile force on the meniscus between planes where it protrudes furthest and planes where it invades furthest. This difference in stress fuels the growth of the three-dimensional disturbance because it acts as the driving force for a transverse flow from the planes where the meniscus invades to the planes where it protrudes, and thereby causes the disturbance to grow.

6.5. Discussion

The results of Section 6.3 show that the method of employing Galerkin/finite element analysis coupled with Fourier normal mode analysis described in Chapter 5 is a practicable means to determine the stabil-

ity of a steady, two-dimensional, free surface flow to three-dimensional disturbances. Furthermore, the eigenvectors which result from the inverse subspace iteration strategy described in Chapter 5 and Appendix A contain valuable information about the dominant disturbance modes, as shown in Section 6.4. The results of Sections 6.3 and 6.4 show now and why flow parameters influence stability, and also why the fastest growing disturbance is three-dimensional.

The decay rates in Figures 6.3-6.7 show that the ribbing instability in slot and knife coating is induced by the following: (1) increasing capillary number; (2) decreasing flow rate; (3) increasing contact angle, i.e. making the solid die less wettable to the liquid; (4) decreasing channel divergence angle; and (5) decreasing Reynolds number. Figures 6.8 and 6.9 show that when parameters are changed in the above directions, the changes in normal tractions near the contact line caused by the dominant two-dimensional disturbance mode all become more negative — i.e. the capillary force in the outward direction is decreased, normal viscous force in the inward direction is decreased, and pressure force in the inward direction is increased. The decreases in normal tractions make a recirculatory flow pattern such as the one shown in Figure 6.1 more likely to grow, as explained in Section 6.4, and thus lead to instability.

The results in Figure 6.10 explain why the fastest growing (slowest decaying) disturbance is at a finite wavenumber. When wavenumber has approximately the same value associated with the fastest-growing disturbance mode, the net tensile force normal to the meniscus, i.e. $2\sigma u_n / \partial n - p$,

is a maximum at transverse coordinate planes where the contact line protrudes furthest downstream and a minimum at transverse coordinate planes where the contact line invades furthest upstream. To understand the connection between the tensile force at the meniscus and the growth rate of a disturbance, it is useful to examine the component of the linearized momentum equation (5.2.4) that is normal to the meniscus.

$$\begin{aligned} \text{Re}\left(\frac{\partial u_n'}{\partial t} + u_z \cdot \frac{\partial u_n'}{\partial z}\right) = \frac{\partial}{\partial n} \left(2 \frac{\partial u_n'}{\partial n} - p'\right) + \frac{\partial}{\partial z} \left(\frac{\partial u_n'}{\partial z} + \frac{\partial u_z'}{\partial n}\right) \\ + \frac{\partial}{\partial z} \left(\frac{\partial u_n'}{\partial z} + \frac{\partial u_z'}{\partial n}\right) \end{aligned} \quad (6.5.1)$$

Here n and z refer respectively to distance normal and tangential to the undisturbed meniscus, and primes denote a disturbance to the baseflow. Only one convective term appears in (6.5.1) because the baseflow has no velocity component normal to the meniscus. The last two terms in (6.5.1) disappear on the meniscus because of the shear stress boundary condition (5.2.22). Furthermore, the second term on the right side must be small near the contact line, for otherwise the contact angle would be perturbed by the disturbance. Therefore, on the meniscus near the contact line (6.5.1) reduces approximately to:

$$\text{Re}(-\lambda u_n') = \frac{\partial}{\partial n} \left(2 \frac{\partial u_n'}{\partial n} - p'\right) \quad (6.5.2)$$

The right hand term is due to the exponential time dependence of the disturbance, i.e. $e^{-\lambda t}$. It follows that when the tensile stress on the meniscus, i.e. $2 \partial u_n' / \partial n - p'$ there, is more positive at locations where

the meniscus protrudes outward than at places where it invades inward, the right side of (6.5.2) must be positive relative to its value for a two-dimensional disturbance. Because the velocity u'_n must also be positive at meniscus protrusions, λ must therefore be negative relative to its value for a two-dimensional disturbance. This explains why the fastest growing disturbance is the one for which the net tensile stress is greatest at meniscus protrusions.

Ruschak (1982) investigated by finite element stability analysis, as explained in Section 5.4, the problem of the displacement of highly viscous liquid contained between two closely spaced parallel surfaces, i.e. creeping flow displacement of liquid in a Hele-Shaw cell, by a relatively inviscid fluid. Saffman and Taylor (1958) first showed by an approximate stability analysis that transversely symmetric displacement of the liquid/fluid interface is always unstable to transversely periodic disturbances. Furthermore, they showed experimentally that the disturbances grow into long narrow fingers. Both Saffman and Taylor's and Ruschak's stability results show that the fastest growing disturbance should occur at finite wavenumber, which is analogous to the results obtained here. However, Ruschak did not explain the mechanism of instability.

Saito et al. (1982) put forward on the basis of their experimental observations of slide coating the hypothesis that unstable flows are associated with large meniscus curvature. Figure 6.11 shows that this hypothesis is not completely valid. Each of the curves there shows how the slowest decay rate (fastest decay rate), i.e. a minimum of one of

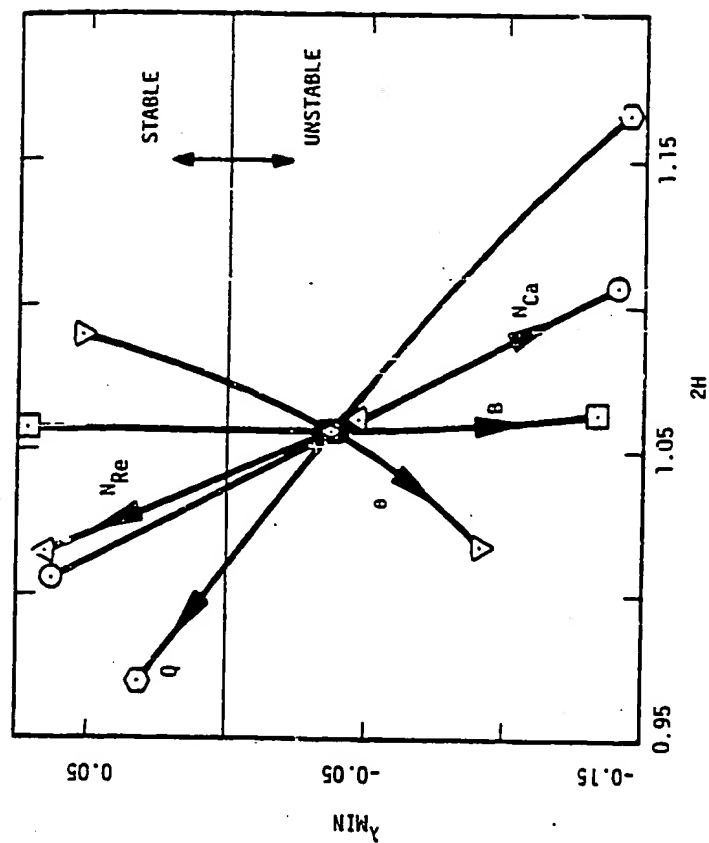


Figure 6.11. Variation of minimum decay rate, λ_{MIN} , and base flow meniscus curvature, $2H$, at the contact line with flow parameters. Arrows indicate direction of increasing parameter values.

the decay rate curves in Figures 6.3-6.7, and meniscus curvature at the contact line of the base flow change as a parameter increases. Their hypothesis is in agreement with the trends as capillary number, flow rate, and Reynolds number are varied. However, their hypothesis is contradicted by the trends as channel divergence angle decreases (B increases) and as contact angle increases. In the case of channel divergence angle the flow becomes less stable while the meniscus curvature remains almost constant; in the case of contact angle the flow becomes less stable as the meniscus curvature decreases.

It is notable that the capillary number at onset of instability as predicted by finite element stability analysis (see Figure 6.3), which is approximately 0.5, is close to the value of 0.45 where ribbing was first observed in the visualization experiment with the cylindrical spreader pictured in Figure 1.7. Furthermore, the wavenumber measured from Figure 1.7c is about 0.53, which is only 2% less than that predicted in Figure 6.2. It should be noted, however, that the configuration of the gap in the experiment was similar but not identical to that illustrated in Figure 6.1, and also that flow rate and contact angle were not measured in the experiment. Nevertheless, the close agreement between the results of the stability analysis and the experimental observations appears to confirm the accuracy of the finite element/Fourier approximation.

Figure 6.12 compares the decay rate results predicted by lubrication theory as described in Chapter 3 with those of finite element stability analysis. The lubrication analysis is for flow rate specified at

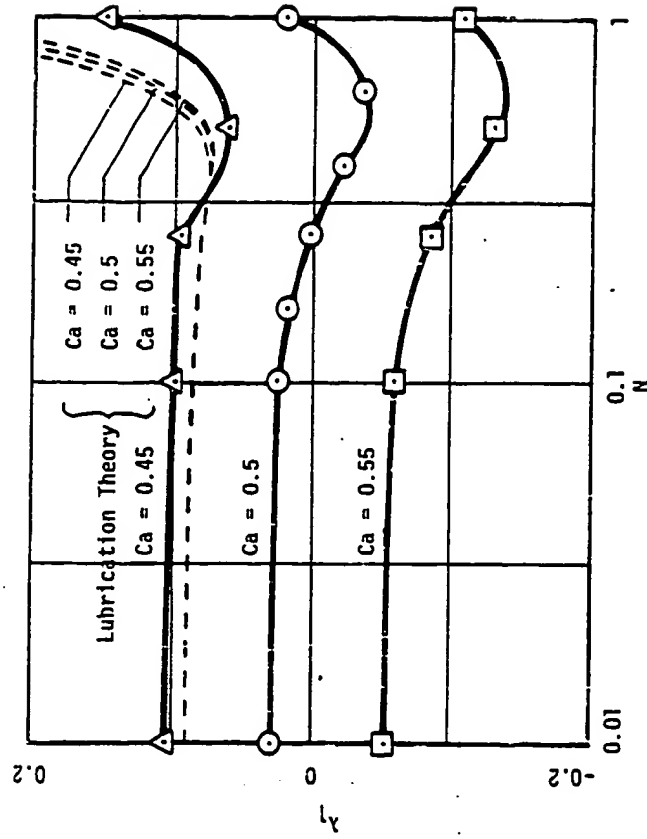


Figure 6.12. Comparison of finite element and lubrication stability results. Finite element stability results are those of Figure 6.3; lubrication results are those obtained in Chapter 3.

the inflow boundary, which is taken to be asymptotically far upstream, and for Coyne-Elrod type conditions at the separating meniscus. The meniscus conditions had to be computed from the finite element base flow solutions because the contact angle, which is 125.3° , is much larger than those tabulated by Coyne and Elrod. The meniscus conditions that were used are given in Table 6.3. Lubrication theory does not predict the onset of instability at a capillary number close to 0.5, but instead predicts that the flow is stable. It would be interesting to see at what capillary number lubrication stability analysis does predict onset of instability. However, it was not possible to find out because the contact line in the base flow generated by Galerkin/finite elements reaches the parallel portion of the channel at capillary numbers only slightly higher than 0.55 and therefore it was impossible to generate the appropriate meniscus conditions to use in the lubrication analysis. The reason for the failure of lubrication theory to correctly predict the onset of instability is almost certainly that it does not account for normal viscous stresses on the meniscus, which are shown to be important in Tables 6.1 and 6.2 and also in Figures 6.8-6.10.

Finite element stability calculations were also made for the exponential slot coater for the case where the contact line is pinned and for capillary number ranging from 0.01 to 1, Reynolds number ranging from 2 to 20, and flow rate ranging from 0.35 to 0.5, but no loss of stability was uncovered. It is notable that at capillary numbers near unity and at low Reynolds number the dominant disturbance mode is predicted to be time oscillatory when the contact line is pinned, in con-

trast to the situation when the contact line is free to move along the die. If this mode were excited, the result would be cross-web barring. Higgins (1980) found by lubrication analysis that the extrusion coater, of which the slot coater is the downstream portion as shown in Figure 1.1, can suffer temporal oscillations which lead to cross-web bars. Thus the stability of slot and knife coating appears to be sensitive to the physics that governs the contact line. The best avenue for verifying hypotheses of contact line physics might be to compare experimental data with predicted stability behavior rather than with predicted base flow behavior.

Table 6.3. Coyne-Elrod type boundary conditions used to generate the growth rate curves shown in Figure 6.12. Boundary conditions were computed from finite element calculations for a Reynolds number of 0.2, flow rate of 0.5, contact angle of 125.3° , and capillary numbers of 0.45, 0.5, and 0.55.

N_{ca}	d/h_∞	R/d
0.45	2.69	0.821
0.5	2.39	0.791
0.55	2.15	0.763

POSTLUDE

Now for the first time, questions about the stability of a relatively complicated coating flow — an example of a viscous free surface flow — can be answered with confidence. No longer is it necessary to put trust in the lubrication approximation for lack of a more reliable approach. The key is a finite element/Fourier representation of possible modes of instability. Finite element analysis opens the way not only to determining the stability of a steady, two-dimensional base flow, but also to understanding the mechanism of instability. Such understanding will make it possible to avoid, or at least control, imperfections and incipient film breakdowns whenever they are not absolutely inherent in a coating system.

The methods of finite element stability analysis developed here are novel. They are applicable to the entire class of steady two-dimensional flows with or without free surfaces. While the development here is for Newtonian liquids with uniform properties, the methods can be generalized to flows of non-Newtonian liquids and to flows in which temperature and composition are nonuniform. The feasibility and usefulness of finite element stability analysis is demonstrated here for slot and knife coating. This work is the first of its kind, although it is paralleled by some ongoing research of Ruschak (1982) on free surface flows and of Brown (1982) on partially confined flows. Their analyses, however, are less general in applicability, as discussed below.

Perhaps the biggest uncertainty of the demonstration of finite element stability analysis in slot and knife coating is the question of how

fine a tessellation is needed to accurately represent the dominant disturbance modes. Finer tessellations than the ones used here were not possible, owing to the limited memory of the Cybers 74 and 730. The effects of the tessellation were explored instead by varying the size of the forming zone and by refining the tessellation in the vicinity of the contact line. The results indicated that the tessellation used here was fine enough to limit error in the estimates of the decay rate of the dominant mode to less than 5%. However, the effects of tessellation refinement should be tested further. This testing is now made feasible at the University of Minnesota by the acquisition of a vector-processor, the CRAY-1.

Finite element stability analysis can be applied to each of the flows illustrated in Figure 1.1. The first extension of this thesis is by the author's colleague Dennis Coyle, who is beginning to investigate the stability of roll coating and has plans to investigate the stability of reverse roll coating as well. Coyle will be carrying out most of the computations on the CRAY-1, so that he will be afforded the opportunity to further test the effects of tessellation refinement. Another extension is being planned to slide coating, which is one of the most widely used methods in the manufacture of photographic films.

The uses of finite element stability analysis of coating flows are many. It is possible to predict just what influence changes in each of the operating parameters and liquid properties will have on stability. Complete parametric studies can be carried out to identify stable operating regions or "windows". Furthermore, changes in die design, such as

the channel divergence angle in the slot or knife coater, can be investigated without recourse to pilot plant experimentation. Indeed, new methods to apply coatings can be screened first by numerical analysis, so that less experimentation is needed and fewer dies need be machined.

Finite element stability analysis can also be used to probe the mechanisms of instabilities wherever they occur. For instance, the importance of normal viscous stress on the interface to the mechanism of ribbing in slot and knife coating is shown here for the first time. Previous analyses using lubrication theory have ignored normal viscous stress altogether. Another important example is in slide coating. Two postulates have been proposed concerning the mechanism of ribbing in slide coating: one is that instability is viscocapillary in origin, and so is analogous to ribbing in slot or knife coating; the other is that instability is akin to the centrifugal instability in film flows uncovered by Schweizer and Scriven (1982). Evidence was recently presented by Saito et al. (1982) that the mechanism is viscocapillary in nature, but the issue is not completely settled. The controversy could be resolved once and for all by a finite element stability analysis of slide coating.

Finite element analyses of steady base flows and their stability would not be possible without the modern high-speed digital computer. Without it, the sophisticated matrix calculations needed to solve efficiently the large systems of algebraic equations to which base flow and stability analyses lead would be completely impracticable. Stability calculations are carried out efficiently on computers such as the

University of Minnesota Cyber 730 which can rapidly access at least 200,000 words of memory. For example, one stability point of the slot and knife coating flows reported here usually took about one minute of central processor time. Virtual memory machines, such as the VAX and some of the newer IBM machines, could also be used, but would normally require longer computation times. Vector machines, such as the CRAY-1, are probably ideal for stability analyses because of their large memories, high speeds, and vector capabilities. Steve Kistler and Dennis Coyle are already exploiting the University of Minnesota CRAY-1 in their steady two-dimensional flow calculations of curtain coating and roll coating, respectively, and Haroon Kheshgi is doing so in unsteady two-dimensional film flow calculations. However, even with the CRAY-1 stability calculations will remain relatively expensive. Therefore it is imperative, especially for university research, to develop efficient strategies and algorithms.

A useful strategy to treat more efficiently most flow problems that are defined on very large domains is to divide the entire domain up into those zones, if any, in which the flow is nearly rectilinear, or otherwise close to an exact solution, and those in which it is not. The idea is to describe the nearly rectilinear flows by asymptotic analysis and to describe the more complicated flows in the remaining zones by finite element analysis. The asymptotic equations are often linear, and when they are they can be solved once and for all. Matching conditions between asymptotic zones and zones in which finite element analysis is needed lead to vector Robin conditions which can be imposed as natural

boundary conditions in the finite element formulation. The result is that the finite element domain can be shrunk from what it would be, were more conventional Dirichlet or Neumann conditions used at the open-flow boundaries, and so the number of algebraic equations and unknowns can be reduced. In other words, the power of the finite element method can be concentrated where it is most needed. The final outcome is that computational costs can be cut without sacrificing accuracy. This novel strategy is used in Chapter 4 to represent two-dimensional base flows and in Chapter 6 to represent unsteady three-dimensional disturbances. The same strategy should prove useful in analyzing many other free surface flow problems, and in particular those in Figure 1.1. Kistler (1982) has developed an analogous method for jets and falling curtains, except that the asymptotic analysis there is nonlinear so that it has to be carried out simultaneously with the finite element analysis of the zone where the curtain is formed.

Calculating stability by the approach followed here requires solving a large matrix eigenproblem that is asymmetric, as brought out in the Prelude. To the author's knowledge, this thesis puts Stewart's 1978 algorithm for asymmetric eigenproblems to practical use for the first time. Stewart's algorithm is a relatively sophisticated method to track the most dangerous disturbances in a stability analysis. Used in concert with a bilinear mapping, a simple transformation borrowed from the methods of complex algebra, Stewart's algorithm can be used to track time oscillatory modes, even if they have relatively high frequency (in which case they are harder to find). Stewart's algorithm was implemented

here by using continuation, i.e. by specifying a previously determined set of dominant modes as initial guess, to improve efficiency. The eigenanalysis usually required about 2/3 of the computer time needed for one stability calculation, or about 40 seconds on the University of Minnesota Cyber 730.

Although the lubrication approximation has been used by others for stability analysis (see Pearson 1960, Pitts and Greiller 1961, and Savage 1977; see also Taylor 1963) the influence of boundary conditions on stability predictions is established here for the first time by means of a side-by-side comparison. The results (see Figures 1.2 and 1.8) show that the influence is strong indeed. Furthermore, the Coyne-Elrod boundary condition, which appears to be the most reasonable of those compared, disagrees quantitatively with the finite element stability analysis (see Figure 1.9). Consequently, lubrication theory cannot be relied on for stability predictions. Moreover, lubrication theory is limited to flows in which the domain is nearly a parallel channel, and thus it would be completely inadequate for flows such as slide coating.

Several possibilities exist for improving or extending the stability analysis presented here, and some of them are in the offing. One improvement is to discard the independent free surface representation used here in favor of one that is consistent with the isoparametric mapping as devised by Kistler (see Kistler and Scriven 1982). This idea is already being applied to finite element stability analysis by Dennis Coyle. By exploiting the CRAY-1, he intends to examine more thoroughly than was possible in this first work the sensitivity of the dominant modes and

their growth rates to the tessellation. Another avenue of research that Coyle is beginning to undertake is a comparison of the efficiency and accuracy of Ruschak's approximate finite element stability analysis with the one employed here. Ruschak's (1982) method sets the time derivatives in the Navier-Stokes equations (1.2.1) and (1.2.2) to zero even when Reynolds number $Re \equiv U_d/v$ is appreciable, so that the stability problem is reduced to a much smaller size. Standard algorithms can then be used to solve the eigenproblem.

Another idea, which was suggested by the author to colleagues Osman Basaran and Robert Benner, is based on the method of Sturm sequences (see e.g. Wilkinson 1965). The idea is to examine the sign of the pivotal elements of the Jacobian matrix during Gaussian elimination. A change in sign of one of the pivotal elements signals that a real eigenvalue has crossed through zero. By keeping track of the signs of all the pivotal elements, the stability of a flow can be determined — it is stable to modes which are not time-oscillating if pivots are positive (provided the signs of the rows are chosen appropriately). Basaran and Benner are currently employing this method in problems where all the eigenvalues are real. Brown (1982) is employing a somewhat cruder method in which only the sign of the determinant of the Jacobian matrix is examined. What is greatly needed is an idea like the Sturm sequence method, perhaps even a simple extension of it, for detecting a change in the sign of the real part of a complex pair of eigenvalues, i.e. loss of stability of a flow state to a time-oscillating disturbance mode. Such an extension would be an extremely important step towards building a more efficient

algorithm to evaluate the stability of a free surface flow.

One major aspect of a full bifurcation analysis, i.e. branching of families of flow states, is missing from this work. Because the bifurcating solution families are three-dimensional, a three-dimensional finite element algorithm would be needed to track those families. The present analysis is only for small-amplitude, three-dimensional disturbances, which can be represented in the transverse direction by Fourier normal modes. Either standard three-dimensional "brick" elements could be used, or perhaps special ones could be constructed to represent the ribs with fewer degrees of freedom. In either case, the finite element domain would need be of only half-wavelength's width in the transverse direction. The possibility of solving three-dimensional flow problems at reasonable cost is just coming into view with the advent of larger and faster computers. Thus it may soon be possible to trace out the whole bifurcation diagram for coating flow problems.

The main achievement of this thesis is to originate and advance methods to evaluate the stability of coating flows, and more generally viscous flows of all kinds, by finite element analysis. Finite element stability analyses should prove to be powerful tools in designing, optimizing, and controlling coating devices, as well as understanding better the ways that flows lose stability.

APPENDIX A

Stewart's Algorithm for the Asymmetric Eigenproblem

In two papers Stewart (1976 and 1978) presented his algorithm for finding the m -dimensional dominant, invariant subspace of a real, asymmetric, $N \times N$ matrix, \underline{A} — or equivalently, finding the subspace spanned by the m dominant eigenvectors, \underline{z}_i , which satisfy

$$\underline{A} \underline{z}_i = \lambda_i \underline{z}_i \quad i = 1, 2, \dots, m \quad (\text{A.1})$$

where $|\lambda_1| > |\lambda_2| > \dots > |\lambda_m|$. In the first paper he laid out the mathematical foundations; in the second, the practical details. Here, Stewart's algorithm is described, with emphasis on the main ideas and algorithmic structure.

Schur's theorem (see Stewart 1973 for proof), the cornerstone upon which Stewart's method is built, states that for every square complex matrix \underline{A} there exists a unitary matrix, \underline{X}' , the columns of which, \underline{x}_1' , \underline{x}_2' , ..., \underline{x}_N' , are Schur vectors of \underline{A} , i.e. vectors such that

$$\underline{S}' = \underline{X}'^H \underline{A} \underline{X}' \quad , \quad \underline{S}', \underline{X}', \underline{A} \in \mathbb{C}^{N \times N} \quad (\text{A.2})$$

is an upper-triangular matrix. The superscript H indicates the Hermitian transpose (i.e., the complex conjugate of the transpose) and $\mathbb{C}^{N \times N}$ signifies the space of $N \times N$ complex matrices. Obviously Equation (A.2) must hold under the restriction here that \underline{A} be real. The unitary matrix, \underline{X}' , may additionally be chosen so that the diagonal elements of \underline{S}' , which are the eigenvalues of \underline{A} , appear in descending order of absolute value

(i.e., absolute value of the square root of the product of an eigenvalue with its complex conjugate). This ordering is assumed in the following discussion. A method for finding the ordered triangular matrix \underline{S}' and Schur matrix \underline{X}' is given below.

The Schur vectors of a non-Hermitian matrix (i.e., matrix for which the Hermitian transpose is not equal to the matrix) enjoy many of the properties of the eigenvectors of a Hermitian matrix. They form an orthonormal basis set and are unique provided that the absolute values of the eigenvalues of \underline{A} are all distinct. If they are not and $|\lambda_{i-1}| > |\lambda_i| = |\lambda_{i+1}| = \dots = |\lambda_j| > |\lambda_{j+1}|$, then the Schur vectors $x'_i, x'_{i+1}, \dots, x'_j$ are not unique, but the subspace spanned by them is. Provided that $|\lambda_r| > |\lambda_{r+1}|$, the first r Schur vectors span the r -dimensional dominant subspace of \underline{A} , i.e., the subspace spanned by the eigenvectors corresponding to the r eigenvalues which are largest in absolute value. This is easily shown by multiplying Equation (A.2) by \underline{X}' to get

$$\underline{A} \underline{X}' = \underline{X}' \underline{S}' \quad , \quad (\text{A.3})$$

for if $\underline{X}'_r = (x'_1, x'_2, \dots, x'_r)$ and if \underline{S}'_r is the $r \times r$ leading principal submatrix of the upper-triangular matrix \underline{S}' , it follows that

$$\underline{A} \underline{X}'_r = \underline{X}'_r \underline{S}'_r \quad , \quad (\text{A.4})$$

which validates the above assertion. In the case where the absolute values of the eigenvalues of \underline{A} are distinct, it follows from the triangu-

larity of \underline{S}_r^i and the arbitrariness of r that: (1) the first Schur vector is the first eigenvector of \underline{A} ; (2) the second Schur vector is the linear combination of the first two eigenvectors of \underline{A} that makes it orthogonal to the first Schur vector; and (3) the k -th Schur vector is likewise that linear combination of the first k eigenvectors of \underline{A} that makes it orthogonal to the first $k-1$ Schur vectors. Because of the uniqueness properties of the Schur vectors, the third point holds for \underline{X}^i whenever $|\lambda_{k-1}| > |\lambda_k| > |\lambda_{k+1}|$ even if the absolute values of the eigenvalues of \underline{A} are not all distinct.

The eigenproblem is practically solved once the solution to equation (A.5) is found, because the r dominant eigenvalues appear along the diagonal of \underline{S}_r^i , and the corresponding eigenvectors can easily be computed by solving the $r \times r$ eigenproblem

$$\underline{S}_r^i \underline{y}_k^i = \lambda_k \underline{y}_k^i \quad k = 1, 2, \dots, r \quad (\text{A.5})$$

for \underline{y}_k^i and then premultiplying by \underline{X}_r^i to get

$$\underline{z}_k = \underline{X}_r^i \underline{y}_k^i \quad k = 1, 2, \dots, r \quad (\text{A.6})$$

Equations (A.4) and (A.5) imply Equation (A.6) because

$$\underline{A}(\underline{X}_r^i \underline{y}_k^i) = (\underline{X}_r^i \underline{S}_r^i) \underline{y}_k^i = \lambda_k (\underline{X}_r^i \underline{y}_k^i), \quad (\text{A.7})$$

so that $(\underline{X}_r^i \underline{y}_k^i)$ must be the eigenvector of \underline{A} corresponding to the eigenvalue λ_k , and therefore it must be the same as \underline{z}_k .

The original problem of finding the dominant subspace of \underline{A} is now

reduced to two subproblems. First, Equation (A.4) must be solved to find the Schur matrix, \underline{X}' , and the upper triangular matrix, \underline{S}' . Then, Equations (A.5) and (A.6) have to be solved to find the eigenvectors, \underline{z} . A difficulty with this strategy is that complex arithmetic has to be used extensively whenever two or more of the eigenvalues are complex conjugate pairs. Furthermore, solving Equation (A.5) requires using an algorithm to find the eigenvectors of a complex matrix. As a result, the computer memory required to store \underline{X}' and \underline{S}' would be doubled and the computation time needed to find the dominant subspace of \underline{A} would be significantly greater than in the situation where only real arithmetic is required. Fortunately, complex arithmetic can be avoided entirely by working with what Stewart calls the "quasi-Schur form." The triangular \underline{S}' is traded for a quasi-triangular \underline{S}_r :

$$\underline{S}_r = \underline{X}_r^T \underline{A} \underline{X}_r, \quad \underline{S}_r \in \mathbb{R}^{r \times r}, \quad \underline{X}_r \in \mathbb{R}^{n \times r} \quad (\text{A.8})$$

and the matrix of quasi-Schur vectors, $\underline{X}_r = (\underline{x}_1, \underline{x}_2, \dots, \underline{x}_r)$, needs only to be orthogonal instead of unitary. By quasi-triangular is meant that either $|x|$ or 2×2 block matrices appear along the diagonal; the $|x|$ and 2×2 blocks contain real eigenvalues and complex conjugate pairs, respectively. The existence of a solution to Equation (A.8) for arbitrary real \underline{A} was proved by Wilkinson (1965). Schur's theorem can be applied to \underline{S}_r to show that

$$\underline{S}' = \underline{X}^{*H} \underline{S}_r \underline{X}^* = (\underline{X}_r \underline{X}_r^*)^H \underline{A} (\underline{X}_r \underline{X}_r^*) = \underline{X}_r'^H \underline{A} \underline{X}_r' \quad (\text{A.9})$$

and therefore that

$$\underline{X}' = \underline{X} \underline{X}^* \quad (\text{A.10})$$

The first equality in Equation (A.9) follows from the uniqueness properties of the triangular matrix \underline{S}' . Equation (A.10) establishes that the Schur matrix, \underline{X}' , is just the product of the orthogonal quasi-Schur matrix, \underline{X} , and an $r \times r$ unitary matrix, \underline{X}^* . The first equality in Equation (A.9) also establishes that

$$\underline{S}_r = \underline{X}^* \underline{S}' \underline{X}^{*H} \quad (\text{A.11})$$

so that the quasi-triangular \underline{S}_r can always be constructed by a unitary transformation of the triangular \underline{S}' .

In practice, \underline{S}_r can be found directly, and thus \underline{S}' need never be obtained. This is what Stewart's method does, and thereby it avoids complex arithmetic. The eigenvectors of \underline{A} can be found once \underline{S}_r and \underline{X} are known by using the quasi-Schur equivalents of Equations (A.5) and (A.6):

$$\underline{S}_r \underline{y}_k = \lambda_k \underline{y}_k \quad k = 1, 2, \dots, r \quad (\text{A.12})$$

$$\underline{z}_k = \underline{X} \underline{y}_k \quad k = 1, 2, \dots, r \quad (\text{A.13})$$

The next few paragraphs sketch out the three main steps in Stewart's algorithm for solving Equation (A.9). A simple numerical example serves to illustrate each of the main steps. Subsequent paragraphs describe how these three main steps and interconnecting logic form the overall algo-

rithm. The final paragraph summarizes some of the practical aspects of implementing this algorithm.

The power step is, in the iterative procedure of the algorithm, the most frequently executed, and in a sense it is the most important of the three main steps. It is solely responsible for the convergence from an initial subspace represented by the matrix $Q_r^{(0)} \equiv (q_1^{(0)}, q_2^{(0)}, \dots, q_r^{(0)})$ to the dominant subspace, which is represented by the quasi-Schur matrix $X_r = (\underline{x}_1, \underline{x}_2, \dots, \underline{x}_r)$. The power step is amazingly simple: it is little more than a matrix multiplication. In the case that only one eigenpair is sought, the v -th iterate $q^{(v)}$ defined by

$$q^{(v)} \equiv A^v q^{(0)} / \lambda_1^v \quad (A.14)$$

converges to \underline{z}_1 as v increases provided that γ_1 is nonzero in the expansion

$$q^{(0)} = \sum_{i=1}^N \gamma_i \underline{z}_i \quad (A.15)$$

and also that the first eigenvalue of A dominates:

$$|\lambda_1| > |\lambda_2| > |\lambda_3| > \dots > |\lambda_N|. \quad (A.16)$$

This is easily shown, because Equation (A.14) is equivalent to

$$q^{(v)} = \gamma_1 \underline{z}_1 + \sum_{i=2}^N \gamma_i |\lambda_i / \lambda_1|^v \underline{z}_i, \quad (A.17)$$

and $|\lambda_i / \lambda_1| < 1$ for $i = 2, 3, \dots, N$. Equation (A.14) cannot be used in

practice because λ_1 is not known a priori. Furthermore, computation of \underline{A}^v requires an inordinate amount of work, about N^3 multiplications and additions per iteration when \underline{A} is full. These problems are overcome by replacing Equation (A.16) by

$$\underline{q}^{(v+1)} = \underline{A} \cdot \underline{q}^{(v)} / c^{(v)} \quad , \quad (\text{A.18})$$

where $c^{(v)}$ is the Euclidean norm of $\underline{A} \cdot \underline{q}^{(v)}$, i.e., $c^{(v)}$ is the square root of the sum of the squares of the absolute values of the elements in $\underline{A} \cdot \underline{q}^{(v)}$. In practice, the normalization need not be done at each iteration. For comparison, Equation (A.18) requires only about $N^2 + N$ multiplications and additions per iteration. Unfortunately, $\underline{q}^{(v)}$ will not converge when the first two eigenvalues have equal absolute values. For example, if the eigenvalues are dominated by a complex pair so that the first inequality in Equation (A.16) does not hold, but

$$|\lambda_1| > |\lambda_2| > |\lambda_3| > \dots > |\lambda_N| \quad . \quad (\text{A.19})$$

does hold, then the iteration defined by

$$\underline{Q}_2^{(v+1)} = \underline{A} \underline{Q}_2^{(v)} (\underline{C}^{(v)})^{-1} \quad , \quad (\text{A.20})$$

where $\underline{Q}_2^{(v)} \equiv (\underline{q}_1^{(v)}, \underline{q}_2^{(v)})$ and $\underline{C}^{(v)}$ is diagonal matrix with elements equal to the Euclidean norms of $\underline{A} \underline{q}_1^{(v)}$, and $\underline{A} \underline{q}_2^{(v)}$, converges to the dominant subspace. However, convergence of $\underline{Q}_r^{(v)}$ to the dominant subspace of \underline{A} cannot be guaranteed even when $|\lambda_r| > |\lambda_{r+1}|$ if finite decimal arithmetic is used. Consider the third-order matrix

$$A \equiv \begin{bmatrix} 3 & 0 & 0 \\ 4 & 2 & 0 \\ 0 & 0 & 1 \end{bmatrix}, \quad (A.21)$$

which has eigenvalues and eigenvectors

$$(\lambda_1, \lambda_2, \lambda_3) = (3, 2, 1), \quad (\underline{z}_1, \underline{z}_2, \underline{z}_3) = \begin{bmatrix} 1 & 0 & 0 \\ 4 & 1 & 0 \\ 0 & 0 & 1 \end{bmatrix} \quad (A.22)$$

If the initial guess is

$$\underline{Q}_2^{(0)} \equiv \begin{bmatrix} 1 & 1 \\ 1 & 0 \\ 1 & -1 \end{bmatrix}, \quad (A.23)$$

equation (A.21) gives the result (without normalization):

$$\underline{Q}_2^{(v)} = \begin{bmatrix} 3^v & 3^v \\ 4 \cdot (3^v - 2^v) + 2^v & 4 \cdot (3^v - 2^v) \\ 1 & -1 \end{bmatrix} \quad (A.24)$$

Taking the limit $v \rightarrow \infty$ and normalizing gives

$$\underline{Q}_2 \equiv \lim_{v \rightarrow \infty} \underline{Q}_2^{(v)} = \begin{bmatrix} 1 & 1 \\ 4 & 4 \\ 0 & 0 \end{bmatrix} / \sqrt{17} \quad (A.25)$$

Both vectors converge to the dominant eigenvector, \underline{z}_1 ! This could have

been foreseen inasmuch as $|\lambda_1| > |\lambda_2|$ and both $\underline{q}_1^{(0)}$ and $\underline{q}_2^{(0)}$ contain some component of the first eigenvector. In finite decimal arithmetic the problem is even more severe; after a finite number of steps $\underline{q}_1^{(v)}$ and $\underline{q}_2^{(v)}$ become identical. This shortcoming is remedied by periodically orthonormalizing the columns of $\underline{Q}_2^{(v)}$. This orthonormalization is the second main step in Stewart's algorithm.

A Gram-Schmidt orthonormalization step is the second step. In it the columns of $\underline{Q}_r^{(v)}$ are normalized and made orthogonal:

$$\bar{\underline{Q}}_r^{(v)} = \underline{Q}_r^{(v)} (\underline{R}_r^{(v)})^{-1} \quad (\text{A.26})$$

where $\underline{R}_r^{(v)}$ is an $r \times r$ upper triangular matrix chosen by a modified Gram-Schmidt algorithm to orthonormalize $\underline{Q}_r^{(v)}$ (see Stewart 1973 and, for a program, Rutishauser 1970). The second step need not be executed after each power step, but just frequently enough to assure that the columns of $\underline{Q}_r^{(v)}$ do not become linearly dependent. While the Gram-Schmidt method is less stable numerically than Householder's method (see Stewart 1973), it is computationally efficient and simple to program. In practice, numerical instability is restrained by adopting a conservative criterion for the frequency to perform the orthonormalization step. This criterion is described below.

In the above example an orthonormalization of $\underline{Q}_2^{(v)}$ before taking the limit $v \rightarrow \infty$ produces the result:

$$\bar{\underline{Q}}_2 = \begin{bmatrix} 1 & 4 \\ 4 & -1 \\ 0 & 0 \end{bmatrix} / \sqrt{17} \quad (\text{A.27})$$

The column vectors of \underline{Q}_2 do span the dominant subspace of \underline{A} , and in fact \underline{Q}_2 is identical to the quasi-Schur matrix \underline{X}_2 . The dominant eigenvalues are found by forming the unitary projection of the matrix \underline{A} into \underline{Q}_2 , as defined in Equation (A.8):

$$\underline{S}_2 = \begin{bmatrix} 3 & 4 \\ 0 & 2 \end{bmatrix} \quad (\text{A.28})$$

The diagonal elements of \underline{S}_2 are the dominant eigenvalues of \underline{A} , which are recorded in Equation (A.22). The eigenvectors of \underline{A} are found by solving Equation (A.12) for (y_1, y_2) and then solving Equation (A.13) for (z_1, z_2) .

$$(y_1, y_2) = \begin{bmatrix} 1 & 4/\sqrt{17} \\ 0 & -1/\sqrt{17} \end{bmatrix} \quad (\text{A.29})$$

$$(z_1, z_2) = \begin{bmatrix} 1/\sqrt{17} & 4/\sqrt{17} \\ 4/\sqrt{17} & -1/\sqrt{17} \\ 0 & 0 \end{bmatrix} \begin{bmatrix} 1 & 4/\sqrt{17} \\ 0 & -1/\sqrt{17} \end{bmatrix} = \begin{bmatrix} 1/\sqrt{17} & 0 \\ 4/\sqrt{17} & 1 \\ 0 & 0 \end{bmatrix} \quad (\text{A.30})$$

These are indeed the first and second eigenvectors of \underline{A} , which are recorded in Equation (A.22).

The above solution was obtained as a limit, i.e. by letting the iteration count v increase without bound. A numerical algorithm on the other hand must terminate after a finite number of iterations. Obviously, a convergence criterion has to be constructed. This leads to the third main step in Stewart's algorithm, which he calls the Schur-Rayleigh-Ritz step, or SRR step for short. The SRR step is exe-

cuted prior to each convergence test, and it can accelerate convergence as well. The acceleration of convergence is not due to an improvement in the current estimate of the dominant subspace, but rather to an "unscrambling" of the vectors which span the current estimate of the dominant subspace. This unscrambling of vectors amounts to improving the accuracy of the more dominant quasi-Schur vector approximates by using information contained in the less dominant approximates. For example, if an r -dimensional subspace is carried in the iteration process, but only an m -dimensional dominant subspace is sought, where $m < r$, the SRR step reduces the number of iterations needed to obtain a solution of given accuracy, as compared with the number needed without the SRR step. On the other hand, where $m = r$ the number of iterations would not be reduced by the SRR step, but the computational work would be reduced nevertheless because of a deflation process that is included in Stewart's algorithm, as discussed below. The SRR step proceeds as follows. First, \underline{A} is projected into the subspace the basis of which is the approximate set of quasi-Schur vectors, $\tilde{\underline{Q}}^{(v)}$:

$$\underline{B}^{(v)} = (\tilde{\underline{Q}}^{(v)})^T \underline{A} \tilde{\underline{Q}}^{(v)} \quad (\text{A.31})$$

Then Schur's theorem is applied to $\underline{B}^{(v)}$:

$$\underline{T}^{(v)} = (\underline{Y}^{(v)})^T \underline{B}^{(v)} \underline{Y}^{(v)} \quad (\text{A.32})$$

to obtain the set of quasi-Schur vectors, $\underline{Y}^{(v)}$, and $\underline{T}^{(v)}$, the quasi-triangular unitary transformation of $\underline{B}^{(v)}$. The method employed to

solve Equation (A.32) is the well-known QR algorithm with double implicit shifts (see Stewart 1973 and Wilkinson 1965 for a comprehensive description) modified to order blocks of eigenvalues as they emerge (see Smith et al. 1974 and Wilkinson and Reinsch 1971 for FORTRAN programs). The dominant eigenvalues of \underline{A} are approximated by the eigenvalues of the 1×1 and 2×2 diagonal blocks of $\underline{T}^{(v)}$, and the dominant quasi-Schur vectors are approximated by the columns of

$$\underline{\tilde{Q}}^{(v)} \equiv \underline{\tilde{Q}}^{(v)} \underline{Y}^{(v)} \quad . \quad (\text{A.33})$$

Stewart (1976) showed that $\underline{\tilde{Q}}^{(v)}$ is a better approximation to the quasi-Schur matrix than $\underline{\tilde{Q}}^{(v)}$. This fact can be understood in an intuitive way by noting that in

$$\underline{T}^{(v)} = (\underline{Y}^{(v)})^T \underline{B}^{(v)} \underline{Y}^{(v)} = (\underline{Y}^{(v)} \underline{\tilde{Q}}^{(v)})^T \underline{A} (\underline{Y}^{(v)} \underline{\tilde{Q}}^{(v)}) = (\underline{\tilde{Q}}^{(v)})^T \underline{A} \underline{\tilde{Q}}^{(v)} \quad . \quad (\text{A.34})$$

the columns of $\underline{\tilde{Q}}^{(v)}$ form a different basis set for the same subspace as is spanned by $\underline{\tilde{Q}}^{(v)}$, a basis set so chosen that it quasi-triangularizes \underline{A} . Although Equations (A.34) and (A.8) look alike, they are not identical because $\underline{\tilde{Q}}^{(v)}$ need not span the dominant subspace. However, as v increases, $\underline{\tilde{Q}}^{(v)}$ and $\underline{T}^{(v)}$ do approach \underline{X} and \underline{S} , respectively.

The benefit of introducing the SRR step is brought out clearly by returning to the previous example. Setting $v = 5$ in Equation (A.24) provides an approximation to the dominant subspace of \underline{A} :

$$\underline{Q}_2^{(5)} = \begin{bmatrix} 243 & 243 \\ 844 & 812 \\ 1 & -1 \end{bmatrix} \quad (\text{A.35})$$

An application of the orthonormalization step produces

$$\tilde{\underline{Q}}_2^{(5)} = \begin{bmatrix} 0.27668 & 0.93820 \\ 0.96096 & -0.26987 \\ 0.00114 & -0.21667 \end{bmatrix} \quad (\text{A.36})$$

The accuracy of $\tilde{\underline{Q}}_2^{(5)}$ can be determined by forming its product with the exact quasi-Schur matrix from Equation (A.27),

$$\tilde{\underline{Q}}_2 \cdot \tilde{\underline{Q}}_2^{(5)} = \begin{bmatrix} 0.99937 & -0.03426 \\ 0.03535 & 0.97564 \end{bmatrix}. \quad (\text{A.37})$$

The departure of this result from the 2 x 2 identity matrix indicates the magnitude of the remaining error. Equation (A.37) also conveys the following information: (1) the first column vector in $\tilde{\underline{Q}}_2^{(5)}$ is much more closely parallel to its corresponding quasi-Schur vector than is the second column of $\tilde{\underline{Q}}_2^{(5)}$, as revealed by the closeness to unity of the diagonal elements; (2) the two column vectors of $\tilde{\underline{Q}}_2^{(5)}$ contain about equal components of the opposite quasi-Schur vectors, as revealed by the off-diagonal elements; and (3) therefore the second vector in $\underline{Q}_2^{(5)}$ contains a larger component of the omitted third quasi-Schur vector. The third

point results from the fact that the complete set of quasi-Schur vectors forms an orthonormal basis for the vector space. All three points are predicted by Stewart's convergence rate analysis, which is set out below.

The estimate of the dominant quasi-Schur vectors in Equation (A.36) can be improved by taking an SRR step. First, equation (A.31) is solved for $\underline{B}_2^{(5)}$ and then Equation (A.32) is solved for $\underline{Y}_2^{(5)}$ and $\underline{T}_2^{(5)}$:

$$\underline{B}_2^{(5)} = \begin{bmatrix} 3.14005 & 3.86636 \\ -0.03861 & 1.82052 \end{bmatrix} \quad (\text{A.38})$$

$$\underline{Y}_2^{(5)} = \begin{bmatrix} 0.99948 & 0.03230 \\ -0.03230 & 0.99948 \end{bmatrix} \quad (\text{A.39})$$

The first column vector of $\underline{Y}_2^{(5)}$ is the normalized dominant eigenvector of $\underline{B}_2^{(5)}$; the second is chosen to make the pair orthonormal.

$$\underline{T}_2^{(5)} = \begin{bmatrix} 3.01509 & 3.90498 \\ 0 & 1.94549 \end{bmatrix}. \quad (\text{A.40})$$

The dominant eigenvalues are approximated by the diagonal elements of $\underline{T}_2^{(5)}$ (cf. Equations (A.22) and (A.28)). Finally, $\underline{Q}_2^{(5)}$ is computed from Equation (A.33):

$$\underline{Q}_2^{(5)} = \begin{bmatrix} 0.24623 & 0.94665 \\ 0.96133 & -0.23869 \\ 0.00814 & -0.21652 \end{bmatrix} \quad (\text{A.41})$$

Premultiplying $\tilde{Q}_2^{(5)}$ by the exact quasi-Schur matrix, \tilde{Q}_2 , given in Equation (A.27) then leads to a revealing comparison with equation (A.37)

$$\tilde{Q}_2 \tilde{Q}_2^{(5)} = \begin{bmatrix} 0.99235 & -0.00197 \\ 0.00572 & 0.97628 \end{bmatrix} \quad (\text{A.42})$$

The off-diagonal elements in Equation (A.42) are smaller in magnitude than those in Equation (A.37) by an order of magnitude. The unscrambling process performed by the SRR step brings about an improvement in the approximate quasi-Schur vectors by making each of them more nearly orthogonal to all of the exact quasi-Schur vectors except the one to which it is converging. The convergence criterion used in Equations (A.37) and (A.42) cannot be used in practice because the exact quasi-Schur matrix is not known a priori. A suitable convergence criterion is to require that the first m column vectors of the residual matrix defined by

$$\underline{R}^{(v)} = \underline{A} \tilde{\underline{Q}}^{(v)} - \tilde{\underline{Q}}^{(v)} \underline{T}^{(v)} \quad (\text{A.43})$$

have small norms:

$$\|\underline{R}_i^{(v)}\|_\infty < \epsilon \quad \text{for } i = 1, 2, \dots, m, \quad (\text{A.44})$$

where $\underline{R}^{(v)} \equiv (\underline{R}_1^{(v)}, \underline{R}_2^{(v)}, \dots, \underline{R}_r^{(v)})$ and $\|\cdot\|_\infty$ is the Chebyshev norm, i.e., the maximum of the absolute values of the elements in a vector.

Computing $\underline{R}_2^{(5)}$ for the above example gives

$$\underline{R}_2^{(5)} = \begin{bmatrix} -0.00372 & 0.03673 \\ 0.00908 & 0.01961 \\ -0.01640 & -0.17293 \end{bmatrix} \quad (\text{A.45})$$

The Chebyshev norms of the column vectors of $\underline{R}_2^{(5)}$ are 0.01640 and 0.17293. These indicate the errors in the two approximate quasi-Schur vectors, $\underline{q}_1^{(5)}$ and $\underline{q}_2^{(5)}$, respectively. The first is seen to be more accurate than the second by an order of magnitude.

Stewart (1976) proved that this scheme converges provided $|\lambda_r| > |\lambda_{r+1}|$. Furthermore, he proved that if $|\lambda_r| > |\lambda_{r+1}|$, the subspace spanned by the first r vectors in $\underline{Q}_r^{(v)}$ converges to the r -dimensional dominant subspace of \underline{A} at the rate $O(|\lambda_{r+1}/\lambda_r|^v)$. Unfortunately, the requirement that $|\lambda_r| > |\lambda_{r+1}|$ is necessary for convergence. In practice, there is a danger that r could be so chosen that a complex conjugate pair of eigenvalues straddles the cutoff. Stewart (1976) shows by a 3×3 example that this would prevent the algorithm from converging. The only practical insurance against this hazard is to increase or decrease the subspace dimension, r , by one when it appears that the iterative procedure is not converging.

Figure A.1 is a flowchart of Stewart's algorithm which shows the three main steps and interconnecting logic. This flowchart is described in the following paragraph with emphasis on the interconnecting logic.

The algorithm begins by initializing $\underline{Q}^{(0)}$, either by continuation or by a random process. If zeroth-order continuation is used, the initial guess is a set of vectors which span the dominant subspace at a

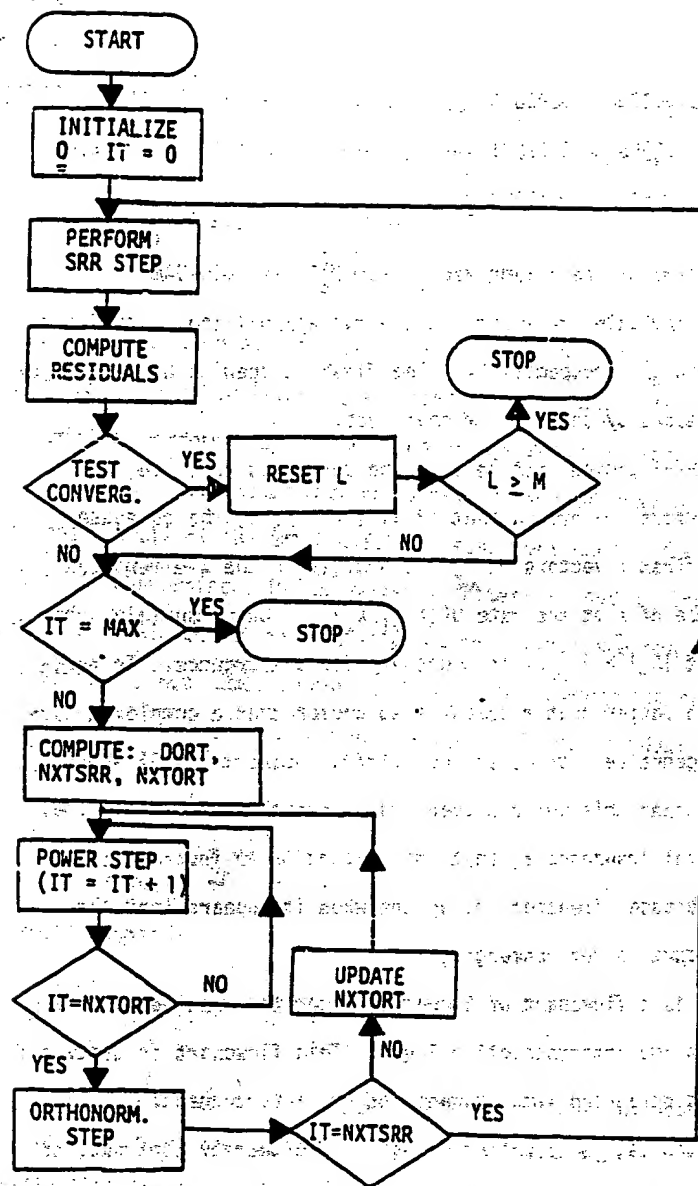


Figure A.1. Flowchart of Stewart's Algorithm.

nearby point in the parameter space; if first-order continuation is used, the initial guess is generated by linear extrapolation from a nearby point in the parameter space, as described by Silliman (1979). The alternative to continuation is to assign values to the elements of $\underline{Q}^{(0)}$ by using a random number generator. In either case, orthonormalization is performed (unless unnecessary) to complete the initialization, after which an SRR step is taken and residuals computed. A check is made to see if the first previously unconverged column vector has converged (initially the first vector). If so, the parameter, L , which points to the first unconverged vector in $\underline{Q}^{(v)}$, is incremented. The $(L-1)$ converged column vectors in $\underline{Q}^{(v)}$ are skipped over in most subsequent operations in order to save computation time. This process is called deflation (see Stewart 1976). When $L > M$, M being the dimension of the dominant subspace which is sought, the calculations are halted. Eigenvectors, if desired, are computed in a post-processing step as described above. If $L < M$, the iteration counter, I , is compared with a user-specified maximum, MAX . The computations stop if $I = MAX$; otherwise, the parameters $NXTSRR$ and $NXTORT$ are calculated, these being the iteration numbers at which the next SRR and orthonormalization steps, respectively, should be performed. $NXTSRR$ is set to the minimum of three values: (1) the maximum number of iterations, MAX ; (2) the iteration at which the next quasi-Schur vector is expected to converge; and (3) twice the previous value of $NXTSRR$ (set to 5 initially). The iteration number on which the next quasi-Schur vector is expected to converge is computed by extrapolation using the linear convergence rate predicted by Stewart. The

third criterion is necessary because linear convergence only occurs asymptotically. NXTORT is set to the minimum of SRR and $I + \text{DORT}$, where DORT is calculated from a conservative formula (see Stewart 1976) which insures that no more than eight decimals of accuracy can be lost during an orthonormalization step. Next, the power step is repeated until $I = \text{NXTORT}$. I is incremented after each power step. An orthonormalization step is then taken, after which NXTORT is set to the minimum of NXTSRR and $I + \text{DORT}$. The power and orthonormalization steps are continued in this fashion until $I = \text{NXTSRR}$. The cycle is then repeated beginning with the SRR step and continuing until either the convergence criterion is satisfied or the maximum number of iterations is reached.

A single call to a subroutine called SRRIT, which drives other subroutines, is required to activate Stewart's algorithm. The user must specify parameters which set the number of column vectors in the matrix, $Q^{(v)}$, the dimension of the dominant subspace to be found, the maximum number of power step iterations to be taken, and the method of initialization for $Q^{(0)}$ — either by continuation or by a random assignment process. The writer found that the number of iterations needed to attain convergence (with $\epsilon = 10^{-8}$ in Equation (A.44)) was typically reduced by an order of magnitude when the initial guess was generated by zeroth-order continuation rather than by random guess. A subroutine, which Stewart called ATQ, must be supplied by the user to premultiply $Q^{(v)}$ by A . The smallest eigenvalues (in the sense of absolute value) of Equation (A.1) can be found by Stewart's algorithm by rewriting that equation as

$$\underline{A}^{-1} \underline{z}_i = \eta_i \underline{z}_i, \quad (\text{A.46})$$

where $\eta_i = 1/\lambda_i$, inasmuch as the largest η_i correspond to the smallest λ_i . The smallest eigenvalues of the generalized eigenproblem,

$$\underline{J} \underline{z}_i = \lambda_i \underline{M} \underline{z}_i, \quad (\text{A.47})$$

can also be found by transforming the problem to

$$\underline{J}^{-1} \underline{M} \underline{z}_i = \eta_i \underline{z}_i. \quad (\text{A.48})$$

Only the subroutine ATQ need be changed to solve Equation (A.48). Given the iterate, $\underline{Q}^{(v)}$, the next iterate is calculated by first premultiplying it by \underline{M} and then solving the linear system

$$\underline{J} \underline{Q}^{(v+1)} = \underline{M} \underline{Q}^{(v)} \quad (\text{A.49})$$

for $\underline{Q}^{(v+1)}$. Because this linear system has to be solved many times during the iteration process, much computational efficiency is gained by computing the triangular decomposition of \underline{J} (see Wilkinson 1965) before the first iteration. When \underline{J} is the Jacobian matrix for a set of equations generated by the finite element method, it is convenient to use Hood's frontal method (see Hood 1976) to triangularize \underline{J} . Solving Equation (A.49) then requires only a call to Hood's subroutine RESOL, which needs to be modified to accommodate multiple right-hand sides.

The eigenvalues of Equation (A.47) found by the strategy outlined

above are those of smallest magnitude; the eigenvalues sought in coating flow stability analysis are those of smallest real part. These two sets of eigenvalues — the ones found by applying Stewart's algorithm to Equation (A.48) and those of greatest importance to stability assessment — will be the same provided the eigenvalues nearest the imaginary axis do not have imaginary parts that are large compared with the magnitude of other eigenvalues near the imaginary axis (see also Chapter 5). A bilinear mapping, described in Chapter 5, can be used to transform eigenvalues of smallest real part into ones of smallest magnitude so that they can be identified easily.

Bibliography

- Amundson, N. R. 1966 Mathematical Methods in Chemical Engineering. Prentice-Hall, Englewood Cliffs.
- Anderson, R. G., Irons, B. M., and Zienkiewicz 1968 Vibration and stability of plates using finite elements. Int. J. Solids and Structures. 4, 1031.
- Anshus, B. E. 1973 The leveling in polymer powder painting — a three-dimensional approach. ACS Org. Coating and Plastics Chem. 33, 493.
- Aris, R. 1962 Vectors, Tensors, and the Basic Equations of Fluid Mechanics. Prentice-Hall, Englewood Cliffs.
- Batchelor, G. K. 1973 An Introduction to Fluid Mechanics. Cambridge University Press, Cambridge.
- Bathe, K. J., and Wilson, E. L. 1972 Large eigenvalue problems in dynamic analysis. ASCE, J. Engng. Mech. Div. 98, 1471.
- Bathe, K. J., and Wilson, E. L. 1973 Solution methods for eigenvalue problems in structural mechanics. Int. J. Num. Meth. Engng. 6, 213.
- Bauer, F. L. 1957 Das verfahren der treppeniteration und verwandte verfahren zur lösung algebraischer eigenwertprobleme. Z. Angew. Math. Phys. 8, 214.
- Bretherton, F. P. 1961 The motion of long bubbles in tubes. J. Fluid Mech. 10, 166.
- Brown, R. A. 1979 The shape and stability of three-dimensional interfaces. Ph.D. Thesis, University of Minnesota, Minneapolis.
- Brown, R. A. and Scriven, L. E. 1980a On the multiple equilibrium shapes and stability of an interface pinned on a slot. J. Colloid Interf. Sci. 78, 528.
- Brown, R. A. and Scriven, L. E. 1980b The shapes and stability of captive rotating drops. Phil. Trans. Roy. Soc. London 297, 51.
- Brown, R. A. 1982 Private communication.
- Cameron, A. 1976 Basic Lubrication Theory. Wiley, New York.
- Carson, W. G. and Newton, R. E. 1969 Plate buckling analysis using a fully compatible finite element. J.A.I.A.A. 8, 527.

- Chandrasekhar, S. 1961 Hydrodynamic and Hydromagnetic Stability. Oxford University Press, Oxford.
- Churchill, R. V., Brown, J. W., and Verhey, R. F. 1974 Complex Variables and Applications. McGraw-Hill, New York.
- Clint, M., and Jennings, A. 1971 A simultaneous iteration method for the unsymmetric eigenvalue problem. J. Inst. Maths. Applics. 8, 111.
- Cox, C. B. 1962 On driving a viscous fluid out of a tube. J. Fluid Mech. 14, 81.
- Coyle, D. J., Macosko, C. W., and Scriven, L. E. 1982a Finite element analysis of reverse roll coating. To be presented at the Annual Meeting of the American Institute of Chemical Engineers, Los Angeles, California.
- Coyle, D. J., Macosko, C. W., and Scriven, L. E. 1982b Computer simulation of nip flow in roll coating. Computer Applications in Coatings and Plastics. ACS Symposium Series.
- Coyne, J. C. and Elrod, H. G. 1969 An exact asymptotic solution for a separating film. J. Lub. Tech. Oct., 651.
- Dong, S. B. 1977 A block-Stodola eigensolution technique for large algebraic systems with nonsymmetrical matrices. Int. J. Num. Meth. Engng. 11, 247.
- Dong, S. B., Wolf, J. A. Jr., and Peterson, F. E. 1972 On a direct-iterative eigensolution technique. Int. J. Num. Meth. Engng. 4, 155.
- Drazin, P. G. and Reid, W. H. 1981 Hydrodynamic Stability. Cambridge University Press, Cambridge.
- Fall, C. 1978 Surface ribbing of a thin viscous fluid film emerging from a spreader or roller. J. Lub. Tech. 100, 462.
- Friedman, B. 1956 Principles and Techniques of Applied Mathematics. John Wiley & Sons, Inc., New York.
- Francis, J. G. F. 1961 The QR transformation, Part I. Computer J. 4, 265.
- Francis, J. G. F. 1962 The QR transformation, Part II. Computer J. 4, 332.
- Gallagher, R. H. and Padlog, J. 1963 Discrete element approach to structural instability analysis. J.A.I.A.A. 1, 1537.

- Groenvelt, P. and Van Dortmund, R. A. 1970 The shape of the air interface during the formation of viscous liquid films by withdrawal. Chem. Eng. Sci. 25, 1571.
- Gumbel, L. R. K. 1921 Vergleich der Ergelbrusse der rectinerischen Behandlung des Lagerschmierangsproblem mit neueren Veisuchsergebrussen. Monatsbl. Berliner Bez. Ver. Dtsch. Ing., Sept., 125.
- Gupta, K. K. 1969 Free vibrations in single-branch structural systems. J. Inst. Math. Applics. 5, 351.
- Gupta, K. K. 1970 Vibration of frames and other structures with banded stiffness matrix. Int. J. Num. Meth. Engng. 2, 221.
- Gupta, K. K. 1973 Eigenproblem solution by a combined Sturm sequence and inverse iteration technique. Int. J. Num. Meth. Engng. 7, 17.
- Gupta, K. K. 1972 Solution of eigenvalue problems by Sturm sequence method. Int. J. Num. Meth. Engng. 4, 379.
- Higgins, B. G. 1980 Capillary hydrodynamics and coating beads. Ph.D. Thesis, University of Minnesota, Minneapolis.
- Higgins, B. G. 1982 Downstream development of two-dimensional visco-capillary film flow. I & EC Fundam., submitted for publication.
- Higgins, B. G., Silliman, W. J., Brown, R. A., and Scriven, L. E. 1977 Theory of meniscus shape in film flows. A synthesis. I & EC Fundam. 16, 801.
- Hildebrand, F. B. 1974 Introduction to Numerical Analysis. McGraw-Hill, New York.
- Hopkins, M. R. 1957 Viscous flow between rotating cylinders and a sheet moving between them. Brit. J. Apply. Phys. 8, 442.
- Hood, P. 1976 Frontal solution program for unsymmetric matrices. Int. J. for Num. Meth. in Engng. 10, 379.
- Huh, C., and Scriven, L. E. 1971 Hydrodynamics model of steady movement of a solid/liquid/fluid contact line. J. Colloid Interf. Sci. 35, 85.
- Huyakorn, P. S., Taylor, C., Lee, R. L., and Gresho, P. M. 1978 A comparison of various mixed-interpolation finite elements in the velocity-pressure formulation of the Navier-Stokes equations. Computers and Fluids 6, 25.
- Isaacson, E. and Keller, H. B. 1966 Analysis of Numerical Methods. Wiley, New York.

- Jacobi, C. G. J. 1846 Über ein leichtes verfahren die in der theorie der secularstörungen vorkommenden gleichungen numerisch aufzulösen. Crelle's J. 30, 51.
- Jennings, A., and Orr, D. R. L. 1971 Application of the simultaneous iteration method to undamped vibration problems. Int. J. Num. Meth. Engng. 3, 13.
- Kapur, K. K. and Hartz, E. J. 1966 Stability of thin plates using the finite element method. Proc. Am. Soc. Civ. Eng. EM2, 177.
- Kheshgi, H. S. and Scriven, L. E. 1982 Measurement of liquid film profiles by More topography. Chem. Engng. Sci., in press.
- Kistler, S. F. and Scriven, L. E. 1982 Coating flow computations in Computers in Polymer Processing. (eds. J. R. A. Pearson and S. M. Richardson, to be published).
- Kobayashi, C., Saito, H., and Scriven, L. E. 1982 Study of slide coating by finite element method. Presented at the Winter National Meeting of the American Institute of Chemical Engineers, Orlando, Florida.
- Kraynik, A. M. and Schowalter, W. R. 1977 Wall slip and extrudate roughness of aqueous solutions of polyvinyl alcohol and sodium borate. Presented at 48th Annual Meeting of the Society of Rheology, Univ. of Wisconsin, Madison, Wisconsin.
- Lamb, H. 1945 Hydrodynamics. Dover Publications, New York.
- Lin, C. C. and Segal, L. A. 1974 Mathematics Applied to Deterministic Problems in the Natural Sciences. Macmillan, New York.
- Martin, H. C. 1965 On the derivation of stiffness matrices for the analysis of large deflection and stability problems. Proc. Conf. Matrix Methods in Structural Mechanics. Wright-Patterson A.F. Base, Ohio.
- Mitchell, A. G. M. 1950 Lubrication, its Principles and Practice. Blackie & Son, Ltd., London.
- Moler, C. B. and Stewart, G. W. 1973 An algorithm for generalized matrix eigenvalue problems. SIAM J. Numer. Anal. 10, 241.
- Morse, P. M., Feshbach, H. 1953 Methods of Theoretical Physics, Part I. McGraw-Hill, New York.
- Navier, C. L. M. H. 1827 Mémoire sur les lois du mouvement des fluides. Mem. Acad. R. Sci. Inst. Fr. 6, 389.

- von Neumann, J., and Goldstine, H. H. 1947 Numerical inverting of matrices of high order. Bull. Amer. Math. Soc. 53, 1021.
- Oden, J. T. 1972 Finite Elements of Nonlinear Continua. McGraw-Hill, New York.
- Orchard, S. E. 1962 On surface levelling in viscous liquids and gels. Appl. Sci. Res. 11, 451.
- Orr, F. M. 1976 Numerical simulation of viscous flow with a free surface. Ph.D. Thesis, University of Minnesota, Minneapolis.
- Ortega, J. M. and Rheinboldt, W. C. 1970 Iterative Solutions of Non-linear Equations of Several Variables. Academic Press, New York.
- Pearson, J. R. A. 1960 The instability of slow viscous flow under rollers and spreaders. J. Fluid Mech. 7, 481.
- Pitts, E. and Greiller, J. 1961 The flow of thin liquid films between rollers. J. Fluid Mech. 11, 33.
- Prandtl, L. 1937 General discussion on lubrication. Proc. Inst. Mech. Eng. 182, 104.
- Reynolds, O. 1886 On the theory of lubrication and its application to Mr. Beauchamp Tower's experiments, including an experimental determination of the viscosity of olive oil. Phil. Trans. Roy. Soc. Lon. 177, 157.
- Ruschak, K. J. 1974 The fluid mechanics of coating flows. Ph.D. Thesis, University of Minnesota, Minneapolis.
- Ruschak, K. J. 1980 A method for incorporating free boundaries with surface tension in finite element fluid flow simulators. Int. J. Num. Meth. Engng. 15, 639.
- Ruschak, K. J. 1982 Linear stability analysis for free boundary flows by the finite element method. Presented at the Winter National Meeting of the American Institute of Chemical Engineers, Orlando, Florida.
- Rutishauser, H. 1955 Bestimmung der Eigenwerte und eigenvektoren einer matrix mit hilfe des quotienten-differenzen-algorithmus. Z. Angew. Math. Phys. 6, 387.
- Rutishauser, H. 1958 Solution of eigenvalue problems with the LR-transformation. Appl. Math. Ser. Nat. Bur. Stand. 49, 47.
- Rutishauser, H. 1960 Über eine kubisch konvergente der LR-transformation. Z. Angew. Math. Mech. 40, 49.

- Rutishauser, H. 1963 On Jacobi rotation patterns. Proceedings A.M.S. Symposium in Applied Mathematics 15, 219.
- Rutishauser, H. 1970 Simultaneous iteration method for symmetric matrices. Numer. Math. 16, 205.
- Saffman, P. G. and Taylor, G. I. 1958 The penetration of a fluid into
- Saito, H. and Scriven, L. E. 1981 Study of coating flow by the finite element method. J. Comp. Phys. 42, 53.
- Savage, M. D. 1977 Cavitation in lubrication. Part 2. Analysis of wavy interfaces. J. Fluid Mech. 80, 757.
- Schweitzer, P. M. and Scriven, L. E. 1982 Centrifugal instabilities in curved film flow. Presented at the Winter National Meeting of the American Institute of Chemical Engineers, Orlando, Florida.
- Silliman, W. J. and Scriven, L. E. 1978 Slip of a liquid inside a channel exit. Phys. Fluids 21, 2115.
- Silliman, W. J. 1979 Viscous film flows with contact lines. Ph.D. Thesis, University of Minnesota, Minneapolis.
- Silliman, W. J. and Scriven, L. E. 1980 Separating flow near a static contact line: slip at a wall and shape of a free surface. J. Comp. Phys. 34, 287.
- Smith, B. T., Boyle, J. M., Garbow, B. S., Ikebe, Y., Kiem, V. C., and Moler, C. B. 1974 Matrix Eigensystems Routines — EISPACK Guide. Springer-Verlag, New York.
- Stadtherr, M. A., Gifford, W. A., and Scriven, L. E. 1974 Efficient solution of sparse sets of design equations. Chem. Engng. Sci. 29, 1025.
- Stewart, G. W. 1969 Accelerating the orthogonal iteration for the eigenvectors of a Hermitian matrix. Numer. Math. 13, 362.
- Stewart, G. W. 1973 Introduction to Matrix Computations. Academic Press, New York.
- Stewart, G. W. 1975 Methods of simultaneous iteration for calculating eigenvectors of matrices. Topics in Numerical Analysis II, 185. Academic Press, New York.
- Stewart, G. W. 1976a Simultaneous iteration for computing invariant subspaces of non-Hermitian matrices. Numer. Math. 25, 123.

- Stewart, G. W. 1976b A bibliographical tour of the large, sparse generalized eigenvalue problem. Sparse Matrix Computations. (eds. J. R. Bunch and D. J. Rose, Academic Press, New York.)
- Stewart, G. W. 1978 SRRIT — a FORTRAN subroutine to calculate the dominant invariant subspaces of a real matrix. Technical Report TR-514, ONR-N00014-76-C-0391. University of Maryland Computer Science Center, College Park.
- Stieber, W. 1933 Das Schwimmlager. Ver. Dtsch. Ing., Berlin.
- Strang, G. and Fix, G. F. 1973 An Analysis of the Finite Element Method. Prentice-Hall, Englewood Cliffs.
- Swift, H. W. 1931 The stability of lubricating films in journal bearings. J. Inst. Civ. Eng. 233, 267.
- Taylor, G. I. 1963 Cavitation of a viscous fluid in narrow passages. J. Fluid Mech. 16, 595.
- Tipei, N. 1962 Theory of Lubrication, with Applications to Liquid- and Gas-Film Lubrication. Stanford University Press, Stanford.
- Traub, J. F. 1964 Iterative Methods for the Solution of Equations. Prentice-Hall, Englewood Cliffs.
- Weatherburn, C. E. 1927 Differential Geometry of Three Dimensions. Cambridge University Press, Cambridge.
- Wilkinson, J. H. 1965 The Algebraic Eigenvalue Problem. Clarendon Press, Oxford.
- Wilkinson, J. H. and Reinsch, C. (eds.) 1971 Handbook for Automatic Computation VII: Linear Algebra. Springer, New York.
- Wilson, S. 1969 The development of Poiseuille flow. J. Fluid Mech. 38, 793.

THIS PAGE BLANK (USPTO)